Spring 2023

Cyclodextrin Impedimetric Biosensors for the Detection of Hydrophobic Metabolites

Zahra Panahi
University of New Hampshire, Durham

Cyclodextrin Impedimetric Biosensors for the Detection of Hydrophobic Metabolites

By

Zahra Panahi

B.S. and M.S. in Chemical Engineering

Dissertation

Submitted to the University of New Hampshire

in Partial Fulfillment of

the Requirements for the Degree of

Doctor of Philosophy

In

Chemical Engineering

May 2023

This dissertation was examined and approved in partial fulfillment of the requirements for the degree of Doctor of Philosophy in Chemical Engineering by:

Dissertation Director, Dr. Jeffrey Halpern, Associate Professor of Chemical Engineering

Dr. Kyung Jae Jeong, Associate Professor of Chemical Engineering

Dr. Linqing Li, Assistant Professor of Chemical Engineering

Dr. Roy Planalp, Associate Professor of Chemistry

Dr. MD Shaad Mahmud, Assistant Professor of Electrical & Computer Engineering

On December 19, 2022.

Approval signatures are on file with the University of New Hampshire Graduate School.

Table of Contents

Acknowledgments

I would first like to express my special thanks to my advisor, Dr. Jeffrey Halpern for his support, patience, and guidance during this research. He is an excellent mentor and he helped me to grow inside and outside of my professional life. I would also like to thank my committee members, Dr. Kyung Jae Jeong, Dr. Roy Planalp, Dr. Linqing Li, and Dr. MD Shaad Mahmud for their time and feedback in reviewing my thesis. I want to acknowledge all the faculty members of Chemical Engineering Department and SEEDS Lab members both present and past. I would additionally thank Darcy Silver at Technical Service Center and John Wildermann and other members of University Instrumentation Center.

I would like to acknowledge the Graduate School and Department of Chemical Engineering and all the funding sources for this project including Institutional Development Award (IDeA) from the National Institute of General Medical Sciences of the NIH (#P20GM113131), NH BioMade Project Award (# 1757371), and National Science Foundation EPSCoR Award (#2119237).

Lastly, I would like to thank my husband, parents, brothers, and all my friends for their constant love, support, and encouragement during the last five years.

List of Tables

List of Figures

Abstract

Sepsis is a complicated medical emergency and critically ill patients suffering from infectious diseases are at a high risk for developing and dying from sepsis. According to a recent (2019) cohort study from six United States hospitals, suboptimal care (e.g., delay in antibiotics, inappropriate antibiotic therapy) is responsible for 22.7 % of in-hospital sepsis-associated deaths. In September 2020, the World Health Organization called on the scientific community to develop rapid, effective, and affordable tools to improve diagnosis, surveillance, and treatment of sepsis. Our long-term goal throughout this project is to develop a cyclodextrin (CD) impedimetric tongue that can provide early warning of sepsis by continuous monitoring the course of the disease and real-time profiling of urine samples in hospitalized patients. The cyclodextrin impedimetric tongue will also enable healthcare professionals to closely monitor the patients, predict sensitivity and resistance to therapies, decide about the dose of medications, and develop more effective personalized therapies for septic patients.

Cyclodextrins, oligosaccharides with a hydrophobic cavity and a hydrophilic surface, are promising biorecognition elements in development of reusable impedimetric tongues. Cyclodextrins can semi-selectively detect different metabolites in the solutions through hydrophobic interactions, Van der Waals forces, and hydrogen bonding. The first aim of this thesis was to develop the first reusable nanostructured cyclodextrin platform using αCD and a weak surface αCD mediator: polyethylene glycol (PEG). To create the Gold-PEG:αCD surface, gold surface was modified with PEG via thiol-gold chemistry and the PEG support enabled reversible immobilization of αCD. We investigated the performance of this platform for detection of a

model hydrophobic analyte, trans-resveratrol. Non-faradaic electrochemical impedance spectroscopy (EIS) measurement of the surface suggested that when αCD surfaces are introduced to a solution containing trans-resveratrol, αCD molecules leave the PEG support to interact with trans-resveratrol in the solution. After use, the surface could be regenerated by reloading of αCD. The second aim of this thesis was to improve the stability and reusability of cyclodextrin sensing platform by replacing gold-thiol bonds with carbon-carbon covalent bonds between glassy carbon (GC) and 4-carboxyphenyl diazonium salt. The GC-carboxyphenyl was modified with polypropylene glycol (PPG) through EDC/NHS chemistry. The PPG surface was then loaded with βCD. We used the GC-carboxyphenyl-PPG:βCD surface for sensitive detection of cortisol in biofluids (i.e., urine and saliva), and demonstrated the successful regeneration and reuse of the GC-carboxyphenyl-PPG:βCD surface for ten times. Finally, we employed sensitive, stable, and reusable cyclodextrin nanostructured surfaces to develop the first-generation cyclodextrin impedimetric tongue for separation and classification of four classes of bioanalytes including creatinine, cortisol, glucose, and fumarate. We applied linear discriminant analysis (LDA) to integrate and map the data, and by using the normalized changes in imaginary capacitance of three cyclodextrin surfaces (γCD at 79 Hz, hydroxypropyl-βCD at 0.25 Hz, and hydroxypropyl-γCD at 63.34 Hz), we achieved the 5-fold cross validation accuracy of 69%. Different methods of data preparation, EIS signal processing, and determining the characteristic frequencies of different analytes and single frequencies of cyclodextrin surfaces affect the accuracy of the impedimetric tongue. By optimizing these parameters, we can improve the performance and accuracy of the impedimetric tongue and apply this device for point of need applications.

1. Background

Measurement of hydrophobic molecules has gained increasing attention in clinical research. Hydrophobic molecules are barely soluble in aqueous solutions which leads to very low concentrations in biological fluids. Therefore, sensitive and selective analysis of hydrophobic molecules is difficult in biological fluids.

Biosensors based on specific biorecognition elements such as antibodies or enzymes (immunoassays) exhibit high sensitivity and selectivity; however, they suffer from some limitations. Due to intrinsic instability of antibodies and enzymes, immunoassays are physically and chemically unstable, and they have low reproducibility. In addition, immunoassays are expensive and complicated procedures are usually required for enzyme immobilization [1]. In recent years, there have been numerous artificial receptors and chemically modified surfaces developed to address the drawbacks of immune recognition or enzyme-based biosensors for detection of hydrophobic molecules.

In this chapter we will discuss some of the most important non-enzymatic surface modification technologies including carbon materials, metals, conjugated polymers, and cyclodextrins for sensing of several classes of hydrophobic metabolites. We defined metabolites as “hydrophobic” if they have water solubility less than 6 g/L (**Figure 1.1**). The hydrophobic metabolites in **Figure 1.1** are small molecules with clinical relevance; i.e., purine nucleobases (uric acid, adenine, and guanine), pyrimidine nucleobases (thymine and cytosine), an aromatic amino acid (tyrosine), a catecholamine synthesized from tyrosine (epinephrine), a sterol hormone (cortisol), and a hormone precursor (cholesterol).

Uric acid ($C_5H_4N_4O_3$) is the planar, heterocyclic end-product of purine metabolism in humans [2]. Uric acid is electrochemically active and readily undergoes redox processes (**Figure 1.2A**) that can be quantitatively detected by electroanalytic techniques [3] but conventional electrodes struggle to differentiate uric acid from other species with similar oxidation potentials (e.g. dopamine, ascorbic acid, epinephrine) present in body fluids [4].

The cationic catecholamine epinephrine ($C_9H_{13}NO_3$), also known as adrenaline, is both a neurotransmitter and hormone [6]. Epinephrine is easily oxidized and therefore highly electrochemically active (**Figure 1.2B**) but very low concentrations in body fluids and presence of interfering substances with similar oxidation potentials (e.g. ascorbic acid) makes epinephrine sensing challenging [5]. Additionally, the final product of epinephrine oxidation – epinephrinechrome – easily polymerizes to block electrode surfaces [5].

Cortisol ($C_{21}H_{30}O_5$) is a glucocorticoid (steroidal hormone) synthesized from cholesterol with significant long and short-term regulatory impact on immunologic, metabolic, cardiovascular, and homeostatic functions [6]. Cortisol is particularly challenging to electrochemically sense without antibodies or aptamers because it is uncharged at physiological pH and electrochemically inactive.

Cholesterol ($C_{27}H_3O_6$) is a major component of cell membranes and is the sterol precursor to steroidal hormones, vitamin D, and bile acids [7]. Cholesterol also presents a challenge for electrochemical sensing without antibodies or enzymes due to its uncharged status at physiological pH and negligible electrochemical activity (**Figure 1.2C**).

Tyrosine ($C_9H_{11}NO_3$) is an aromatic, polar, non-essential amino acid that may be synthesized by hydroxylation of phenylalanine [8]. Tyrosine, like most amino acids, is weakly electrochemically active (**Figure 1.2D**) and generates poor responses at bare electrode surfaces. Tyrosine is also uncharged at physiological pH.

Adenine and Guanine are purine nucleobases that form hydrogen bonds with pyrimidine nucleobases Thymine and Cytosine respectively to hold together two strands of DNA. Nucleobases are considered electrochemically active (**Figure 1.2E-H**) and all can be oxidized at solid electrodes [9].

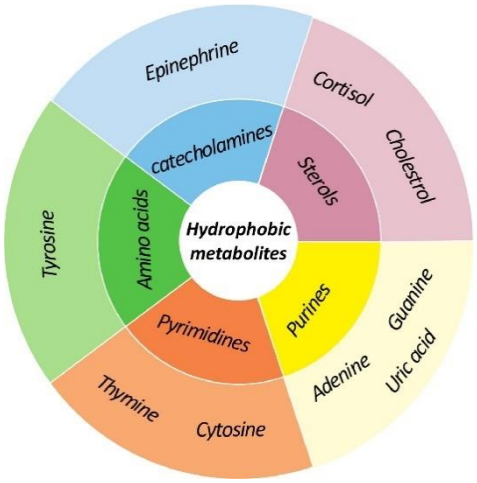

Figure 1.1. Different hydrophobic metabolites, defined as solubility less than 6 g/L, discussed in this Chapter [10], 3, Z. Panahi, L. Custer, J.M. Halpern, Copyright 2021, with permission from Elsevier.

While the focus of this Chapter is mostly on hydrophobic metabolites, there are many clinically relevant hydrophobic proteins. Proteins consist of long chains of amino acids and have the ability to fold to a specific functional three-dimensional shape. Because there are many types of amino acids, and their ordering determines how the protein chain will fold, protein molecules show characteristics of complex systems in terms of their structure, dynamics, and function [11].

Therefore, proteins are very different from small molecule metabolites and they have a different sensing paradigm. Due to the complex structure of proteins, sensing of hydrophobic proteins can be even more challenging than sensing of hydrophobic metabolites and will not be covered in the scope of this chapter.

1.1 Common Technologies for Electrochemical Detection of Hydrophobic Metabolites

Various equilibrium and non-equilibrium transduction techniques have been used in electrochemical biosensors. Amperometric, voltametric, and impedimetric methods are mainly used in electrochemical biosensors to study the interfacial properties of electrode-electrolyte interface and the biorecognition events that happen in presence of analytes. In amperometric biosensors current resulting from the oxidation or reduction of an electroactive analyte is measured when a fixed potential is applied, whereas voltammetry measures the current response while varying potential. During impedimetric techniques such as electrochemical impedance spectroscopy (EIS), an AC potential is applied to the electrochemical cell and the current is measured. EIS biosensors are typically either based on the measurement of the change in charge transfer resistance (faradaic EIS) or capacitance (non-faradaic EIS).

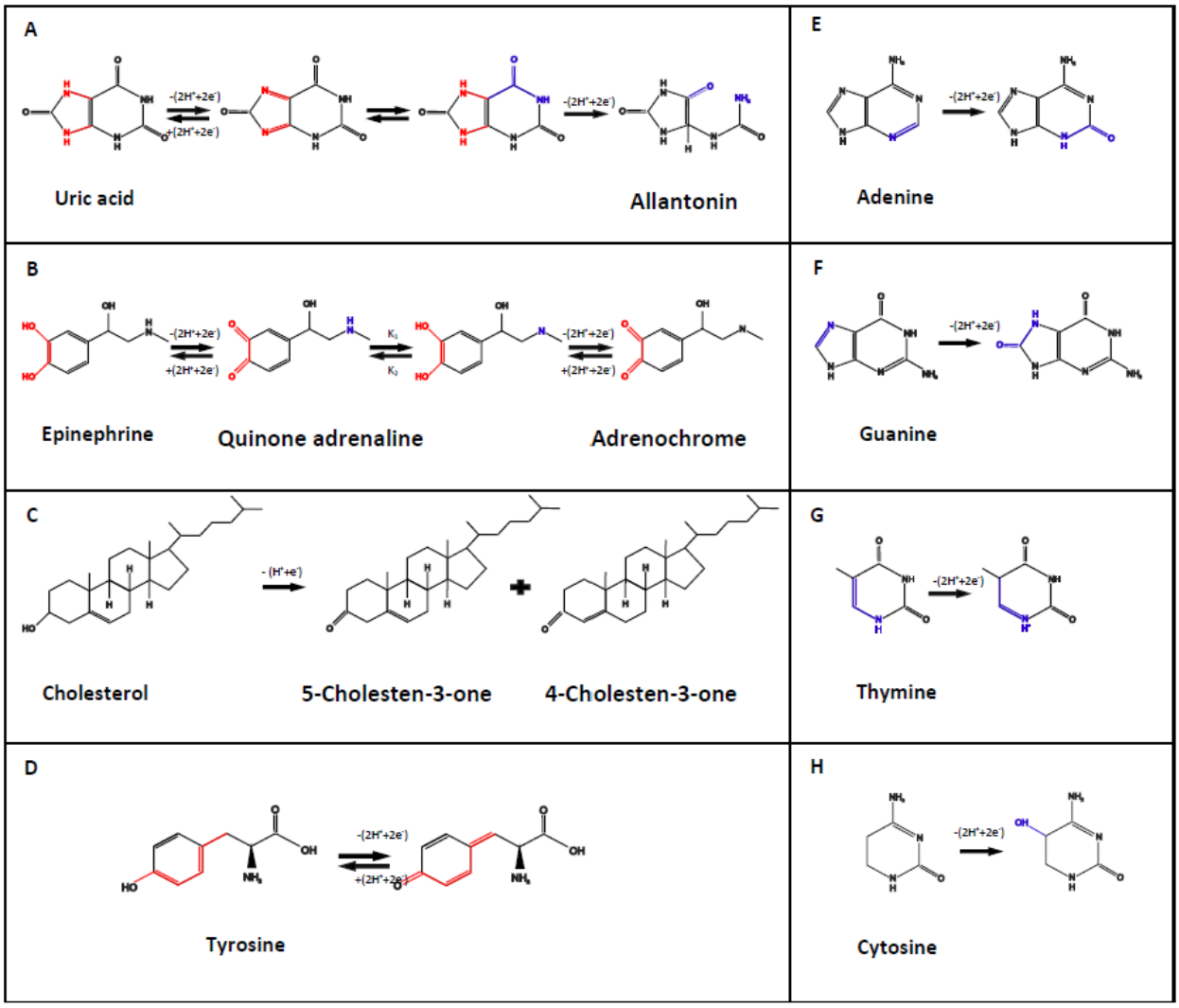

Figure 1.2. Proposed mechanisms for electrochemical oxidation of different hydrophobic metabolites: (A) Oxidation of uric acid on a polydopamine/polypyrrole (PDA/PPY) at 0.3 V vs. Ag/AgCl (in saturated KCl, 3M) [12]. (B) Oxidation of epinephrine on a zinc oxide/ferrocene functionalized graphene (ZnO/3D graphene@Fc) at 0.15 V vs. Ag/AgCl (contained 3 M KCl) [13]. The oxidation product of epinephrine (Quinone adrenaline) can be further oxidized to produce Adrenochrome at 1.15 V vs. Ag/AgCl (contained 3 M KCl) [13]**.** (C) Oxidation of Cholesterol on manganese oxide/graphene (MnO_2/GR) at -0.24 V vs. standard calomel [14] (D) Oxidation of tyrosine on cupric oxide oxide/ β cyclodextrin nanocomposite nafion (CuO/βCD/Nf) at 0.69 V vs. Ag/AgCl [15]. (E) Oxidation of adenine on graphene oxide nanoribbons-chitosan (GONRs-CH) at 0.89 V vs. Ag/AgCl [16]. (F) Oxidation of guanine on GONRs-CH at 0.63 V vs. Ag/AgCl [16]. (G) Oxidation of thymine on GONRs-CH at 1.13 V vs. Ag/AgCl [16]. (H) Oxidation of cytosine on GONRs-CH at 1.27 V vs. Ag/AgCl [16]. 3, Z. Panahi, L. Custer, J.M. Halpern, Copyright 2021, with permission from Elsevier.

Chronoamperometry (CA), differential pulse voltammetry (DPV), square wave voltammetry (SWV), linear sweep voltammetry (LSV), cyclic voltammetry (CV), and faradaic EIS have been among the most used electrochemical techniques for surface monitoring and hydrophobic biomarker detection over the past few years. Compared with CV and LSV, DPV results can provide improved selectivity for observing different redox processes [17]. SWV allows faster analysis times compared to other pulse techniques, such as differential pulse voltammetry or normal pulse voltammetry. Many of these methods such as DPV and SWV are sensitive only to faradaic processes of interest and are used for direct measurement of peak potentials and peak currents of electrochemically active species. However, analysis of non-electroactive species can be achieved indirectly by measuring the signals of redox couples or other substances [18]. In this regard, cholesterol as a weak electrochemically active analyte, is a good test molecule for improving electrochemical sensor capabilities towards non-faradaic processes.

Electrocatalytic oxidation of cholesterol has been reported on biosensor surfaces such as MnO_2/GR/PGE [14] and GO-MIP [19] and the oxidation mechanisms of cholesterol in phosphate-buffered solution (PBS) are shown in **Figure 1.2C**. Despite the fact that the redox potential of cholesterol has been shown to be close to the redox potential of uric acid and acetic acid for the GO-MIP modified sensor, some researchers believe that cholesterol is not electrochemically active and redox couples like ferri/ferrocyanide [20] or electroactive probes like methylene blue [21] are needed as signal indicators.

In recent years, disposable carbon or metal screen-printed electrodes (SPEs) have been implemented for low-cost biosensors. SPEs are more suitable for point-of-care, electrochemical, on-site detection with low-cost. For example, a carbon SPE with a cortisol-alkaline phosphatase

(AP) conjugate was developed to measure cortisol using SWV in PBS and saliva [22]. However, bare SPEs have a series of disadvantages, including poor sensitivity, instability, low reproducibility, large response times, high overpotential for electron transfer reactions, and small peak current [23,24]. Additionally, the slow electron transfer kinetics of hydrophobic analytes, such as tyrosine, can limit the redox reaction rate and deteriorate biosensor performance [15].

Unmodified bare electrodes perform poorly because other interfering species present can be oxidized non-selectively. Surface modification can catalyze the oxidation of analytes to improve selectivity of biosensors in complex biological solutions. For example, the coexistence of interferents, such as dopamine, acetic acid, and epinephrine, can obscure the biosensor response to uric acid because they have very similar oxidation potentials. Additionally, oxidation products of the hydrophobic analytes can adsorb or electropolymerize on bare electrode surfaces, blocking further analyte oxidation and decreasing the reusability and reproducibility of these electrodes. Therefore, modifying different electrode surfaces is important to enhance sensitivity by increasing electron transfer rates, improve class-recognition selectivity in complex biological solutions, and prevent electrode fouling [25].

In this section, we will summarize some of the most effective surface modification technologies to address the problems of poor sensitivity and selectivity of biosensors. Various carbon materials (**Table 1.1**), metals (**Table 1.2**), conjugated polymers (**Table 1.3**) have an outstanding ability to combine with sensing elements and improve the electrochemical response in biosensors for detection of hydrophobic biomarkers.

1.1.1 Carbon Nanomaterials

Common carbonous materials, including graphene, graphene oxide, reduced graphene oxide, carbon nanotubes, carbon dots, carbon nanofibers, and carbon black have drawn attention for electrochemical sensing of various metabolites. High electrical conductivity and high surface area of these materials mediate fast electron transfer between electroactive metabolites and electrode surface [26,27]. Besides this, carbonous materials can improve biosensor performance due to their wide potential window, high electrochemical stability, high mechanical resistance, and biocompatibility [26–28].

However, incorporating carbonous materials into the surfaces can be challenging as simple drop-casting can result in unstable layers. Also, being too conductive and having high surface area poses problems in terms of controlling the electrical current and lack of selectivity. To address these problems, different polymers and sensing elements can be immobilized onto the carbonous materials through physical adsorption and different covalent and non-covalent interactions. The choice of immobilization technology is significant. While physical adsorption is not a controllable process and non-covalent bindings may not be strong and stable enough, covalent modifications can cause changes in the properties of materials such as carbon nanotubes and graphene by disturbing their aromaticity [26,29]. Recent reviews have been written on different functionalization strategies and the design of various carbon materials [29–32].

Extensive applications of graphene in electrochemical detection of hydrophobic biomarkers such as uric acid [33], epinephrine [13] and tyrosine [34] have been reported.

Graphene is a two-dimensional carbon material and a zero-bandgap semiconductor. Doping of graphene with nitrogen is mostly done to open up its band gap, enhance control of its electronic properties, and activate interaction between graphene surface and various biomarkers [33]. Graphene oxide (GO) and reduced graphene oxide (RGO) which are among derivatives of graphene, find many applications for a wide variety of hydrophobic analytes such as uric acid [35,36], epinephrine [37], cortisol [38,39], cholesterol [19], adenine [16,35,40], guanine [16,35], cytosine [16], and thymine [16]. Oxygen containing groups on GO and RGO are useful for post-processing steps and enhance sensitivity of electrochemical biosensors by improving electron transfer rates and water solubility [26,41]. Various electrochemical, thermal, and chemical methods are applied for conversion of GO into RGO. RGO can be functionalized with metal nanoparticles such as ZnO that enhance electroactive surface area and electrochemical oxidation of different hydrophobic biomarkers [36]. Another simple epinephrine biosensor was developed by combination of tetrahexahedral (THH) Au-Pd bimetallic nanocrystals with RGO nanosheets [37]. THH Au-Pd nanocrystals improved both electrocatalytic activity and conductivity of graphene. Further discussion of metallic elements is in Section 1.1.2.

Carbon quantum dots (CQD) and graphene quantum dots (GQD) are electrochemically active species. Due to extremely small sizes and large surface area CQD and GQS have been recently used for detection of uric acid [42] and tyrosine [43], respectively. Besides, Quantum dots (QDs) can be synthesized with various functional groups and modification of surfaces with these materials allow electrochemical signal amplification and improvement of class-recognition selectivity [44,45].

Carbon nanotube (CNT) electrochemical biosensors are of great interest to researchers in recent years and can be classified into single-walled carbon nanotubes (SWCNT) and multi-walled Carbon nanotubes (MWCNT) sensors. CNTs consist of rolled graphene sheets and show different properties from graphene due to their unique structure. CNTs can enhance electrochemical activity of some biomarkers and have lower limit of detection (LOD), higher sensitivity, wider ranges of detection, and shorter detection times [32,46]. CNTs have been applied for recognition of many hydrophobic biomarkers, such as uric acid [47], tyrosine [48–50], and cholesterol [20]. Carbon nanotubes (CNTs) with small scale have been found to be able to increase the electrochemical sensitivity of numerous analytes [51]. A glycine polymer/multi-walled carbon nanotubes modified carbon paste electrode (Poly(Gly)/MWCNTs/CPE) was employed for detection of tyrosine [50]. Using this surface, a great sensitivity and accuracy was achieved in practical samples of human serum.

Carbon nanofibers (CNF) and CNTs have similar conductivity and stability; however, CNFs have larger surface area exposed to the solution and therefore have higher electron transfer rates. Transition metal dichalcogenides (TMDs) catalysts are also commonly supported on carbon nanofibers. As an example, a high-throughput three-dimensional WS_2 nanosheet/graphite microfiber hybrid electrode biosensor was used for electrochemical detection of adenine and guanine in complex solutions and in vivo [52].

Other carbon materials such as carbon black, mesoporous carbon and fullerenes have been shown to be promising materials for biomedical analysis although their potential applications for detection of hydrophobic biomarkers are yet to be investigated.

There are some challenges with carbon based biosensors, especially with regard to insolubility of CNTs in aqueous solutions and reproducibility in producing identical batches of CNTs with high quality and minimal impurities [47,49]. However, combining the advantages of carbonous materials with different metals and polymers such as conjugated polymers and cyclodextrins gives a synergistic performance as electrode materials through which their advantages can outweigh their limitations.

Table 1.3. Carbon based biosensors. 3, Z. Panahi, L. Custer, J.M. Halpern, Copyright 2021, with permission from Elsevier.

Analyte	Sensor	E-Chem method	Detection range* (µM)	LOD* (µM)	Medium	Ref.
Uric acid	RGO–ZnO/GCE	DPV	1-70	0.33	Plasma and urine	[36]
	N-doped graphene	CV	0-600	0.13	Serum	[33]
	P-GLY/GO	DPV	0.1-105	0.061	Urine	[35]
Epinephrine	Flower-like ZnO/3D graphene@Fc	DPV	0.02 - 216	0.0093	Serum	[13]
	Au-Pd/RGO	CV&DPV	0.001- 1000	0.0012	Serum	[37]
Cholesterol	GO-MIP	CV	0.1 10^{-3} - 10,000	0.1 10^{-3}	Serum	[19]
Tyrosine	EFTA/G/CPE	SWV	5 - 180	2	Serum and urine	[34]
	MCPE/COOH-MWCNT	CA	0.8-100	14 nM	Serum and cow's milk	[49]
	MW-FEs	DPV	25-750	8	Plasma and whole blood	[48]
Adenine	GONRs-CH	DPV	0.11-172	0.023	Buffer	[16]
	BODIPY functionalized SWCNT	DPV	4-20	2.91	Buffer	[51]
	WS_2/Graphite nanofiber	DPV	0.5-20	5×10^{-8}	Buffer	[52]
	TNFs/GONs/SPCE	CA	0.1-10	1.71 nM	Buffer	[40]
	P-GLY/GO	DPV	0.09-103	0.03	Urine	[35]
Thymine	GONRs-CH	DPV	6-855	1.330	Buffer	[16]
Guanine	GONRs-CH	DPV	0.013-256	0.002	Buffer	[16]
	BODIPY functionalized SWCNT	DPV	4-20	1.07	Buffer	[51]
	WS_2/Graphite nanofiber	DPV	0.5-20	9×10^{-8} M	Buffer	[52]
	P-GLY/GO	DPV	0.15-48	0.026	Urine	[35]
Cytosine	GONRs-CH	DPV	3.5-342	0.641	Buffer	[16]

*Detection range and LOD are typically determined in buffer and would likely be different in complex media.

1.1.2 Metal Materials

A wide variety of metals have been used to produce hydrophobic biosensors, including noble metals (e.g. Au [37,53,54], Pd [37]), transition metals (e.g. Co [53], Cu[55], W[56]), metal oxides/hydroxides (e.g. MnO_2[14], SnO_2 [57], $Zn(OH)_2$ [58], NiO [59]), metal chalcogenides (e.g. $FeTe_2$[2], CdSe[60]), metal organic frameworks (MOFs) [61], and polyoxometalates (POMs) [62,63]. Metallic materials have primarily been incorporated into these biosensors as a nonenzymatic electrocatalyst, providing crucial improvements in sensor sensitivity that in turn enable determination of biomarkers. The enhanced electrocatalysis of hydrophobic metabolites was achieved through several mechanisms: direct electron transfer mediation between metal and biomarker [64], coordination and activation of functional groups on the biomarker [64], improved electrostatic affinity between sensor and biomarker [5,54,62,65], enhanced mass transport due to expansion of the electrochemically active surface area [2,3,37,54–58,60–63,65] and/or intrinsic adsorptive properties of the metal [3,14,66]. Metals, especially transition metals with an abundance of unpaired d-orbital electrons, have multiple oxidation states and readily transition between oxidation states through electron transfer reactions with coordinating electrochemically active species [64]. This direct redox between metal and biomarker can facilitate faster electron transfer at lower oxidation potentials, as observed for the oxidation of epinephrine upon addition of copper nanoparticles to an Al_2O_3 nanofiber/graphene composite [55]. Since some hydrophobic metabolites like epinephrine and uric acid are electrochemically active and coexist with other electrochemically active species in complex media, metals present a useful option for enhancing sensitivity for these species creating some class-recognition type selectivity.

Interactions between two metals can also have an enhancing effect on biomarker redox processes, which could explain the enhanced oxidation of epinephrine upon addition of gold to a Schiff-base Iron (III) complex film [5]. However, Schiff-base complexes have been shown to degrade and corrode a metal oxide surface signifying limited long-term use of these in some applications [59]. Other examples of enhanced oxidation of uric acid with a second metal were gold added to a β-NiS/RGO composite [54] and a cobalt decorated hollow nanoporous carbon framework [53]. Enhanced oxidation of uric acid was also observed at α-$Ni_{0.75}Zn_{0.25}(OH)_2$ alloy nanoparticles compared to α-$Ni(OH)_2$ and $Zn(OH)_2$ [58]. Increase sensitivity to adenine and guanine was observed when gold was added to a CdS/GO modified electrode [65]. Some metals and metal composites have electrostatic affinity for the biomarkers of interest at tested pH that improve sensitivity for the target analytes. The negative charge of the Au/β-NiS/RGO [54], CdS@ZnS/GO [65], and Au/Schiff-base iron(III) [5], composites each attracted positively charged uric acid, adenine and guanine, and epinephrine, respectively. Conversely, the POM composite of $H_3PW_{12}O_{40}$/RGO contained positively charged surface groups that enhanced affinity for the negatively charged groups on tyrosine at tested pH [62].

If not directly participating in redox reactions with the biomarker, metal ions can bind functional groups on biomarkers with electron-donor properties [64] such as the amine groups on uric acid, adenine, guanine, cytosine, and thymine. Binding not only keeps the biomarker close to the electroactive surface but polarizes the functional group and activates adjacent sites on the molecule, thus promoting further interactions [64]. This effect may be responsible for the enhanced response of CdSe quantum dots in hollow extraction fibers towards uric acid versus just the hollow fibers, as each CdSe quantum dot binds at least one target analyte from solution

and promotes oxidation [60]. While not necessarily specific to hydrophobic biomarkers, the binding to pull out of solution and activation of nearby sites is valuable when seeking higher sensitivities and wider peak separations for hydrophobic biomarkers with Lewis base groups.

Metal nanostructures such as nanospheres, nanofibers, nanosheets, nanoclusters, and quantum dots may also improve sensitivity by increasing the electrochemically active surface area of the sensor, providing more accessible sites for redox. Morphology is key to this effect; although discal, cubic, and thorhombic Fe_2O_3 nanoparticles can all catalyze the oxidation of uric acid, the larger surface area/volume ratio and increased surface defects afforded by discal Fe_2O_3 nanoparticles yielded higher peak currents [3]. Quantum dot core-shell nanostructures were of particular note, with CdS@ZnS producing even larger conductive surface areas than nanoparticles of the same metals [65]. Unfortunately, many metal nanoparticles are prone to agglomeration [3], and must be suitably dispersed (either by modifying synthesis technique or supporting on another structure) to reap the benefits of higher surface area.

Some metals (particularly iron oxides and metal chalcogenides) have notable impacts on mass transport due to their adsorptive abilities. Although pure unsupported iron oxide nanoparticles have poor electrical conductivity and are prone to agglomeration, the adsorptive ability of Fe_2O_3 and Fe_3O_4 were used to enhance the response of graphene oxide sheets towards uric acid [3] and adenine/guanine [66], respectively. However, some metals have been shown to reduce mass transport rates, such as $Fe_2V_4O_{13}$[67].

MOFs are highly tunable, porous, extended crystalline structures where metal cations or clusters called “nodes” are connected by organic “linker” ions or molecules [68]. MOFs can improve sensitivity with their electrocatalytically active metal nodes and selectivity by the

modifiable pore sizes of the organic framework, often yielding wide detection ranges and very low limits of detection [68]. A CdO/carbon nitride/polyaniline MOF for epinephrine sensing demonstrates some of the advantages of MOFs with rapid diffusion, large surface area, improved peak separation between epinephrine and interferents, a higher oxidation current, and lower overpotential [61].

Although less explored in the literature, polyoxometalates (POMs) are worth mentioning for their remarkably low limits of detection and wide range. POMs are molecular oxides containing oxygen and tens to hundreds of early transition metal atoms that can accept and release specific numbers of electrons without decomposing or changing structure [69]. POMs can vastly expand the electrochemically active surface area, enhancing electron transfer rate and sensitivity. A novel use of POMs was reported for nonenzymatic cholesterol sensing [63], yielding the lowest limit of detection with the widest range of the articles surveilled. The highly active sandwich POM in combination with a PVIM+ ionic liquid support showed cathodic shifts in peaks and an increase in reduction and oxidation currents of typically electrochemically inactive cholesterol. Additionally, a POM/RGO/GCE sensor was reported for the determination of tyrosine [62], with electrostatic affinity for tyrosine as mentioned previously.

Table 1.2. Metal based biosensors. 3, Z. Panahi, L. Custer, J.M. Halpern, Copyright 2021, with permission from Elsevier.

Analyte	Sensor	E-Chem method	Detection range (μM)*	LOD (μM)*	Medium	Ref
Uric acid	Au/NiS/RGO/GCE	SWV	0.1-1000	0.006	Urine and serum	[54]
	Fe_2O_3/GO/GCE	DPV	10-100	0.0025	Urine and serum	[3]
	CdSe/ionic liquid/hollow polypropylene fibers/PGE	DPV	0.297-2970	0.083	Urine and serum	[60]
	$FeTe_2$/GPE	DPV	3-120	0.042	Urine and serum	[2]
	Au/Co/nanoporous hollow carbon framework/GCE	DPV	0.1-2500	0.023	Serum	[53]
Epinephrine	Au-Pd/RGO/GCE	DPV	0.001-1000	0.0012	Serum	[37]
	Al_2O_3/Cu/ graphene/GCE	DPV	1-1200	0.027	Urine	[55]
	CdO/PANI/ g-C_3N_4/GCE	DPV	0.05-1000	0.011	Serum	[61]
Tyrosine	$H_3PW_{12}O_{40}$/RGO /GCE	SWV	0.01-1.0 x 10^{-3}	2 x 10^{-6}	Serum	[62]
Cholesterol	PVIM-Co_5POM/MNC/ Filter paper electrode	DPV	1 x 10^{-8} -5000	1 x 10^{-9}	Serum	[63]
	MnO_2/PGE	DPV	1.2-24 x 10^{-3}	4.2 x 10^{-4}	Serum	[14]
Adenine	ZnS@CdS/GO/GCE	DPV	0.01-50	0.00181	Blood	[65]
	Fe_3O_4/GO/GCE	DPV	0.05-25	0.003	Urine	[66]
	$FeTe_2$/GPE	DPV	3-100	0.097	Urine and serum	[2]
Guanine	ZnS@CdS/GO/GCE	DPV	0.01-50	0.00145	Blood	[65]
	Fe_3O_4/GO/GCE	DPV	0.05-25	0.004	Urine	[66]
	$FeTe_2$/GPE	DPV	1-160	0.034	Urine and serum	[2]
	$Fe_2V_4O_{13}$/CPE	DPSV	0.5-60	0.032	Buffer	[67]
Cytosine	WO_2/W@C/GCE	DPV	1-3000	0.20	Urine and serum	[56]
Thymine	WO_2/W@C/GCE	DPV	1-4000	0.20	Urine and serum	[56]

*Detection range and LOD are typically determined in buffer and would likely be different in complex media.

1.1.3 Conjugated Polymers

Conjugated polymers (CPs) are biocompatible polymeric materials with conjugated pi-orbital systems that may permit electron movement from end-to-end [70]. While in a pristine (neutral) state, CPs are poorly conductive [70,71]; conductivity of CPs is altered by several orders of magnitude via reversible oxidation (p-doping) or reduction (n-doping) of their pi-orbital system [70,71]. CPs can be polymerized in various conformations with unique behavior, including films [12,72–75], nanofibers/wires [12,76], nanospheres [4,77–80], and hydrogels [81]. CPs exhibit highly customizable structural, electronic, and optical properties that are sensitive to small perturbations, and therefore have been used for a variety of chemical sensing applications [70]. Common CPs for sensing include poly(thiophene)s like poly(3,4-ethylenedioxythiophene) (PEDOT), poly(aniline)s (PANIs), and poly(pyrrole)s (PPYs) [70].

CPs can also improve the stability of sensors by providing functional groups for strong attachment to surfaces [4,72] and blocking surface fouling [73,82]. While some CPs like PPY or PANI are mechanically weak and degrade readily [72,78,82], others like PEDOT contribute decent mechanical strength as well as good thermal, environmental, and cycling stability [79]. CPs are also relatively cheap [70] and may be easily fabricated directly onto electrodes via electropolymerization [72,74]. However, CP only based sensors often have poor selectivity and are unsuited to discrimination of biomarkers in complex media outside of cross reactive sensor arrays [70]. Efforts to improve selectivity includes the integration of molecularly imprinted polymer concepts [83] or use of receptor monomers such as cyclodextrin [84].

As an element of biosensors, the large specific surface area [77], high conductivity [85], and fast redox activity [85] of CPs can improve sensitivity towards hydrophobic biomarkers (see **Table 4**). Many CPs like PANI have aromatic groups in their pi-orbital system that facilitate pi-pi stacking with aromatic hydrophobes like uric acid [82], tyrosine [72], adenine [75], and guanine [75]. Charged groups on certain CPs at specific pH can change the overall charge of the composite to facilitate electrostatic interactions with hydrophobic biomarkers that are ionized at testing pH, such as uric acid [78], epinephrine [74], tyrosine [80], adenine [75], and guanine [75]; hydrogen bonding may also occur between proton donor regions of biomarkers and electronegatively rich groups of the CP that increase affinity for biomarkers [72,73,78] or weaken other bonds to enhance the likelihood of redox interactions [72]. Many CPs like PEDOT have more hydrophobic regions like repeated aromatic rings [76,78] or inclusion pockets [84] that can specifically interact with hydrophobic metabolites via hydrophobic interactions. Additionally, some CPs can catalyze the direct redox of a biomarker, such as poly(L-arginine) and epinephrine [74].

CPs are typically integrated into composites to great synergistic effect. For example, negatively charged carbon nanotubes form stable composites with positively charged PEDOT that have higher capacitance and enhanced mechanical properties as compared to electrodes modified with individual components [86]. Positively charged CPs have also been used to form p/n junctions with negatively charged materials like zinc oxide to substantially increase the magnitude of response towards epinephrine and uric acid [85]. CPs can enhance dispersal and prevent agglomeration of electrochemically active nanomaterials such as reduced graphene oxide [82], metal oxide nanoparticles [85], metal sulfide nanostructures [75,78], and noble metal nanoparticles [85,87], yielding more homogeneous higher sensitivity constructs capable of

selectivity. Carbon structures like reduced graphene oxide [85] or metal components [82] can compensate for the poor strength and stability of some CPs. However, compositing does not automatically yield better sensitivity; in particular, composites of CPs and 2-D carbon nanomaterials tend to have poorer (>0.5 μM) LOD [88,89].

While CPs are powerful due to their diversity of characteristics and synergy within composites, they require extensive optimization during polymerization/composite formation, doping, and sensing to maximize capabilities. Electro-polymerization conditions such as pH [4,87], solvent [76,87], supporting electrolyte [76], concentration of monomer [4,72,77], and choice of electrode substrate [4,76] influence the morphology and electrochemical properties of CPs and should be carefully selected for the biomarker of choice. Features such as thickness, permeation, and charge transport of CP films may be tuned by adjusting electrochemical parameters such as cycle number [72,73,87] and potential scan range [87].

Doping can be accomplished chemically or electrochemically, but electrochemical doping is preferable for reproducible fine tuning of oxidation state [70,71]. Different dopants produce CPs with varying characteristics [76]; sometimes other electrocatalytic hydrophobic materials like carbon nanotubes can be used as the dopant to enhance sensitivity [86]. Counterions are incorporated to compensate charges created by doping the polymer backbone. The type of counterion determines the character of local charge carriers along the polymer backbone [70], thereby determining ion exchange properties of the CP [71] and its interactions with ionized hydrophobic biomarkers. Further irreversible oxidation (over-oxidation) can turn some conductive CPs into insulating polymers [90], though recently over-oxidized PEDOT has been found to retain conductivity with the advantage of improved stability [76]. Over-oxidation may

expose more hydrophobic regions of CPs such as PEDOT, facilitating hydrophobic interactions between the CP and un-ionized biomarkers for enhanced sensitivity and class-recognition selectivity [76]. CPs have also recently been electronically excited by electron beam irradiation, resulting in intermolecular cross linking or chain scission of the polymer [80] that manifests as altered electronic properties and mass transport behavior [77,80].

In addition to oxidation state, the electroactivity of CPs can be modified by protonation state. For certain CPs like PANI or PI, proton release and uptake are directly coupled to the oxidation or reduction of the polymer, such that changes in pH directly affect conductivity [71]. This feature of CPs, along with the ionization of several hydrophobic biomarkers at varying pH [72,76], necessitates experimentation with pH to determine optimal sensing conditions [4,72–80,82–87].

Table 1.3. Conjugated polymer based biosensors. 3, Z. Panahi, L. Custer, J.M. Halpern, Copyright 2021, with permission from Elsevier.

Analyte	Sensor	detection method	Detection range (μM)*	LOD (nM)*	Medium	Ref.
Uric acid	Poly(DA)/AuNp/SPCE	DPV	10-350	0.1	Buffer	[4]
	Poly(DA)/PPY/GCE	DPV	0.5-40	110	Urine	[12]
	Poly(HQ)/crown ether/CNT/GCE	DPV	0.005-15	0.769	Serum	[73]
	PANI/ZnO/RGO/GCE	DPV	0.5-1000	122	Urine and serum	[82]
	PPY/β-NiS/SPE	SWV	0.02-1000	5	Urine and serum	[78]
	PEDOT/AuNp/ MWCNT/GCE	DPV	0.1-800	199.3	Urine and serum	[86]
	Ox-PEDOT/PGE	AdDPSV	0.01-20	1.3	Urine and serum	[76]
	PPY hydrogels/GCE	SWV	0.2-1000	46	Urine	[81]
	Poly(BCG)/AuNp/GCE	DPV	7.0-1500.0	4	Urine	[87]
Epinephrine	Poly(L-aspartic acid)/RGO/GCE	SWV	0.1-110	25	Buffer	[74]
	Poly(BCG)/AuNp/GCE	DPV	4.0-903.0	10	Urine	[87]
	PPY/ZnO/AuNp/ RGO/GCE	DPV	0.6-500	60	Buffer	[85]
	EB-PPY/BSA/GCE	SWV	0.1-400	7.4	Buffer	[77]
Tyrosine	Poly(BCP)/ MWCNT/ CPE	CA	2-100	191	Buffer	[72]
	EB-PPY/BSA/GCE	SWV	0.1-400	5.9	Buffer	[77]
Cholesterol	PEDOT/taurine/SPE	CA	3-1000	950	Buffer	[79]
Adenine	PANI/MoS_2/CPE	DPV	0.05-1	6.3	Buffer	[75]
Guanine	PANI/MoS_2/CPE	DPV	1-100	4.5	Buffer	[75]

*Detection range and LOD are typically determined in buffer and would likely be different in complex media.

1.2 Why Cyclodextrin Based Biosensors – Advantages

Cyclodextrins (CD) consisting of six (αCD), seven (βCD), or eight (γCD) glucose units are oligosaccharides composed of a hydrophobic inner cavity and a hydrophilic outer surface (**Figure 1.3**). The hydrophobic cavity of cyclodextrins is due to the skeletal carbons and ether-like oxygens of glucose molecules which cause a lipophilic character [91,92]. The hydrophobic cavity of cyclodextrins allows them to make stable inclusion complexes with various guest molecules through hydrophobic interactions, Van der Waals forces, and hydrogen bonding [93–95]. CD biosensors have good selectivity because different metabolites differ not only in terms of the nature and placement of a hydrogen-donor units, but also in terms of the number of hydrogen donors. The host guest interaction energies between cyclodextrins and different guest molecules are different, permitting the semi-selective determination of the target molecules.

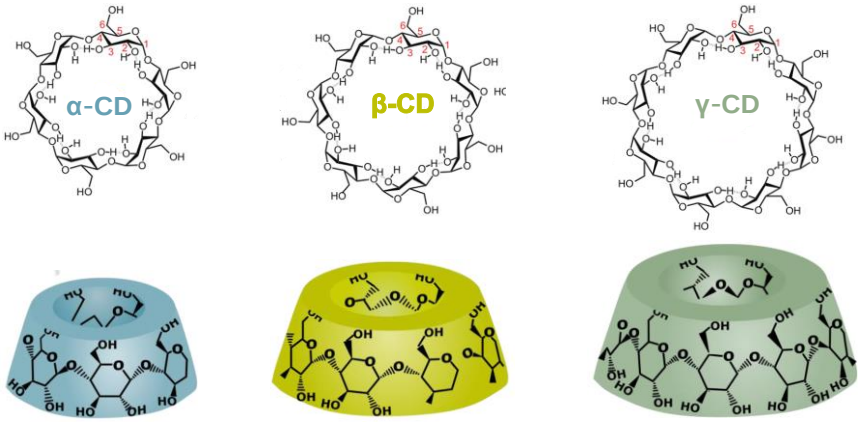

Figure 1.3. αCD, βCD, and γCD molecular structures. αCD, βCD, and γCD contain six, seven, and eight glucose units, respectively.

For example, cholesterol is a hydrophobic molecule composed of a steroid, an OH group and eight CH_3 groups [94]. Therefore, βCD molecules have high affinity for cholesterol and in recent years βCDs have been incorporated in development of various electrochemical [20,91,96–

98] and non-electrochemical [94,96,99,100] cholesterol biosensors. **Figure 1.4** demonstrates a cholesterol βCD/AuNCs biosensor based on fluorescence enhancement technique and the inclusion complexes between βCD and cholesterol, and each cholesterol molecule is encapsulated by three βCD molecules [96]. Glutamic acid, cysteine, ascorbic acid, and dopamine can be found in serum and are among the potentially interfering components for cholesterol sensing. Glutamic acid and cysteine molecules contain two and one hydrophobic CH_2 groups, respectively and they can bind with βCD. However, the inclusion complexes of βCD with glutamic acid and cysteine are weak due to the mismatch between sizes of CH_2 groups and βCD cavity. Similarly, the lactone ring of ascorbic acid and the benzene ring of dopamine can fit loosely in βCD cavity and they fit better in αCD cavity [100].

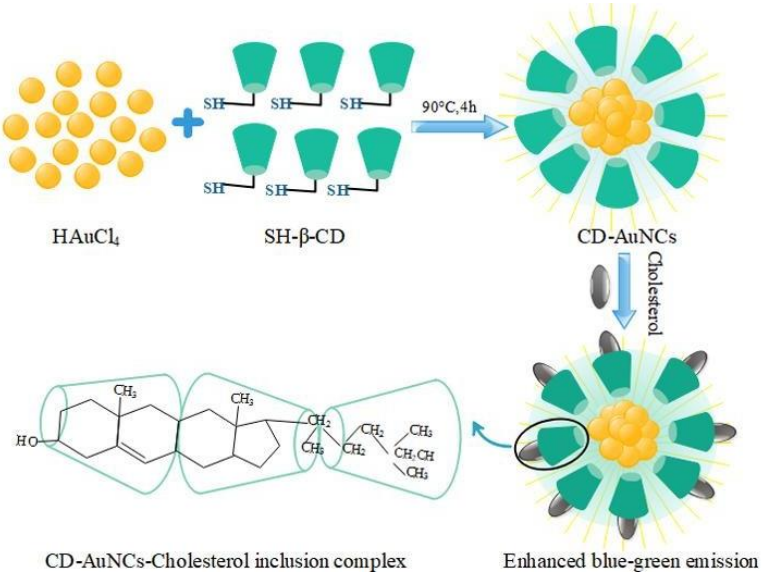

Figure 1.4. Schematic illustration of βCD/AuNCs biosensor based on fluorescence enhancement technique. βCD and cholesterol host-guest interactions with the molar ratio of 3:1 [96]. Reprinted from Sensitive cholesterol determination by β cyclodextrin recognition based on fluorescence enhancement of gold nanoclusters, 175, W. Xiao, Z. Yang, J. Liu, Z. Chen, and H. Li, pp. 107125, Copyright 2022, with permission from Elsevier.

In addition to the cyclodextrins' cavity size, steric hindrance and hydrogen-bonding interaction controls the selectivity of cyclodextrin biosensors [84]. For example, tyrosine enantiomers (L-Tyr and D-Tyr) can both enter the βCD cavity and make inclusion complexes with βCD. However, due to different steric hindrance and hydrogen-bonding interaction between βCDs and L-Tyr, βCD:L-Tyr complex are shown to be more stable than βCD:D-Tyr [43]. Additionally, cyclodextrin molecules can be modified with different functional groups to improve their selectivity. For example, sulfato-βCD derivative has better selectivity than original βCD molecule toward tyrosine enantiomers because electrostatic interaction from sulfonate groups enhance the binding ability [101].

1.3 Current Cyclodextrin Biosensors for Hydrophobic Metabolite Sensing – Challenges

CDs have been used as molecular receptors in biosensors for detection of various hydrophobic biomarkers that match their cavity size [42]. In particular αCD has a smaller cavity (inner radius 0.57 nm) and has been used for detection of adenine, guanine, and thymine [102]. βCD (inner radius 0.78 nm) has been found to be the most efficient sterol-acceptor molecule, due to its inner cavity diameter which is consistent with the size of these molecules [20]. However, γCD (inner radius 0.95 nm) has a larger cavity which may not be suitable for detection of important biomarkers. For example it has been shown that sensitivity of βCD/MWCNT sensor is higher than similar biosensors with αCD and γCD for uric acid detection, thus demonstrating size of cyclodextrins is critical for small hydrophobic metabolite detection [103].

Carbon-based materials have been broadly used as supporting materials for electrochemical cyclodextrin biosensors to increase electron transfer rates and enhance

electrochemical activity of these biosensors. Reduced graphene oxide has been used together with αCD for detection of adenine, guanine, and thymine. αCD ensures both more accessible active sites to capture analyte and RGO accelerates electron transfer leading RGO/αCD to show high electrochemical activity [102]. Graphene quantum dots combined with βCD for the fabrication of a tyrosine and uric acid biosensor and a βCD/MWCNT surface has been incorporated for detection of uric acid [42,43].

One of the methods to improve sensitivity of layer-by-layer carbon/cyclodextrin biosensors is to optimize the interactions between carbon materials and cyclodextrins. **Figure 1.5** shows different fabrication stages of a βCD/Nafion-MWCNT biosensor for uric acid detection [103]. In this method, first, Nafion-ethanol solution was used to disperse pristine MWCNT and then βCD was electropolymerized on Nafion-MWCNT film. However, the use of Nafion for MWCNT dispersion interferes with βCD coupling to MWCNT. Alternatively, MWCNT–COOH (instead of unfunctionalized MWCNT) can be easily dispersed in aqueous solution and a layer of βCD could be adsorbed directly on MWCNT layer [47]. By maximizing the interactions between MWCNT and βCD sensitivity of biosensor increased from 2.11 to 4.28 μA mM^{-1} [47].

However, one of the problems with cyclodextrin biosensors is associated with the immobilization of cyclodextrins on electrode surfaces due to their poor conductivity and high water solubility [84]. One solution is to introduce functional groups (such as –SH, $–NH_2$ and –COOH) on the CD, providing more effective binding sites.

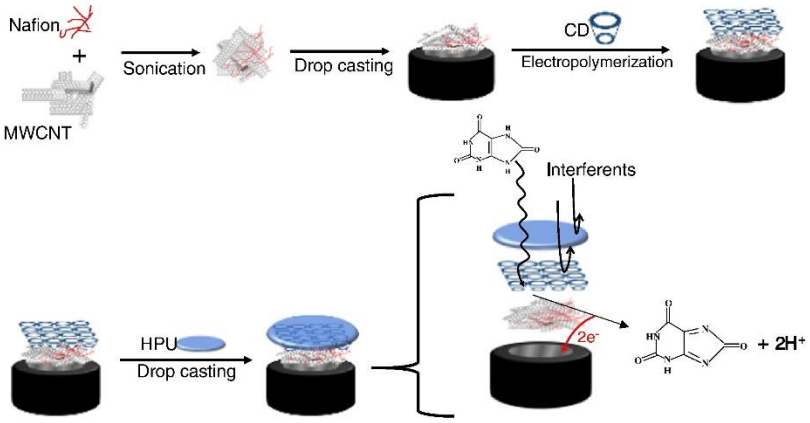

Figure 1.5. Schematic illustration of βCD/Nafion-MWCNT for detection of uric acid [103].Reprinted from Electropolymerization of β cyclodextrin onto multi-walled carbon nanotube composite films for enhanced selective detection of uric acid, 783, M.B. Wayu, L.T. DiPasquale, M.A. Schwarzmann, S.D. Gillespie, M.C. Leopold, pp. 192-200, Copyright 2016, with permission from Elsevier.

Covalent bindings between graphene and cyclodextrin can limit the amount of cyclodextrin immobilized on the surface and result in low sensitivity of biosensor. Furthermore, cyclodextrins are not conductive and cyclodextrin functionalized surfaces have lower conductivity. Therefore, introduction of cyclodextrins onto surface can decrease the sensitivity of sensors that are based on oxidation or reduction of electroactive analytes. To enhance the sensitivity of the sensors, cyclodextrins can be modified with sulfonate groups and sulfato-βCD derivative has higher sensitivity than original βCD molecule toward tyrosine enantiomers due to the ionic conductivity of sulfonate groups [101].

Dispersed cyclodextrin surfaces offer higher conductivity and perform better compared to cyclodextrin functionalized electrodes. Alternatively, competitive host-guest inclusion complexes between hydrophobic analytes and a redox indicator can be used to determine concentrations of analyte. For example, **Figure 1.6** shows that methylene blue can be replaced by cholesterol molecules because binding affinity of cyclodextrin and cholesterol is higher than cyclodextrin and methylene blue [97,98].

Reusable sensors are critical in applications where automated in-process analyte sensing is essential, as in environmental screening [104], cellular monitoring [105], food monitoring [106], and biopharmaceutical applications [107,108]. A reusable sensor surface would reduce material and reagent costs, and, once an appropriate calibration curve is obtained, it can be applied for subsequent sample screenings [109,110]. Currently, all current cyclodextrin biosensors such as cyclodextrin self-assembled monolayers with thiolated cyclodextrins or cyclodextrin surface free-radical polymerization, are single use due to strong analyte complexation [111–114]. However, using surfaces where cyclodextrin is complexed to a weakly hydrophobic self-assembled monolayer has the capability of overcoming the aforementioned challenges with surface functionalization and creating a reusable biosensor for hydrophobic metabolites sensing.

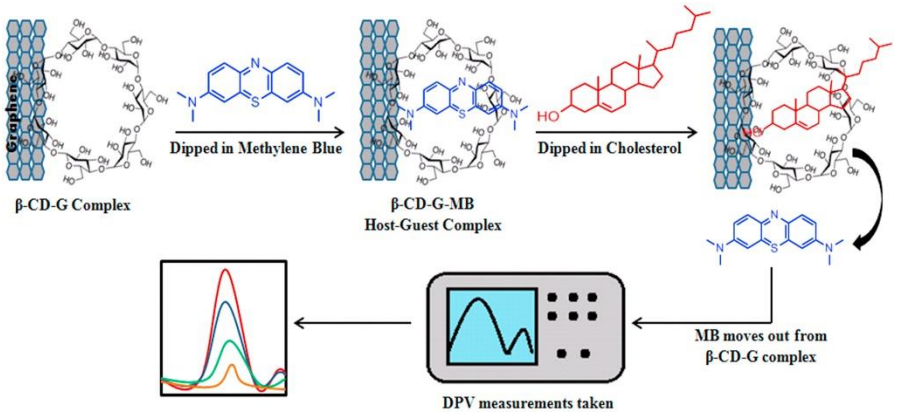

Figure 1.6. Schematic demonstration of βCD/graphene platform for cholesterol detection [97]. Reprinted from Non-enzymatic electrochemical detection of cholesterol using β cyclodextrin functionalized graphene, 63, N. Agnihotri, A.D. Chowdhury, A. De, pp. 212-217, Copyright 2015, with permission from Elsevier.

Table 1.4. Cyclodextrin based biosensors

Analyte	Sensor	Detection method	Detection range (µM)	LOD (µM)	Medium	Ref.
Uric acid	Poly (βCD)/CQDs/GCE	DPV	0.3 - 200	0.01	Urine	[42]
	βCD/ MWCNT–COOH	CA	100 - 700	100**	Buffer	[47]
	βCD/RGO	DPV	0.08 - 150	0.026	Serum	[84]
	βCD/selenium-CQDs/	DPV	10-1000	0.03	Urine and serum	[93]
Cholesterol	βCD/MWCNTs/ SPCE	DPV	0.001 - 3	0.0005	Serum	[20]
	βCD/3D-ePAD	DPV	0.1-1000	0.03	Serum	[91]
Tyrosine	CuO/βCD/ Nafion /GCE	CA	0.01 - 100	0.0082	Urine and serum	[15]
	βCD/CQDs	CV-DPV	0.2 - 100	0.00607	Serum	[43]
	βCD–GQD/GCE	DPV	0.1 - 1.5	0.1**	Buffer	[115]
	βCD/Pt NPs/PPy/ chiral -CNT	DPV	3-30	0.000107	Buffer	[116]
	MPC-sulfato-βCD/GCE	DPV	1-500	0.26	Tap water	[101]
Adenine	α-CD/RGO	DPV	10 - 50	0.1455	Serum	[102]
Thymine	α-CD/RGO	DPV	10 - 50	0.0529	Serum	[102]
Guanine	α-CD/RGO	DPV	10 - 50	0.0389	Serum	[102]

*Detection range and LOD are typically determined in buffer and would likely be different in complex media.

**Limit of quantification (LOQ)

1.4 Sensitivity, Stability, and Selectivity in Hydrophobic Metabolite Sensing

1.4.1 Sensitivity

Sensitivity is an important characteristic of the biosensor, and it is defined as the slope of the calibration curve [117]. Different surface modification methods are employed to enhance the sensitivity of biosensors; however, this parameter is often overlooked and receives less attention than LOD [118]. **Figure 1.7** demonstrates sensitivity of some of the reported amperometric biosensors, and the sensitivity of hydrophobic metabolite biosensors is usually between 1-10 µA μM^{-1} cm^{-2} [2,12,86,119]. However, in case of an Au/Co/nanoporous hollow carbon framework/GCE surface for uric acid detection the sensitivity can be as high as 48.4 µA μM^{-1} cm^{-2} [53] and MnO_2/PGE biosensor can detect cholesterol with sensitivity of 63869 µA μM^{-1} cm^{-2} [14].

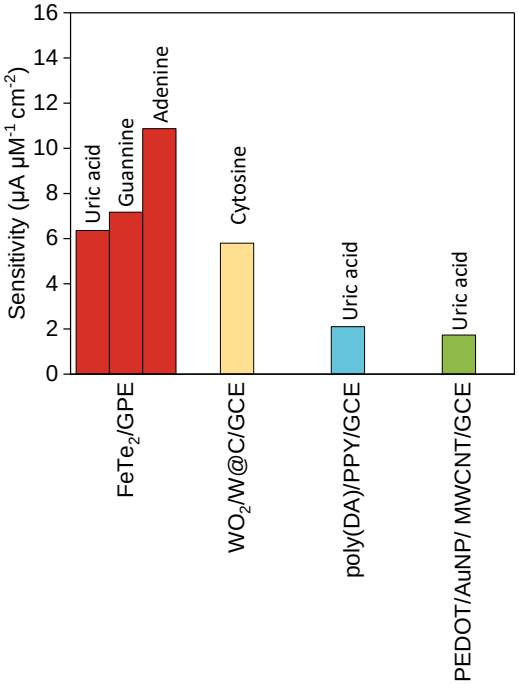

Figure 1.7. Sensitivity of some of the electrochemical biosensors for detection of hydrophobic metabolites.

1.4.2 Stability

Short-term (or sensing) stability as well as long-term (or storage) stability are widely used to describe biosensor performance. Sensing stability evaluates the effect of surface fouling on biosensors response. For example, constant amperometric response of MCPE/COOH-MWCNT for 20 min suggested the biosensor was stable in solution during sensing of tyrosine [49]. Additionally, after 80 continuous DPV sweeps using ZnS@CdS/GO/GCE surface, adenine and guanine oxidation peak currents only dropped to 90.7 and 91.2 % of their original values, respectively [65]. Similarly, 25 CV cycles were repeated to show antifouling property of poly(HQ)/crown ether/CNT/GCE surface for uric acid detection [73].

Moreover, long storage stability of biosensors is required for clinical applications. **Figure 1.8** represents storage stability of various biosensors in dry room temperature (**Figure 1.8A**), dry low temperatures (**Figure 1.8B**), and buffer solutions (**Figure 1.8C**) where the biosensor retains at least 90% of their original response after storage period.

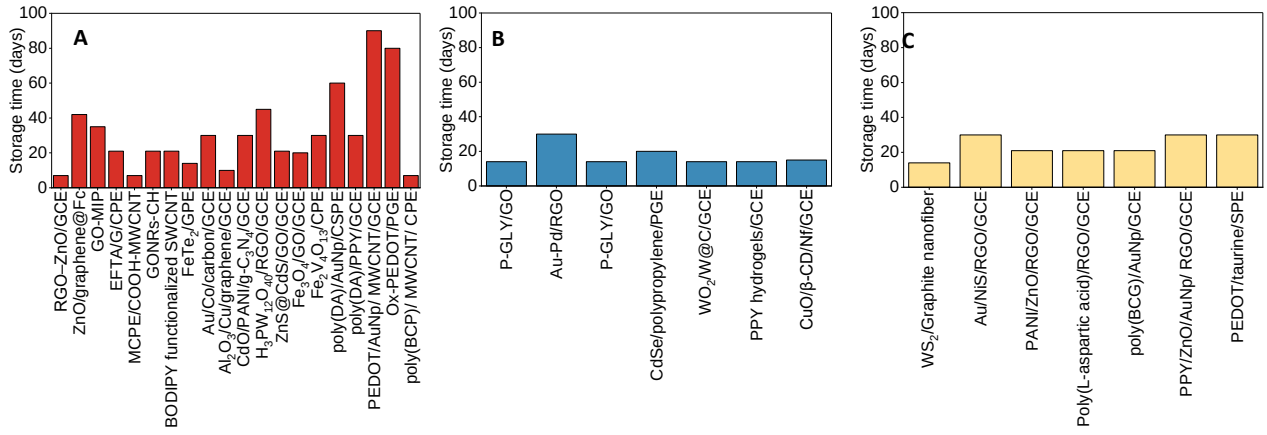

Figure 1.8. Storage stability of various biosensors in A) dry room temperature, B) dry low temperatures, and C) buffer solutions.

1.4.3 Selectivity

While biosensors with low sensitivity generate more false negatives, non-selective biosensors are likely to produce false positive results. Therefore, cross interference studies are performed to investigate the influence of potentially interfering compounds on biosensors response. These general points should be considered when selecting interfering compounds for selectivity experiments:

- Composition of biological solution: For example, uric acid as an important organic constituent of urine can interfere with various hydrophobic metabolites detection. Therefore, uric acid should always be tested when the biosensors are developed to detect analytes in urine.
- Electrochemical detection technique: For example, in amperometric biosensors various electroactive molecules can be oxidized or reduced at the surface. Therefore, all electroactive species that coexist with target analyte can be potential interferents.
- Nature of modified surface: For example, cyclodextrins can make inclusion complexes with various hydrophobic guest molecules. Therefore, it is important to note the presence of coexisting hydrophobic molecules in the solution.

1.5 Electrochemical Cross-Reactive Sensor Arrays for Disease Diagnosis

So far in this Chapter we discussed the non-enzymatic electrochemical affinity based biosensors that are designed based on a “lock-and-key” platform, wherein the surfaces are modified with receptors with high selectivity and specificity towards the target analyte. The affinity based biosensors often provide useful **quantitative** information about a single target analyte [120] (**Figure 1.9.A**).

Electrochemical tongue or electrochemical nose is a type of biosensor that mimics the pattern recognition performance of gustatory (taste) or olfactory (smell) sensory systems and does not follow the strict "lock-and-key" design principle. The mammalian olfactory system contains more than 1000 different unspecific and unselective receptors which respond to many different analytes. The olfactory receptors' responses are processed in the olfactory cortex and the achieved "signature" or "finger print" allows the classification and identification of different smells [121]. Similarly, electrochemical tongue biosensors are based on an array of surfaces modified with various cross-reactive receptors and the surfaces have partial cross specificity to various compounds that exist in the complex solutions. The advantage of electrochemical tongue biosensors over affinity based biosensors is that electrochemical tongues provide a better **qualitative** information of the sample because different surfaces interact with multiple analytes simultaneously [120,122] (**Figure 1.9.B**).

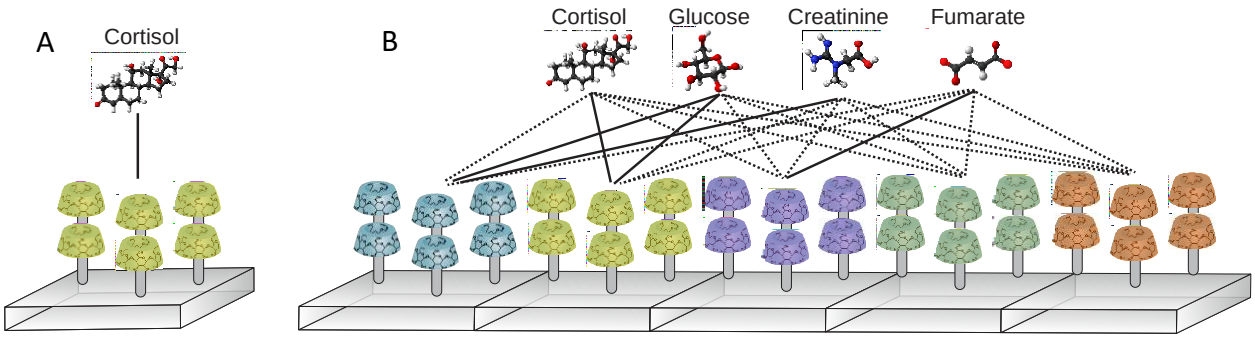

Figure 1.9. A schematic of (A) an electrochemical affinity-based (selective) biosensor vs. (B) a cross-reactive sensor array (electrochemical tongue)

In electrochemical tongues different surfaces respond to different compounds causing overlapping of analytical signals; therefore, often complex chemometric data analysis methods are required for data analysis. The chemometric methods are a range of techniques that remove redundant data, improve signal to noise ratio, and employ multivariant data treatment and pattern recognition techniques such as **supervised** Linear Discriminant Analysis (**LDA**) and **unsupervised** Principal Component Analysis (**PCA**) to discriminate between complex solution samples [123,124]. Electrochemical tongues have different applications in pharmaceuticals [125,126], agriculture and food processing [127–129], cosmetics [123], and biosensors [130–132]. For example, in case of biosensors, an electrochemical nose has been developed to analyze breath samples of 276 volunteers to differentiate between healthy, benign (non-cancerous lesions), and ductal carcinoma in situ (DCIS) samples [130]. Additionally, electrochemical tongues were designed to discriminate saliva samples of oral cavity cancer patients and healthy individuals [131] and analyze urine samples to make a separation between prostate cancer patients and control samples [132]. The electronic tongue employed for prostate cancer diagnosis was an array of seven working electrodes; therefore, seven variables existed in the system. The reason that usually this many electrodes (variables) exist in electronic tongue systems is that it is possible to get a better separation between different groups compared to when fewer electrodes (variables) are used. However, it is not possible to plot the data with this many variables; therefore, dimension reduction techniques such as PCA and LDA are needed to combine variables to simplify analysis, visualize data, and identify individuals with a similar health profile [123,125–132].

Equation 1.1 shows that PCA combines n variables (X_1 to X_n) to 1 variable ($\mathrm{PC1}$). α_1 to α_n are weights of different variables and PCA finds the optimal values for α_1 to α_n so that the combined variable (first principal component ($\mathrm{PC1}$)) has a maximum variance. Therefore, PCA is a method to find the linear combination that accounts for as much **variability** as possible. The weights for the PCA are extracted from the first eigenvector of the covariance matrix. PCA is referred to as an **unsupervised** method because it discovers hidden patterns in **unlabeled** data sets [133].

$$\mathrm{PC1} = \alpha_1 \mathrm{X}_1 + \alpha_2 \mathrm{X}_2 + \cdots + \alpha_\mathrm{n} \mathrm{X}_\mathrm{n} \qquad \text{Equation 1.1}$$

LDA is a similar method which aims to maximize the **separation** between two or more groups. Therefore, LDA combines variables X_1 to X_n by using optimal values for α_1 to α_n so that the combined variable, i.e., first linear discriminant ($\mathrm{LD1}$) shows maximum separation between the groups (Equation 1.2). LDA is a **supervised** technique and to find the best separation between the groups, a **labeled** (training) data set must be used [134].

$$\mathrm{LD1} = \alpha_1 \mathrm{X}_1 + \alpha_2 \mathrm{X}_2 + \cdots + \alpha_\mathrm{n} \mathrm{X}_\mathrm{n} \qquad \text{Equation 1.2}$$

While both PCA and LDA are dimensionality reduction techniques, if the variables are correlated, only PCA can address the collinearity problem. In other words, if the variables are somehow correlated, PCA and LDA can be combined, and the principal components of the data can be used as input for LDA [134]. Additionally, while PCA is a popular pattern recognition method in some recent developed electrochemical tongues [123,125–127], PCA is mainly a dimensionality reduction technique, is not optimized for class separability, and LDA is a better

approach for classification [135]. However, when the training set is too small, PCA can outperform LDA [136].

Similar to the conventional electrochemical affinity-based biosensors, electronic tongues can be based on amperometric [137], voltametric [123,125,126], or impedimetric [127,138–141] transducers. While amperometric and voltametric tongues are based on oxidation of electroactive analytes on the electrode surface, impedimetric tongues can be used for detection of both electroactive and non-electroactive species. This is especially an important consideration when choosing electrochemical transducers for clinical biosensors because not all disease biomarkers are necessarily electroactive. For example, cortisol, a non-electroactive molecule, is an important sepsis biomarker.

In the following chapters, we will thoroughly discuss the impedimetric electrochemical biosensors (Chapter 2). Then, we will show the applications of impedimetric methods in development of the first reusable cyclodextrin sensing platforms for detection of trans-resveratrol (Chapter 3), and cortisol (Chapter 4). Finally, in Chapter 5 of this thesis we will employ a cross-reactive sensor array (impedimetric tongue) consisting of various cyclodextrin surfaces for separation and classification of different samples.

1.6 Conclusion

Cyclodextrin biosensors have advantages over other non-enzymatic surface modification strategies for sensing of hydrophobic metabolites. Cyclodextrins improve the selectivity of biosensors because the formation and stability of inclusion complexes of cyclodextrins and hydrophobic analytes depend on various factors including but not limited to the size of the cyclodextrin cavity, the size of the hydrophobic section of the hydrophobic analyte, the number and placement of hydrogen donors. However, reversible immobilization of cyclodextrins on the electrodes and fabrication of reusable cyclodextrins remains a challenge and all current cyclodextrin biosensors are single use. Designing a stable platform for reversible immobilization of cyclodextrins allows us to develop stable and reusable cyclodextrin surfaces for detection of hydrophobic metabolites. Further, various cyclodextrin surfaces can be integrated to create a cross-reactive sensing array for recognition of a class of biomarkers that interact with cyclodextrins.

2. Electrochemical Impedance Spectroscopy (EIS)

2.1 Rational: The need for Electrochemical Impedance Spectroscopy

In Chapter 1, we mostly talked about various DC based electrochemical biosensors with amperometric and voltametric transducers. In DC circuits (frequency of zero), the resistors are the only elements that can create resistance and the resistance to the DC current through a resistor can easily be determined by Ohm's law. However, other circuit elements such as capacitors or inductors can also slow the flow of current. For example, in the case of capacitors, the current flows only when the capacitor is charging or discharging. In AC circuits, the resistance is called impedance and since the impedance of some circuit elements such as capacitors and inductors is frequency dependent and does not follow Ohm's law, an AC based electrochemical technique (EIS) is needed to measure their impedance. In other words, EIS allows us to measure the impedance of everything in the system that slows down the current and we can collect more data compared to DC based techniques [142,143]. Additionally, different electrochemical phenomena occur at the same time but at different time scales (or at different frequencies). For example, while diffusion is a slow process (large time constant, low frequency), the charging of the electrode-electrolyte interface (double layer charging) happens faster (shorter time response, higher frequency) [144]. In a DC voltammetry experiment, the potentiostat can only measure the total current resulting from all the electrochemical processes that are occurring at that time and it cannot distinguish what part of the current is associated with double layer charging or diffusion. In contrast, EIS is able to distinguish between different electrochemical phenomena because they occur at different characteristic frequencies. Finally, while

amperometric and voltametric techniques can simply measure the faradaic current, measurement of non-faradaic current by these techniques is almost impossible. However, using EIS we can measure faradaic and non-faradaic currents and non-faradaic EIS can be used as the transduction technique in development of point of care (POC) sensors. Despite the many advantages the EIS offers, it is a complicated technique and requires complex data processing steps. In this chapter we will discuss EIS data collection and data analysis which is necessary for development of EIS based biosensors in detail.

2.2 Faradaic vs. Non-Faradaic Electrochemical Biosensors

In Chapter 1, we extensively reviewed the electrochemical biosensors for detection of electroactive analytes that can oxidize on various modified electrode surfaces (**Figure 1.2**). However, a lot of important disease biomarkers and metabolites such as cholesterol and cortisol are not electrochemically active. We can divide the electrochemical biosensors for measurement of non-electroactive species into two groups of Faradaic and non-Faradaic based biosensors. **Figure 2.1** demonstrates a polymeric surface that cyclodextrins (blue) are used as mediators. When the surface is incubated in a solution that contains an analyte that cyclodextrins can interact with, the cyclodextrins leave the surface and force the surface polymers to change into a mushroom configuration. In faradaic based biosensors, there are some electroactive components in the system; i.e., redox couples such as ferri/ferrocyanide in the solution (**Figure 2.1.A**) or redox labels such as ferrocene on the surface (**Figure 2.1.B**) [145]. Faradaic current is generated as a result of oxidation/reduction reactions that take place on the electrode-electrolyte interface [146]. In **Figure 2.1.A**, the faradaic current is generated when the ferri and ferrocyanide ions in the solution can diffuse through the initial porous surface. But as the

cyclodextrins leave the surface, the polymers bend and the surface becomes less porous, the amount of faradaic current decreases. In **Figure 2.1.B**, ferrocene molecules are chemically attached to the polymers and the faradaic current is only generated when ferrocene labels are close enough to the surface. Therefore, the initial surface generates less faradaic current compared to when surface polymers bend and create the mushroom-like structure.

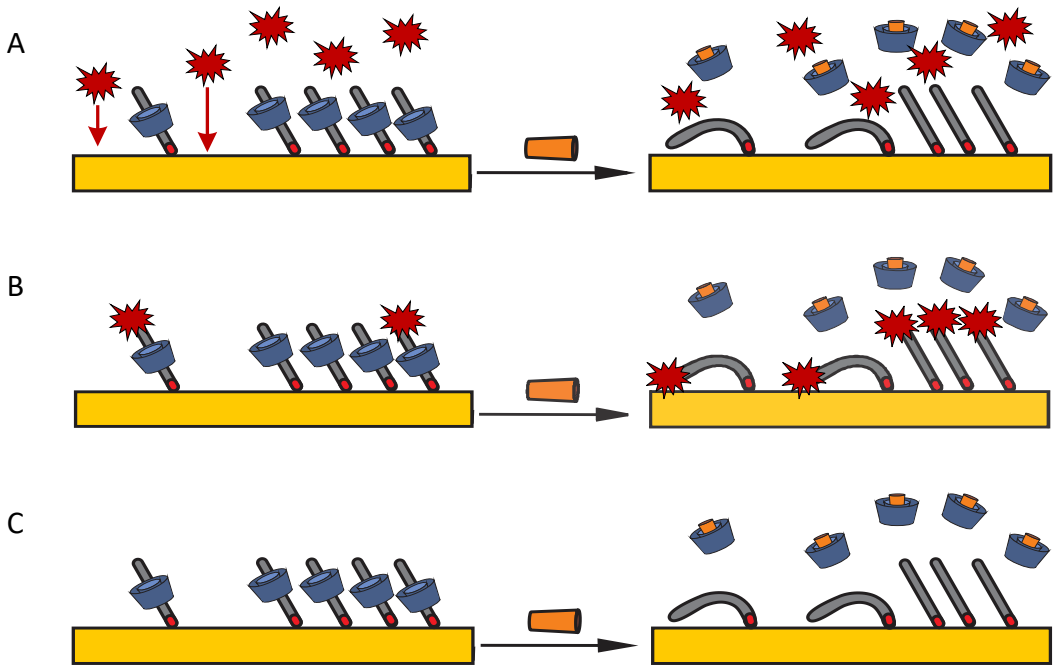

Figure 2.1. A schematic of a polymer surface loaded with cyclodextrins. This surface can be used to develop (A) a faradaic biosensor with redox probes in the solution, (B) a faradaic biosensor with polymers modified with redox tags, (C) a non-faradaic biosensor

Figure 2.1.C demonstrates a non-faradaic biosensor because there are no redox probes present in the system. In a non-faradaic biosensor, no redox reactions happen and the non-faradaic current is mostly generated due to the charging and discharging of the double layer capacitance [146]. Multiple studies have shown that employing redox probes in the biosensor system can limit the practical uses of the biosensors for multiple reasons [147–154]. First, the

redox couples such as ferri/ferrocyanide, can interact with surface or analytes and deteriorate surface sensitivity and selectivity. Second, the use of redox couples limits the practical applications of biosensors in complex biological fluids [153]. In addition, non-faradaic analysis is more sensitive to changes in the interface between the electrode and the solution because the faradaic charge-transfer resistive process can mask simultaneous surface resistive and capacitive effects [147]. For these reasons, throughout this thesis a non-faradaic approach is used for more sensitive measurement of trans-resveratrol (Chapter 3), cortisol (Chapter 4), and various sepsis biomarkers (Chapter 5).

Figures 2.2, **2.3**, and **2.4** show the amperometric, voltametric, and impedimetric responses to the changes of the polymeric surface in faradaic and non-faradaic systems. The comparison between these methods show that EIS is the most important electrochemical technique that can be used for analysis of non-faradaic systems. However, the changes in non-faradaic EIS tend to be small which requires a perfectly fit circuit to monitor and predict these changes. As an alternative to fitting the data to an equivalent circuit is to develop an empirical correlation using an EIS parameter at a single frequency.

2.3 EIS Data Collection

During a potentiostatic EIS experiment, the potentiostat (**Figure 2.5**) applies sinusoidal potentials (Equation 2.1) to an electrochemical system at multiple frequencies and measures the corresponding sinusoidal currents (Equation 2.2) at all these frequencies to create a spectrum.

$$E_t = E_0 \, Sin \, (\omega t) \qquad \text{Equation 2.1}$$

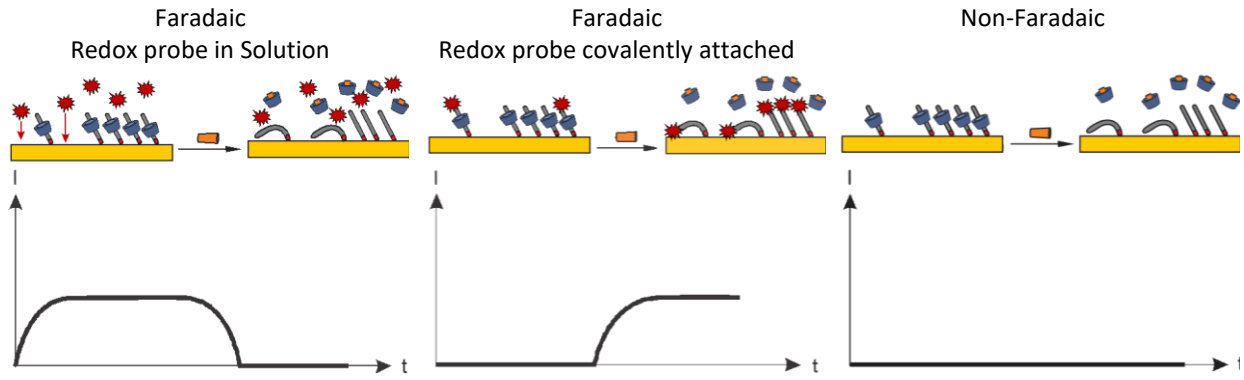

Figure 2.2. Amperometric method for analysis of surface in faradaic and non-faradaic systems. The amperometric technique cannot measure the non-faradaic changes of the surface.

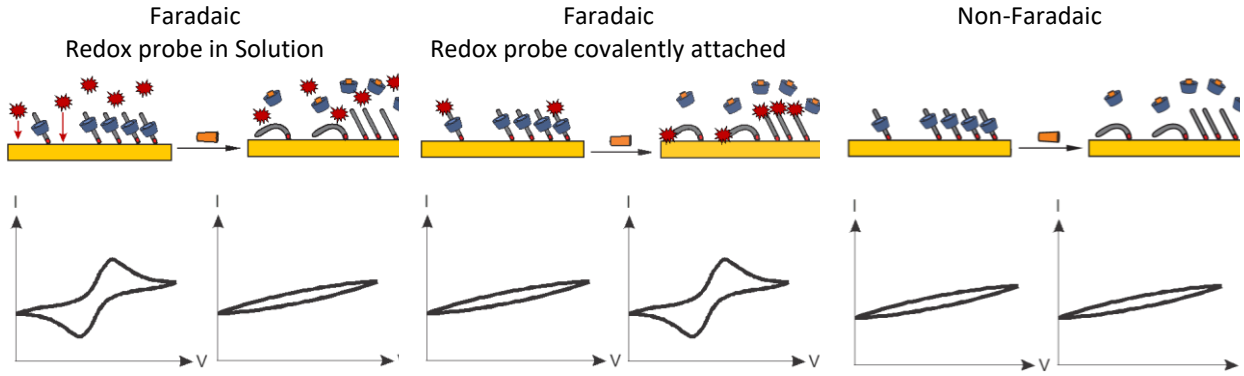

Figure 2.3. Voltametric method for analysis of surface in faradaic and non-faradaic systems. The voltametric technique cannot measure the non-faradaic changes of the surface.

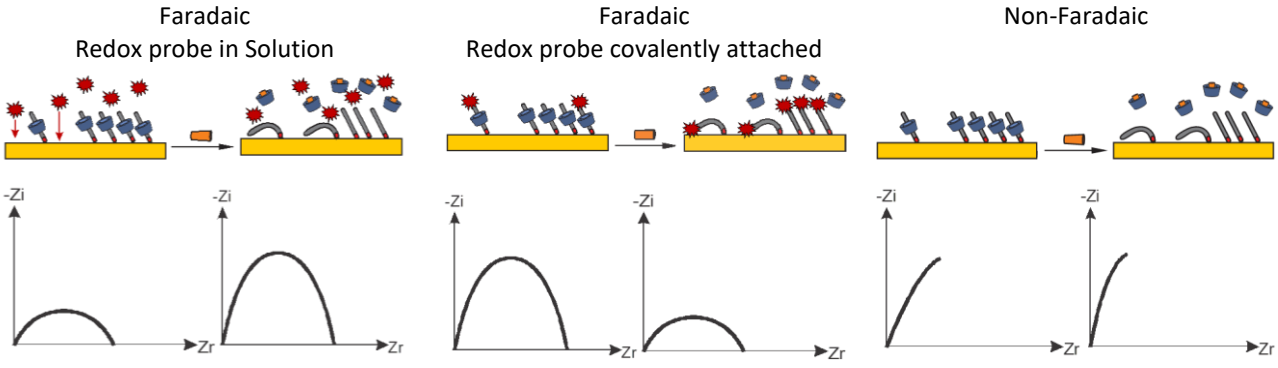

Figure 2.4. Impedimetric method for analysis of surface in faradaic and non-faradaic systems. EIS can measure both faradaic and non-faradaic changes of the surface.

$$I_t = I_0 \, Sin \, (\omega t + \Phi)$$ Equation 2.2

The applied sinusoidal potential fluctuates as a function of time (t). E_0 is the amplitude of the signal and represents the amount of applied potential. ω is the angular frequency and shows how frequently the signal oscillates. The term ωt represents the phase of the waveform. The output sinusoidal current has the same frequency but may be offset from the input sinusoidal potential by a phase shift or phase angle (Φ) (**Figure 2.5**).

Some operations that are hard to perform in time domain, may be easier in frequency domain. Mathematical Fourier Transform functions are used to convert time domain data to frequency domain data. The potentiostat takes a Fourier transform of all the input and output signals to convert all the time (s) domain data into the frequency domain data. The potentiostat uses ratios of the frequency dependent potential over the frequency dependent current to find the impedance Z (Equation 2.3) at different frequencies.

$$Z = \frac{\bar{E}(\omega)}{\bar{I}(\omega)}$$ Equation 2.3

In Equation 2.3, $\bar{E}(\omega)$ and $\bar{I}(\omega)$ are Fourier transformed potential and current, respectively. Equation 2.3 is analogous to Ohm's law and in a potentiostatic EIS system, impedance can be defined as the resistance in an alternating potential. So, rather than plotting the current and potential as we would normally see in DC voltammetry techniques like CV, in EIS, the potentiostat provides us with two measurables: the magnitude of impedance ($|Z|$) and phase angle (Φ).

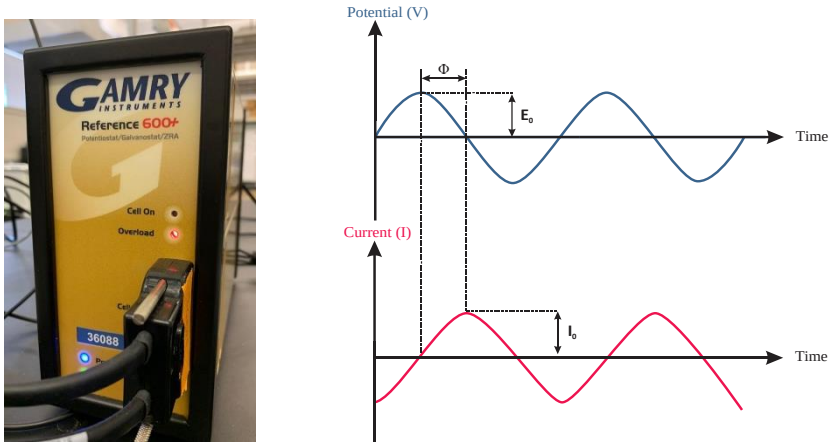

Figure 2.5. During a potentiostatic EIS experiment, the potentiostat (shown on the left) applies a sinusoidal potential and measures the current. (shown on the right)

The magnitude of impedance ($|Z|$) is a ratio of the potential and current amplitudes at a specific frequency (Equation 2.4).

$$|\mathrm{Z}| = \frac{\mathrm{E_0}}{\mathrm{I_0}} \qquad \text{Equation 2.4}$$

Impedance is a complex number. Therefore, impedance can be shown in polar coordinate as ($|\mathrm{Z}|, \Phi$) (**Figure 2.6**). Another common way to show impedance is in a cartesian coordinate. If we convert from the polar coordinate to the cartesian coordinate (Equation 2.5), we can break down the magnitude of the impedance ($|Z|$) and the phase angle (Φ) to get the impedance that is associated with the X axis which is referred to a real impedance (Z') and the impedance associated with the Y axis which is called the imaginary impedance (Z'').

$$\mathrm{Z} = \mathrm{Z'} + \mathrm{jZ''} \qquad \text{Equation 2.5}$$

$$\mathrm{Z'} = |\mathrm{Z}|\cos\Phi \qquad \text{Equation 2.6}$$

$$Z'' = |Z|sin\Phi \qquad \text{Equation 2.7}$$

If we substitute the $Z'$and $Z^{"}$in Equation 2.5, we can write:

$$Z = |Z|(\cos\Phi + j\sin\Phi) \quad \text{Equation 2.8}$$

Using Euler's formula ($e^{ix} = \cos x + j\sin x$), the impedance Z can be written as:

$$Z = |Z|\, e^{j\Phi} \quad \text{Equation 2.9}$$

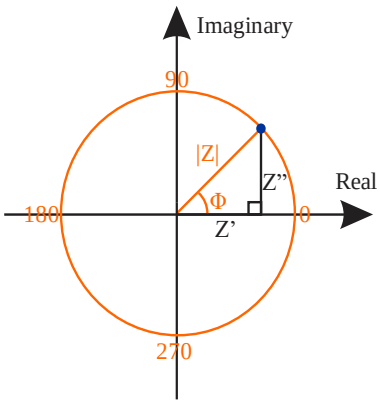

Figure 2.6. Impedance is an imaginary number and can be shown in a polar or cartesian coordinate. $|Z|$ and Φ are the impedance variables in polar coordinate; while, Z' *and* $Z^{"}$ are impedance variables in cartesian coordinate.

Similar to impedance, capacitance can be shown in a cartesian coordinate as a complex number and the total capacitance (C), is represented by the real part (C') and the imaginary part (C") and it is expressed as Equation 2.10-2.12 [155]:

$$C = C' + jC^{"} \quad \text{Equation 2.10}$$

$$C' = -\frac{-Z^{"}}{\omega(Z'^{2}+Z^{"2})} \quad \text{Equation 2.11}$$

$$C^{"} = -\frac{-Z'}{\omega(Z'^{2}+Z^{"2})} \quad \text{Equation 2.12}$$

2.4 EIS Data Analysis

EIS data is usually interpreted with the use of equivalent electrical circuits (EEC). Fitting the EIS data with electrical circuit models allow us to collect quantitative information about the electrochemical phenomena that happen in the system. For example, the solution resistance and the electrochemical double layer can be modeled as a resistor and capacitor, respectively and the charge transfer resistance is often used to monitor the surface changes in faradaic EIS experiments.

While extensive research has been conducted to analyze faradaic EIS data [156], some problems still remain with the analysis of non-faradaic EIS. In a typical non-faradaic EIS measurement, the parameters associated with electron transfer such as charge transfer resistance and Warburg impedance are eliminated and this makes finding the equivalent electrical circuit (EEC) that fits the data challenging [157,158]. The second approach for analysis of EIS data is to use a single EIS parameter such as real impedance (Z'), imaginary impedance ($Z^{"}$), magnitude of impedance ($|Z|$), real capacitance (C'), imaginary capacitance (C"), total capacitance (C), and phase angle (Φ) at a designated frequency and develop an empirical correlation between that parameter at that frequency and the surface changes. The single frequency EIS approach allows us for simultaneous EIS data collection and analysis; however, it is often difficult to develop any meaningful or scientific reasoning for selecting a specific frequency.

2.4.1 Faradaic EIS Data Analysis of an Unmodified Glassy Carbon Surface

A BASi® glassy carbon electrode was polished with 0.55 µm alumina for 1 min and was then sonicated in UHP water for 1 min. The electrode was rinsed thoroughly with UHP water and the faradaic EIS measurements were carried out in 20 mL of 20 mM ferri/ferrocyanide in UHP (**Figure 2.7**). Bode and Nyquist plots are two different representations of EIS data. If we plot the magnitude of the impedance ($|Z|$) and phase angle (Φ) as a function of frequency, we get Bode plot. The Nyquist plot shows the negative imaginary part of the impedance ($-Z^{"}$) in the y axis and the real part of the impedance (Z') in the x axis. **Figure 2.8A** and **Figure 2.8B** show faradaic Nyquist and Bode plots of glassy carbon electrode after polishing.

Figure 2.7. Faradaic EIS in ferri/ferrocyanide solution in UHP. The yellow color of the solution is due to the presence of in ferri/ferrocyanide ions.

The most common electrical circuit to fit faradaic EIS data is Randle's circuit (**Figure 2.9**). The Randles circuit consists of a solution resistance R_s in series with the double layer capacitance C_{dl}, charge transfer resistance R_{ct}, and Warburg impedance. Double layer capacitance deviates from ideal behavior due to surface roughness and constant phase element (CPE) is often used in equivalent circuit model. While the impedance of the resistors is not frequency dependent (Equation 2.13), the impedance of the capacitor (Equation 2.14) and Warburg element (Equation

2.15) is frequency dependent and is larger at lower frequencies. The A_w in Equation 2.15 is called the Warburg coefficient and is the diffusion coefficient of ions in solution.

$$Z_{Resistor} = R \qquad \text{Equation 2.13}$$

$$Z_{Capacitor} = \frac{1}{j\omega C} \qquad \text{Equation 2.14}$$

$$Z_{Warburg\ Element} = \frac{A_w}{(j\omega)^{0.5}} \qquad \text{Equation 2.15}$$

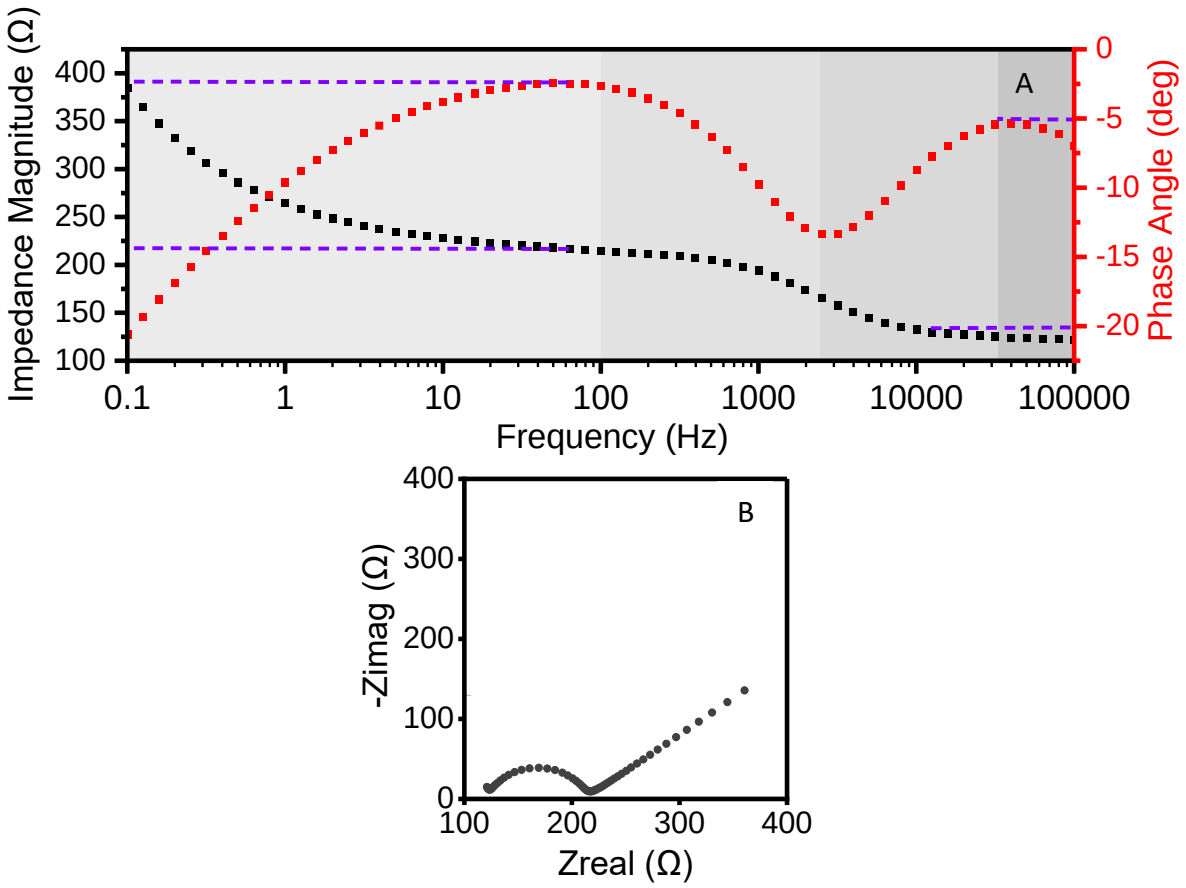

Figure 2.8. Faradaic EIS data of a glassy carbon electrode: (A) Bode and (B) Nyquist plot. The red and black dotted lines show the data points. The purple dash lines in Bode plot shows the theoretical values in the absence of reference electrode artifacts (in high frequencies) and Warburg impedance (in low frequencies).

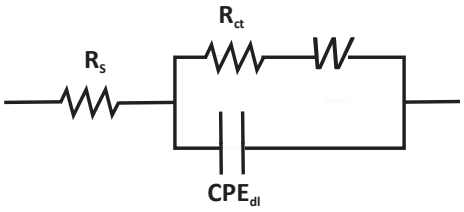

Figure 2.9. The Randle's circuit is the most common electrical circuit to model the EIS data.

In theory, at very high frequencies (39890-100078 Hz), C_{dl} should effectively have no impedance and all of the current should go through the C_{dl} and R_s and none of the current should flow through the R_{ct} (**Figure 2.8A**). The deviation between the purple dash lines (theory) and the red and black dotted lines (data) is due to the large impedance of reference electrode in high frequencies [159].

At medium frequencies (63.3-39890 Hz), the C_{dl} has some impedance. Therefore, as the frequency decreases from 39890 Hz to 2527 Hz, the impedance magnitude increases from 124.2 Ω to 165.241 (**Figure 2.8A**). Additionally, because this increase in impedance is caused by a capacitor, the phase angle starts to deflect away from 0 and goes toward -90. However, the phase angle does not get to -90 because the impedance of R_{ct} and R_s is independent of frequency and therefore R_{ct} has still some meaningful contribution to the impedance.

At very low frequencies (0.1-63.3 Hz), the C_{dl} has a much greater impedance than R_{ct} and almost all of the current flows through the R_{ct} and Warburg element. If diffusion of ions had not occurred in the system, Warburg impedance would have not existed, R_{ct} would have been the only element creating the impedance, and instead of the increase in impedance at low

frequencies (black impedance magnitude data points), we would have seen the purple straight lines because the impedance of R_{ct} is independent of frequency (**Figure 2.8A**).

2.4.2 Faradaic vs Non-Faradaic EIS Data Analysis of a Polymer Surface

One of the most common applications of faradaic EIS is monitoring the charge transfer resistance after each modification step. For example, **Figure 2.10** shows the EIS data of a glassy carbon electrode (GCE) before (**Figure 2.10A**) and after modification with carboxyphenyl groups (**Figure 2.10B**). The carboxyphenyl groups were then modified with polypropylene glycol (PPG) (**Figure 2.10C**). The faradaic EIS measurements were carried out in 20 mL of 20 mM ferri/ferrocyanide in UHP and Randle's circuit was used to model the EIS data of GCE, GCE-carboxphenyl, and GCE-carboxphenyl-PPG surfaces. Comparison of different circuit elements after each modification stage (**Figure 2.10D**) shows that the charge transfer resistance (R_{ct}) and Warbug element (W) increase after each modification stage. The faradaic current in this system is generated due to the presence of ferri/ferrocyanide ions. Therefore, modifying the glassy carbon electrode with carboxyphenyl and polypropylene glycol on one hand decreases the redox reactions on the electrode and electron transfer rate (increase in R_{ct}) and on the other hand hinders the diffusion of these ions to the electrode surface. Depletion of these ions in front of the electrode causes the increase in W.

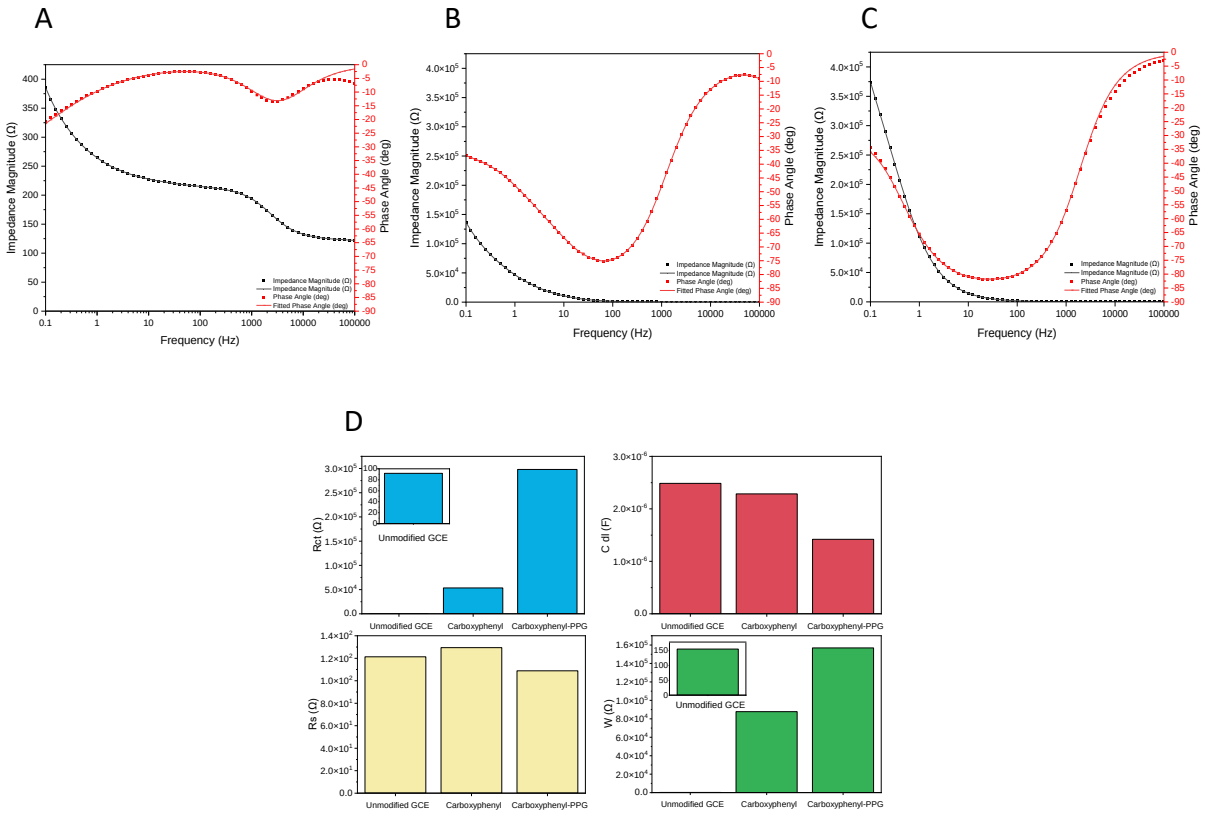

Figure 2.10. Bode plots of faradaic EIS in 20 mM ferri/ferrocyanide in UHP: (A) an unmodified glassy carbon electrode, (B) after modification with carboxyphenyl groups, and (C) after modification with PPG. Randle's circuit was used to model the data and (D) is the changes in different circuit elements upon surface modification.

We additionally performed non-faradaic EIS experiments in a blank PBS buffer solution (**Figure 2.11**) and the non-faradaic EIS data of GCE, GCE-carboxphenyl, and GCE-carboxphenyl-PPG surfaces are shown in **Figure 2.12**. We fitted the non-faradaic data with Randle's circuit and **Figure 2.12D** shows the Randle's circuit components of each surface. **Figure 2.12D** shows no meaningful trend in R_{ct} upon surface modification since there are no redox couples in the solution, and only the non-faradaic current flows through the system. Therefore, Randle's circuit cannot be used to model this system because it does not describe the electrochemical phenomena appropriately. In the following sections of this chapter, the appropriate methods for analysis of non-faradaic EIS data will be discussed.

Figure 2.11. Non-Faradaic EIS in PBS buffer. The solution is clear because there are no ferri/ferrocyanide ions present.

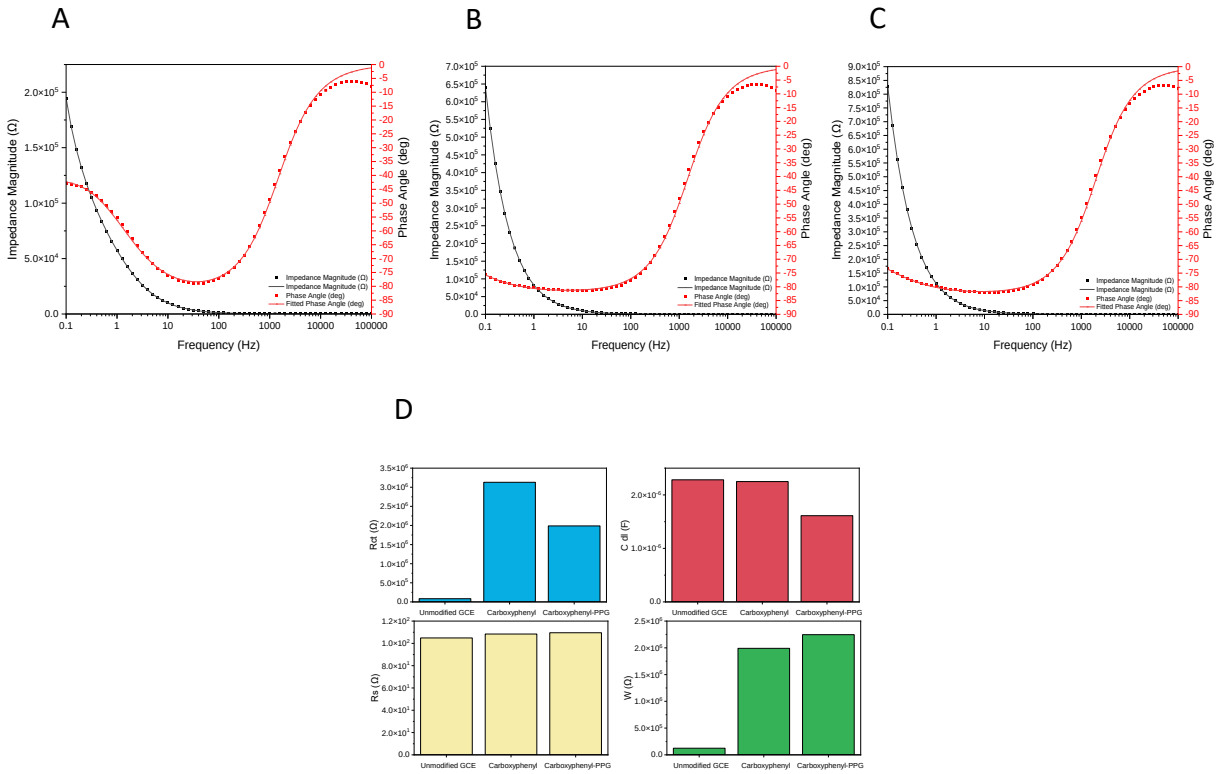

Figure 2.12. Bode plots of non-faradaic EIS in PBS buffer: (A) an unmodified glassy carbon electrode, (B) after modification with carboxyphenyl groups, and (C) after modification with PPG. Randle's circuit was used to model the data and (D) is the changes in different circuit elements upon surface modification.

2.4.3 Non-Faradaic EIS Analysis of a Polymer-Cyclodextrin Surface

As we mentioned in Section 1.3, all current cyclodextrin biosensors are single use and one of the important aims of this project was development of the first reusable cyclodextrin biosensors. Therefore, throughout this thesis and specifically in Chapters 3 and 4, we will use EIS to investigate the reusability of our cyclodextrin surfaces. In Chapter 3, we will use faradaic EIS to show reusability of α-CD surface and in Chapter 4 we will use non-faradaic EIS to demonstrate reusability of βCD surface. Since in this section we want to focus on analysis of non-faradaic EIS data, we chose the EIS reusability data of βCD surface for this section.

To collect the non-faradaic reusability data, we first modified a glassy carbon electrode with carboxyphenyl and polypropylene glycol (PPG). Then we incubated the surface in the βCD solution for 1 hr to allow the cyclodextrin mediators load on PPG polymers. We assumed the interaction between cyclodextrins and PPG polymers are reversible and the cyclodextrins can be removed by a 1 hr ethanol soak. Further, we hypothesized the cyclodextrin surface can be regenerated by reincubation of the surface in the cyclodextrin solution (**Figure 2.13**). To prove our hypothesis, we modified three independent polymer surfaces (N=3) and for each surface we performed the cycle of cyclodextrin loading and removal of cyclodextrin by ethanol soak as many as 10 times (n=10). After each cyclodextrin loading and ethanol soak we rinsed the surface with UHP water, dried with N_2, and measured non-faradaic EIS response in blank PBS solution. In this section we will explore the analysis of the collected non-faradaic EIS data using different methods.

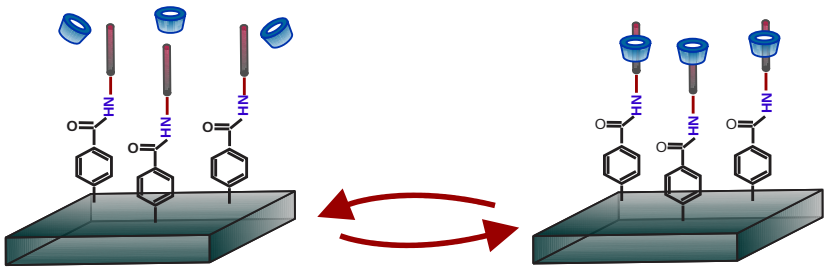

Figure 2.13. The schematic that shows the reversible interactions between CD and PPG polymers. We used EIS to show that we can do this cycle (CD loading and unloading) for 10 times with three different electrodes.

2.4.3.1 Equivalent Circuit Models

To interpret the non-faradaic EIS data, the equivalent circuit models (**Figure 2.14**) were first used to model the electrode-electrolyte interface. The first circuit (**Figure 2.14A**) assumes that the electrode surface is only partially covered by carboxyphenyl-PPG or carboxyphenyl-PPG:βCD chains and the double layer capacitance (CPE_{dl}) is present. It also assumes that the surface modification is a single layer that blocks the current and can be modeled with a layer capacitance (CPE_{layer1}). But since this layer is porous, some current flows through the leakage resistance (R_L) that exists in parallel with the CPE_{layer1}. In the second circuit (**Figure 2.14B**), the modification consists of two separate layers: the inner layer that is thinner and has fewer pores and the outer layer that is thicker and more porous. Similar to the first circuit, the second circuit has a CPE_{dl} due to the partial coverage of the electrode. The third circuit (**Figure 2.14C**) is very similar to the second circuit except it assumes the electrode is fully modified and therefore the CPE_{dl} is no longer present.

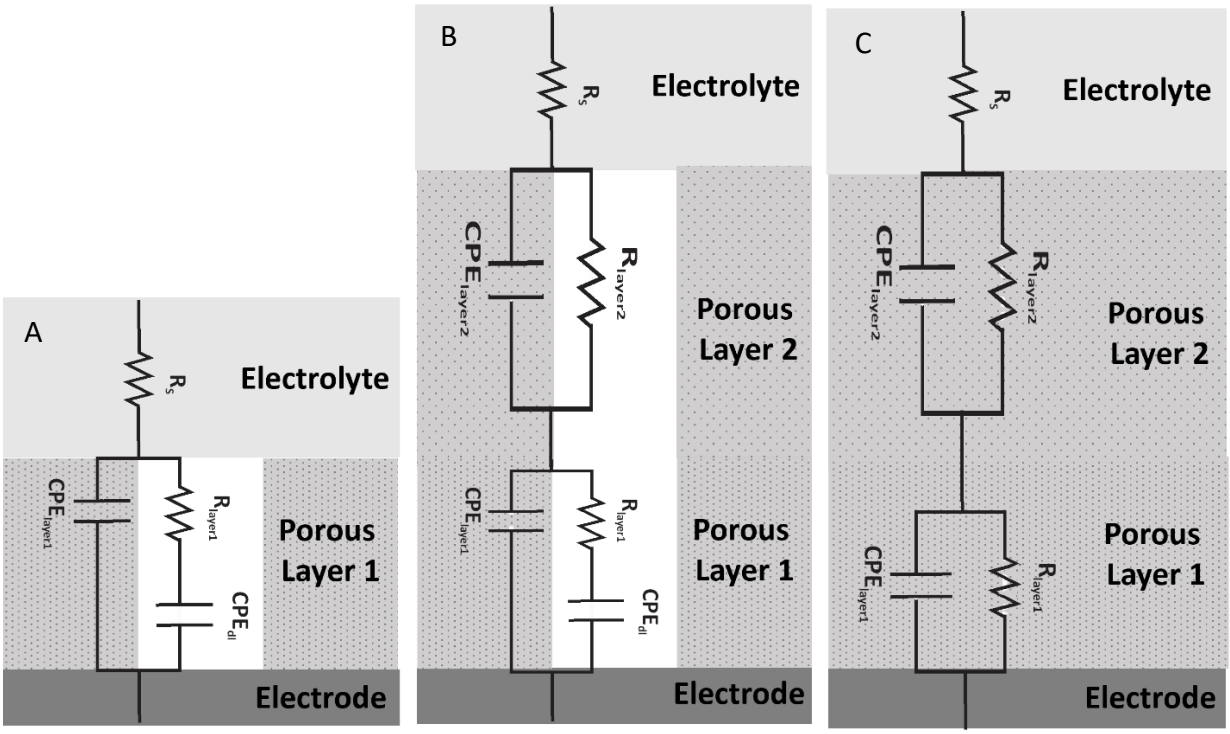

Figure 2.14. The equivalent circuit models that were used to model the non-faradaic EIS data: (A) assuming partial electrode coverage and 1 porous layer, (B) assuming partial electrode coverage and two porous layers, (C) assuming full electrode coverage and two porous layers.

Figure 2.15, **2.16**, and **2.17** show the results of the successful fitting of the same non-faradaic EIS data with the first, second, and third circuit, respectively. The changes in different circuit elements upon cyclodextrin loading (blue bars) and cyclodextrin removal by ethanol soak (red bars) are demonstrated. The summary of the data analysis and quantitative values are shown in **Table 2.1**.

Figure 2.15A and **2.15C** show that the ethanol soak (blue to red) causes an increase in the value of double layer capacitance and a decrease in the value of leakage resistance. Additionally, by cyclodextrin reloading and surface regeneration (red to blue), the double layer decreases and the leakage resistance increases. Therefore, in the first circuit, the double layer capacitance and leakage resistance are both impacted by the cyclodextrin loading and removal and these

parameters can provide useful information about the surface state. **Figure 2.15D** shows that the changes in solution resistance are not significant (84-97 Ω) confirming the first circuit can truly model the surface. **Table 2.1** shows that while the double layer capacitance values of the first circuit are in the range of 1.5 - 2.4 10^{-6} F, the layer capacitance values are in the 0.75 - 1.1 10^{-7} F range. This shows that due to the thickness of the modification layer, the double layer capacitance is one order of magnitude higher than the capacitance of the inert layer [144].

While the results from the first circuit are reasonable (**Figure 2.15**), neither capacitance nor resistance values in **Figure 2.16** are acceptable. The error bars in **Figure 2.16** are large and none of the circuit elements follow any predictable trends. In addition, the large fluctuations of the solution resistance (0.01-95.12 Ω) in **Table 2.1** confirm the second circuit is not an appropriate model to describe the surface. **Figure 2.17A** and **2.17C** show that when cyclodextrins leave the surface (blue to red), the values of layer capacitances C_{layer1} and C_{layer2} decrease and increase, respectively. Although, the error bars especially for the C_{layer1} are relatively large and solution resistance does not stay constant in different measurements and varies between 0.01 and 59.96 Ω.

In conclusion, Circuit 1 (**Figure 2.14A**) which consists of a single porous inert layer partially covering the glassy carbon electrode is the best circuit to model our cyclodextrin surface. Using this circuit, we can show the two states with and without βCD on the surface (**Figure 2.13**), show that the PPG and βCD interactions are reversible, and the cyclodextrin surface can be reusable (**Figure 2.15**).

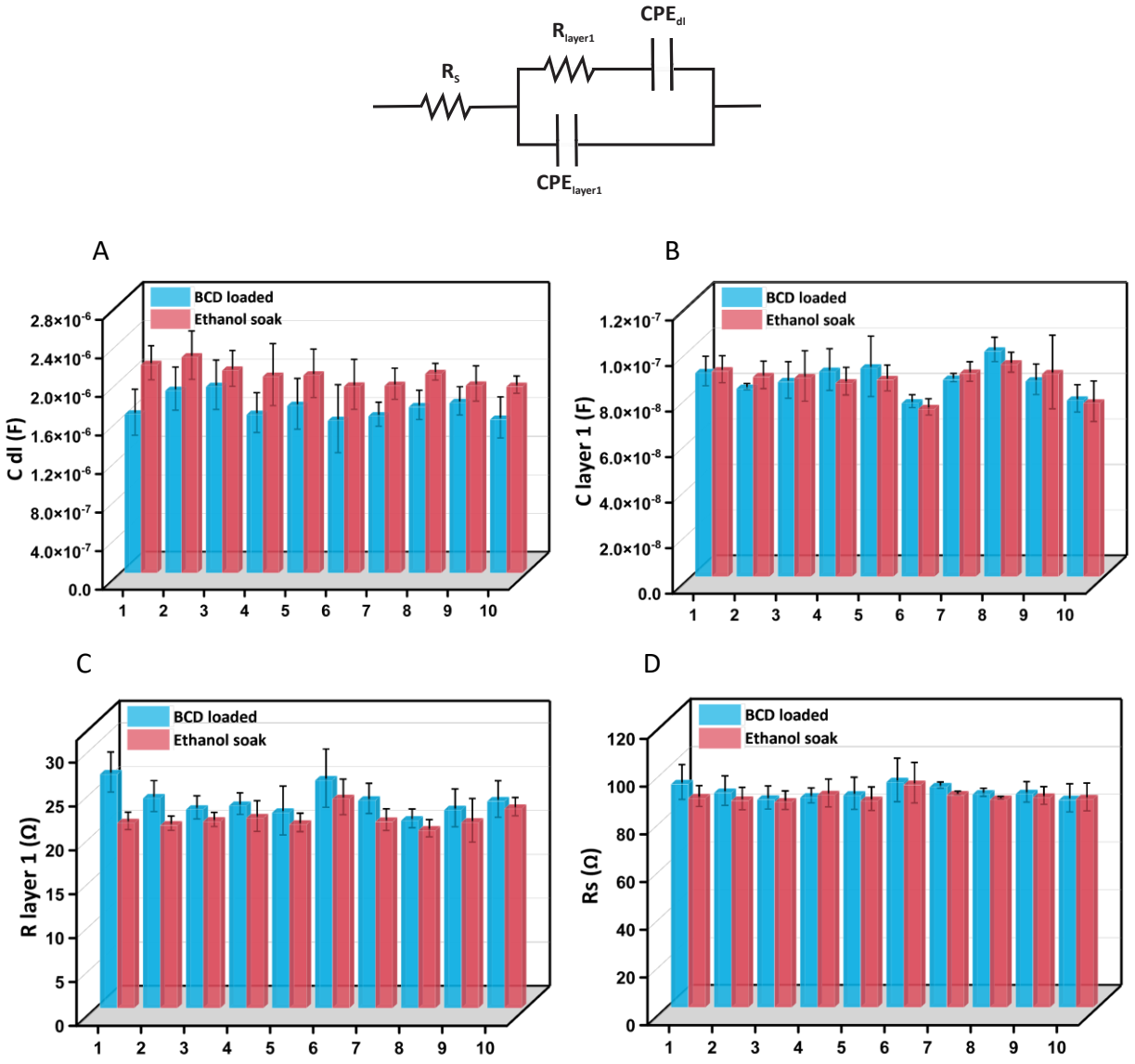

Figure 2.15. Non-faradaic EIS data interpretation using the first circuit. The blue bars show the surface after cyclodextrin loading and red bars show the surface state after cyclodextrin removal by ethanol soak. (A) C_{dl}, (B) C_{layer1}, (C) R_{layer1}, and (D) R_s are different circuit elements that can be affected by the cyclodextrin loading, removal, and reloading process.

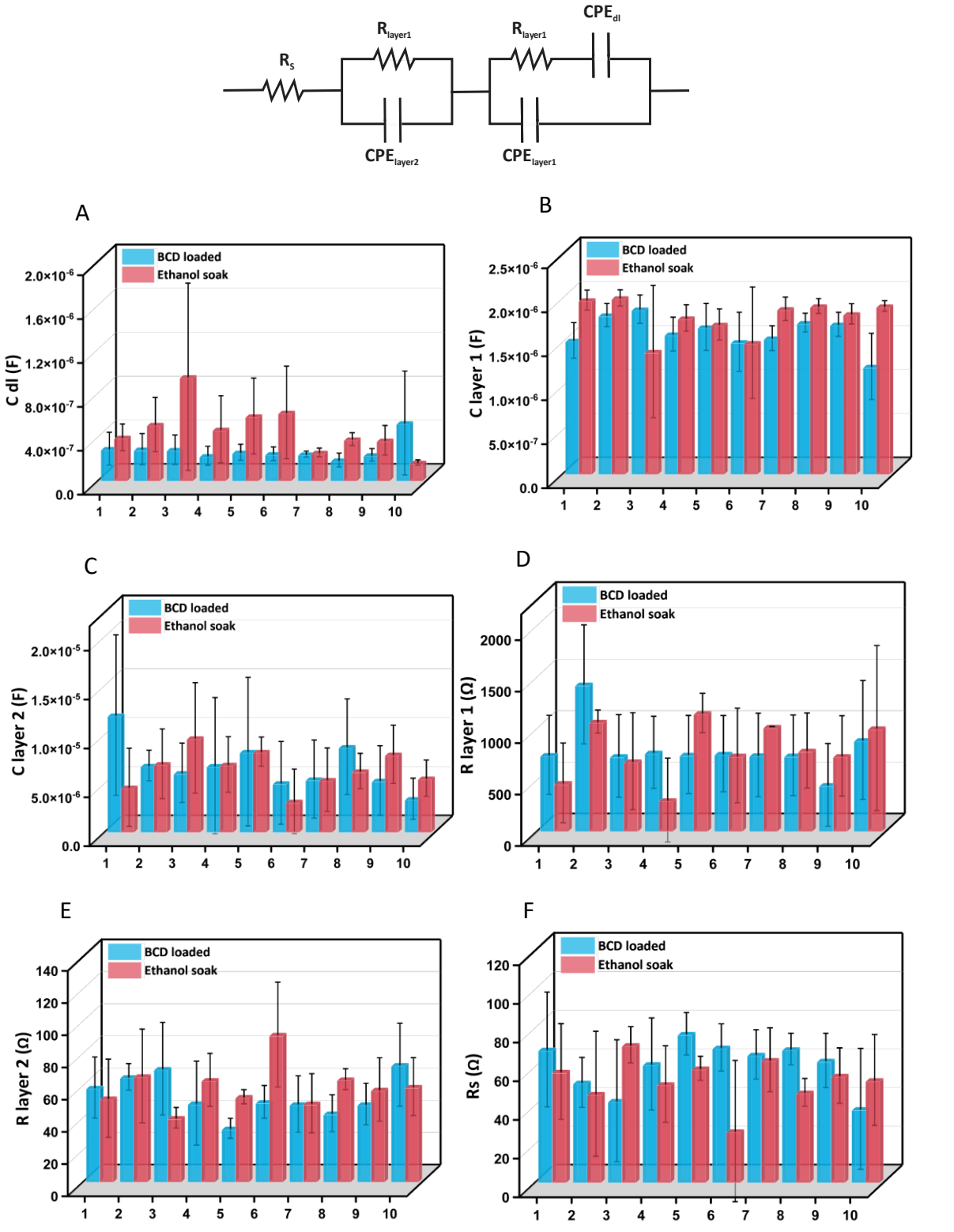

Figure 2.16. Non-faradaic EIS data interpretation using the second circuit: (A) C_{dl}, (B) C_{layer1}, (C) C_{layer2}, (D) R_{layer1}, (E) R_{layer2} and (F) R_s are different circuit elements that can be affected by the cyclodextrin loading, removal, and reloading process.

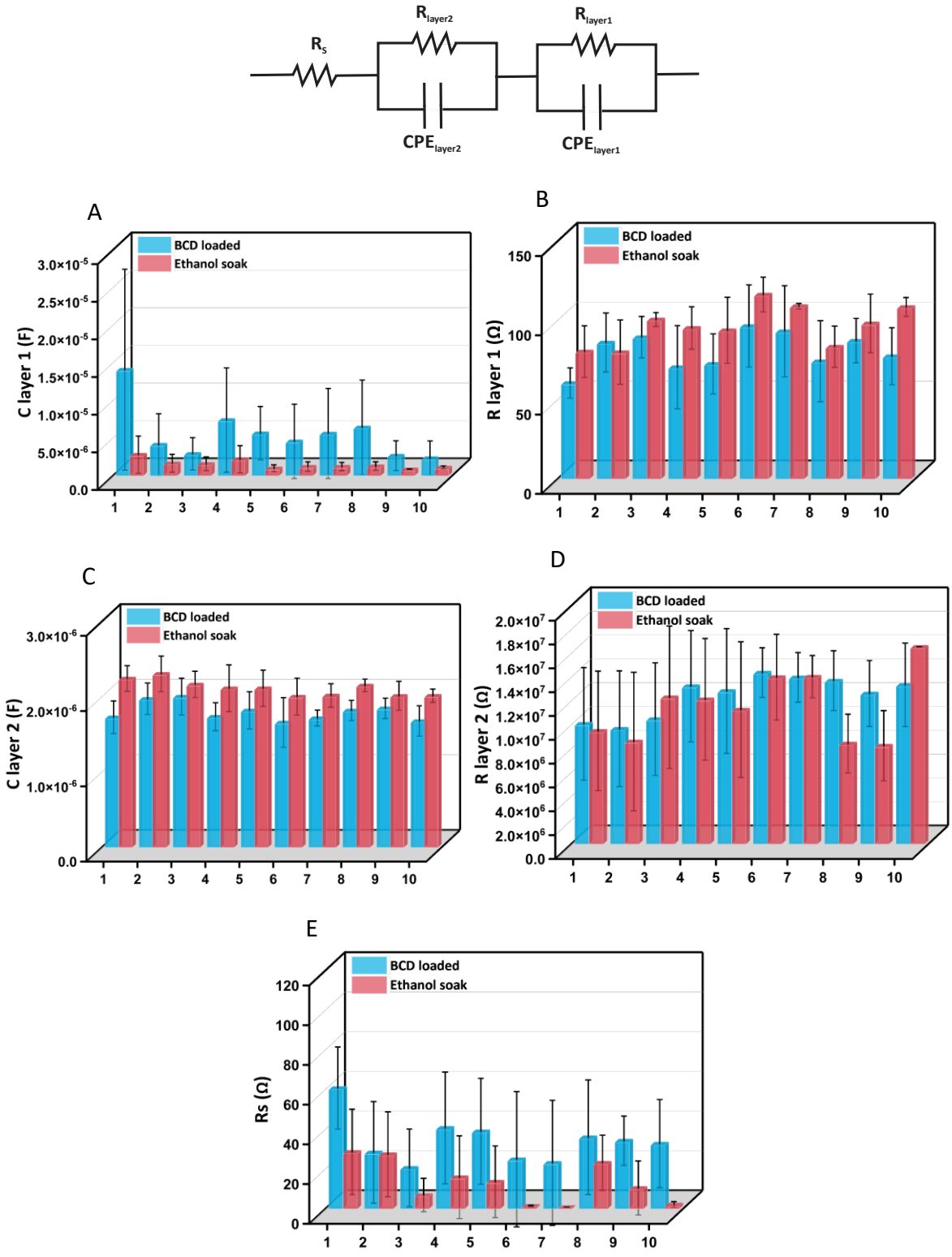

Figure 2.17. Non-faradaic EIS data interpretation using the third circuit: (A) C_{layer1}, (B) R_{layer1}, (C) C_{layer2}, (D) R_{layer2}, and (E) R_s are different circuit elements that can be affected by the cyclodextrin loading, removal, and reloading process.

Table 2.1. The summary of the equivalent circuit models analysis

Circuit Models		C_{dl} (F)	C_{layer1} (F)	R_{layer1} (Ω)	C_{layer2} (F)	R_{layer2} (Ω)	R_S (Ω)
Circuit 1 **Figure 2.15**	**Lower limit**	$1.5\ 10^{-6}$	$0.75\ 10^{-7}$	20			84
	Upper limit	$2.4\ 10^{-6}$	$1.1\ 10^{-7}$	27			97
Circuit 2 **Figure 2.16**	**Lower limit**	$1.9\ 10^{-8}$	$0.32\ 10^{-6}$	0.01	$3.22\ 10^{-8}$	17.95	0.01
	Upper limit	$2.13\ 10^{-6}$	$2.11\ 10^{-6}$	2230	$2.31\ 10^{-5}$	121.57	95.12
Circuit 3 **Figure 2.17**	**Lower limit**		$1.15\ 10^{-7}$	51	$1.52\ 10^{-6}$	$2.63\ 10^{6}$	0.01
	Upper limit		$1.39\ 10^{-5}$	124	$2.52\ 10^{-6}$	$1.64\ 10^{7}$	59.96

2.4.3.2 Single Frequency Data Analysis

While the equivalent circuit models provide valuable information about the surface, finding the equivalent circuits that describe multi-layer complicated surfaces accurately, can be quite difficult. Besides, the process of fitting the data with equivalent circuits is time-consuming and requires a specific software. Therefore, to develop point of care biosensors with EIS transducers, a more efficient method to analyze the non-faradaic EIS data is needed.

In the last couple of years, single frequency data analysis method has been employed in development of non-faradaic EIS biosensors for detection of many analytes in various complex media (**Table 2.2**). In this method, the non-faradaic EIS data can be conveniently analyzed by one

of the EIS parameters that the potentiostat measures at different frequencies. Therefore, deciding on the right EIS parameter at the best frequency can be challenging. While a few researchers [160,161] used the equivalent circuit models alongside the single frequency method, unfortunately most of the research groups did not explain either why they chose a specific EIS parameter, nor how they found the characteristic frequency values [162–169]. This is especially problematic when the effect of EIS drift is not considered and the necessary control experiments are not performed prior or together with the analyte tests [170].

Table 2.2. Non-faradaic EIS data analysis based on characteristic frequency values

Sensor	Analyte	Medium	EIS Data Analysis	EIS parameter	Frequency	Ref
Gold-11 MUA/16 MDA-OMP Ag1 Aptamer	E. coli	PBS	Single Frequency	Impedance Magnitude	10 kHz	[162]
ZnO thin films-Cortisol antibodies	Cortisol	Sweat	Single Frequency	Imaginary Impedance	100 Hz	[163]
PET-ZnO-CRP antibodies	C-reactive protein (CRP)	PBS	Both	Impedance Magnitude	100 kHz	[160]
Aluminium IDE-Con A	Prostate-specific membrane antigen (PSMA)	PBS	Single Frequency	Total Capacitance	1 Hz	[164]
ZnO /CuO -Caspase-9 antibodies	Active capase-9	PBS	Both	Impedance Magnitude	6 MHz	[161]
Gold IDE-LDL Cholesterol antibodies	LDL-cholesterol	PBS	Single Frequency	Total Capacitance	398 mHz	[165]
ICE-SAM- *αβ antibodies*	Amyloid beta (aβ) 1-42	PBS, Serum	Single Frequency	Total Capacitance	1 Hz	[166]
Graphene-MC-LR antibody	Microcystin-LR (MC-LR)	*PBS, Tap Water*	Single Frequency	Phase Angle	167 mHz	[167]
Gold IDE- S. sclerotiorum antibodies	Ascospore	PBS	Single Frequency	Impedance Magnitude	1000 Hz	[168]
Gold IDE-L-Cysteine	Pb(II)	Tap Water	Single Frequency	Total Capacitance	9.37 Hz	[169]

In this section we want to investigate if the equivalent circuit models that were discussed in Section 2.4.3.1, can give us some insight on choosing the best EIS parameter among real impedance (Z'), imaginary impedance (Z''), magnitude of impedance ($|Z|$), real capacitance (C'), imaginary capacitance (C"), total capacitance (C), and phase angle (Φ) at the best frequency. To do so, we modeled a cyclodextrin loaded surface with the Circuit 1 (**Figure 2.14A**) and showed the obtained resistance and capacitance values in **Figure 2.18A**. We also showed the complex impedance and capacitance values in **Figure 2.18B** and **2.18C**, respectively. Then, we tried to find the frequencies that the resistance and capacitance values from modeling cross the complex impedance and capacitance plots. **Figure 2.18B** shows that the leakage resistance and solution resistance cross the complex resistance values at very high frequencies and the potentiostat's inability to measure at sufficiently high frequencies makes it impossible to use this method to find the characteristic frequency values from the complex impedance plots. However, **Figure 2.18C** shows that the double layer capacitance and the real capacitance have an intersection at 0.5 Hz, and the inert layer capacitance intersects with the real and imaginary capacitances at 5015 and 12609 Hz, respectively. Therefore, we chose the real capacitance at 0.5 Hz (**Figure 2.18D**) , the real capacitance at 5015 Hz (**Figure 2.18E**), and the imaginary capacitance at 12609 Hz (**Figure 2.18F**) to analyze the collected non-faradaic EIS data and evaluate the reusability of βCD surface (**Figure 2.13**). The results show that the real capacitance at 0.5 Hz (**Figure 2.18D**) always increases by cyclodextrin removal (ethanol soak) and decreases by cyclodextrin loading. Therefore, to evaluate the reusability of cyclodextrin surfaces, instead of finding the double layer capacitance values with the circuit model, we can directly use the real capacitance values at a specific frequency of 0.5 Hz.

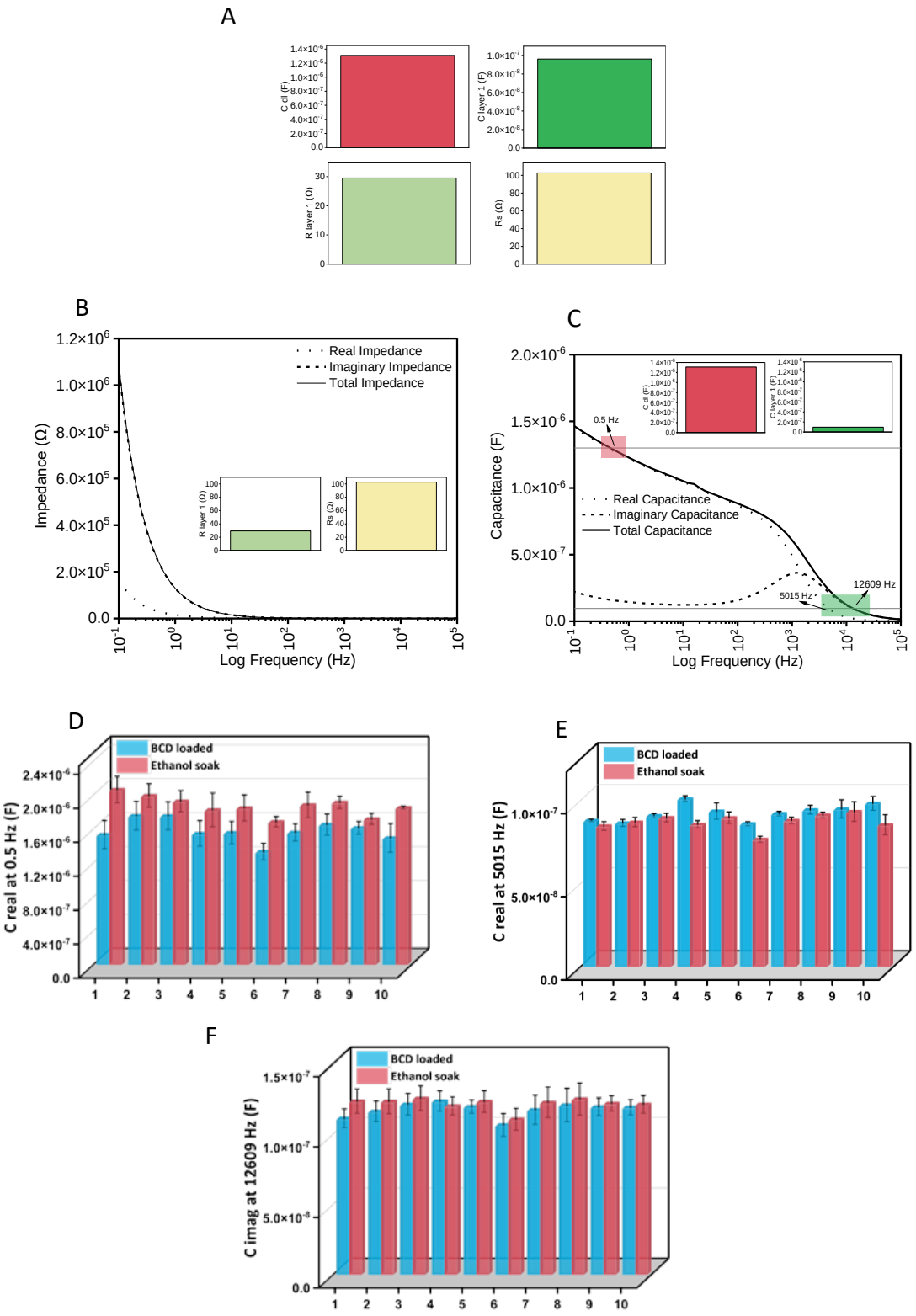

Figure 2.18. Single Frequency analysis of non-faradaic EIS data by the aid of equivalent circuit model: (A) modeling of a cyclodextrin surface using Circuit 1, (B) complex impedance plane of the same cyclodextrin surface, (C) complex capacitance plane of the same cyclodextrin surface, (D) real capacitance at 0.5 Hz, (E) real capacitance at 5015 Hz, and (F) imaginary capacitance at 12609 Hz

Additionally, **Figure 2.18C** shows that the imaginary capacitance has a maximum value at 1578 Hz. In supercapacitors, the imaginary capacitance shows the energy dispersion, and the dielectric relaxation time constant can be obtained by the frequency of the maximum imaginary capacitance [171]. Although we do not know the physical meaning of the maximum imaginary capacitance in biosensors, we used the 1578 Hz frequency to plot the imaginary capacitance (**Figure 2.19A**) as well as the real capacitance (**Figure 2.19B**), total capacitance (**Figure 2.19C**), imaginary impedance (**Figure 2.19D**), real impedance (**Figure 2.19E**), impedance magnitude (**Figure 2.19F**), and phase angle (**Figure 2.19G**). Comparing the results in **Figure 2.19** show that imaginary capacitance, imaginary impedance, and phase angle data at 1578 Hz frequency can all provide a signal when the cyclodextrin loading or removal causes a change in surface state. This makes sense because these parameters (imaginary capacitance, imaginary impedance, and phase angle) are all somehow related to the capacitance of the surface and indicate the capacitance changes when a non-faradaic process occurs.

Finally, we created the decision map (**Figure 2.20**) to summarize different methods of analysis of non-faradaic EIS data that were discussed in Section 2.4.3 and can be applied in design of non-faradaic biosensors.

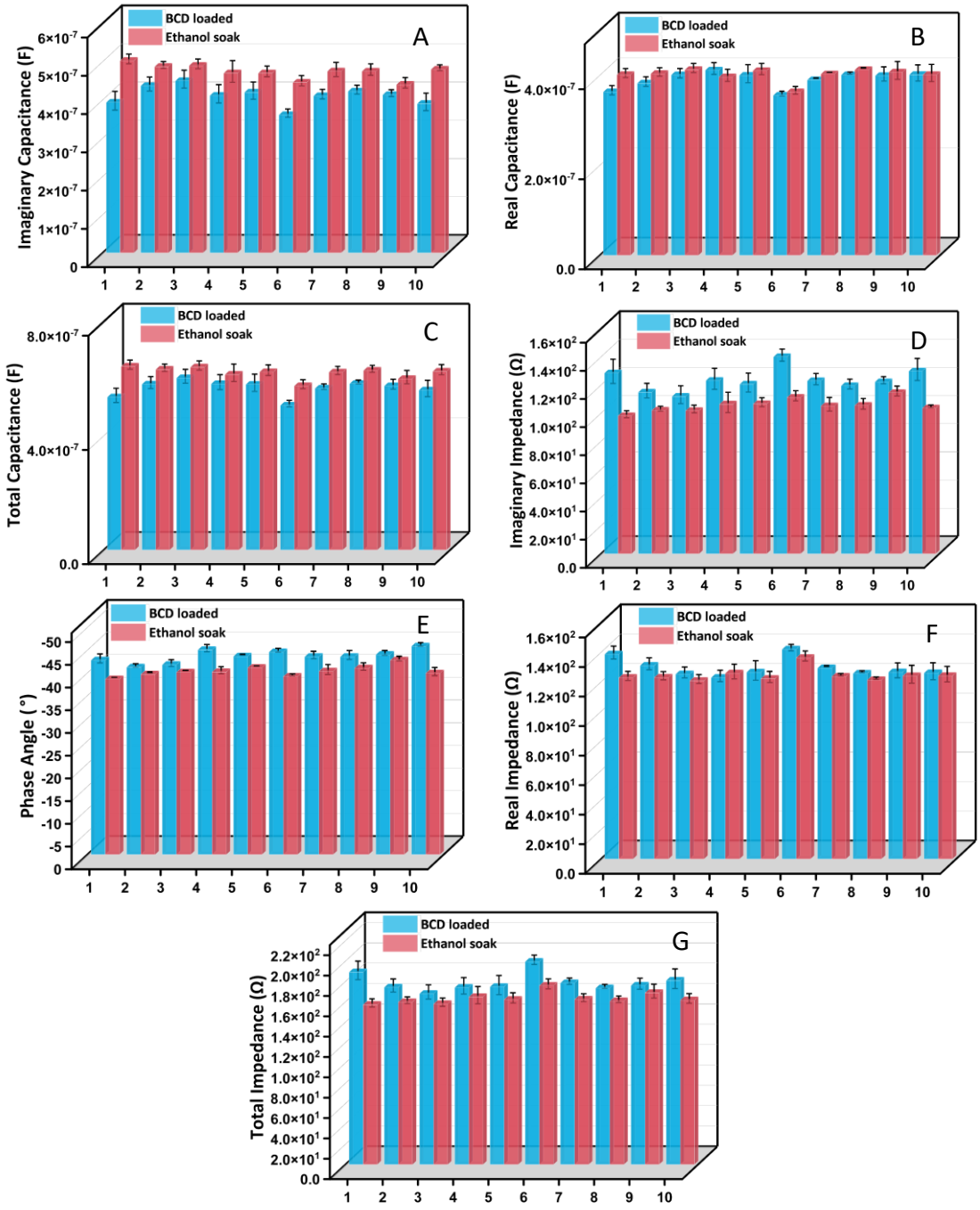

Figure 2.19. Single Frequency analysis of non-faradaic EIS data by using the 1578 Hz frequency at the maximum imaginary capacitance: (A) imaginary capacitance, (B) real capacitance, (C) total capacitance, (D) imaginary impedance, (E) real impedance, (F) impedance magnitude, and (G) phase angle

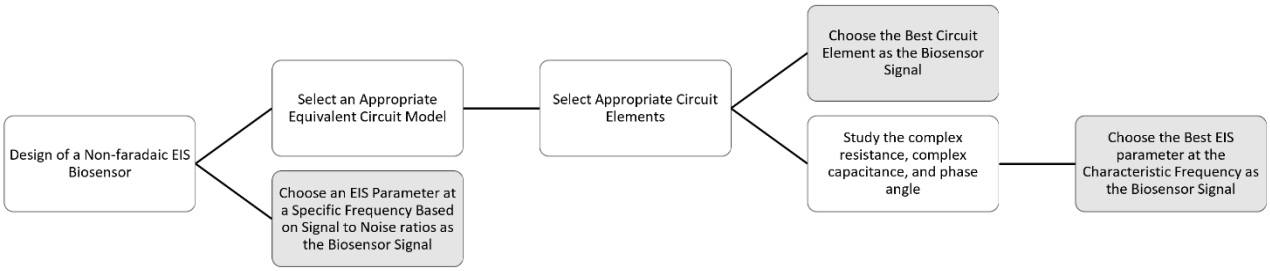

Figure 2.20. Summary of non-faradaic EIS data analysis methods that can be used to design non-faradic biosensors

2.5 Conclusion

EIS can distinguish between multiple surface phenomena that occur at the same time and it can provide valuable information about non-faradaic processes. Generally, there are two methods for analysis of non-faradaic EIS: equivalent circuit models and EIS parameters at a single Frequency. Choosing an equivalent circuit model that properly explains the system or selecting an appropriate EIS parameter at the correct characteristic frequency can be quite challenging. However, by using both methods simultaneously, we can perform a more accurate data analysis and improve our understanding of the surface.

3. Development of the First Reusable Cyclodextrin Biosensor

3.1 Rational: The Need for Reusable Cyclodextrin Biosensors

In recent years, different strategies have been directed toward the development of reusable aptamer-based sensors and immunosorbent surfaces; although, regeneration of aptamer and antibody surfaces is difficult after multiple uses [172]. Single use biosensors are not appropriate for applications where on-line continuous measurement of analytes is required. Therefore, the main goal of this chapter is to create a reusable cyclodextrin surface that can be implemented in a cross-reactive biosensor for continuous monitoring of urine samples. As it was explained in Section 1.3, cyclodextrins (CDs) can capture various organic and inorganic hydrophobic molecules into their cavity by reversible binding, which made them promising candidates for use as hydrophobic recognition elements in our reusable biosensor development. To create a reusable CD surface, we propose to use a weak surface CD mediator: surface-bound polyethylene glycol (PEG). A gold surface can be modified with carboxy-PEG 12-Thiol (PEG-SH) via thiol chemistry. αCD forms inclusion complexes with PEG if the molecular weight is higher than 200 [173,174]. A single αCD molecule is estimated for every two CH_2-O-CH_2 PEG groups, indicating a surface-based rotaxane can be created [173,174]. Surface PEG will be complexed with αCD; the carboxyl end-group of PEG allows for an additional CD to potentially hydrogen bond with COOH. Among hydrophobic molecules of interest, trans-resveratrol offers ideal characteristics for a model analyte to demonstrate the reusability of PEG:αCD surface and evaluate the sensitivity and selectivity of the proposed sensor; trans-resveratrol is largely hydrophobic with a strong

association to αCD, being the functional component of the proposed class recognition hydrophobic analyte sensor [175].

Animal studies and preliminary clinical trials have shown the effect of trans-resveratrol on general health maintenance and prevention of various diseases and disorders [176–178]. Although, due to rapid metabolism and poor bioavailability, many of the promising health-promoting effects of trans-resveratrol in animal models have not yet been confirmed in humans, and trans-resveratrol is currently not prescribed for the treatment of any human disease [177,178]. Previous clinical studies indicate nanomolar range of trans-resveratrol sensing is necessary for pharmacokinetics, bioavailability, and metabolite studies of trans-resveratrol in humans [179,180]. A CD modified glassy carbon electrode for trans-resveratrol detection has been engineered for single-use applications; trans-resveratrol adsorbed strongly to the surface and could not be removed by polishing or cleaning the electrode [175]. Here, to demonstrate the reusability of GOLD-PEG:αCD surface, we will show consecutive trans-resveratrol serial dilution results using a single surface [181]. Chemical structures of the sensor compounds and trans-resveratrol are demonstrated in **Figure 3.1**.

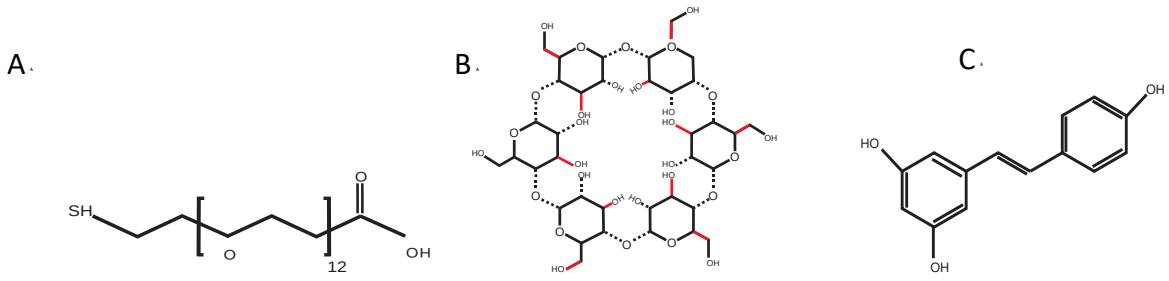

Figure 3.1. Chemical structures of the reusable sensor compounds and the model hydrophobic analyte, trans-resveratrol: (A) Carboxy-PEG 12-Thiol ($CT(PEG)_{12}$), (B) α cyclodextrin (αCD), and (C) Trans-resveratrol. Reprinted with permission from Panahi, Zahra, Mckenna A. Merrill, and Jeffrey Mark Halpern. "Reusable Cyclodextrin-Based Electrochemical Platform for Detection of trans-Resveratrol." ACS applied polymer materials 2.11 (2020): 5086-5093. Copyright 2020 American Chemical Society.

3.2 Preparation of a Reusable Gold-PEG:αCD Surface

A gold electrode was polished in a figure-eight by 3 µm diamond for 1 min followed by 1 µm diamond for 1 min. After each polishing step, the electrode was rinsed with methanol and ultra-high purity (UHP) water for 1 minute. The electrode was then polished with 0.55 µm alumina for 1 min. The electrode was rinsed with UHP and dried with nitrogen. Oxygen plasma was used to remove any remaining surface organic impurities. The gold surface was modified by carboxy-PEG 12-Thiol. 5 mg of thiolated polyethylene glycol (PEG-SH) was added to 10 ml of PBS and stirred by sonication for 10 min at room temperature. The gold surface was incubated in the solution for 30 min to allow the -SH groups to covalently bond with gold surface[182]. After PEG modification, the surface was washed with UHP water for 90 seconds to remove nonspecific bindings, leaving adsorbed and covalently-bound PEG. The third step consisted of immobilizing αCD on the PEG-modified surface via incubation in a 5 mM αCD deionized water solution for 45 min at room temperature. The surface was then incubated in 160 nM trans-resveratrol in phosphate buffered solution (PBS), pH = 7.4 for 5 minutes. To regenerate the αCD surface, the surface was washed thoroughly with UHP after exposure to trans-resveratrol and the surface was then reloaded with a 45 min soak in 5 mM αCD solution at room temperature.

3.3 Surface Characterization Using Faradaic EIS, XPS, and FTIR

The electrodes were carefully rinsed with UHP thoroughly before and after each EIS experiment to remove any excess and weakly adsorbed chemicals. The electrochemical experiments were performed with Gamry Instruments Reference 600+ potentiostat in a Vista Shield faradaic cage at room temperature. The results were analyzed by Gamry Echem Analyst.

Platinum wire auxiliary electrode, Ag/AgCl/ 3M NaCl reference electrode, and a gold disc electrode (BASi, area=0.0201 cm^2) working electrode. These measurements were performed by scanning the frequency from 100 kHz to 0.1 Hz, acquiring 10 points per decade, unless stated otherwise. DC voltage was 0 V versus open circuit potential, and the AC voltage was 10 mV. The faradaic EIS measurements for monitoring surface modification were carried out in 20 mL of 20mM ferri/ferrocyanide in UHP.

Gold-coated silicon wafers were used for ATR-FTIR and XPS analysis for better contact with the analytical equipment; the gold-coated silicon wafer was prepared the same as the gold disc electrodes. ATR–FTIR data collection was conducted with Thermo Nicolet iS10 equipped with air purge with a dew point of -95 °F. Spectra were the results of 128 scans. XPS analyses were performed using Kratos Axis Supra XPS (X-ray Photoelectron Spectroscopy).

3.4 EIS Results of the Gold Modification with PEG and αCD Immobilization

Figure 3.2A shows a schematic illustration of the reusable αCD biosensor: a gold surface is modified with carboxy-PEG 12-Thiol (PEG-SH), and the PEG surface is complexed with αCD. When the PEG:αCD surface was exposed to a solution containing trans-resveratrol, a measurable amount of αCD decoupled from the surface to form a complex in solution with trans-resveratrol because trans-resveratrol had a greater affinity with αCD compared to PEG. **Figure 3.2B** shows that the initial PEG modified surface had an increase in charge transfer resistance following αCD loading on the surface. These results indicate that there was some remaining weakly adsorbed carboxy-PEG 12-Thiol. During the first αCD loading, αCD molecules complexed with physiosorbed

PEGs, and the charge transfer resistance increased because a layer of αCD was formed on the surface. Thus, for the first αCD loading, αCD favorably bound to physiosorbed PEG, compromising of hydrogen bonding between the -OH of αCD to the COOH end groups or the C-O-C chain groups of PEG. By exposing the PEG:αCD modified surface to trans-resveratrol solution, αCD molecules dissociated from the surface, and the charge transfer resistance decreased. The action of αCD removal also caused the removal of physiosorbed PEG, further allowing the incomplete PEG surface to form a bent over shape keeping a consistent impedance response.

3.5 Confirmation of Surface Regeneration

The schematic in **Figure 3.3A** illustrates the surface regeneration with a second αCD soak and αCD release following the incubation of surface in trans-resveratrol solution. A decrease in charge transfer resistance was observed following αCD reloading, and an increase was observed after the αCD was fully removed following serial dilution (**Figure 3.3B**). The αCD cavity threads the chemisorbed PEG chains to form channel-type crystalline microdomains resulting in a faster electron transfer and easier diffusion of ions through the surface [183]. When there is no αCD on surface, chemisorbed PEG groups have a mushroom configuration, which resulted in the PEG layer becoming a less porous surface and a decreasing electron transfer rate (**Figure 3.3A** and **3.3B**). Unloaded states were generated after serial dilutions with trans-resveratrol (**Figure 3.3B**). We were able to obtain a similar response from ethanol soaking to remove the αCD from the surface (**Figure 3.3C** and **Figure 3.4**).

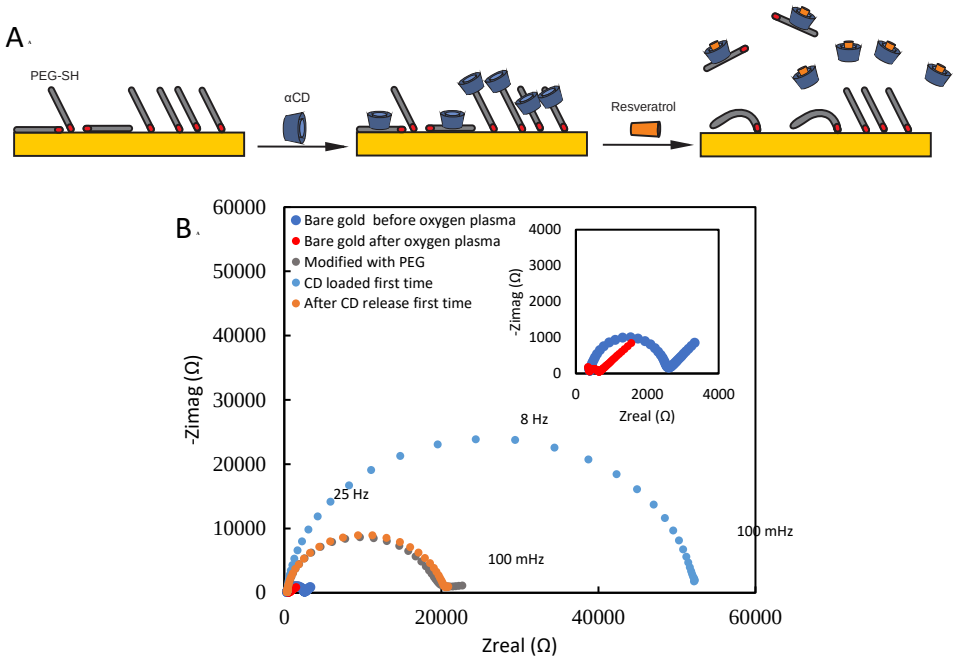

Figure 3.2. Developing a sensor for trans-resveratrol detection: (A) (left) Schematic representation of surface PEG modification, (middle) the first αCD loading, and (right) the first αCD release by trans-resveratrol, (B) EIS Nyquist plots in 20 mM ferri/ferrocyanide in deionized water after each modification step. αCD release was after exposure to 160 nM trans-resveratrol in PBS. After αCD loading, the impedance increased due to the formation of an αCD layer on physiosorbed PEG. Reprinted with permission from Panahi, Zahra, Mckenna A. Merrill, and Jeffrey Mark Halpern. "Reusable Cyclodextrin-Based Electrochemical Platform for Detection of trans-Resveratrol." ACS applied polymer materials 2.11 (2020): 5086-5093. Copyright 2020 American Chemical Society.

X-ray photoelectron spectroscopy (XPS) and Attenuated total reflectance-Fourier transform infrared spectroscopy (ATR-FTIR) were used to further investigate both αCD-loaded and unloaded surface states as described in **Figure 3.3**. XPS analysis (**Figure 3.5** and **Table 3.1**) revealed that after PEG modification, the relative-intensity of Au peaks decreased with respect to carbon, and an Au-S peak was observed at 160 eV, indicating the surface was covered by thiol groups covalently attached to the gold surface. In addition, when αCD was loaded on the surface, the Au peaks were weaker compared to when αCD had been released from the surface indicating a surface complexation. The XPS results indicate the αCD had a strong interaction with the PEG surface, and the signal was reversible and repeatable.

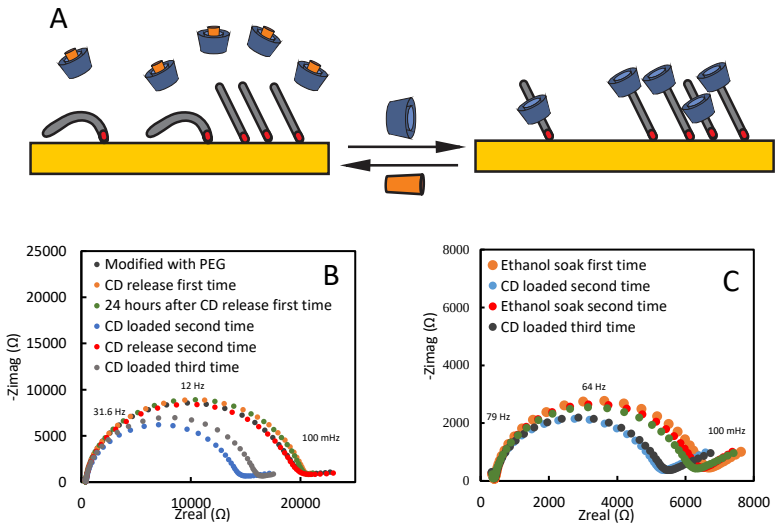

Figure 3.3. Reversible binding of αCD on PEG: (A) (left) the αCD release by trans-resveratrol, (right) regeneration of surface by αCD loading, (B) Nyquist plots of reloading and release of αCD by 160 nM trans-resveratrol in PBS, and (C) αCD release by ethanol soaking for 45 min. (B&C) The surface is fully reloadable and reusable showing it can return to original sensing state. Reprinted with permission from Panahi, Zahra, Mckenna A. Merrill, and Jeffrey Mark Halpern. "Reusable Cyclodextrin-Based Electrochemical Platform for Detection of trans-Resveratrol." ACS applied polymer materials 2.11 (2020): 5086-5093. Copyright 2020 American Chemical Society.

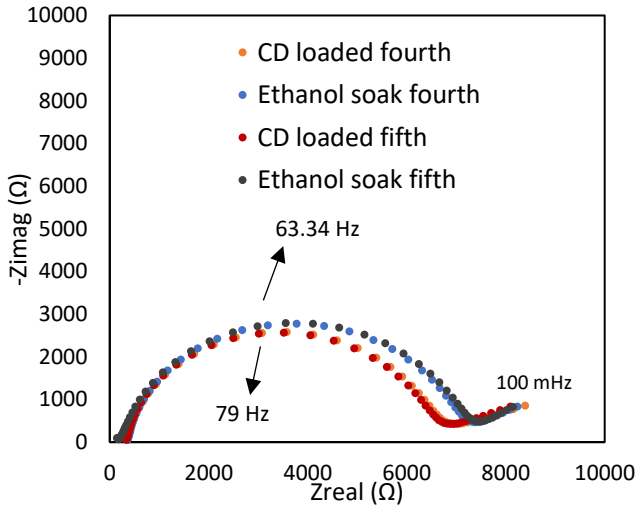

Figure 3.4. Reversible binding of αCD confirmed by ethanol soak: A PEG modified gold surface was loaded by αCD and unloaded by ethanol for 5 times. The fourth and fifth loading/unloading is displayed (the second and third are shown in Figure 3.3C). When αCD is loaded on the surface, charge transfer resistance decreases due to a change of the PEG mushroom structure to a more oriented channel type microcrystalline domain structure. Reprinted with permission from Panahi, Zahra, Mckenna A. Merrill, and Jeffrey Mark Halpern. "Reusable Cyclodextrin-Based Electrochemical Platform for Detection of trans-Resveratrol." ACS applied polymer materials 2.11 (2020): 5086-5093. Copyright 2020 American Chemical Society.

ATR-FTIR analysis (**Figure 3.6**) showed the presence of C=O bonds of the PEG end-groups at 1750 cm^{-1} and the C-O-C PEG bonds at 1260 cm^{-1}. After αCD loading, C=O double bonds and C-O-C bonds were replaced by C-OH bonds from αCD, because the αCD host is dominating the spectra of the PEG guest indicating the αCD is forming surface rotaxane supramolecules and hydrogen bonding with the COOH groups. The intensity of PEG peaks at 1750 and 1260 cm^{-1} increased after the αCD is released. A similar response can be observed after αCD reloading, reconfirming the EIS and XPS results indicating the successful development of reusable CD surface.

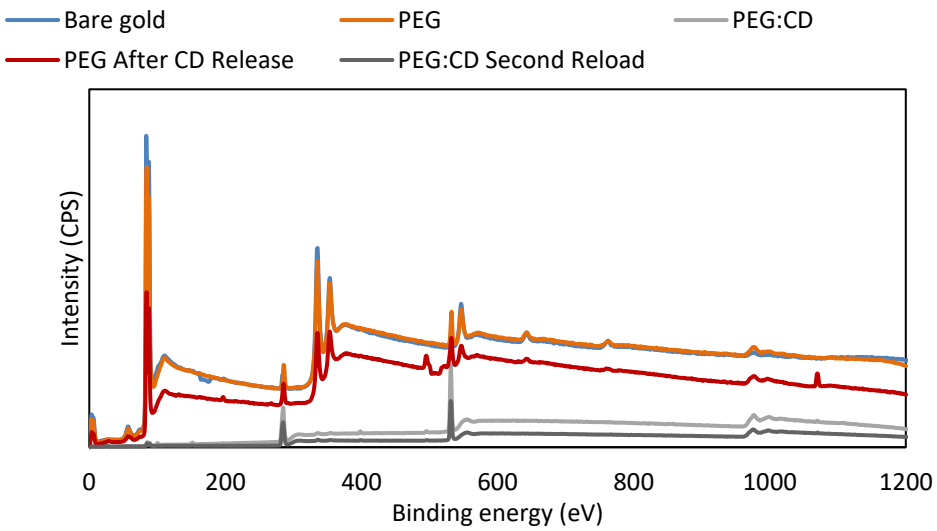

Figure 3.5. Characterizing the electrode after different modification steps with XPS. Intensity of Au peaks (Au 4f:84.4, Au 5S:125.4, Au 4d:336.4 and 354.4, and Au 4p:533 eV) decrease during different steps of surface development, i.e., PEG modification and αCD loading. Au peak intensities return after 160 nM trans-resveratrol soak for 10 min, which confirms the release of αCD from the surface to bind with trans-resveratrol. Au-S peak at 160 eV shows the presence of covalently attached PEG on the surface. Similarity between the spectra before αCD loading and after αCD release confirms the reproducibility of the surface and reversible binding of αCD on PEG. Reprinted with permission from Panahi, Zahra, Mckenna A. Merrill, and Jeffrey Mark Halpern. "Reusable Cyclodextrin-Based Electrochemical Platform for Detection of trans-Resveratrol." ACS applied polymer materials 2.11 (2020): 5086-5093. Copyright 2020 American Chemical Society.

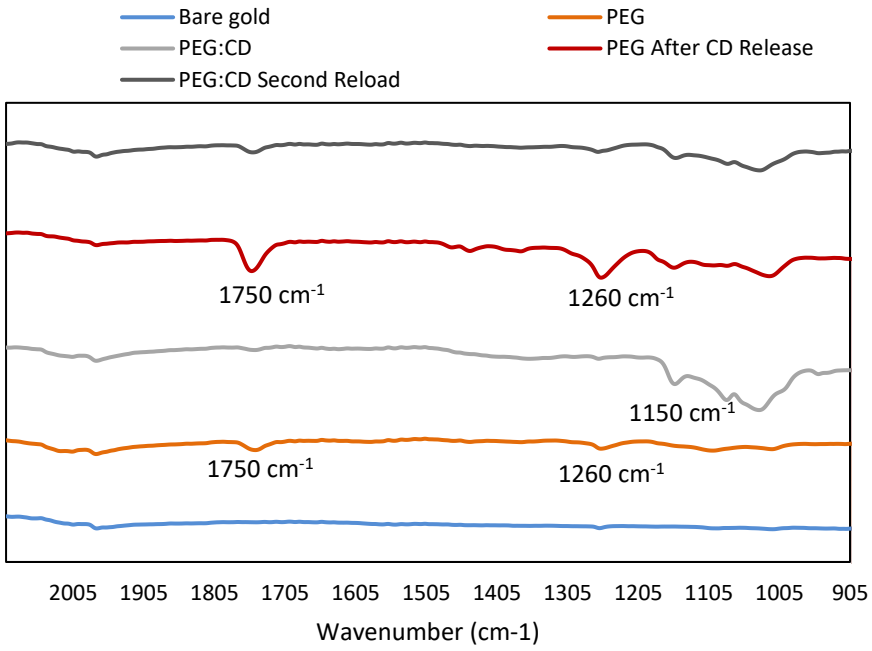

Figure 3.6. Characterizing the electrode after different modification steps with ATR-FTIR. After PEG-gold modification, C=O at 1750 cm^{-1} and C-O-C bindings at 1260 cm^{-1} appear. After αCD loading, COH bonds (1150 cm^{-1}) of αCD dominate the spectra; masking the PEG signal. The spectra after (1) αCD release returns in similarity to a PEG-gold modification (orange vs red) and (2) after αCD reloading returns in similarity to the initial αCD loading (grey lines), confirming reusability of the surface. Reprinted with permission from Panahi, Zahra, Mckenna A. Merrill, and Jeffrey Mark Halpern. "Reusable Cyclodextrin-Based Electrochemical Platform for Detection of trans-resveratrol." ACS applied polymer materials 2.11 (2020): 5086-5093. Copyright 2020 American Chemical Society.

Table 3.1. Quantification of Au 4f, C 1s, and O 1s with XPS. Similarity between the Ratio of Au/C and C/O after the first and the second CD loading confirms the reproducibility of the Gold-PEG:αCD surface. Reprinted with permission from Panahi, Zahra, Mckenna A. Merrill, and Jeffrey Mark Halpern. "Reusable Cyclodextrin-Based Electrochemical Platform for Detection of trans-resveratrol." ACS applied polymer materials 2.11 (2020): 5086-5093. Copyright 2020 American Chemical Society.

Assigned peak	**Binding energy (eV)**	**Bare gold**	**Mass concentration (%)**			
			PEG	PEG:CD	PEG After CD Release	PEG:CD Second Reload
Au 4f	84.52 ± 0.5	36.3	35.57	2.04	26.9	2.64
	87.92 ± 0.6	59.46	28.6	1.57	21.89	1.83
C 1s	284.92 ± 0.65	2.26	4.32	56.88	10.73	51.61
O 1s	531.72 ± 0.58	1.98	5.75	43.54	6.67	40.98
Ratio Au/C	-	42.37	14.85	0.063	4.547	0.087
Ratio C/O	-	1.14	0.75	1.306	1.609	1.259

3.6 Trans-resveratrol Serial Dilution in PBS Buffer Procedure

All trans-resveratrol stock solutions were stored in a dark fridge to prevent trans-resveratrol from changing to its cis isomer conformation. 1.08 mg of trans-resveratrol was added to 50 ml of PBS to make a concentrated trans-resveratrol solution. Then the solution was sonicated for 10 min. Serial dilutions of the trans-resveratrol solutions were done in a beaker containing PBS (pH 7.4) by adding the concentrated solution to 15 ml of PBS solution to get 2.5, 5.4, 11.1, 20.8, 40.35, 80.6, and 160.5 nM concentrations. For lower concentrations, concentrations of 0.5, 1.5, 3, 5, 7.5, 10, 13, and 17 nM were used. The modified surface was incubated in the trans-resveratrol solution, with the desired concentration, for 5 min prior to running EIS. For non-faradaic analysis, EIS was performed in PBS without added redox active molecules. All other parameters were kept the same as Section 3.3.

3.7 Results for Trans-resveratrol Detection by Gold-PEG:αCD Surface in PBS Buffer

The surface's ability to monitor repeated non-faradaic impedance response to nM concentrations of trans-resveratrol was first explored in a PBS solution. All experiments were performed in triplicate to confirm reproducibility and standard variation. Original Bode plots for four different concentrations are presented in **Figure 3.7** (PEG:αCD modified surface - test) and **Figure 3.8** (bare gold electrode - control).

The magnitude and phase of the impedance are shown for 20 nM concentration (**Figure 3.9A)** indicating the difference between the control and test case. The capacitive behavior of the modified surface at low frequencies is indicative of the PEG coating layer which blocked the current. Based on these results, the equivalent circuit that best described and fitted our sensor was proposed as a coating with porous structure (**Figure 3.9B and 2.14A**) [144]. We extensively discussed this model in Section 2.4.3.1.

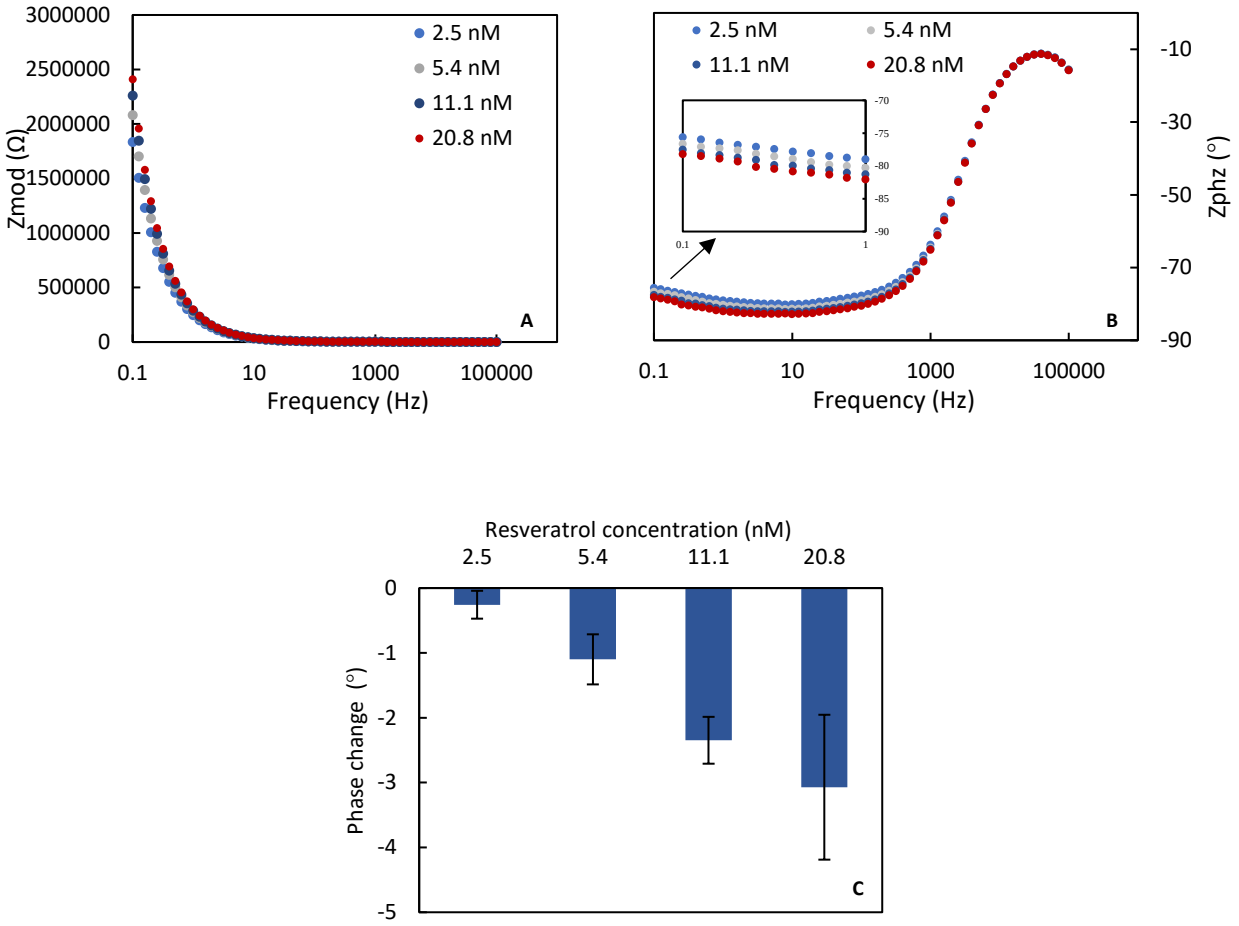

Figure 3.7. Trans-resveratrol serial dilutions by a Gold-PEG:αCD modified surface in PBS. Bode plot of four different concentrations of trans-resveratrol in PBS at a PEG:αCD modified surface. (A) Magnitude, and (B) phase of the impedance versus frequency. (C) Shows the resulting phase change at 0.1 Hz; average and standard deviation of triplicate data of three unique sensors displayed. The data shows that as αCD molecules leave the PEG surface to complex with trans-resveratrol in PBS; the phase angle decrease. Reprinted with permission from Panahi, Zahra, Mckenna A. Merrill, and Jeffrey Mark Halpern. "Reusable Cyclodextrin-Based Electrochemical Platform for Detection of trans-Resveratrol." ACS applied polymer materials 2.11 (2020): 5086-5093. Copyright 2020 American Chemical Society.

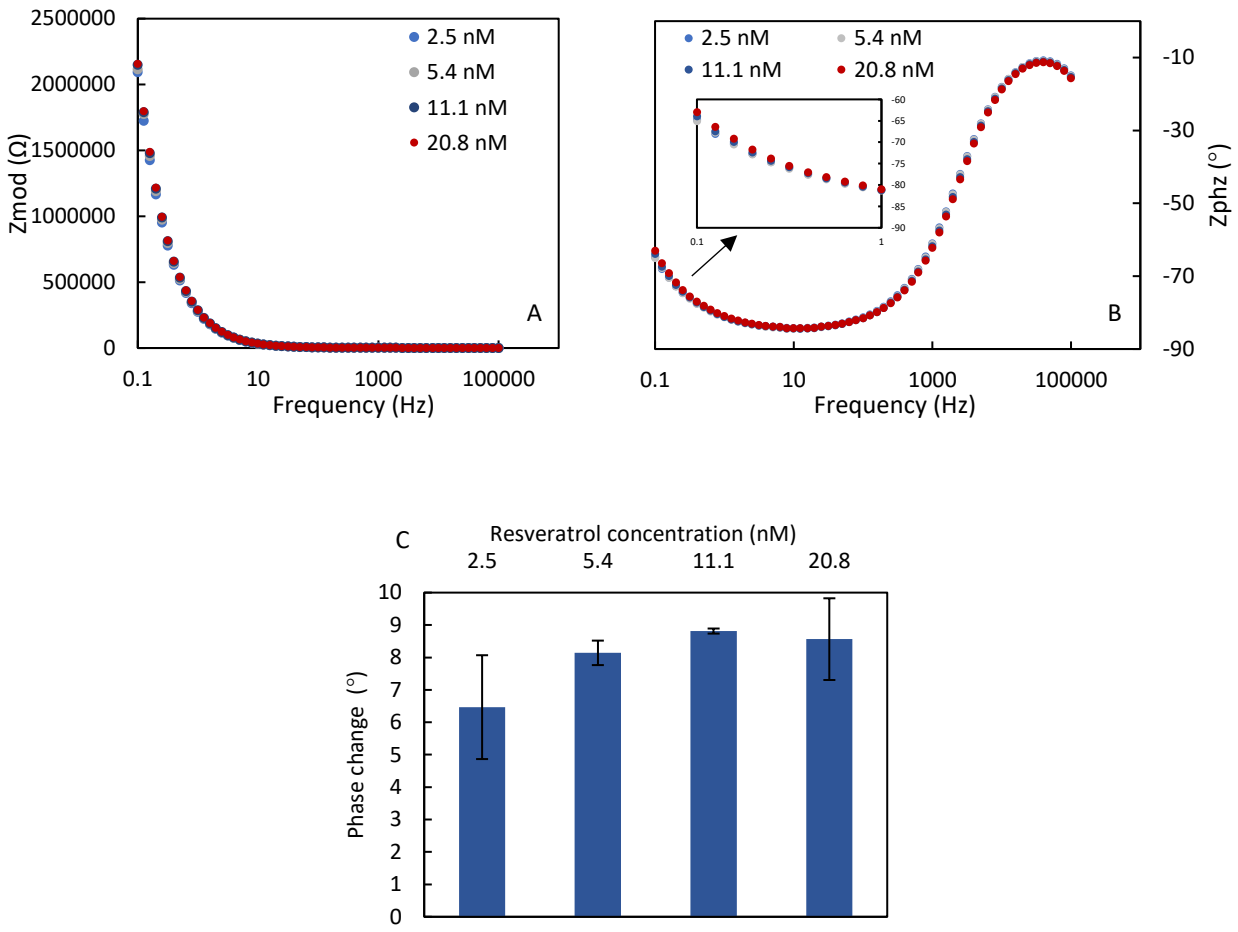

Figure 3.8. Trans-resveratrol serial dilutions by a bare gold surface. Bode plot of four different concentrations of trans-resveratrol at a bare gold surface. (A) Magnitude, and (B) phase of the impedance versus frequency. (C) Shows the resulting phase change at 0.1 Hz; average and standard deviation of triplicate data of three unique sensors displayed. The data shows no change in phase angle was observed by trans-resveratrol serial dilution with a bare gold surface. Reprinted with permission from Panahi, Zahra, Mckenna A. Merrill, and Jeffrey Mark Halpern. "Reusable Cyclodextrin-Based Electrochemical Platform for Detection of trans-Resveratrol." ACS applied polymer materials 2.11 (2020): 5086-5093. Copyright 2020 American Chemical Society.

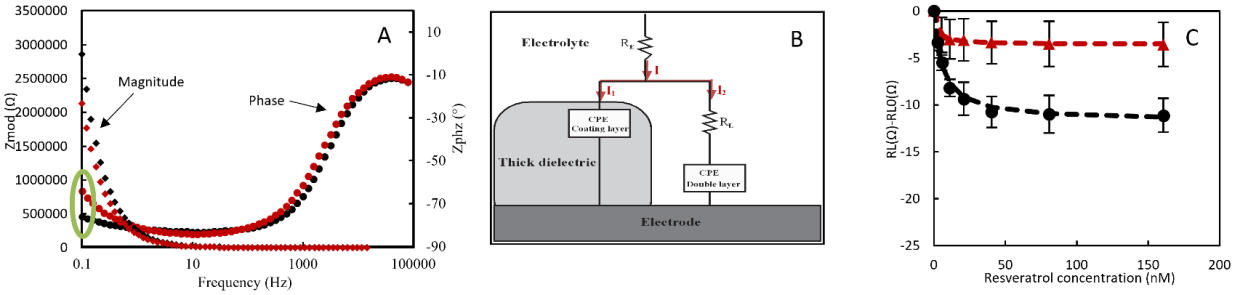

Figure 3.9. The developed Gold-PEG:αCD surface for trans-resveratrol detection: (A) Magnitude and phase of the impedance for 20.8 nM concentration of (red) a bare gold surface and (black) a Gold-PEG:αCD modified surface. The green circle shows that the phase of the modified surface is closer to -90°C and is more capacitive. (B) Equivalent circuit model used to fit the data for the Gold-PEG:αCD surface. Leakage resistance (R_L) was used as the dominating element of interest. I is the total current; I_1 and I_2 are the current through the blocking PEG layer and leakage resistor, respectively. (C) Calibration curve of (red) a bare gold surface and (black) an Gold-PEG:αCD surface indicating greater sensitivity in the αCD surface. Reprinted with permission from Panahi, Zahra, Mckenna A. Merrill, and Jeffrey Mark Halpern. "Reusable Cyclodextrin-Based Electrochemical Platform for Detection of trans-Resveratrol." ACS applied polymer materials 2.11 (2020): 5086-5093. Copyright 2020 American Chemical Society.

In parallel with the coating capacitance, a resistive path could be modeled by leakage resistance (R_L), due to the small ionic current that flew through the surface pores of the sensing layer. The serial dilution results show that leakage resistance was the main affected circuit element, and the leakage resistance provided the most detailed information about the physiochemical processes of the αCD release and PEG flattening into a mushroom configuration. The change in leakage resistance between a certain concentration and the 0 nM concentration base signal was then used for the analysis ($\Delta R_L=R_L-R_{L0}$). The sensor was first tested for concentrations in the range of 2.5 to 160 nM (**Figures 3.7** and **3.9C, black**). As the surface was exposed to trans-resveratrol, αCD was released from the surface, and a decrease in leakage resistance was observed. Theoretically, for an ideal insulating layer, R_L would be infinite and the current through the leakage resistance (I_2) would equal zero (**Figure 3.9B**). However, PEG coating layer imperfectly blocks ionic current and R_L is finite. With decrease in leakage resistance followed by an increase in trans-resveratrol concentration, the current through the leakage

resistance (I_2) increased and the current through the coating capacitance (I_1) decreased. This suggests that the PEG capacitive layer became less porous and more capacitive due to flattening into a mushroom structure as described earlier. Additionally, **Figure 3.8** shows the decrease in phase angle at 0.1 Hz frequency following the increase in concentration of trans-resveratrol.

From **Figure 3.9C**, we can observe that 20 nM was the saturation concentration; the leakage resistance remained constant at concentrations higher than 20 nM because all αCD molecules were removed from the surface. In contrast, almost no response was observed by the bare gold surface (**Figures 3.8 and 3.9C, red**). Likewise, a surface employing αCD produced a weaker response to cortisol, a competing analyte that is mostly known for making complexes with βCD (**Figure 3.10**).

Two additional controls showing minimal response were: (1) a PEG surface not loaded with αCD to confirm trans-resveratrol was not physisorbing to PEG (**Figure 3.11**) and (2) no trans-resveratrol in the solution to show the stability of αCD surface in PBS (**Figure 3.12**). We observed Langmuir isotherm unbinding with an equilibrium constant of 0.0904 nM^{-1} for the Gold-PEG:αCD surface after first modification (**Figure 3.13A**) and 0.1439 nM^{-1} after subsequent αCD loadings (**Figure 3.13B**). Finally, the third serial dilution was performed to confirm the reusability of the sensor and reproducibility of the surface (**Figure 3.13C**).

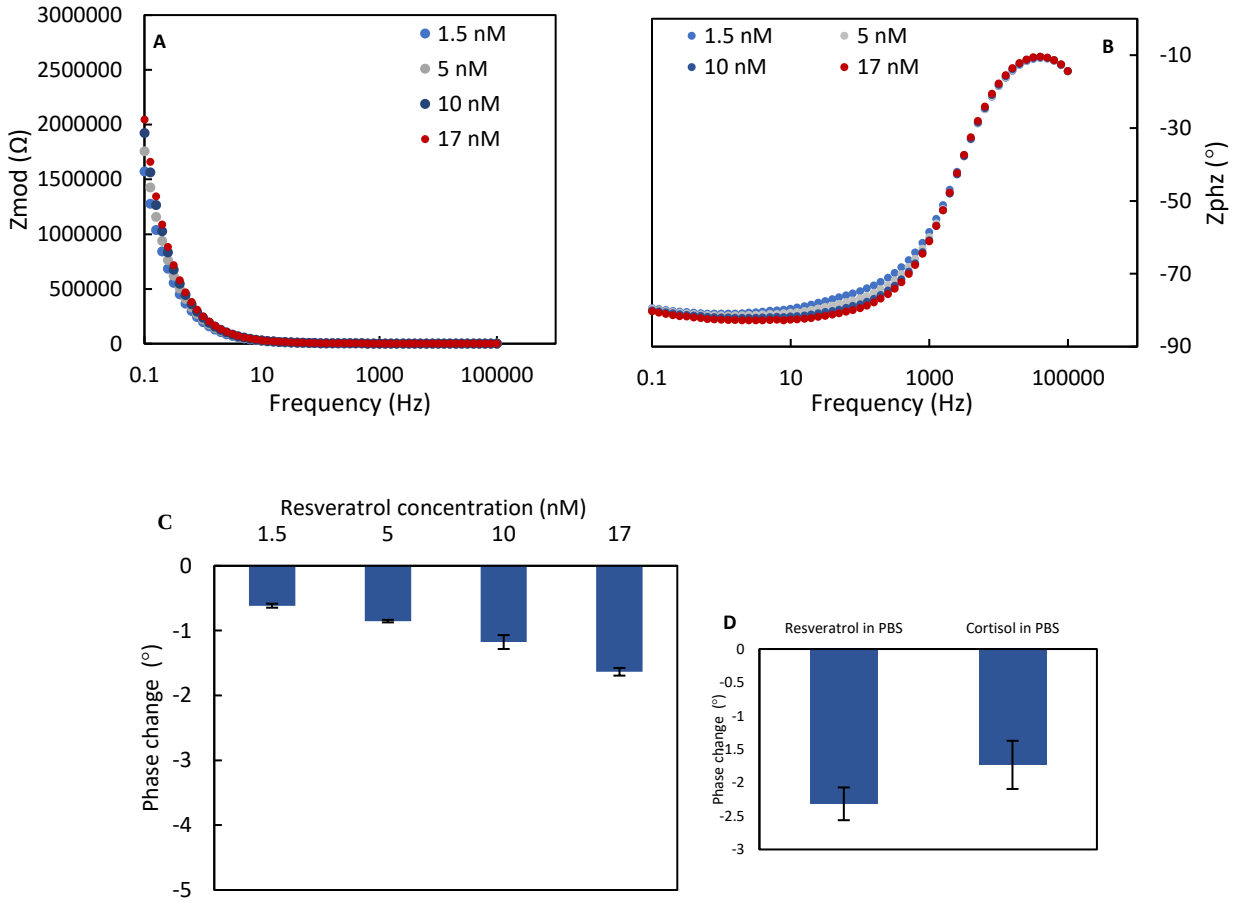

Figure 3.10. Cortisol serial dilution with PEG:αCD modified surface. Bode plot of four different concentrations of cortisol at a PEG:αCD modified surface. (A) Magnitude, (B) phase of the impedance versus frequency. (C) Shows the resulting phase change at 0.1 Hz; average and standard deviation of triplicate data of three unique sensors displayed. (D) Compares the response of the surface to trans-resveratrol with cortisol. This data indicates that the surface is semi-selective to trans-resveratrol and responds better to analytes that have a higher affinity with αCD. Reprinted with permission from Panahi, Zahra, Mckenna A. Merrill, and Jeffrey Mark Halpern. "Reusable Cyclodextrin-Based Electrochemical Platform for Detection of trans-Resveratrol." ACS applied polymer materials 2.11 (2020): 5086-5093. Copyright 2020 American Chemical Society.

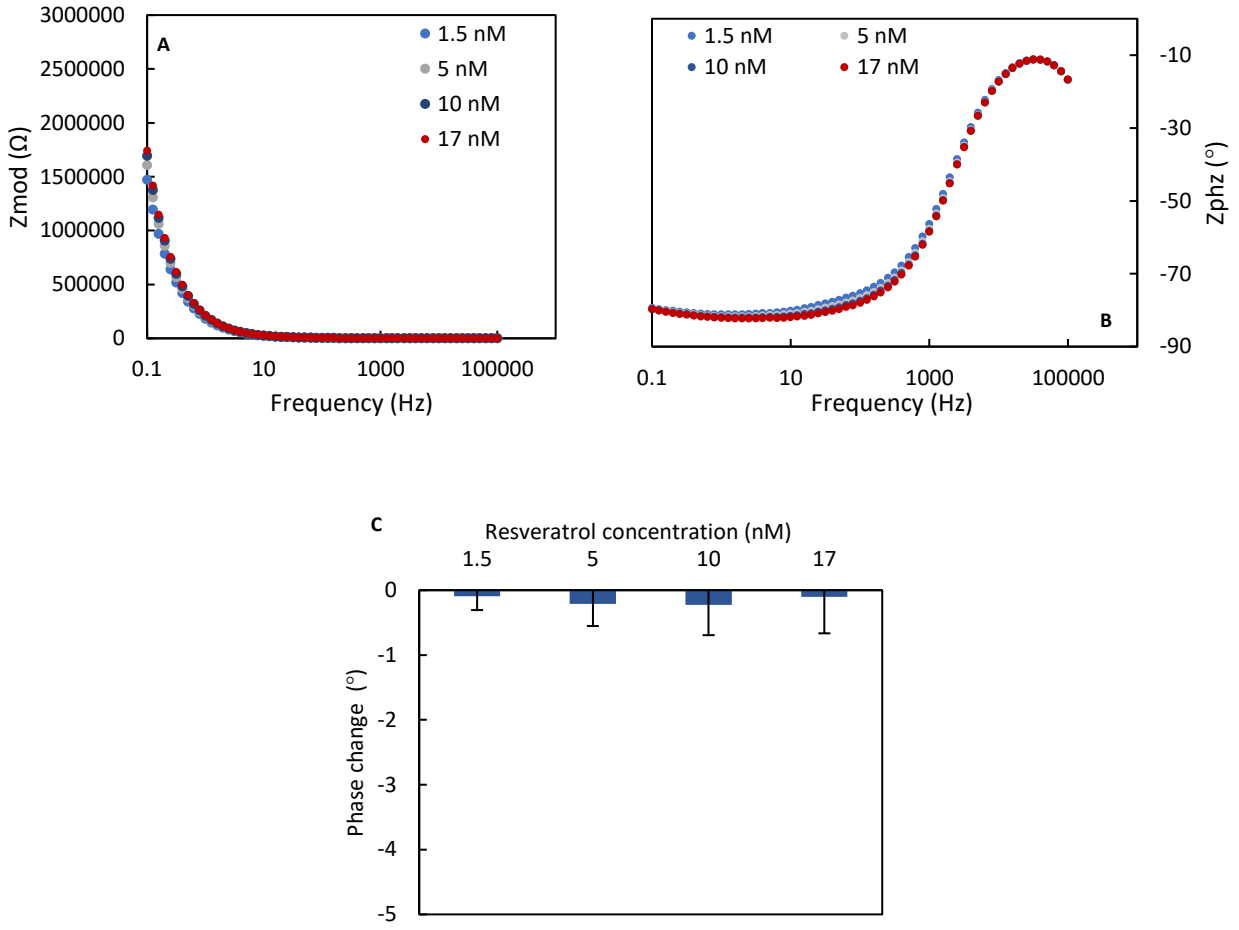

Figure 3.11. Trans-resveratrol serial dilution with a PEG modified surface without αCD immobilization. Bode plot of four different concentrations of trans-resveratrol at a PEG modified surface (with no αCD). (A) Magnitude and (B) phase of the impedance versus frequency. (C) Shows the resulting phase change at 0.1 Hz; average and standard deviation of triplicate data of three unique sensors displayed. This data confirms that αCD is needed to cause a response with trans-resveratrol. Reprinted with permission from Panahi, Zahra, Mckenna A. Merrill, and Jeffrey Mark Halpern. "Reusable Cyclodextrin-Based Electrochemical Platform for Detection of trans-Resveratrol." ACS applied polymer materials 2.11 (2020): 5086-5093. Copyright 2020 American Chemical Society.

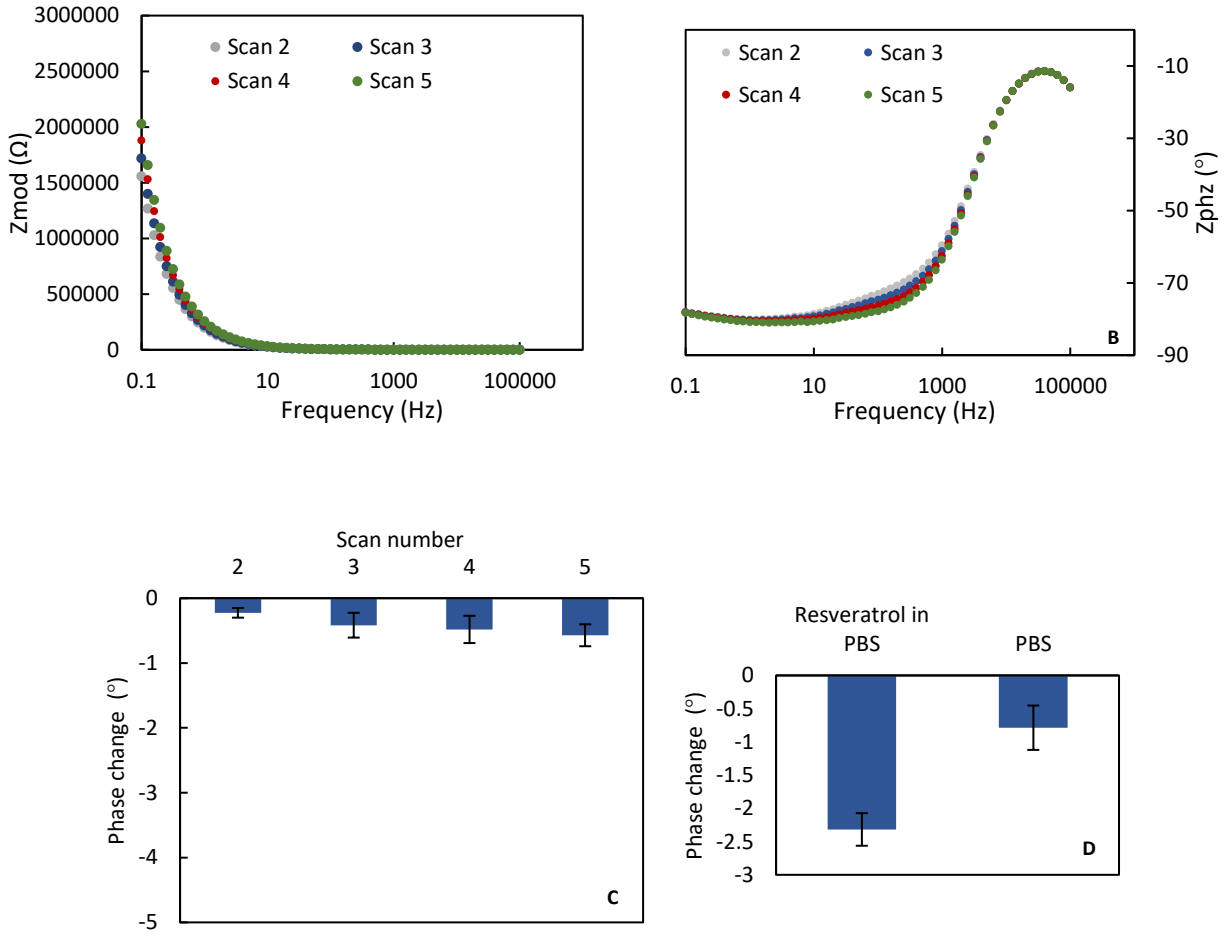

Figure 3.12: Multiple EIS scans of a PEG:αCD modified surface in PBS with no addition of trans-resveratrol. Bode plot of five different scans at a PEG:αCD modified surface with no trans-resveratrol added in PBS. (A) Magnitude and (B) phase of the impedance versus frequency. (C) Shows the resulting phase change at 0.1 Hz; average and standard deviation of triplicate data of three unique sensors displayed, and (D) Comparison between test and control, p-value<0.05. The data confirms the surface is stable in a solution without hydrophobic analytes, and in the presence of trans-resveratrol, the phase change is larger due to αCD disassociating from the surface. Reprinted with permission from Panahi, Zahra, Mckenna A. Merrill, and Jeffrey Mark Halpern. "Reusable Cyclodextrin-Based Electrochemical Platform for Detection of trans-Resveratrol." ACS applied polymer materials 2.11 (2020): 5086-5093. Copyright 2020 American Chemical Society.

3.8 Trans-resveratrol Serial Dilution in Urine

Received pooled urine was filtered through 0.2 µm Polyethersulfone (PES) membrane filter and it was stored in -20°C freezer. Stock solution was prepared by adding 0.447 mg trans-resveratrol to 100 mL of urine prior to filtering. The concentrated trans-resveratrol solution in urine was serially diluted in 20 mL of filtered urine. The non-faradaic EIS analysis in urine was performed without added redox active molecules. All other parameters were kept the same as Section 3.3.

3.9 Results for Trans-resveratrol Detection by Gold-PEG:αCD Surface in Urine

To test the non-specific response of the surface in a complex media, the proposed surface was tested in human urine (**Figure 3.13D**, **3.13E**, and **3.14**). Langmuir equilibrium constants were found to be 0.5640 and 0.5106 nM^{-1} for initial modified surface and regenerated surface, respectively. Additionally, a control experiment was performed in urine with no trans-resveratrol addition (**Figure 3.15**). The cyclodextrin sensor in PBS and human urine showed significantly higher phase change in the presence of trans-resveratrol compared with controls (p-values <0.05 and <0.01, respectively) (**Figure 3.13F**) indicating αCD and trans-resveratrol binding and release occurring at the surface. The discrepancy between Langmuir equilibrium constants in PBS (pH=7.4) and urine (pH= 6.3) can be attributed to the difference in conductivity, ionic strength of the solutions, and pH of the two solutions [184]. This difference can be also explained by additional αCD decoupling due to unspecific bindings of αCD with other molecules in urine which are not present in PBS (**Figure 3.13F**).

After gold surface modification with PEG, the surface was rinsed with UHP to remove excess physiosorbed PEG molecules. However, the first serial dilution showed some physiosorbed PEGs still exist on the surface (**Figure 3.2**, **3.13A** and **3.13D**). Consequently, the sensor response after the first αCD loading (**Figure 3.13A** and **3.13D**) had larger error bars indicating a less precise response due to the presence of physiosorbed PEG that bound with αCD (**Figure 3.2**). When trans-resveratrol was introduced to the solution, the physiosorbed PEGs decoupled from the surface with the αCD: trans-resveratrol complexes. The second trans-resveratrol serial dilution, after reloading of αCD on the surface, showed smaller error (**Figure 3.13B** and **3.13E**). **Figure 3.13C** showed the consistency between the second and third serial dilution in the absence of physiosorbed PEG molecules.

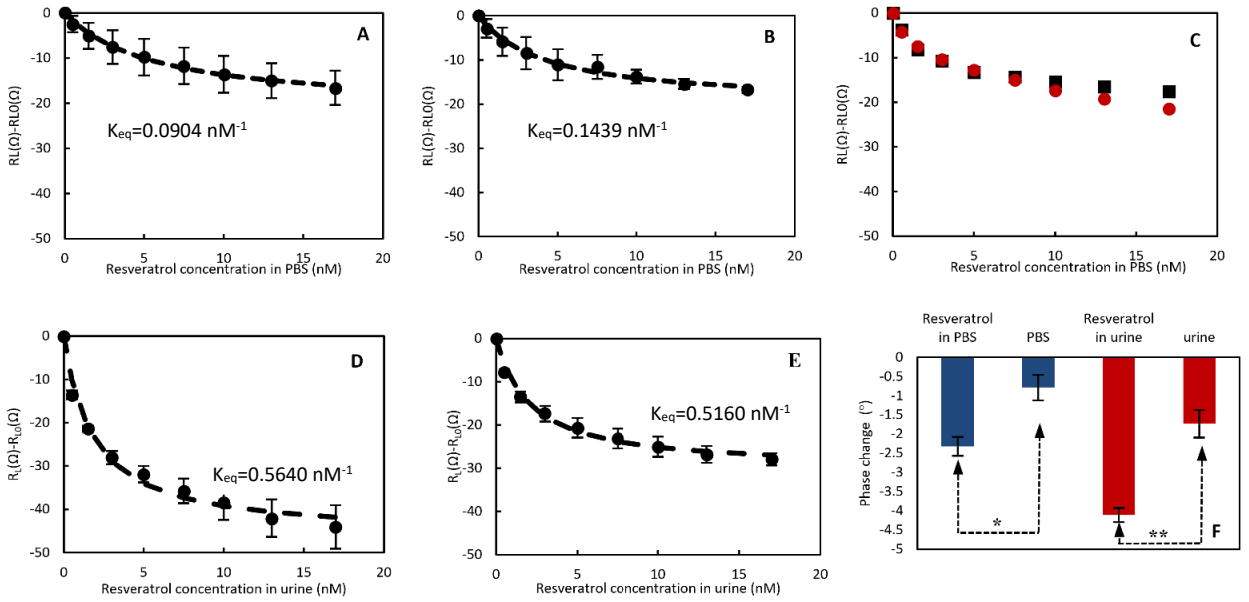

Figure 3.13. Calibration curve of the average of PEG:αCD surfaces response to trans-resveratrol during the (A) first usage in PBS pH=7.4 and the (B) second usage in PBS pH=7.4. Data points (dots) and calculated Langmuir isotherm fit (dotted line) with the standard deviation error of quadruplicate data. (C) Calibration curve comparison of (black) second) and (red) third usage in PBS pH=7.4 showing minimal loss of activity from subsequent serial dilutions. Calibration curve of the average of PEG:αCD surfaces response to trans-resveratrol during the (D) first usage in urine pH=6.3 and the (E) second usage in urine pH=6.3. Data points (dots) and calculated Langmuir isotherm fit (dotted line) with the standard deviation error of triplicate data. (F) Average phase change at 0.1 Hz comparing the baseline to 17nM trans-resveratrol in PBS, PBS only (no trans-resveratrol), trans-resveratrol in urine, and urine only (no trans-resveratrol); *p-value<0.05 & **p-value<0.01. Reprinted with permission from Panahi, Zahra, Mckenna A. Merrill, and Jeffrey Mark Halpern. "Reusable Cyclodextrin-Based Electrochemical Platform for Detection of trans-Resveratrol." ACS applied polymer materials 2.11 (2020): 5086-5093. Copyright 2020 American Chemical Society.

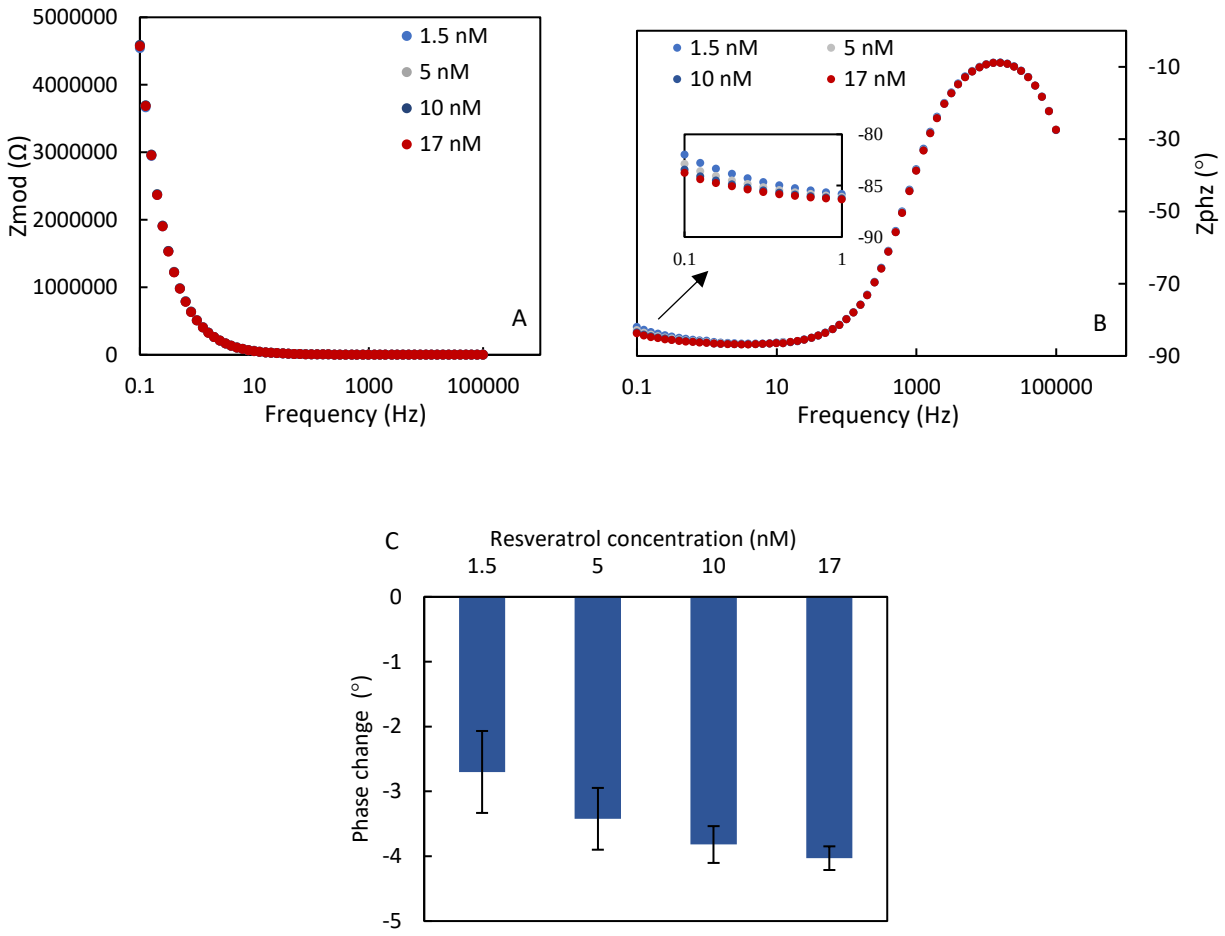

Figure 3.14. Trans-resveratrol serial dilutions by a Gold-PEG:αCD modified surface in urine Bode plot of four different concentrations of trans-resveratrol in urine at a Gold-PEG:αCD modified surface. (A) Magnitude and (B) phase of the impedance versus frequency. (C) Shows the resulting phase change at 0.1 Hz; average and standard deviation of triplicate data of three unique sensors displayed. The data shows that as αCD molecules leave the PEG surface to complex with trans-resveratrol in urine; the phase angle decreases. This data confirms the Gold-PEG:αCD modified surface shows a response to trans-resveratrol in urine. Reprinted with permission from Panahi, Zahra, Mckenna A. Merrill, and Jeffrey Mark Halpern. "Reusable Cyclodextrin-Based Electrochemical Platform for Detection of trans-Resveratrol." ACS applied polymer materials 2.11 (2020): 5086-5093. Copyright 2020 American Chemical Society.

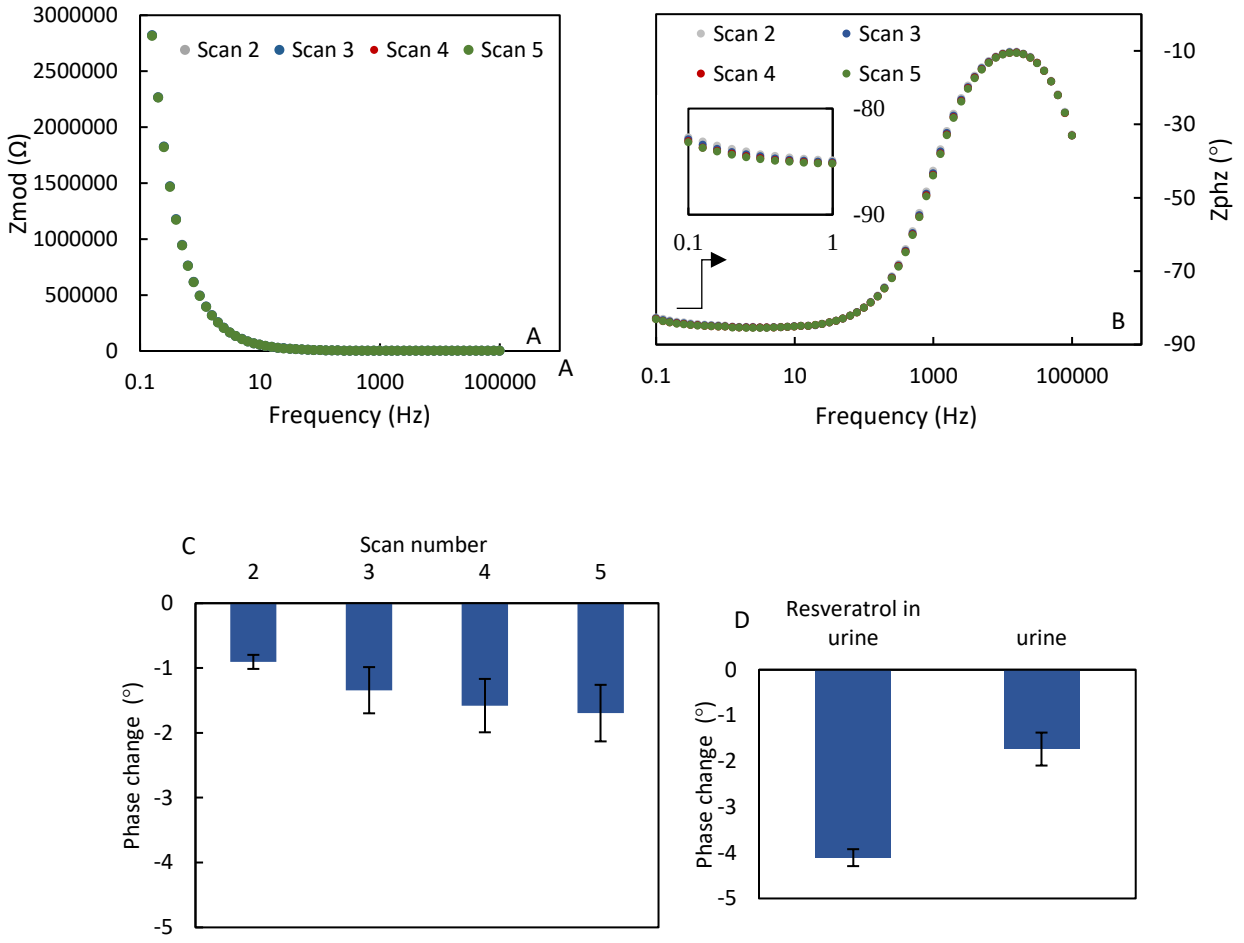

Figure 3.15: Multiple EIS scans of a Gold-PEG:αCD modified surface in urine with no addition of trans-resveratrol Bode plot of five different scans at a Gold-PEG:αCD modified surface with no trans-resveratrol added in urine. (A) Magnitude and (B) phase of the impedance versus frequency. (C) Shows the resulting phase change at 0.1 Hz; average and standard deviation of triplicate data of three unique sensors displayed. (D) Comparison between test and control, p-value<0.01. The data confirms the surface is stable in a complex solution (*e.g.* urine) with some competing hydrophobic analytes, and in the presence of trans-resveratrol, the phase change is larger due to αCD disassociating from the surface. Reprinted with permission from Panahi, Zahra, Mckenna A. Merrill, and Jeffrey Mark Halpern. "Reusable Cyclodextrin-Based Electrochemical Platform for Detection of trans-Resveratrol." ACS applied polymer materials 2.11 (2020): 5086-5093. Copyright 2020 American Chemical Society.

3.10 Conclusion

In this Chapter, we developed the first reusable cyclodextrin surface which showed excellent sensitivity to nM ranges of hydrophobic analytes demonstrated with trans-resveratrol. Specifically, we modified a gold surface with PEG and then αCD was loaded on PEG surface. Faradaic EIS was used to monitor charge transfer resistance during sensor modification steps. ATR-FTIR and XPS techniques were further used to characterize the surface and verify the impedance response. A large conformational change takes place when αCD releases from PEG surface to make inclusion complexes with trans-resveratrol in solution. In the absence of αCD, PEG flattening on the surface allows measurement of leakage resistance. The change in leakage resistance is further proportional to trans-resveratrol concentration in PBS or urine. These findings were in line with faradaic EIS results in the presence of ferri/ferrocyanide and can substantially affect the ability to improve the performance of non-faradaic sensors.

4. Enhancing Stability of Reusable Cyclodextrin Biosensor

4.1 Rational: The Need for Improving Stability of Cyclodextrin Biosensors

In the Chapter 3, a gold electrode modified with a thiol containing polyethylene glycol (thiol-PEG) was used as a support for αCD [181]. We showed that the PEG:αCD surface could be regenerated for three times; however, the surface lost its stability after four or five uses. We hypothesize this limitation was imposed by low stability of the covalent bond between gold and thiol-PEG. Alternatively, surface-immobilization can be performed by reduction of diazonium salts and formation of carbon-carbon bonds between a diazonium salt and a carbon surface [185–187].

In this Chapter we will compare the stability of gold-thiol versus carbon-carbon covalent bonds to develop the most stable PPG:βCD biosensor [188]. The -OH groups of βCD allow hydrogen bonding with polymer materials such as poly propylene glycol (PPG) derivatives. The molecular weight of the PPG main chain as well as the size and shape of the PPG end group affect the efficiency of the complex formation between βCD and PPG. For example, βCD can form channel type crystallin complexes with PPG (MW=2000) with NH_2 end groups because the NH_2 groups are small enough to pass through βCD molecules [189,190].

βCD and cortisol can make host/guest inclusion complexes, and βCD has been used as a carrier for cortisol in various drug delivery systems [191,192]. Elevated levels of stress hormones such as cortisol have been demonstrated in sepsis [193]. Septic patients typically will see an increase of urinary cortisol of 3-8 times higher than normal levels and salivary cortisol levels in severe sepsis patients is 2.6 times higher than healthy subjects [193,194]. Unlike some other

sepsis biomarkers that have a short half-life, cortisol is a stable sepsis biomarker [195]. A study that observed and analyzed inflammatory parameters of 62 intensive care unit (ICU) patients, demonstrated a significant positive correlation between blood cortisol concentrations and daily Sequential Organ Failure Assessment (SOFA) scores [196]. However, cortisol levels change rapidly and measurement of blood cortisol concentrations requires the blood test which may increase stress hormone levels [197]. Therefore, measurement of cortisol in noninvasive relevant biofluids such as urine and saliva can yield better data [198].

Various electrochemical [10,199–204], colorimetric [197,205], and surface plasmon resonance [206] methods have been used to develop cortisol biosensors. Despite the progress made in recent years, most of the research in this area has focused on employing different methods to immobilize antibodies or aptamers on the surface. However, a recent study has shown that compared to reference method of high performance liquid chromatography (HPLC), biosensors based on antibody or aptamer recognition mechanisms can have a wide range of interassay and intraassay variation leading to an over or under estimate the true cortisol concentrations [207]. Therefore, the development of a chemically modified reusable biosensor would provide a potential tool for clinicians to continuously measure the cortisol levels and monitor the course and severity of sepsis in hospitalized patients. To our knowledge, no reusable biosensor for continuous cortisol measurements has ever been developed and all the current cortisol biosensors are single use.

To compare the stability of gold-thiol versus carbon-carbon covalent bonds, we developed and characterized two PPG surfaces: The gold-PPG surface **(Figure 4.1A)** was fabricated based on thiol self-assembled monolayers (SAMs) of 3-Mercaptopropionic Acid

(3MPA). Adsorption of 3MPA thiols on a gold surface produces ordered monolayers and the carboxylic acid end group allows further modification with PPG. The second PPG surface **(Figure 4.1B)** was prepared based on carbon-carbon covalent bond between glassy carbon and aryl diazonium salt. Among all diazonium salts with various functional groups, 4-carboxyphenyl diazonium salt with a carboxylic acid group was selected to make the two surfaces comparable. Therefore, carboxylic acid groups of both 3MPA and carboxyphenyl surfaces could be activated and modified with NH_2-PPG-NH_2 via carbodiimide/succinimide (EDC/NHS) chemistry (**Figure 4.1**).

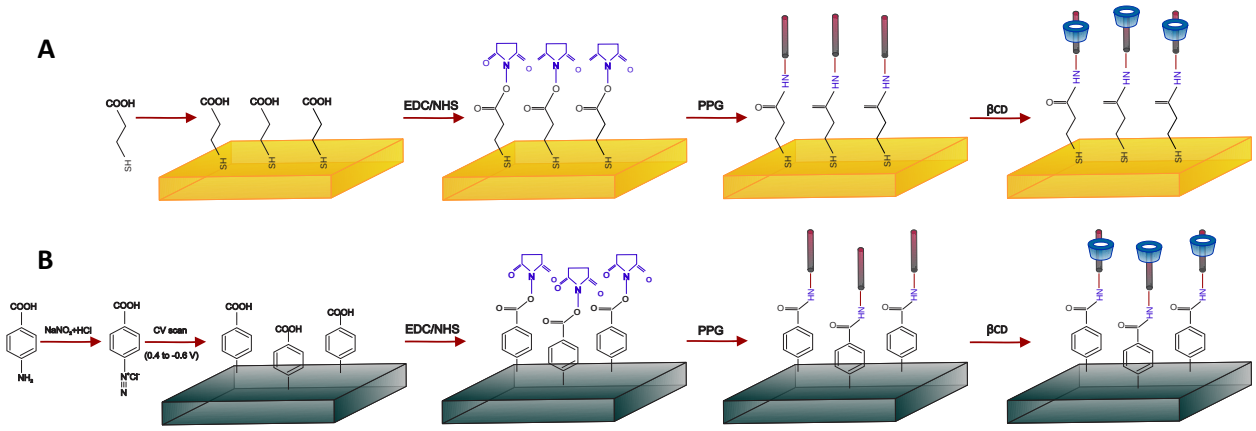

Figure 4.1. Schematic that illustrates surface modification steps of (A) Gold-3MPA-PPG:βCD and (B) GC-carboxyphenyl-PPG:βCD. Reprinted with permission from Panahi, Zahra, Tianyu Ren, and Jeffrey Mark Halpern. " Nanostructured Cyclodextrin-Mediated Surface for Capacitive Determination of Cortisol in Multiple Biofluids." ACS Applied Materials & Interfaces (2022). Copyright 2022 American Chemical Society.

4.2 Gold-3MPA Modification Procedure

A BASi® gold disk electrode was polished in a figure-eight pattern by 1 µm diamond for 1 min and then it was rinsed with methanol and UHP water [181]. The electrode was then polished with 0.55 µm alumina for 1 min and it was sonicated for 1 min in UHP water to remove residual alumina particles. The electrode was dried with nitrogen and oxygen plasma was used to remove

any remaining organic contaminations. The gold surface was then modified by 10 mM 3MPA in ethanol [208]. The gold surface was incubated in the 3MPA solution for 24 h to allow thiol groups to covalently bond with gold surface. The electrode was then rinsed thoroughly with UHP water to remove physiosorbed molecules and dried with N_2 prior to PPG modification.

4.3 Electrografting of 4-carboxyphenyl Diazonium Salt on Glassy Carbon

A BASi® glassy carbon disk electrode was polished with 0.55 μm alumina for 1 min and the electrode was then sonicated in UHP water for 1 min and rinsed thoroughly with UHP water. *In situ* generation of 4-carboxyphenyl diazonium salt was performed by the reaction between 4-aminobenzoic acid ($C_7H_7NO_2$), sodium nitrite ($NaNO_2$), and hydrochloric acid (HCl) [187]. Since this reaction is exothermic, the reaction vessel was placed in ice bath to control the temperature. First, 10 mL of 2mM 4-aminobenzoic acid was added to 10 mL of 0.5 M hydrochloric acid. Then 10 mL of 2 mM sodium nitrite was slowly added and the solution was stirred for 10 min. 15 mL of 4-carboxyphenyl diazonium salt solution was transferred into a shot glass and the polished glassy carbon surface was immersed in the solution. The electrochemical grafting of glassy carbon surface was performed with Gamry Reference 600+ potentiostat. Three cyclic voltammetry (CV) scans were run to graft 4-carboxyphenyl diazonium salt on the surface. CV scans were conducted at 100 mV/s by potential cycling between 0.4 and -0.6 V vs Ag/AgCl. The electrode was then rinsed with UHP water and dried with N_2 prior to the next step. The remaining 4-carboxylphenyl diazonium salt solution was quenched with hypophosphorous acid (H_3PO_2) immediately after modification of the electrodes [209].

4.4 PPG Attachment on Gold-3MPA and GC-carboxyphenyl Surfaces

The carboxylic groups are present on both Gold-3MPA and GC-carboxyphenyl surfaces. EDC/NHS chemistry was used to activate carboxylic groups. 10 mL of 100 mM EDC/20 mM NHS in MES buffer (pH=5) was prepared and the electrodes were incubated in the solution for 90 min. Then the electrodes were rinsed with UHP water and modified with poly (propylene glycol) bis (2-aminopropyl ether). 5 ml of PPG was added to 20 ml of PBS and stirred by sonication for 10 min. Gold-3MPA-PPG and GC-carboxyphenyl-PPG surfaces were prepared by immersing the electrodes in the PPG solution for 30 min. The electrodes were rinsed with UHP water followed by incubating the surfaces in 1 M ethanolamine solution in PBS for 10 min to deactivate excess reactive groups [210]. Finally, the electrodes were rinsed with UHP water and dried with N_2 and stored in UHP water.

4.5 Surface Characterization Procedure (EIS, ATR-ATR-FTIR, and XPS)

All electrochemical measurements were performed with Gamry Instruments Reference 600+ potentiostat in a C3 Cell Stand. Three electrode system compromising an Ag/AgCl/3 M NaCl reference electrode, a platinum wire auxiliary electrode, and a gold or glassy carbon disc electrode working electrode was used for electrochemical experiments. These measurements were performed within the frequency range of 0.1 to 100 kHz, acquiring 10 points per decade with DC potential of 0 V versus open-circuit potential, and the AC voltage of 10 mV. The faradaic EIS measurements for surface characterization and monitoring the surface stability were carried out in 20 mL of 20 mM ferri/ferrocyanide in UHP [181]. The faradaic data was fitted with Randles circuit to find charge transfer resistance R_{ct} for different surfaces. Non-faradaic EIS was conducted

in the indicated buffer without a supporting electrochemical mediator. Non-faradaic EIS was interpreted through the capacitive components of the impedance.

ATR-FTIR measurements were performed with Thermo Nicolet (iS10 ATR-FTIR) and XPS data collection was conducted using Kratos AXIS Supra XPS at university instrumentation center of University of New Hampshire. To prepare samples for these tests, gold-coated silicon wafers and screen-printed carbon electrodes were used to prepare Gold-3MPA-PPG and GC-carboxyphenyl-PPG, respectively. All samples were rinsed with UHP water prior to ATR-FTIR and XPS characterization.

4.6 Results for Gold-3MPA-PPG and GC-carboxyphenyl-PPG Characterization

Selection of a robust and stable support is an important step in developing reusable biosensors. In an attempt to develop a reusable βCD platform, we evaluated two different PPG surfaces, as a βCD support, to evaluate the long-term stability and reuse of each surface. The first surface (Gold-3MPA-PPG:βCD) was constructed through the covalent modification of 3MPA on gold via thiol bond. The second surface (GC-carboxyphenyl-PPG:βCD) was glassy carbon modified by reduction of in situ electrochemically generated 4-carboxyphenyl diazonium salt. Grafting onto the glassy carbon electrode was performed by CV and the first scan showed a cathodic peak at -0.25 V vs. Ag/AgCl reference electrode as shown in **Figure 4.2**. This cathodic peak is resulted from the loss of a N_2 molecule, formation of an aryl radical, followed by covalent binding of the aryl radical to the glassy carbon surface [187]. Disappearance of the cathodic peak in the second and third CV scans indicates the glassy carbon surface is fully modified with carboxyphenyl groups.

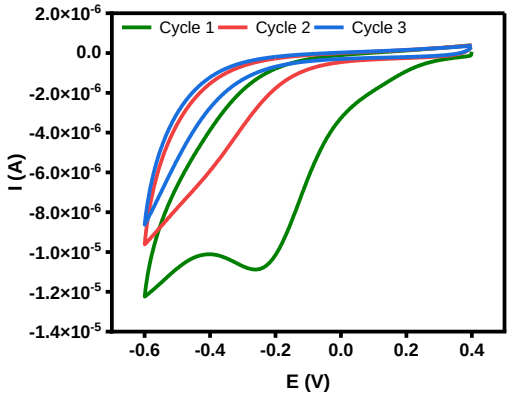

Figure 4.2. Cyclic voltammograms of electrochemical grafting of carboxyphenyl groups on GCE in 4-carboxyphenyl diazonium salt solution from +0.4 to -0.6 vs. Ag/AgCl at scan rate of 100 mV s^{-1}. The characteristic cathodic peak in the first CV scan suggests the formation of a carboxyphenyl layer. Due to blocking effect of carboxyphenyl layer the cathodic peak disappears in the second and third CV scans. Reprinted with permission from Panahi, Zahra, Tianyu Ren, and Jeffrey Mark Halpern. "Nanostructured Cyclodextrin-Mediated Surface for Capacitive Determination of Cortisol in Multiple Biofluids." ACS Applied Materials & Interfaces (2022). Copyright 2022 American Chemical Society.

We studied surface modification of both surfaces using EIS, ATR-FTIR, and XPS. The results of the faradic EIS in 20 mM ferri/ferrocyanide are demonstrated in **Figure 4.3**. The insets in **Figure 4.3A** and **4.3B** show the Nyquist plots of an unmodified gold (orange circle) and an unmodified glassy carbon (black circle), respectively. The diameter of the semicircle in Nyquist plot is directly proportional to the charge transfer resistance. An increase in charge transfer resistance is observed by attachment of 3MPA (green triangle) and carboxyphenyl (blue triangle) followed by modification of both surfaces with PPG (red square) due to the additional passivation of electrode. We infer from these graphs that we successfully modified both PPG surfaces.

In order to confirm successful PPG modification on electrode surfaces, we analyzed the functional groups of Gold-3MPA-PPG and carbon-carboxyphenyl-PPG surfaces by ATR-FTIR (**Figure 4.4A and 4.4B**). According to **Figure 4.4A**, two peaks at 1239 and 1400 cm^{-1} are noticed for 3MPA spectrum (green). These peaks correspond to C-O and belong to aliphatic chain of

3MPA. The peak at 1695 cm^{-1} is assigned to the carboxylic acid end group of 3MPA. However, this peak disappears after PPG modification (red), suggesting the binding interaction of PPG to the carboxylate on-top of 3MPA surface. The peaks at 1100, 1376, and 1450 are due to C-O stretch and the peaks at 2865, and 2972 cm^{-1} arise from C-H stretching groups of PPG [211]. In **Figure 4.4B**, the presence of carboxyphenyl groups of diazonium salt can be confirmed by peaks observed at 1520 and 1660 cm^{-1} (blue). These peaks may be attributed to the aromatic and/or carboxylic acid groups and they vanish after the attachment of PPG (red) [212]. The C-O stretching peaks of PPG appear in the 1000-1500 cm^{-1} range and the 2865, and 2972 cm^{-1} peaks indicate the presence of C-H groups of PPG [211].

XPS analysis was performed to verify the EIS and ATR-FTIR results (**Figure 4.4C and 4.4D**). The orange graph in **Figure 4.4C** shows an unmodified gold surface with dominant gold (Au 4f) peaks. After modification of gold surface with 3MPA (green), the intensity of gold peak decreases and some carbon (C1s) and oxygen (O1s) peaks appear. The presence of sulfur peak in 3MPA spectrum is due to the thiol-gold bonding. Appearance of nitrogen (N 1s) peak after PPG modification can be assigned to unreacted NH_2 groups of PPG. **Table 4.1** shows the decrease in Au/C ratio from 122.1 to 18.8 by 3MPA modification and increase in C/O from 1.75 to 5.37 by PPG modification. Wide XPS spectrum of carbon-carboxyphenyl-PPG surface is shown in **Figure 4.4D**. The presence of carboxyphenyl groups and PPG molecules is supported by the increase in C 1s and O 1s signals after modification of carbon surface with diazonium salt (blue) and PPG (red), respectively. Also, the N 1s peak appears upon modification of diazonium surface with PPG. Finally, **Table 4.2** indicates that by modification of carboxyphenyl surface with PPG, the C/O ratio increases from 0.63 to 4.14.

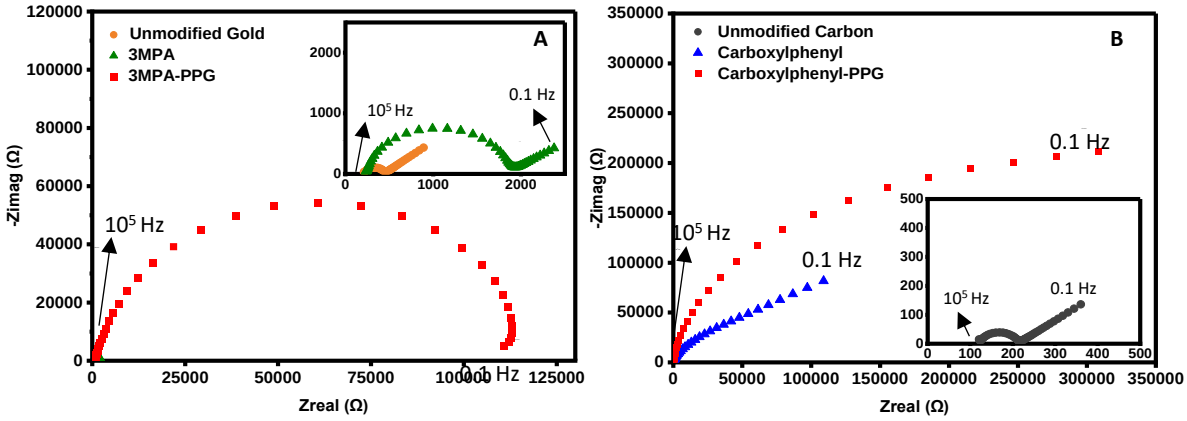

Figure 4.3. Nyquist plots of faradaic EIS in 20 mM ferri/ferrocyanide in UHP: (A) a gold surface before and after modification with 3MPA and PPG and (B) a glassy carbon surface before and after modification with carboxyphenyl and PPG. The increase in diameter of the semicircle in Nyquist plots indicates an increase in the charge transfer resistance. Reprinted with permission from Panahi, Zahra, Tianyu Ren, and Jeffrey Mark Halpern. " Nanostructured Cyclodextrin-Mediated Surface for Capacitive Determination of Cortisol in Multiple Biofluids." *ACS* Applied Materials & Interfaces (2022). Copyright 202*2* American Chemical Society.

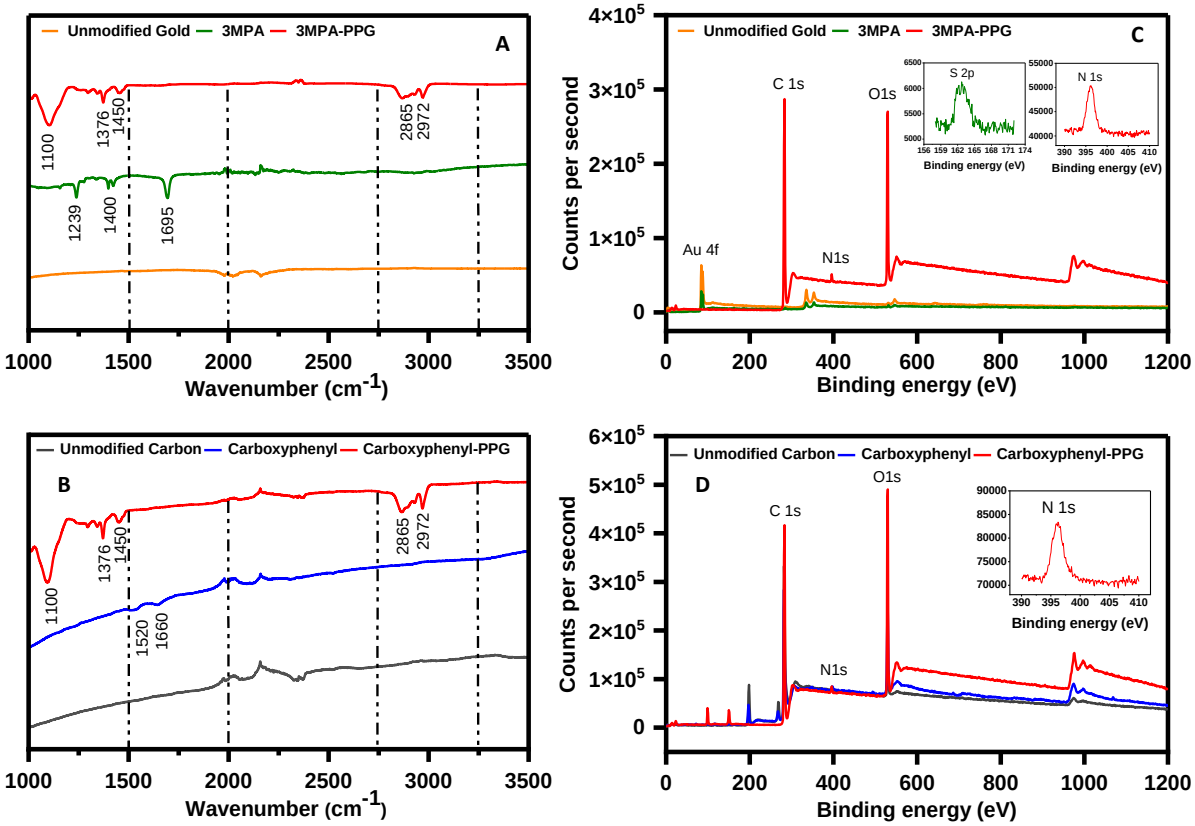

Figure 4.4. ATR-FTIR and XPS characterization of surfaces: (A) ATR-FTIR of Gold-3MPA-PPG, (B) ATR-FTIR of Carbon-carboxyphenyl-PPG, (C) XPS of Gold-3MPA-PPG, and (D) XPS of Carbon-carboxyphenyl-PPG. The ATR-FTIR peaks at 1239 and 1400 cm^{-1} in (A) are assigned to C-O and the peak at 1695 cm^{-1} belongs to C=O binding of 3MPA. The peaks at 1520 and 1660 cm^{-1} in (B) can be attributed to the aromatic and/or carboxylic acid groups of carboxyphenyl surface. In both 3MPA and carboxyphenyl surfaces in (A) and (B), after PPG modification, C-H stretching groups (at 2865 and 2972 cm^{-1}) of PPG dominate the spectra and mask 3MPA and carboxyphenyl signals. The comparison of XPS data after different modification steps in (C) and (D) shows successful modification of Gold-3MPA-PPG and Carbon-carboxyphenyl-PPG surfaces. Reprinted with permission from Panahi, Zahra, Tianyu Ren, and Jeffrey Mark Halpern. " Nanostructured Cyclodextrin-Mediated Surface for Capacitive Determination of Cortisol in Multiple Biofluids." ACS Applied Materials & Interfaces (2022). Copyright 2022 American Chemical Society.

Table 4.1. Quantification of Au 4f, C 1s, O 1s, and N 1s of gold electrode after different modification steps with XPS. By modification of gold surface with 3MPA, the Au/C ratio decreses and by modification of gold-3MPA surface with PPG, the C/O ratio increases. Reprinted with permission from Panahi, Zahra, Tianyu

Ren, and Jeffrey Mark Halpern. " Nanostructured Cyclodextrin-Mediated Surface for Capacitive Determination of Cortisol in Multiple Biofluids." ACS Applied Materials & Interfaces (2022). Copyright 2022 American Chemical Society.

Assigned peak	Binding energy (eV)	Mass concentration (%)		
		Unmodified Gold	Gold-3MPA	Gold-3MPA-PPG
Au 4f	84.2 ± 0.5	54.3	52.3	0
	87.2 ± 0.5	43.4	39.9	0
C 1s	284.8 ± 0.5	0.8	4.9	82.8
O 1s	532 ± 0.5	1.5	2.8	15.4
N 1s	398 ± 0.5	0	0	1.8
Ratio Au/C	-	122.1	18.8	0
Ratio C/O	-	0.53	1.75	5.37

Table 4.2. Quantification of C 1s, O 1s, and N 1s of carbon surface after different modification steps with XPS. By modification of Caron-Carboxyphenyl surface with PPG, the C/O ratio increases. Reprinted with permission from Panahi, Zahra, Tianyu Ren, and Jeffrey Mark Halpern. " Nanostructured Cyclodextrin-Mediated Surface for Capacitive Determination of Cortisol in Multiple Biofluids." ACS Applied Materials & Interfaces (2022). Copyright 2022 American Chemical Society.

Assigned peak	Binding energy (eV)	Mass concentration (%)		
		Unmodified Carbon	Carbon-Carboxylpenyl	Carbon-Carboxylpenyl-PPG
C 1s	284.8 ± 0.5	79.7	38.2	80
O 1s	532 ± 0.5	20.3	59.9	19.3
N 1s	398 ± 0.5	0	1.9	0.7
Ratio C/O	-	3.9	0.63	4.14

4.7 Procedure to Evaluate Long-term Stability of Surfaces

Gold-3MPA-PPG (N=3) and GC-carboxyphenyl-PPG (N=3) modified surfaces were stored in UHP water at room temperature and an EIS measurement in 20 mM ferri/ferrocyanide aqueous solution was performed every 7 days for up to a month.

4.8 Long-term Stability of Gold-3MPA-PPG and GC-carboxyphenyl-PPG

EIS data is usually interpreted with the use of equivalent electrical circuits. The most common electrical circuit to fit faradaic EIS data is Randles circuit (**Figure 4.5A**). The Randles circuit consists of a solution resistance R_s in series with the double layer capacitance C_{dl}, charge transfer resistance R_{ct}, and Warburg impedance. Double layer capacitance deviates from ideal behavior due to surface roughness and constant phase element (CPE) is often used in equivalent circuit model. We used Randles circuit to fit the faradaic EIS data shown in **Figure 4.3** [144]. The charge transfer resistance values for Gold-3MPA-PPG and GC-carboxyphenyl-PPG surfaces are represented in **Figure 4.5B** and **4.5C**, respectively (average and standard deviation reported, N=3). To assess the long-term stability of modified PPG surfaces we kept both surfaces in room temperature UHP water and measured the charge transfer resistance weekly. While the charge transfer resistance of Gold-3MPA-PPG surface decreased dramatically after 1 week ($p<0.05$), the charge transfer resistance of GC-carboxyphenyl-PPG surface remained constant (no statistically relevant changes). This data indicates that stability GC-carboxyphenyl-PPG surface is higher than the Gold-3MPA-PPG, and the replacement of thiol bonds by C-C contributes to the higher stability of biosensor.

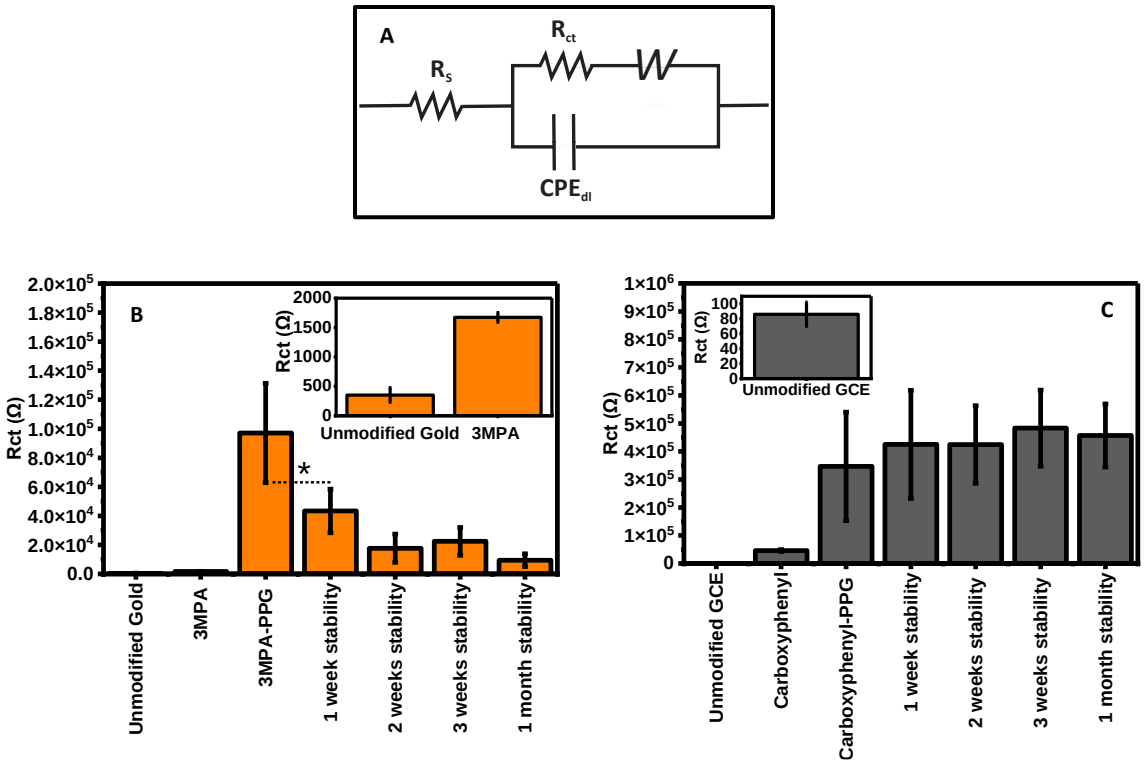

Figure 4.5. Surface modification and stability test of Gold-3MPA-PPG and GC-carboxyphenyl-PPG surfaces for a period of 1 month. Electrodes were stored in UHP water in-between stability tests; stability testing was conducted in 20 mM ferri/ferrocyanide in UHP. (A) The Randles circuit that was used to fit the faradaic EIS data, (B) Average charge transfer resistance (R_{ct}) for 3 Gold-3MPA-PPG surface, (C) Average charge transfer resistance for 3 GC-carboxyphenyl-PPG surface. Error bars indicate the standard deviation of 3 independent surfaces (N=3). The data indicates that the GC-carboxyphenyl-PPG surface is more stable than Gold-3MPA-PPG after just 1 week (*$p<0.05$). Reprinted with permission from Panahi, Zahra, Tianyu Ren, and Jeffrey Mark Halpern. " Nanostructured Cyclodextrin-Mediated Surface for Capacitive Determination of Cortisol in Multiple Biofluids." ACS Applied Materials & Interfaces (2022). Copyright 2022 American Chemical Society.

4.9 Procedure for βCD Loading and Investigating the Reusability of Surfaces

Gold-3MPA-PPG and GC-carboxyphenyl-PPG surfaces were immersed in 5 mM βCD aqueous solution for 1 h to prepare Gold-3MPA-PPG:βCD and GC-carboxyphenyl-PPG:βCD surfaces, respectively. The surfaces were washed thoroughly with UHP and an EIS run was performed in PBS to measure impedance. Then the surfaces were incubated in ethanol for 1 h to remove βCDs from the surface. The surfaces were rinsed with UHP and the impedance was measured. We hypothesized that the surfaces could then be reloaded with another 1 h soak in 5 mM βCD solution. To investigate our hypothesis and evaluate the reusability of surfaces, independent Gold-3MPA-PPG (N=3) and GC-carboxyphenyl-PPG (N=3) were modified the process of βCD loading/ethanol soak was conducted for 10 consecutive times for each surface (n=10).

Throughout this Chapter we use N to indicate the number of different surfaces or electrode preps and n to indicate multiple runs from the same surface. Both N (reproducibility of electrodes, interassay reproducibility) and n (reusability of the same electrode, intraassay reproducibility) are important for this Chapter.

4.10 Capacitive Modeling and Reusability of Surface Construction

Charge transfer resistance is often used to interpret the faradaic EIS in biosensors. However, the use of redox couples limits the practical applications of biosensors in complex biological fluids [153]. Redox couples, such as ferri/ferrocyanide, can interact with surface or analytes and deteriorate surface sensitivity and selectivity. Therefore, a non-faradaic EIS approach, in the absence of redox couples and electrochemical mediators, should be used with cyclodextrin-based biosensors.

The capacitance changes in non-faradaic EIS tend to be small which requires a perfectly fit circuit to monitor and predict these changes. As an alternative to fitting the data to an equivalent circuit is to use total resistance or capacitance data at a fixed frequency. In this work, the imaginary part of the capacitance C" (**Equation 2.12**) has been used to interpret the EIS output of the sensor, since the imaginary part displayed a higher sensitivity than the total capacitance (**Equation 2.10**).

The reusability experiments were performed by developing three surface replicates of Gold-3MPA-PPG (**Figure 4.6A,** N=3) and GC-carboxyphenyl-PPG (**Figure 4.6B,** N=3**)**. The surfaces were loaded with βCD and then soaked in ethanol to remove βCD molecules from the surface; this process was repeated for 10 times measuring the imaginary capacitance after each stage. The reported values (**Figure 4.6**) are the average and standard deviation over the 3 independent surfaces. After each ethanol soak (*i.e.* βCD removal) the imaginary capacitance increased, and the imaginary capacitance decreased after βCD reloading. This result suggests that the GC-carboxyphenyl-PPG:βCD surface can be regenerated and reused up to 10 times. In addition, smaller error bars of GC-carboxyphenyl-PPG:βCD suggests higher measurement and surface-to-surface construct precision.

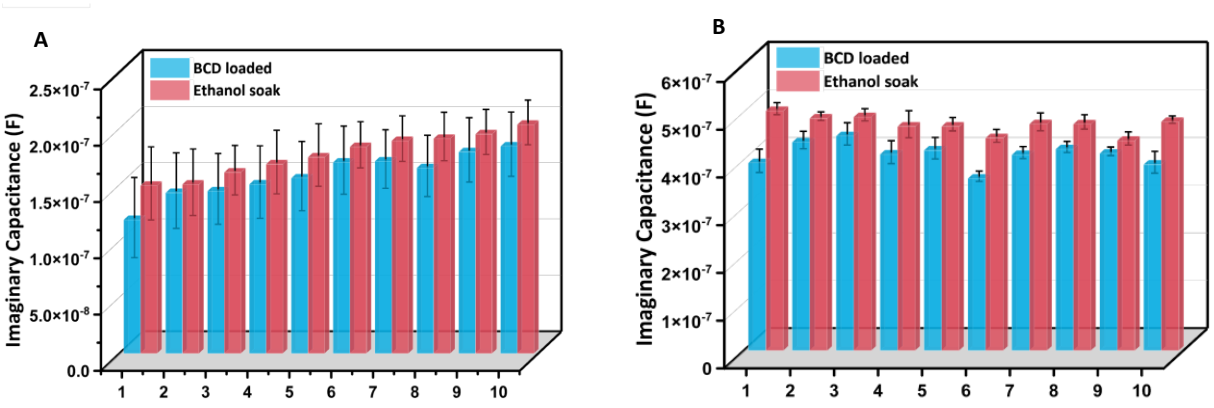

Figure 4.6. Comparison between the reusability of surfaces (N=3): (A) Reusability of Gold-3MPA-PPG:βCD; 10 uses from the same electrode, and (B) Reusability of GC-carboxyphenyl-PPG:βCD; 10 uses from the same electrode. The comparison between (A) and (B) shows that GC-carboxyphenyl-PPG:βCD is more reproducible (smaller drift and run-to-run variation) and can be reused and regenerated for up to 10 times (n=10). Reprinted with permission from Panahi, Zahra, Tianyu Ren, and Jeffrey Mark Halpern. " Nanostructured Cyclodextrin-Mediated Surface for Capacitive Determination of Cortisol in Multiple Biofluids." ACS Applied Materials & Interfaces (2022). Copyright 2022 American Chemical Society.

4.11 Procedure for Evaluation of the Short-term (Sensing Stability) During EIS

To determine measurement drift, after βCD loading (1 h), the electrodes were immediately used for non-faradaic EIS experiments in PBS. Imaginary Capacitance was measured over a frequency spectrum of 0.1 to 10^5 Hz. The normalized imaginary capacitance change ($\frac{C''-C''_0}{C''_0} \times 100$) at all frequencies were calculated for Gold-3MPA-PPG:βCD (N=4) and GC-carboxyphenyl-PPG:βCD (N=5). C''_0 is the imaginary capacitance at t=0 and C'' is the imaginary capacitance at t=30 min.

4.12 Assessment of the Short-term (Sensing Stability) in PBS During EIS

Figure 4.7 demonstrates the short-term (sensing) stability of Gold-3MPA-PPG:βCD and GC-carboxyphenyl-PPG:βCD surfaces in blank PBS over 30 min. Comparison between **Figure 4.7A** and **4.7B** shows that the imaginary capacitance change for Gold-3MPA-PPG:βCD in blank PBS is smaller than GC-carboxyphenyl-PPG:βCD. The sensing stability of GC-carboxyphenyl-PPG:βCD surface was proved to be higher than Gold-3MPA-PPG:βCD; therefore, the diazonium mediated surfaces are more appropriate for sensing applications over thiol surfaces.

4.13 Procedure for Cortisol Detection and Control in PBS, Urine, and Artificial Saliva

To determine the baseline (blank solution with no cortisol) the GC-carboxyphenyl-PPG:βCD surface was first incubated in blank PBS and an EIS was run after 5 min. Then, the surface was immersed in the cortisol solution, with the desired concentration, for 5 min and then EIS was run. The normalized imaginary capacitance change ($\frac{C''-C''_0}{C''_0} \times 100$) was used to plot calibration curves in PBS, urine, and saliva. C''_0 is the imaginary capacitance of baseline (blank solution) and C'' is the imaginary capacitance of concentrated cortisol solution.

The concentrated cortisol stock solutions in PBS (pH 7.4), urine, and saliva were prepared. For PBS experiments, serial dilutions of cortisol solutions were done to get 2.5 to 160 nM concentrations. For urine and saliva experiments, serial dilutions of cortisol solutions were done to get 2.6 to 168.6 nM concentrations. For control experiments in PBS, urine, and saliva, an equivalent volume of blank solutions were added to the test solutions, because the dilution of the solution can decouple the CD from the surface.

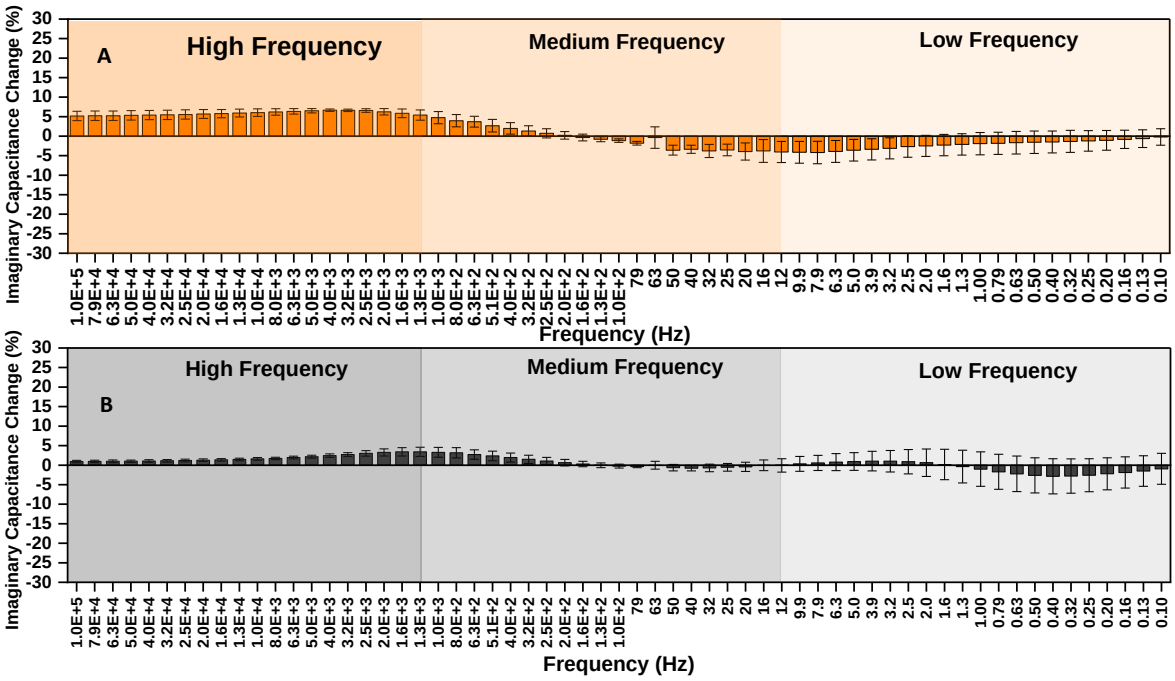

Figure 4.7. Comparison between the stability of surfaces in PBS from t=0 to t=30 min: (A) Gold-3MPA-PPG:βCD (N=4) and (B) GC-carboxyphenyl-PPG:βCD (N=5). This data shows that GC-carboxyphenyl-PPG:βCD has less imaginary capacitance change and higher sensing stability than Gold-3MPA-PPG:βCD surface. Reprinted with permission from Panahi, Zahra, Tianyu Ren, and Jeffrey Mark Halpern. "Nanostructured Cyclodextrin-Mediated Surface for Capacitive Determination of Cortisol in Multiple Biofluids." ACS Applied Materials & Interfaces (2022). Copyright 2022 American Chemical Society.

4.14 Cortisol Detection Results Using Reusable GC-carboxyphenyl-PPG:βCD Surface

Figure 4.8A schematic illustrates the biosensor platform for cortisol detection. When cortisol is introduced into this system, the βCD will depart from the PPG support because of the competitive inclusion interaction between cortisol and βCD, leading to the decrease in impedance and increase in capacitance. To confirm our theory that the increase in capacitance is due to the release of βCD from the surface, XPS was used. Elemental composition of βCD surface before and after cortisol detection was estimated by comparing C1s (**Figure 4.8B** and **4.9**) and O1s (**Figure 4.8C** and **4.10**) spectra. XPS was performed on the following four samples:

1. Carbon-carboxyphenyl-PPG:βCD surface (βCD loaded 1)
2. Carbon-carboxyphenyl-PPG:βCD surface after 1 h exposure to 160 nM cortisol solution (cortisol 1)
3. Regenerated Carbon-carboxyphenyl-PPG:βCD surface (βCD loaded 2) by soaking the electrode in 5 mM βCD solution for 1 h
4. Regenerated Carbon-carboxyphenyl-PPG:βCD surface after 1 h exposure to 160 nM cortisol solution (cortisol 2)

The C 1s spectrum (**Figure 4.9**) can be deconvoluted into three peaks at 284.8, 286.4, and 288.5 eV which can be attributed to C-C or C-H, C-OH or C-O-C, and C=O, respectively. The bar graph in **Figure 4.8B** represents mass concentrations (%) of peaks. All three C 1s components were observed for all samples. Compared to βCD, PPG contains higher amount of C-C and C-H bonds; therefore, the increase in mass concentration of these groups from 31.72 % in βCD loaded 1 surface to 62.14 % in cortisol 1 surface indicates the removal of some βCD molecules followed by the incubation of surface in cortisol solution. After βCD reloading (βCD loaded 2), the mass concentration of C-C and C-H groups decreases to 38.6 %, suggesting the biosensor can be successfully regenerated by βCD reloading. Moreover, the mass concentration of dominant groups of βCD; i.e., C-OH and C-O-C, decrease after the surface is exposed to cortisol solution.

For O1s spectrum (**Figure 4.10**), we can assign the peak with 531.2 eV binding energy to C=O and the components at 532.5 and 533.5 eV can be assigned to C-O-C and OH groups. **Figure 4.8C** demonstrates the mass concentration (%) of different components. By comparing the mass concentration of C-O-C and OH components of different samples, it was found that the changes in the amount of OH groups are more prominent than C-O-C groups since C-O-C groups are

present both in βCD and PPG molecules. The decrease in OH groups after the exposure of surface to cortisol (34.8 % to 12.3 %) confirms release of βCD and the increase in OH groups after reloading of βCD (12.3 to 28.9 %) confirms the reusability of surface.

Another set of XPS experiments on GC-carboxyphenyl-PPG:βCD surfaces were performed to show the effect of ethanol soak on surfaces. **Figure 4.8D and 4.11** represent C1s and **Figure 4.8E and 4.12** represent O1s deconvolution peaks of GC-carboxyphenyl-PPG:βCD surfaces before and after ethanol soak, after βCD reloading, and after second ethanol soak. These results are consistent with **Figure 4.6B**; suggesting βCD can be removed from the surface by ethanol soak instead of exposure to cortisol solution.

A

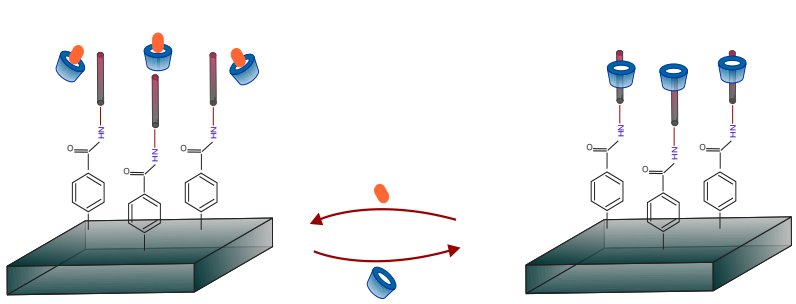

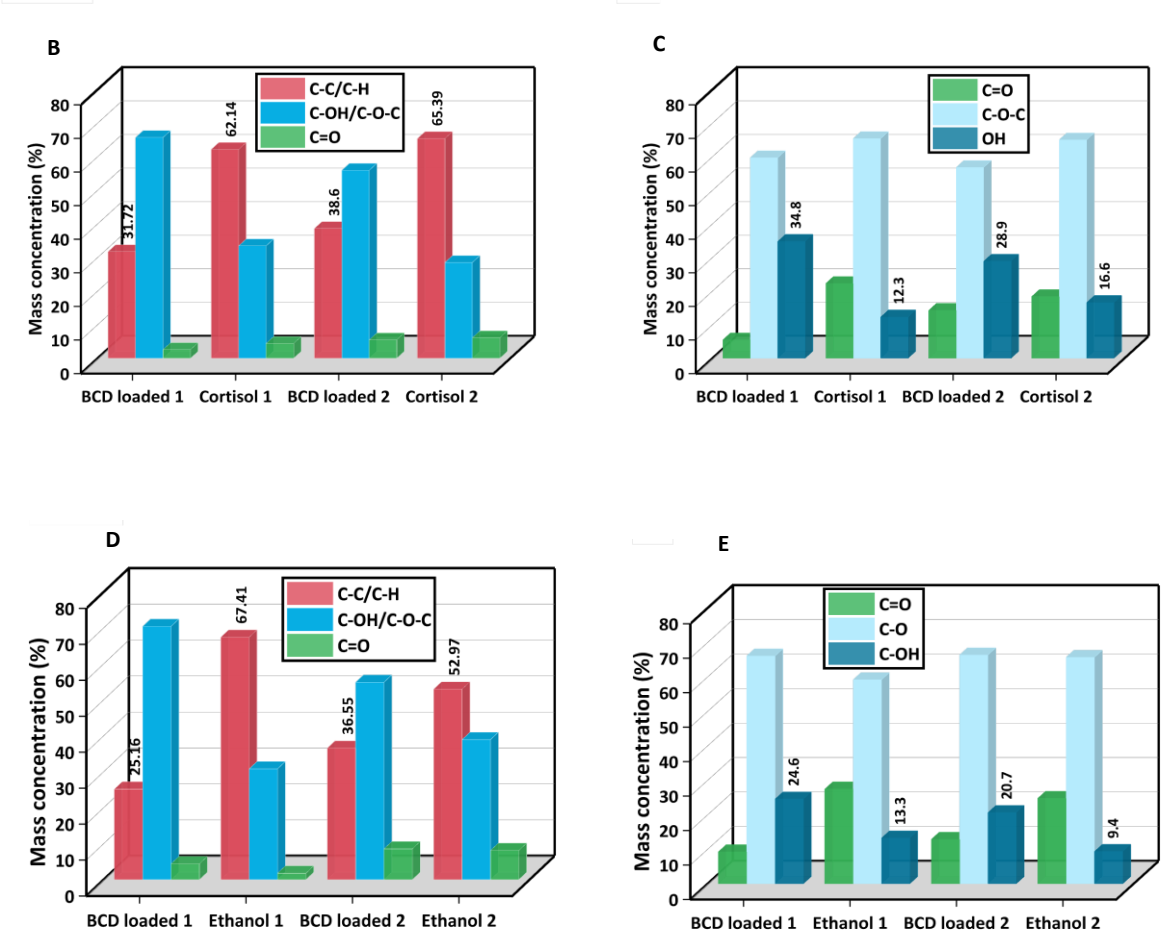

Figure 4.8. Demonstration of GC-carboxyphenyl-PPG:βCD surface for reusable sensing of cortisol: (A) schematic that demonstrates (left) release of βCD from PPG to interact with cortisol and (right) surface regeneration by βCD reloading, (B) Mass concentration (%) of C1s peaks, and (C) O 1s peaks interpreted from XPS performed on βCD surface before and after cortisol detection, (D) Mass concentration (%) of C1s peaks, and (E) O 1s peaks interpreted from XPS performed on βCD surface before and after ethanol soak. This data indicates that βCD can be removed from the GC-carboxyphenyl-PPG surface by immersion in the cortisol solution (B and C) or ethanol soak (D and E). Reprinted with permission from Panahi, Zahra, Tianyu Ren, and Jeffrey Mark Halpern. " Nanostructured Cyclodextrin-Mediated Surface for Capacitive Determination of Cortisol in Multiple Biofluids." ACS Applied Materials & Interfaces (2022). Copyright 2022 American Chemical Society.

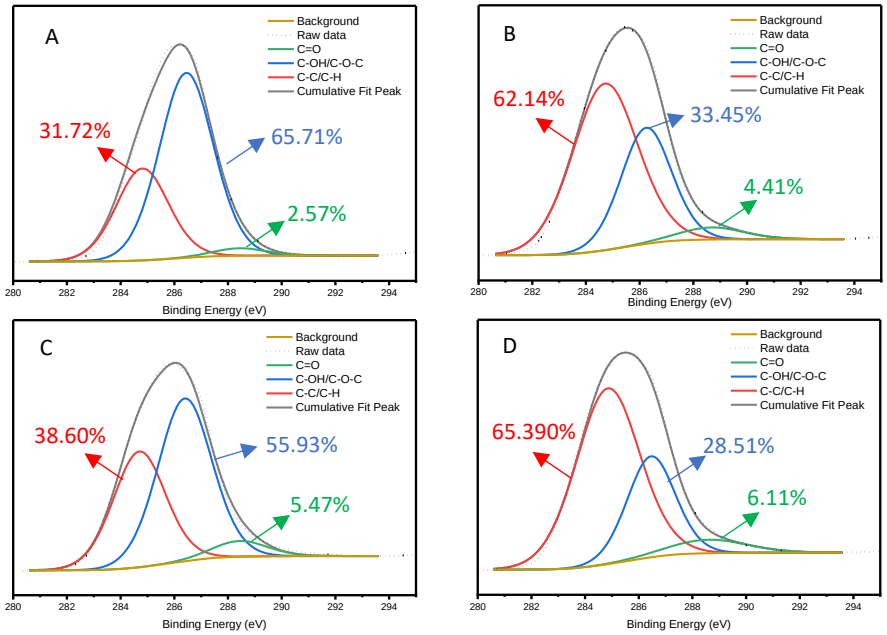

Figure 4.9. High-resolution C1s XPS spectra for 4 different surfaces: (A) Carbon-Carboxyphenyl-PPG:βCD (βCD loaded 1), (B) Carbon-Carboxyphenyl-PPG:βCD surface after 1 hr exposure to 160 nM cortisol (cortisol 1), (C) Regenerated Carbon-Carboxyphenyl-PPG:βCD (βCD loaded 2), and (D) Regenerated Carbon-Carboxyphenyl-PPG:βCD surface after exposure to 160 nM cortisol solution (cortisol 2). Reprinted with permission from Panahi, Zahra, Tianyu Ren, and Jeffrey Mark Halpern. " Nanostructured Cyclodextrin-Mediated Surface for Capacitive Determination of Cortisol in Multiple Biofluids." ACS Applied Materials & Interfaces (2022). Copyright 2022 American Chemical Society.

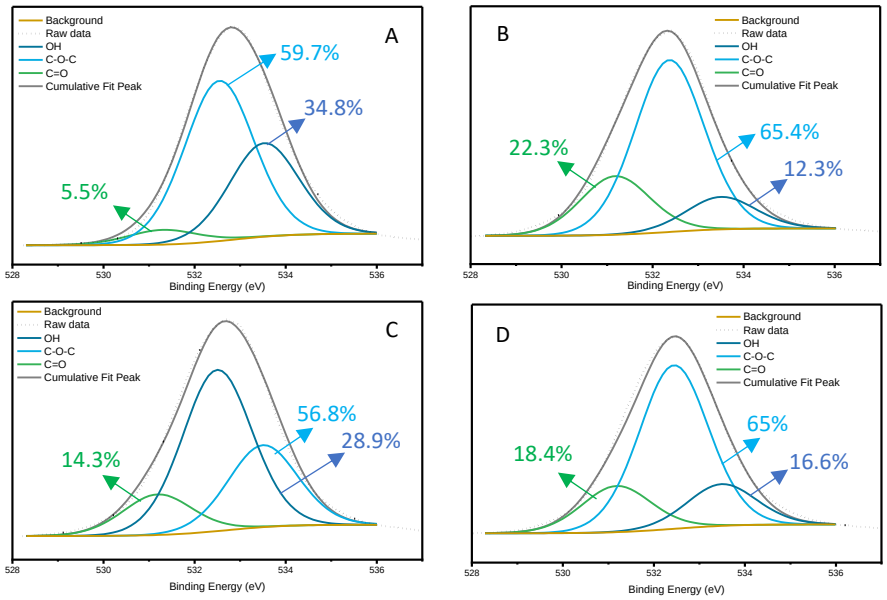

Figure 4.10. High-resolution O1s XPS spectra for 4 different surfaces: (A) Carbon-Carboxyphenyl-PPG:βCD (βCD loaded 1), (B) Carbon-Carboxyphenyl-PPG:βCD surface after 1 hr exposure to 160 nM cortisol (cortisol 1), (C) Regenerated Carbon-Carboxyphenyl-PPG:βCD (βCD loaded 2), and (D) Regenerated Carbon-Carboxyphenyl-PPG:βCD surface after exposure to 160 nM cortisol solution (cortisol 2). Reprinted with permission from Panahi, Zahra, Tianyu Ren, and Jeffrey Mark Halpern. " Nanostructured Cyclodextrin-Mediated Surface for Capacitive Determination of Cortisol in Multiple Biofluids." ACS Applied Materials & Interfaces (2022). Copyright 2022 American Chemical Society.

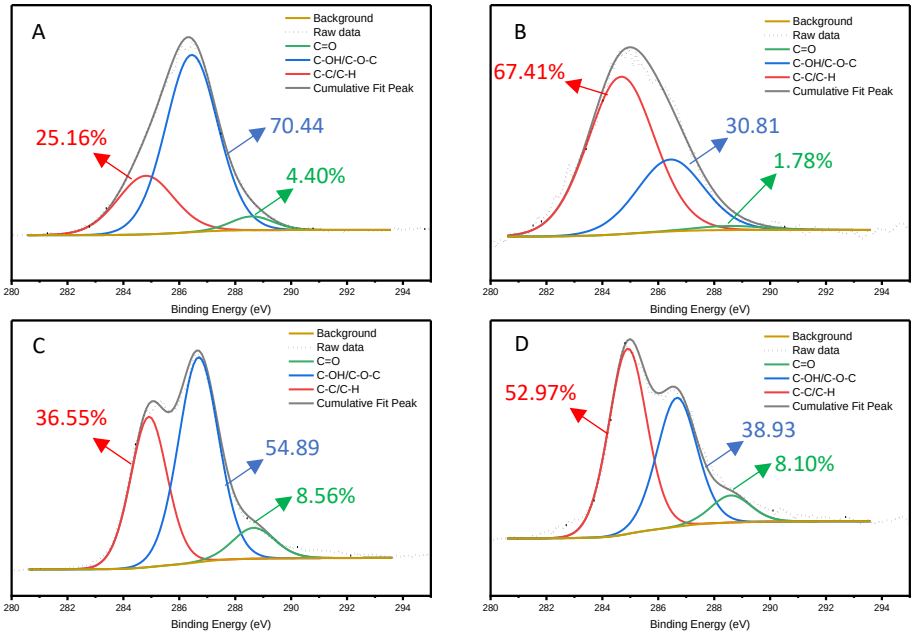

Figure 4.11. High-resolution C1s XPS spectra for 4 different surfaces: (A) Carbon-Carboxyphenyl-PPG:βCD (βCD loaded 1), (B) Carbon-Carboxyphenyl-PPG:βCD surface after 1 hr exposure to ethanol (Ethanol 1), (C) Regenerated Carbon-Carboxyphenyl-PPG:βCD (βCD loaded 2), and (D) Regenerated Carbon-Carboxyphenyl-PPG:βCD surface after exposure to ethanol (Ethanol 2). Reprinted with permission from Panahi, Zahra, Tianyu Ren, and Jeffrey Mark Halpern. " Nanostructured Cyclodextrin-Mediated Surface for Capacitive Determination of Cortisol in Multiple Biofluids." ACS Applied Materials & Interfaces (2022). Copyright 2022 American Chemical Society.

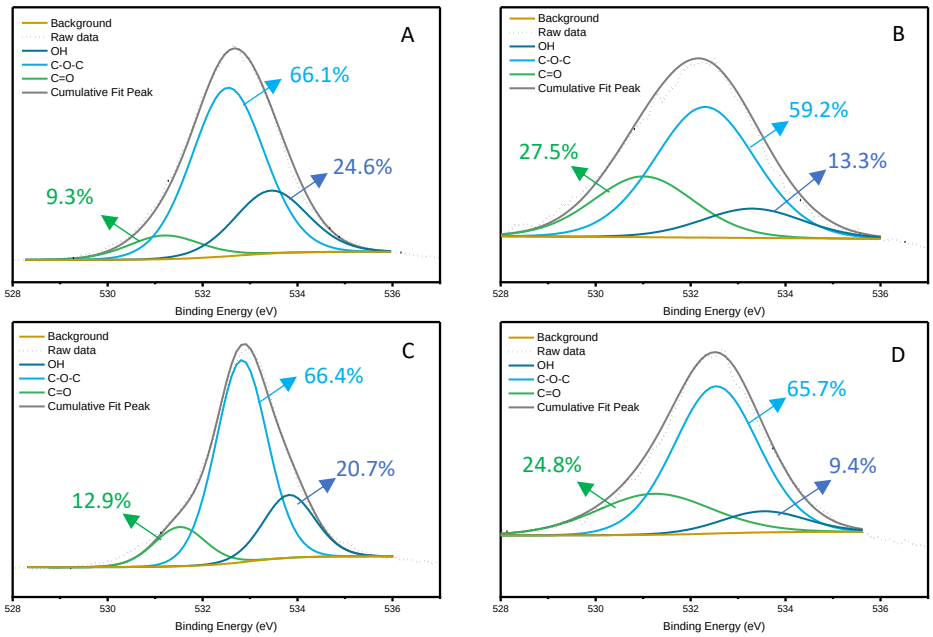

Figure 4.12. High-resolution O1s XPS spectra for 4 different surfaces: (A) Carbon-Carboxyphenyl-PPG:βCD (βCD loaded 1), (B) Carbon-Carboxyphenyl-PPG:βCD surface after 1 hr exposure to ethanol (Ethanol 1), (C) Regenerated Carbon-Carboxyphenyl-PPG:βCD (βCD loaded 2), and (D) Regenerated Carbon-Carboxyphenyl-PPG:βCD surface after exposure to ethanol (Ethanol 2). Reprinted with permission from Panahi, Zahra, Tianyu Ren, and Jeffrey Mark Halpern. " Nanostructured Cyclodextrin-Mediated Surface for Capacitive Determination of Cortisol in Multiple Biofluids." ACS Applied Materials & Interfaces (2022). Copyright 2022 American Chemical Society.

The non-faradaic EIS response of GC-carboxyphenyl-PPG:βCD to 160 nM cortisol is shown in **Figure 4.13A**. To perform these experiments, GC-carboxyphenyl-PPG:βCD surfaces (N=5) were tested in PBS solution with spiked cortisol solutions. Additionally, to investigate the effect of blank PBS on the biosensor response, control experiments were carried out by addition of equivalent volumes of blank PBS to the test solution (N=5). **Figure 4.13B** shows an imaginary capacitance change in response to 122.09 µL of blank PBS solution added to the test solution. The capacitance change in blank solution can be due to the release of βCD molecules into the blank solution [113] or drift in EIS measurements [170]. From **Figure 4.13A** and **4.13B,** the normalized imaginary capacitance change of a frequency with highest signal to noise ratio (SNR) was selected as the biosensor signal. The SNR was defined by **Equation 4.1** and calculated for test (cortisol) and control (PBS).

$$\mathrm{SNR} = \frac{\mu^2}{\delta^2} \qquad \text{Equation 4.1}$$

where μ is the mean and δ is standard deviation. The ratio of the SNR of test to control was calculated at different frequencies, and 1577 Hz, which had the highest SNR between test to control, was selected as the optimal frequency to evaluate the normalized imaginary capacitance change (**Figure 4.14A** and **4.14B**).

The normalized change in imaginary capacitance of GC-carboxyphenyl-PPG:βCD as a function of cortisol concentration at 1577 Hz is plotted to generate a calibration curve in **Figure 4.14C**. The results show that the imaginary capacitance change response increases with increasing cortisol concentration in the range of 2.5-160 nM, and the data can be fit with a Langmuir isotherm. This indicates that the binding affinity of βCD and cortisol must be higher

than the binding affinity of βCD and PPG. Therefore, once the βCD surface is introduced to the cortisol solution, the βCD dissociates from PPG to interact with cortisol in the solution (Equations 4.2-4.4).

$$PPG{:}(\beta CD)_n + Cortisol \rightarrow \beta CD{:}Cortisol$$ Equation 4.2

$$K_d = \frac{[\beta CD{:}Cortisol]}{[PPG{:}(\beta CD)_n]\,[Cortisol]}$$ Equation 4.3

$$Q = \frac{NK_d[\beta CD{:}Cortisol]}{1+K_d[\beta CD{:}Cortisol]}$$ Equation 4.4

In Equations 4.3-4.4, Q is biosensor signal ($\frac{C^{"}-C^{"}_0}{C^{"}_0} \times 100$), N is the maximum capacity of βCD:cortisol interactions, and K_{eq} is equilibrium constant [213–215].

The K_{eq} of cortisol calibration curve in PBS (**Figure 4.14C**, black squares) was determined 0.18 nM^{-1}, and N was calculated to be 5.56. Based on **Equation 4.5 and 4.6** [216], the limit of blank (LOB) and limit of detection (LOD) were calculated to be 0.94 and 2.13 nM, respectively.

$$LOB = mean_{blank} + 1.645\ SD_{blank}$$ Equation 4.5

$$LOD = LOB + 1.645\ SD_{lowest\ concentration\ sample}$$ Equation 4.6

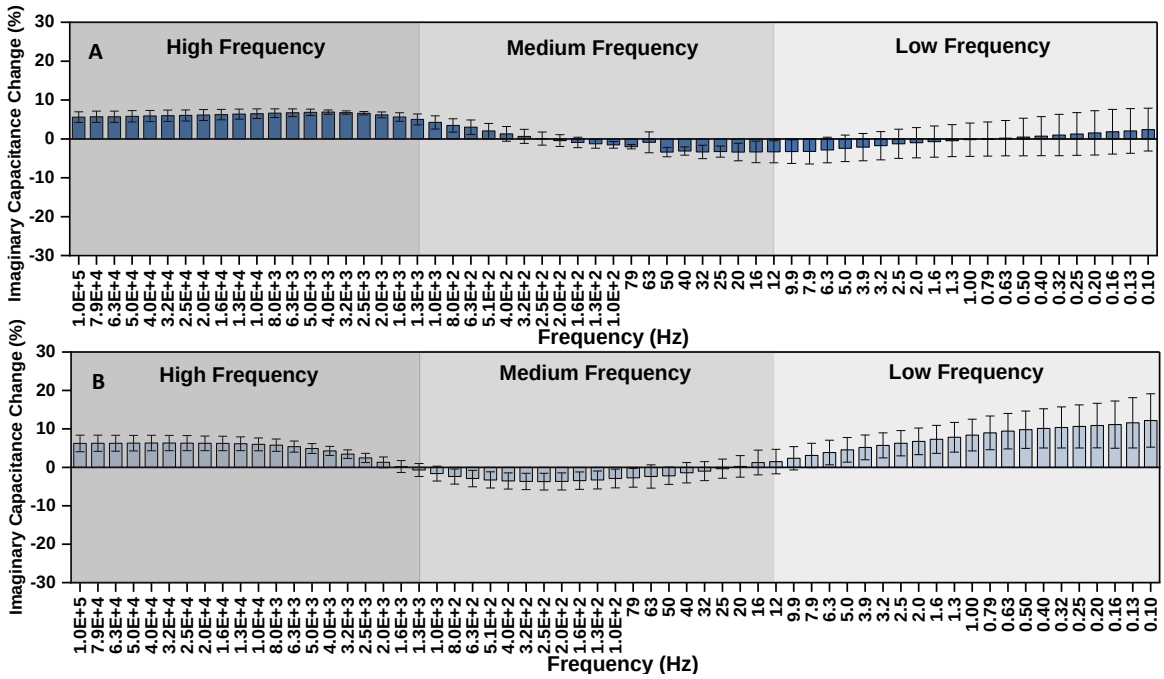

Figure 4.13. Comparison between the GC-carboxyphenyl-PPG:βCD response to: (A) 160 nM cortisol solution (122.09 µL of concentrated cortisol solution added to PBS test solution) (N=5) and (B) 122.09 µL of blank PBS solution added to PBS test solution (N=5). For all frequencies, the ratio of (SNR of (A)/ SNR of (B)) were calculated to find the frequency with highest value to find the best frequency to interpret the data. Reprinted with permission from Panahi, Zahra, Tianyu Ren, and Jeffrey Mark Halpern. " Nanostructured Cyclodextrin-Mediated Surface for Capacitive Determination of Cortisol in Multiple Biofluids." ACS Applied Materials & Interfaces (2022). Copyright 2022 American Chemical Society.

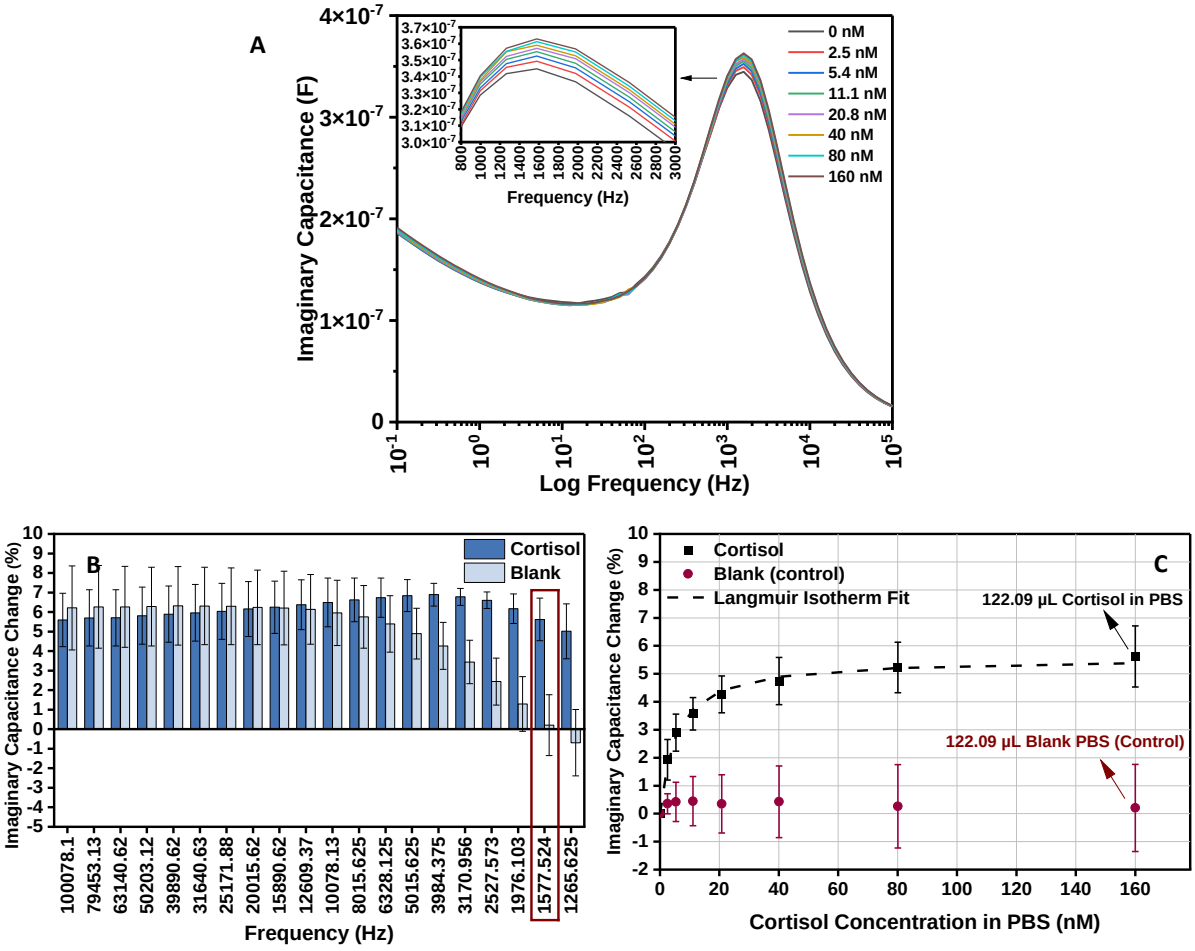

Figure 4.14. Cortisol detection in PBS using GC-carboxyphenyl-PPG:βCD: (A) Imaginary Capacitance vs. frequency plot for various cortisol concentrations, (B) The normalized imaginary capacitance change has the highest SNR at 1577 Hz, and (C) Biosensor response to cortisol (black squares) and blank PBS control (red circles). This data shows that by increasing cortisol concentration the imaginary capacitance change at 1577 Hz increases and was only due to the interaction of βCD with cortisol. Reprinted with permission from Panahi, Zahra, Tianyu Ren, and Jeffrey Mark Halpern. " Nanostructured Cyclodextrin-Mediated Surface for Capacitive Determination of Cortisol in Multiple Biofluids." ACS Applied Materials & Interfaces (2022). Copyright 2022 American Chemical Society.

Finally, the biosensor's response to increasing volumes of blank PBS (**Figure 4.14C**, red circles) cannot be fitted by Langmuir isotherm; confirming that the blank PBS has almost no influence on imaginary capacitance response of cortisol at 1577 Hz. Therefore, increasing concentrations of cortisol was solely responsible for the increase in imaginary capacitance response.

We evaluated capability of our modified GC-carboxyphenyl-PPG:βCD surface to identify cortisol spiked pooled urine and artificial saliva samples. Similar to **Figure 4.14C**, Langmuir isotherm was used to describe desorption of βCD molecules from the surface and in **Figure 4.15** calibration curves of biosensor response to cortisol in human urine and saliva are shown. N values are useful empirical measure of the biosensor performance. For urine, the N value for cortisol solution is 6.69 (as opposed to 2.85 for blank urine) and for saliva the N value is 6.51 (as opposed to 4.70 for blank saliva). N is closely related with the binding affinity of βCDs with cortisol; therefore, in the absence of cortisol N is lower.

Urinary cortisol changes daily in the range of 11 – 281 nM [217] and the LOB and LOD for the surface were found to be 0.84 and 1.29 nM, respectively. In addition, salivary cortisol fluctuates in the range of 3.5 - 27 nM [218] and the LOB and LOD for our biosensor are 1.11 and 1.33 nM, respectively. Accordingly, it can be concluded that the proposed GC-carboxyphenyl-PPG:βCD biosensor can be used for detection of cortisol in urine and saliva samples.

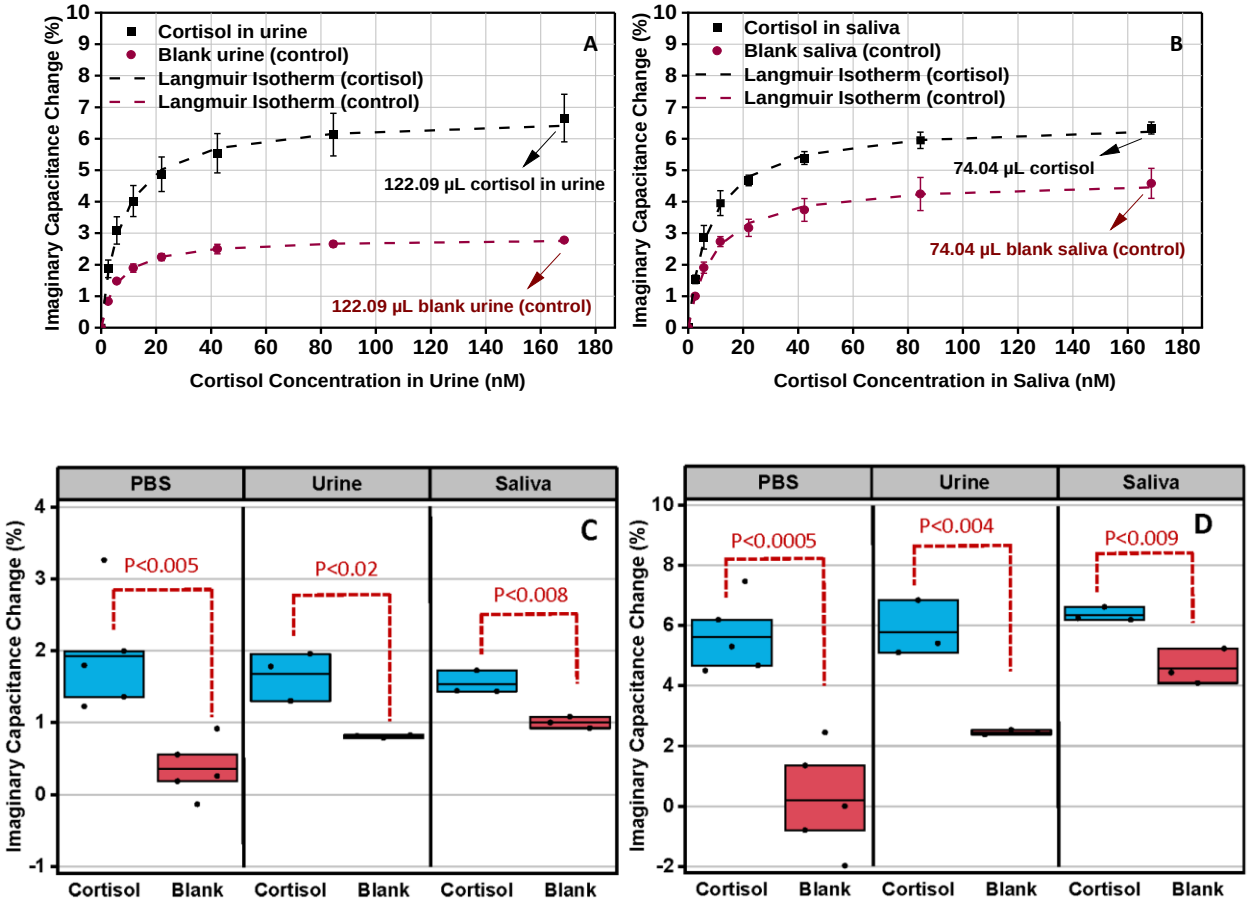

Figure 4.15. Capacitive Determination of Cortisol in Multiple Biofluids: (A) Calibration results for determination of cortisol concentrations urine (N=3), (B) Calibration results for determination of cortisol concentrations in saliva (N=3), (C) Comparison between the biosensor response to addition of 2.5 nM cortisol solution vs. addition of equivalent blank solutions, and (D) Comparison between the biosensor response to addition of 160 nM cortisol in PBS and 168 nM cortisol in urine and saliva solution vs. equivalent blank solutions. Reprinted with permission from Panahi, Zahra, Tianyu Ren, and Jeffrey Mark Halpern. " Nanostructured Cyclodextrin-Mediated Surface for Capacitive Determination of Cortisol in Multiple Biofluids." ACS Applied Materials & Interfaces (2022). Copyright 2022 American Chemical Society.

4.15 Procedure for Evaluation of GC-carboxyphenyl-PPG:βCD Selectivity

The GC-carboxyphenyl-PPG:βCD surface was first immersed in PBS and after 5 min, an EIS was run to determine the baseline value (C''_0). Then different volumes of concentrated solutions were added to get 160 nM *trans*-resveratrol, uric acid, and acetaminophen solutions (C''). Then, the normalized imaginary capacitance change ($\frac{C''-C''_0}{C''_0} \times 100$) was calculated for different analytes.

4.16 Results for Selectivity of GC-carboxyphenyl-PPG:βCD

In order to asses potential interfering analytes for clinical applications with the GC-carboxyphenyl-PPG:βCD sensor, several compounds including uric acid, acetaminophen, and *trans*-resveratrol were evaluated (**Figure 4.16**). Uric acid is one of the most important co-existing analytes in urine and this data suggests that uric acid does not interfere with sensing of cortisol and the biosensor can be tested in urine samples ($p<0.001$). Additionally, contrary to interfering effect of acetaminophen with a previously developed βCD biosensor [103], GC-carboxyphenyl-PPG:βCD does not respond to acetaminophen ($p<0.005$). Finally, while trans-resveratrol can make host-guest inclusion complexes with αCD, trans-resveratrol does not influence the cortisol detection by the developed βCD surface ($p<0.005$). In summary, the normalized imaginary capacitance change in response to cortisol was significantly greater than blank PBS, uric acid, acetaminophen, and trans-resveratrol ($p<0.005$). However, pairwise comparisons between uric acid and acetaminophen, uric acid and trans-resveratrol, uric acid and blank PBS, acetaminophen and trans-resveratrol, acetaminophen and blank PBS, and trans-resveratrol and blank PBS showed these were not significantly different from each other.

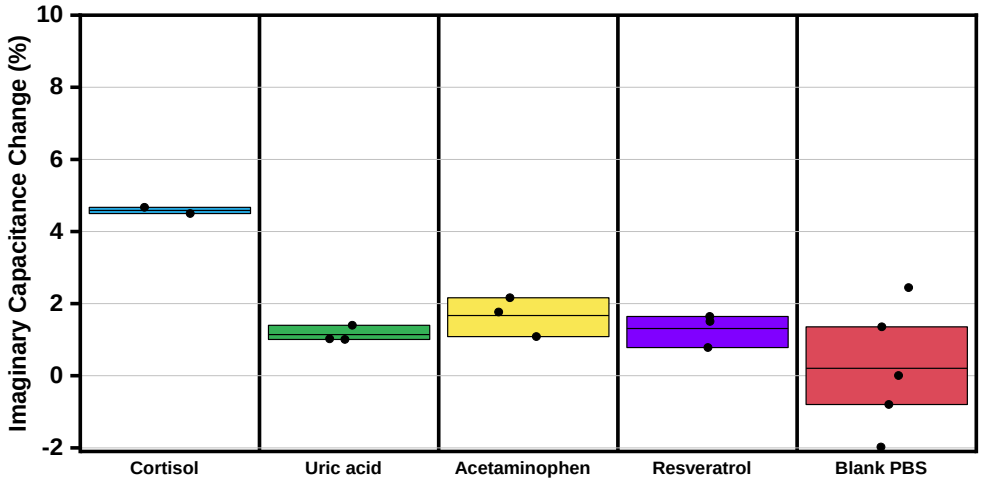

Figure 4.16. Comparison of GC-carboxyphenyl-PPG:βCD biosensor response to cortisol (160 nM) vs. blank PBS and potential interferents including uric acid (160 nM), acetaminophen (160 nM), and trans-resveratrol (160 nM) in PBS. The data confirms that uric acid, acetaminophen, and trans-resveratrol do not interfere with cortisol analysis ($p<0.005$). Reprinted with permission from Panahi, Zahra, Tianyu Ren, and Jeffrey Mark Halpern. " Nanostructured Cyclodextrin-Mediated Surface for Capacitive Determination of Cortisol in Multiple Biofluids." ACS Applied Materials & Interfaces (2022). Copyright 2022 American Chemical Society.

4.17 Comparison of GC-carboxyphenyl-PPG:βCD with other Cortisol Biosensors

We compared the results of GC-carboxyphenyl-PPG:βCD biosensor with other recently developed cortisol biosensors. **Table 4.3** shows that while the LOD is comparable to that of other biosensors, GC-carboxyphenyl-PPG:βCD has three advantages:

- Development of the non-enzymatic GC-carboxyphenyl-PPG:βCD biosensor is simple and it does not require expensive and complicated procedures that are usually involved in development of immunoassays.
- GC-carboxyphenyl-PPG:βCD is the first reusable cortisol biosensor and it does not suffer from the common restrictions of immunoassays including low stability and low reproducibility. The surface is stable for at least a month and it can be reused for up to 10 times.
- GC-carboxyphenyl-PPG:βCD can be used to detect cortisol in various relevant biological fluids such as urine (1.29-168 nM) and saliva (1.33-168 nM). Therefore, the developed biosensor is applicable to detect cortisol levels in urine or saliva samples of septic patients.

Table 4.3. Comparison of various recently developed biosensors for detection of cortisol. Reprinted with permission from Panahi, Zahra, Tianyu Ren, and Jeffrey Mark Halpern. " Nanostructured Cyclodextrin-Mediated Surface for Capacitive Determination of Cortisol in Multiple Biofluids." ACS Applied Materials & Interfaces (2022). Copyright 2022 American Chemical Society.

Biosensor	Detection method	Medium	LOD (nM)	Reusability	Ref.
Aptamer-Based lateral flow assay	Colorimetric	Artificial saliva	*2.73	Single use	[197]
		Human saliva	*1.02		
Hydroxylamine-reduced silver nanoparticles (HA-AgNPs)	Surface enhanced Raman spectroscopy (SERS)	Bovine serum albumin in PBS	**177	Single use	[219]
cortisol antibodies/suspension of magnetic beads	Magnetically Assisted-SERS (MA-SERS)	Human urine simulant and human serum	**19.31	Single use	[220]
cortisol antibodies /gold-coated glass	Rigid Substrate-SERS (RS-SERS)		**8.28		
cortisol antibody/ PEDOT/Ni/Pt micromotor	UV–visible spectrophotometry	PBS Buffer	***275.89	Single use	[221]
GC-carboxyphenyl-PPG:βCD	**Electrochemical (EIS)**	**PBS Buffer**	***2.13 & ****2.5**	**Reusable**	**This work**
		Human urine	***1.29 & ****2.5**		
		Artificial saliva	***1.33 & ****2.5**		

* LOD based on Equation 8-9

**LOD, defined as 3 SD_{blank} /s, where s is the slope of the calibration curve

*** Lowest measured concentration

4.18 Conclusions

We have designed a reusable biosensor platform that integrates the complexation of CDs with various hydrophobic guest molecules and polymers. In this platform, when a hydrophobic guest analyte is introduced into this system, the cyclodextrin will depart from the polymer support due to the competitive inclusion interaction between the analyte and cyclodextrin. In Chapter 3, we applied this technology to create an αCD based surface for detection of trans-resveratrol. In this chapter, we first improved the stability of biosensor by replacing gold-thiol bonds with stronger C-C bonds through diazonium salt chemistry. Second, we applied this technology to develop a cortisol biosensor based on competitive interactions of βCD with PPG and cortisol. As a result of higher stability, the GC-carboxyphenyl-PPG:βCD could be regenerated and reused for up to 10 times.

5. Progress on Development of Cyclodextrin Impedimetric Tongue

5.1 Rational: The Need for Development of Cyclodextrin Based Impedimetric Tongue

Sepsis, a life-threatening medical condition and a major cause of in-hospital deaths, contributes to more than 250,000 deaths in the United States [1]. Sepsis occurs when an infection (e.g., bacteria, virus, mold) triggers the immune system to attack body organs. Patients in the intensive care units (ICU) are at high risk for sepsis and 18% of ICU patients around the world develop sepsis [2]. Unfortunately, in 25.8% of septic patients in the ICU, sepsis leads to septic shock, multiple organ failure, and death [2]. Early administration of antibiotics and infusion of intravenous fluids is essential to decrease in-hospital mortality rates [3]. Currently there is no device for comprehensive testing of sepsis and development of a device for early diagnosis of sepsis, monitoring the course of the disease, and monitoring septic patients' response to the treatment is necessary for full recovery.

Metabolomics is one of the methods to identify new biomarkers by analyzing various endogenous and exogenous metabolites [222]. Metabolomics studies have been conducted to identify sepsis biomarkers in urine and the results are shown in **Table 5.1** [222–227]**.** In a study on 64 critically ill septic patients in ICU, ^{1}H NMR spectroscopy was used to identify sepsis metabolite biomarkers in urine. Elevated levels of ethanol, glucose, hippurate, and lower levels of methionine, glutamine, arginine, and phenylamine were observed in negative prognosis patients [223]. In a different study on 1346 healthy volunteers and 1282 severe sepsis patients, mass spectroscopy was used to identify kynurenic acid, hippuric acid, glycine, 3-methyluridine,

and acetylcysteine as potential urinary sepsis diagnosis biomarkers [224]. Another ^{1}H NMR study on children aged 1 month to 11 years old suggested that septic patients had higher levels of 3-hydroxybutyrate, carnitine, creatinine, creatine, glucose, and acetone compared with those of healthy children [225,226]. Finally, the results of a metabolomic study by ^{1}H NMR and GC-MS revealed an increase in acetate, acetone, glycine, lysine lactate, glucose, maltose in the urine of septic infants. The data also indicated a decrease of ribitol, ribonic acid, pseudo uridine, 2,3,4-trihydroxybutyric acid, 2-ketogluconic acid, 3,4-dihydroxybutanoic acid, citrate and creatinine for infected patients [222,227].

Table 5.1. Summary of the metabolomics human studies to identify sepsis markers in urine

Analytical Method	Study Group	Potential Biomarker	Ref.
^{1}H NMR	64 ICU patients	ethanol, glucose, hippurate, methionine, glutamine, arginine, and phenylamine	[223]
LC-MS	1282 severe sepsis patients and 1346 healthy volunteers (control)	kynurenic acid, hippuric acid, glycine, 3-methyluridine, and acetylcysteine	[224]
^{1}H NMR	60 children with septic shock, 40 SIRS/ICU* children (control), and 40 healthy children (control)	3-hydroxybutyrate, carnitine, creatinine, creatine, glucose, and acetone	[225,226]
^{1}H NMR	6 preterm infants with persistent PDA**, 4 preterm infants without PDA (control), 4 infants born at term (control)	acetate, acetone, citrate, creatinine, glycine, lactate, lysine, and glucose	[222,227]
GC-MS		lactate, glucose, maltose, ribitol, ribonic acid, pseudo-uridine, 2,3,4-trihydroxybutyric acid, 2-ketogluconic acid, and 3,4-dihydroxy butanoic acid	
^{1}H NMR	An infant with fatal MRSA*** pneumonia, 4 children with influenza pneumonia (control), and 7 healthy children (control)	3-hydroxybutyrate, carnitine, creatinine, acetone, acetoacetate, choline, fumarate, glucose, and 3-aminoisobutyrate	[225]

*SIRS/ICU: systemic inflammatory response syndrome/intensive care unit. These children were not suspected of having an infection.

** PDA: patent ductus arteriosus

*** MRSA: methicillin-resistant Staphylococcus aureus

While antibodies are important for measurement of cytokine biomarkers, hydrophobic cavity of cyclodextrins can provide binding sites for low molecular weight metabolites [8]. Many of these relevant urinary sepsis biomarkers in **Table 5.1** bind with different cyclodextrins [73,228–236]. **Table 5.2** shows sepsis metabolites than can interact with various cyclodextrins. In Section 1.2 we discussed that the size, charge density of metabolites, number, and placement of hydrogen donors affect the formation and stability of inclusion complexes. The crystal structure of inclusion complexes between αCD and acetone has been studied by XRD and the suggested stoichiometry for the complex is two αCD molecules per acetone molecule [229]. In another study, XRD, FTIR and Differential Scanning Calorimetry (DSC) were used to characterize 2-hydroxypropyl-β-cyclodextrin: iron (II) fumarate inclusion complexes [233]. Besides, αCD forms inclusion complexes with m-nitrophenyl acetate (mNPA) and p-nitrophenyl acetate (pNPA) and for every 10 αCD molecule, 2 guest molecule is estimated [232]. The interactions between cyclodextrin and glucose has been confirmed by measurement of free glucose with a glucose meter [231]. The addition of αCD or βCD to the solution decreased free glucose concentrations [231]. In another work, αCD was used because glucose (width and length of 5.6 and 6.5 Å) molecule fits better into the cavity of αCD (width and length of 5.7 and 7.8 Å) in comparison to βCD (width and length of 7.8 and 7.8 Å) [230]. Similarly, while the diameter of αCD matches with the dimensions of ethanol, βCD and γCD cavities are too wide to capture this molecule [234]. Imprinted poly (βCD) has been designed for detection of creatinine [228]. To investigate whether the binding of creatinine βCD was due to hydrogen bonds or hydrophobic interactions, they capped the hydroxyl groups on the βCD molecules with chlorotrimethylsilane (CTMS). After capping the hydroxyl groups, the creatinine adsorption decreased significantly suggesting the

binding of creatinine to βCD was caused mainly from hydrogen bonds. Similarly, hydrogen bonds were responsible for the interactions between βCD and glycine [73]. Also, the amino and carboxylic groups of arginine form hydrogen bond interactions with hydroxyl groups of hydroxypropyl-βCD [235,236].

Due to complex pathophysiology of sepsis, combining data from multiple biomarkers improves sensitivity and selectivity of diagnostic tools. Accordingly, various cyclodextrin surfaces can be integrated to create a sensor array (impedimetric tongue) for recognition of sepsis metabolite markers. The cyclodextrin impedimetric tongue that we developed in this Chapter consists of 5 stable diazonium salt based α cyclodextrin (αCD), β cyclodextrin (βCD), γ cyclodextrin (γCD), hydroxypropyl-β cyclodextrin (HP-βCD), and hydroxypropyl-γ cyclodextrin (HP-γCD) surfaces. We employed these surfaces to measure the change in different EIS parameters at different frequencies in response to four different sepsis biomarkers including cortisol, glucose, fumarate, and creatinine in PBS buffer (**Figure 1.9B**).

Table 5.2. Urinary sepsis metabolite biomarkers and cyclodextrin interactions

Metabolite Biomarker	Trend in Septic Patients	Cyclodextrin Interaction	Ref.
Creatinine	Decrease	βCD (hydrogen bonds)	[228]
Acetone	Increase	αCD (inclusion complex)	[229]
Glucose	Increase	αCD (inclusion complex)	[230]
		αCD and βCD (inclusion complex)	[231]
Acetate	Increase	αCD (inclusion complex)	[232]
Glycine	Increase	βCD (hydrogen bonds)	[73]
Fumarate	Increase	hydroxypropyl-βCD (inclusion complex)	[233]
Ethanol	Increase	αCD (inclusion complex)	[234]
Arginine	Decrease	hydroxypropyl-βCD (hydrogen bonds)	[235,236]

5.2 Immobilization of βCD, γCD, HP-βCD, and HP-γCD on GC-carboxyphenyl-PPG

The GC-carboxyphenyl-PPG surfaces were prepared by electrografting of 4-carboxyphenyl diazonium salt on gassy carbon (Section 4.3) following the PPG attachment according to Section 4.4. The GC-carboxyphenyl-PPG surfaces were then immersed in 5 mM solutions of βCD, γCD, HP-βCD, and HP- γCD to prepare GC-carboxyphenyl-PPG: βCD, GC-carboxyphenyl-PPG: γCD, GC-carboxyphenyl-PPG: HP-βCD, and GC-carboxyphenyl-PPG: HP-γCD, respectively.

5.3 GC-carboxyphenyl-PEG modification and immobilization of αCD

In Chapter 3 we showed that a PEG polymer surface can be used as a support for αCD molecules and we modified a gold surface by PEG-12-Thiol to covalently bond with gold surface. In Chapter 4 we showed the carbon-carbon covalent bonds are stronger than gold-thiol bonds and we can improve the stability of our cyclodextrin surfaces by grafting 4-carboxyphenyl diazonium salt on gassy carbon instead of using a gold-thiol surface. To develop a GC-carboxyphenyl-PEG surface we first performed the 4-carboxyphenyl diazonium salt reduction on glassy carbon electrode (Section 4.3). Then, the carboxylic acid groups were activated using EDC/NHS chemistry (Section 4.4) and the surface was incubated in Carboxy-PEG12-Amine (MW 617.72) (5 mg PEG/ 10 mL PBS) solution for 30 min. To deactivate excess reactive groups, the surface was immersed in 1 M ethanolamine solution in PBS for 10 min. The long-term stability of GC-carboxyphenyl-PEG surface was investigated according to Section 4.8. The GC-carboxyphenyl-PEG surface was incubated in 5 mM αCD solution for 1 hr. to immobilize αCD on the surface.

5.4 Modification and Long-term Stability of GC-carboxyphenyl-PEG surface

Figure 5.1 demonstrates the changes in charge transfer resistance of the glassy carbon surface (≈70 Ω) by attachment of carboxyphenyl groups (≈282 kΩ) followed by modification of the surface with PEG (≈85 kΩ). While **Figure 5.1** shows that the electrografting of 4-carboxyphenyl diazonium salt on the glassy carbon resulted the 282 kΩ charge transfer resistance (N=3); in **Figure 4.5C**, we showed that the 4-carboxyphenyl surface had about 46 kΩ charge transfer resistance (N=3). To understand the reason for the discrepancy between the charge transfer resistance values shown in **Figures 5.1** and **4.5C**, we showed the cyclic voltammograms of electrochemical grafting of carboxyphenyl groups on all electrodes in **Figure 5.2** and **5.3**, respectively. Both **Figure 5.2** and **5.3** show the characteristic cathodic peak in the first cycle (green lines) due to the formation of carboxyphenyl layer. Also, in both Figures the reduction peak disappears in the third cycle (blue lines) due to the blocking effect of carboxyphenyl layer. However, the presence and intensity of the cathodic peak in the second cycle (red lines) is different in different plots (stronger reduction peak in the second cycle in electrodes in **Figure 5.2** and weaker reduction peak in the second cycle in electrodes in **Figure 5.3**). Besides, the cathodic current in **Figure 5.3** becomes as high as 14 μA at -0.6 V vs. Ag/AgCl (Electrode 6), whereas in **Figure 5.2** the cathodic current only reaches to the maximum of 12.4 μA at -0.6 V vs. Ag/AgCl (Electrode 4). Therefore, the charge densities of the carboxyphenyl groups in **Figure 5.3** (Electrode 6, 7, and 8) are different from the surfaces in **Figure 5.2** (Electrode 1, 3, and 4).

Figure 5.1 demonstrates that attachment of PEG molecules on the carboxyphenyl surface increases the charge transfer resistance. The changes in surface charges or conformational

properties of the surface may provide faster electron transfer rates for redox reactions. Finally, **Figure 5.1** shows that the charge transfer resistance of the GC-carboxyphenyl-PEG surface remains constant (no statistically relevant changes) for at least 5 weeks indicating that the GC-carboxyphenyl-PEG surface can be used as a stable support for αCD molecules.

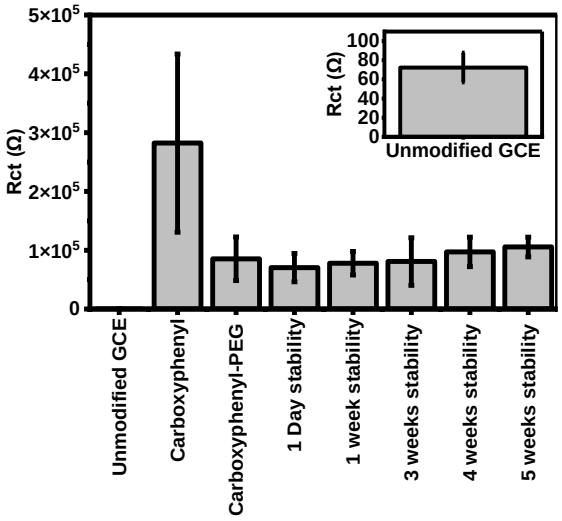

Figure 5.1. Surface modification and stability test of GC-carboxyphenyl-PEG surfaces for a period of 5 weeks. Electrodes were stored in UHP water in-between stability tests; stability testing was conducted in 20 mM ferri/ferrocyanide in UHP. Error bars indicate the standard deviation of three independent surfaces (N=3).

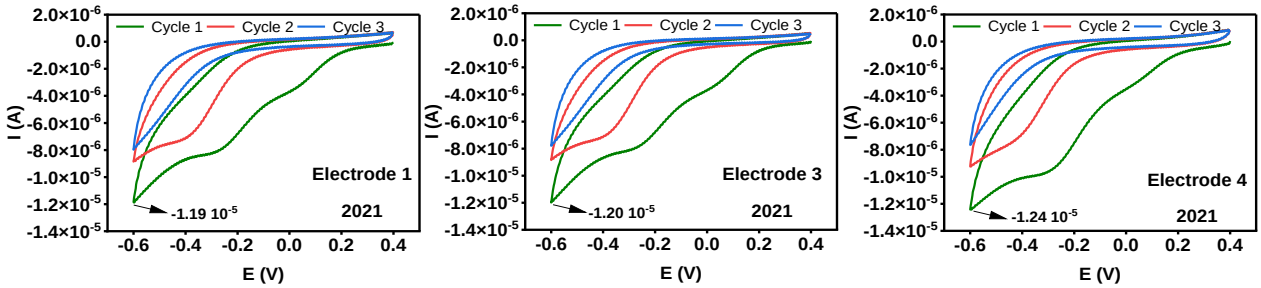

Figure 5.2. Cyclic voltammograms of electrochemical grafting of carboxyphenyl groups on glassy carbon electrodes (electrode 1, 3, and 4) in 4-carboxyphenyl diazonium salt solution from +0.4 to -0.6 vs. Ag/AgCl at scan rate of 100 mV s^{-1}. These electrodes were used to generate the data in Figure 4.5C.

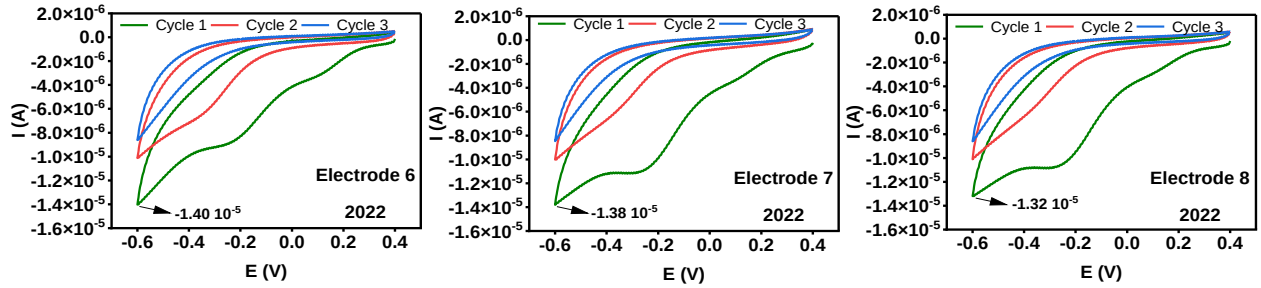

Figure 5.3. Cyclic voltammograms of electrochemical grafting of carboxyphenyl groups on glassy carbon electrodes (electrode 6, 7, and 8) in 4-carboxyphenyl diazonium salt solution from +0.4 to -0.6 vs. Ag/AgCl at scan rate of 100 mV s^{-1}. These electrodes were used to generate the data in Figure 5.1.

5.5 Cortisol, Glucose, Fumarate, and Creatinine Detection and Control in PBS

The concentrated cortisol (3.01 µM), glucose (5.48 µM), creatinine (9.95 µM), and fumarate (39.36 µM) stock solutions in PBS (pH 7.4) were prepared. To measure the changes in the EIS parameters in response to the 100.02 nM creatinine concentration, the cyclodextrin surface were first incubated in 20 mL blank PBS and the EIS was run after 5 min to determine the baseline. Then 203 µL creatinine stock solution was added to the blank PBS and the EIS was run after 5 min. The normalized changes in real impedance ($\frac{Z'-Z'_0}{Z'_0}\times 100$), imaginary impedance ($\frac{Z''-Z''_0}{Z''_0}\times 100$), magnitude of impedance ($\frac{|Z|-|Z_0|}{|Z_0|}\times 100$), phase angle ($\frac{\Phi-\Phi_0}{\Phi_0}\times 100$), and imaginary capacitance ($\frac{C''-C''_0}{C''_0}\times 100$) were used for data analysis. These experiments were done for all 5 αCD, βCD, γCD, HP-βCD, and HP-γCD surfaces independently. Similar experiments were conducted to measure the EIS signals to 100.14 nM glucose, 100.13 nM fumarate, and 100.05 nM cortisol by addition of 372 µL glucose, 51 µL fumarate, and 687 µL cortisol stock solutions to 20 mL blank PBS, respectively. Finally, the control experiments in PBS were done by adding 328 µL PBS to 20 mL blank PBS, because the dilution of the solution can decouple cyclodextrin molecules from the surface. **Table 5.3** shows the detailed information of the experiments that were done to collect the data for this Chapter and in total, 390 EIS experiments were performed. We tried to minimize the effects of electrode variability (Electrode 1-5), carboxyphenyl-PPG modification (Mod. 1-8), carboxyphenyl-PEG modification (Mod 1-5), and cyclodextrin surface regeneration (CD 1-12) on separation and classification results.

Table 5.3. Summary of experiments to evaluate the cyclodextrin impedimetric tongue performance

Row No.	Analyte	αCD	βCD	γCD	HP-βCD	HP-γCD
1	Creatinine_Oct_CD1	Electrode 2 PEG Mod. 1	Electrode 1 PPG Mod. 1	Electrode 2 PPG Mod. 1	Electrode 3 PPG Mod. 1	Electrode 4 PPG Mod. 1
2	Creatinine_Oct_CD2	Electrode 2 PEG Mod. 1	Electrode 1 PPG Mod. 1	Electrode 2 PPG Mod. 1	Electrode 3 PPG Mod. 1	Electrode 4 PPG Mod. 1
3	Creatinine_Oct_CD3	Electrode 2 PEG Mod. 1	Electrode 1 PPG Mod. 1	Electrode 2 PPG Mod. 1	Electrode 3 PPG Mod. 1	Electrode 4 PPG Mod. 1
4	Creatinine_Oct_CD4	Electrode 2 PEG Mod. 1	Electrode 1 PPG Mod. 1	Electrode 2 PPG Mod. 1	Electrode 3 PPG Mod. 1	Electrode 4 PPG Mod. 1
5	Creatinine_May_CD1	Electrode 5 PEG Mod. 3	Electrode 1 PPG Mod. 6	Electrode 2 PPG Mod. 6	Electrode 3 PPG Mod. 6	Electrode 4 PPG Mod. 6
6	Creatinine_May_CD5	Electrode 5 PEG Mod. 3	Electrode 1 PPG Mod. 6	Electrode 2 PPG Mod. 6	Electrode 3 PPG Mod. 6	Electrode 4 PPG Mod. 6
7	Creatinine_May_CD9	Electrode 5 PEG Mod. 3	Electrode 1 PPG Mod. 6	Electrode 2 PPG Mod. 6	Electrode 3 PPG Mod. 6	Electrode 4 PPG Mod. 6
8	Glucose_Oct_CD1	Electrode 3 PEG Mod. 1	Electrode 1 PPG Mod. 3	Electrode 2 PPG Mod. 3	Electrode 3 PPG Mod. 3	Electrode 4 PPG Mod. 3
9	Glucose_Oct_CD2	Electrode 3 PEG Mod. 1	Electrode 1 PPG Mod. 3	Electrode 2 PPG Mod. 3	Electrode 3 PPG Mod. 3	Electrode 4 PPG Mod. 3
10	Glucose_Oct_CD3	Electrode 3 PEG Mod. 1	Electrode 1 PPG Mod. 3	Electrode 2 PPG Mod. 3	Electrode 3 PPG Mod. 3	Electrode 4 PPG Mod. 3
11	Glucose_Oct_CD4	Electrode 3 PEG Mod. 1	Electrode 1 PPG Mod. 3	Electrode 2 PPG Mod. 3	Electrode 3 PPG Mod. 3	Electrode 4 PPG Mod. 3
12	Glucose_May_CD2	Electrode 5 PEG Mod. 3	Electrode 1 PPG Mod. 6	Electrode 2 PPG Mod. 6	Electrode 3 PPG Mod. 6	Electrode 4 PPG Mod. 6
13	Glucose_May_CD6	Electrode 5 PEG Mod. 3	Electrode 1 PPG Mod. 6	Electrode 2 PPG Mod. 6	Electrode 3 PPG Mod. 6	Electrode 4 PPG Mod. 6
14	Glucose_May_CD10	Electrode 5 PEG Mod. 3	Electrode 1 PPG Mod. 6	Electrode 2 PPG Mod. 6	Electrode 3 PPG Mod. 6	Electrode 4 PPG Mod. 6
15	Fumarate_Oct_CD1	Electrode 4 PEG Mod. 1	Electrode 1 PPG Mod. 4	Electrode 2 PPG Mod. 4	Electrode 3 PPG Mod. 4	Electrode 4 PPG Mod. 4
16	Fumarate_Oct_CD2	Electrode 4 PEG Mod. 1	Electrode 1 PPG Mod. 4	Electrode 2 PPG Mod. 4	Electrode 3 PPG Mod. 4	Electrode 4 PPG Mod. 4
17	Fumarate_Oct_CD3	Electrode 4 PEG Mod. 1	Electrode 1 PPG Mod. 4	Electrode 2 PPG Mod. 4	Electrode 3 PPG Mod. 4	Electrode 4 PPG Mod. 4
18	Fumarate_Oct_CD4	Electrode 4 PEG Mod. 1	Electrode 1 PPG Mod. 4	Electrode 2 PPG Mod. 4	Electrode 3 PPG Mod. 4	Electrode 4 PPG Mod. 4
19	Fumarate_May_CD3	Electrode 5 PEG Mod. 3	Electrode 1 PPG Mod. 6	Electrode 2 PPG Mod. 6	Electrode 3 PPG Mod. 6	Electrode 4 PPG Mod. 6
20	Fumarate_May_CD7	Electrode 5 PEG Mod. 3	Electrode 1 PPG Mod. 6	Electrode 2 PPG Mod. 6	Electrode 3 PPG Mod. 6	Electrode 4 PPG Mod. 6
21	Fumarate_May_CD11	Electrode 5 PEG Mod. 3	Electrode 1 PPG Mod. 6	Electrode 2 PPG Mod. 6	Electrode 3 PPG Mod. 6	Electrode 4 PPG Mod. 6
22	Cortisol_Oct_CD1	Electrode 1 PEG Mod. 1	Electrode 1 PPG Mod. 2	Electrode 2 PPG Mod. 2	Electrode 3 PPG Mod. 2	Electrode 4 PPG Mod. 2
23	Cortisol_Oct_CD2	Electrode 1 PEG Mod. 1	Electrode 1 PPG Mod. 2	Electrode 2 PPG Mod. 2	Electrode 3 PPG Mod. 2	Electrode 4 PPG Mod. 2
24	Cortisol_Oct_CD3	Electrode 1 PEG Mod. 1	Electrode 1 PPG Mod. 2	Electrode 2 PPG Mod. 2	Electrode 3 PPG Mod. 2	Electrode 4 PPG Mod. 2

Table 5.3. Continued

25	Cortisol_Oct_CD4	Electrode 1 PEG Mod. 1	Electrode 1 PPG Mod. 2	Electrode 2 PPG Mod. 2	Electrode 3 PPG Mod. 2	Electrode 4 PPG Mod. 2
26	Cortisol_Apr_CD1	Electrode 5 PEG Mod. 2	Electrode 1 PPG Mod. 5	Electrode 2 PPG Mod. 5	Electrode 3 PPG Mod. 5	Electrode 4 PPG Mod. 5
27	Cortisol_Apr_CD2	Electrode 5 PEG Mod. 2	Electrode 1 PPG Mod. 5	Electrode 2 PPG Mod. 5	Electrode 3 PPG Mod. 5	Electrode 4 PPG Mod. 5
28	Cortisol_Apr_CD3	Electrode 5 PEG Mod. 2	Electrode 1 PPG Mod. 5	Electrode 2 PPG Mod. 5	Electrode 3 PPG Mod. 5	Electrode 4 PPG Mod. 5
29	Cortisol_May_CD4	Electrode 5 PEG Mod. 3	Electrode 1 PPG Mod. 6	Electrode 2 PPG Mod. 6	Electrode 3 PPG Mod. 6	Electrode 4 PPG Mod. 6
30	Cortisol_May_CD8	Electrode 5 PEG Mod. 3	Electrode 1 PPG Mod. 6	Electrode 2 PPG Mod. 6	Electrode 3 PPG Mod. 6	Electrode 4 PPG Mod. 6
31	Cortisol_May_CD12	Electrode 5 PEG Mod. 3	Electrode 1 PPG Mod. 6	Electrode 2 PPG Mod. 6	Electrode 3 PPG Mod. 6	Electrode 4 PPG Mod. 6
32	Blank PBS_June_CD1	Electrode 5 PEG Mod. 4	Electrode 1 PPG Mod. 7	Electrode 2 PPG Mod. 7	Electrode 3 PPG Mod. 7	Electrode 4 PPG Mod. 7
33	Blank PBS_June_CD2	Electrode 5 PEG Mod. 4	Electrode 1 PPG Mod. 7	Electrode 2 PPG Mod. 7	Electrode 3 PPG Mod. 7	Electrode 4 PPG Mod. 7
34	Blank PBS_June_CD3	Electrode 5 PEG Mod. 4	Electrode 1 PPG Mod. 7	Electrode 2 PPG Mod. 7	Electrode 3 PPG Mod. 7	Electrode 4 PPG Mod. 7
35	Blank PBS_June_CD4	Electrode 5 PEG Mod. 4	Electrode 1 PPG Mod. 7	Electrode 2 PPG Mod. 7	Electrode 3 PPG Mod. 7	Electrode 4 PPG Mod. 7
36	Blank PBS_July_CD1	Electrode 5 PEG Mod. 5	Electrode 1 PPG Mod. 8	Electrode 2 PPG Mod. 8	Electrode 3 PPG Mod. 8	Electrode 4 PPG Mod. 8
37	Blank PBS_July_CD2	Electrode 5 PEG Mod. 5	Electrode 1 PPG Mod. 8	Electrode 2 PPG Mod. 8	Electrode 3 PPG Mod. 8	Electrode 4 PPG Mod. 8
38	Blank PBS_July_CD3	Electrode 5 PEG Mod. 5	Electrode 1 PPG Mod. 8	Electrode 2 PPG Mod. 8	Electrode 3 PPG Mod. 8	Electrode 4 PPG Mod. 8
39	Blank PBS_July_CD4	Electrode 5 PEG Mod. 5	Electrode 1 PPG Mod. 8	Electrode 2 PPG Mod. 8	Electrode 3 PPG Mod. 8	Electrode 4 PPG Mod. 8

5.6 Manual Assessment of EIS Data Using Single Frequency Analysis

When listening to music, we can differentiate between different instruments that are being played at the same time since different musical instruments have a unique harmonic overtone (**Figure 5.4A**). Similarly, different solution samples have distinctive characteristic frequencies, and we can use the values of normalized changes in EIS parameters at these characteristic frequencies to differentiate between different samples. For example, **Figure 5.4B** demonstrates the characteristic frequencies of four analytes (cortisol, glucose, creatinine, and fumarate) on five cyclodextrin surfaces (αCD, βCD, γCD, HP-βCD, and HP-γCD). The characteristic frequencies in **Figure 5.4B** were calculated based on the normalized changes in imaginary capacitance ($\frac{C''-C''_0}{C''_0} \times 100$).

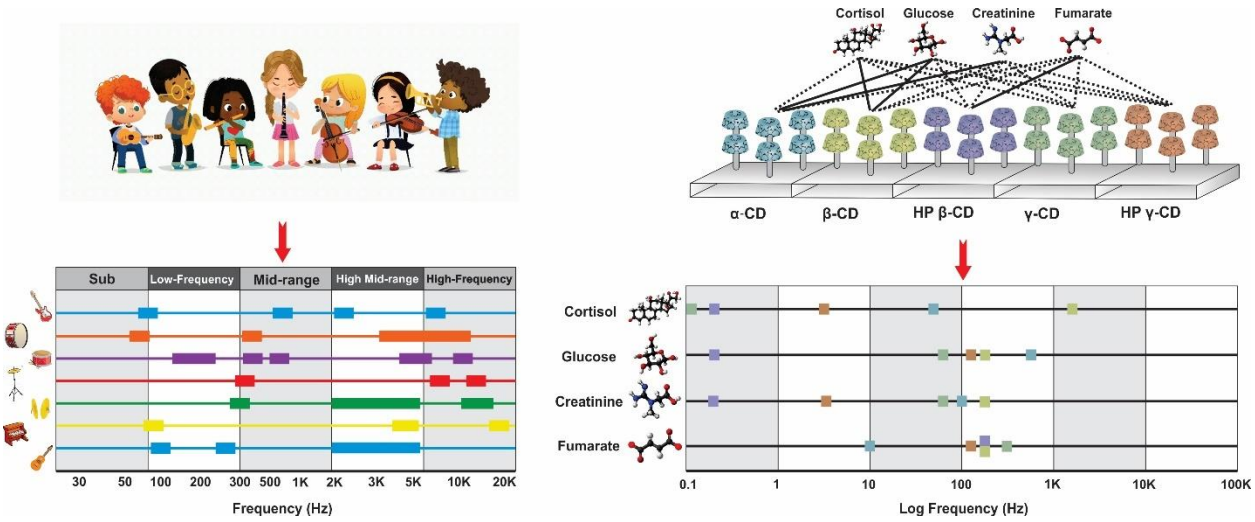

Figure 5.4. The frequency spectrum can be used to differentiate between: (A) different musical instruments (Copyright with permission from VectorStock®) and (B) different analytes in the solution

Figure 5.5 demonstrates the main four steps that we need to take to manually assess our data. First, we need to choose an EIS parameter (real impedance, imaginary impedance, magnitude of impedance, or phase angle) and find the normalized changes in that EIS parameter at all frequencies. The second step is finding the characteristic frequencies followed by finding the normalized changes in the EIS parameter at the characteristic frequencies. Finally, LDA is applied on the normalized changes in the EIS parameter at the characteristic frequencies to classify different samples.

In the following sections of this chapter, we will first discuss different methods for finding the characteristic frequencies (Step 2 in **Figure 5.5**) and then we will show the LDA classification results.

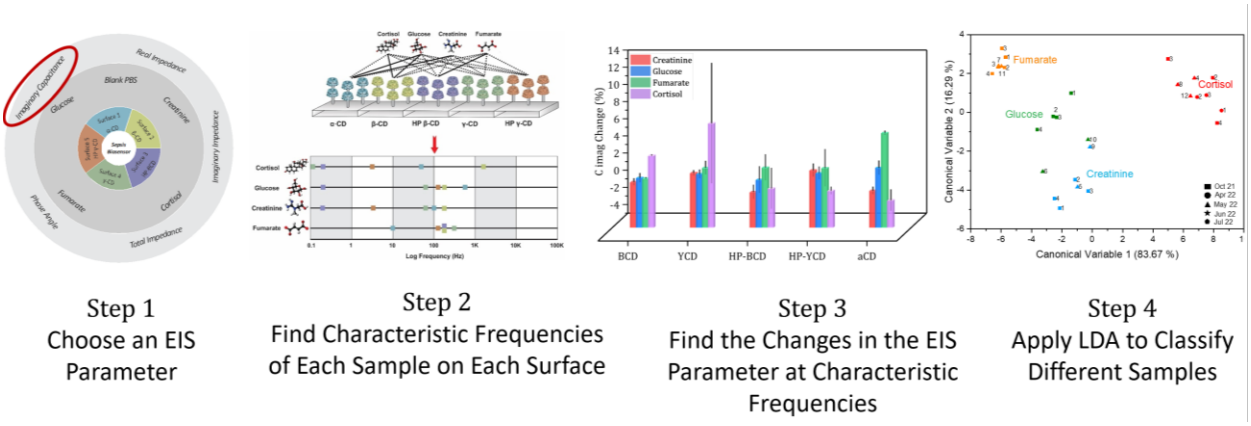

Figure 5.5. The four main steps for manual assessment of EIS data and classification of samples

5.6.1 Finding Characteristic Frequencies

To find the characteristic frequency values, we employed different methods that are shown in **Figure 5.5** and **5.6**. In the methods in **Figure 5.5** we defined the characteristics frequency of sample on surface X as the frequency with the maximum signal to noise ratio (SNR) of sample on surface X (**Equation 5.1**). However, in **Figure 5.6** methods, the characteristics frequency of sample on surface X is the frequency with the maximum ratio of the SNR of sample on surface X to SNR of blank PBS (control) on surface X (**Equation 5.2**).

$$\mathrm{SNR}_{\text{Sample on Surface X}} = \frac{\mu^2_{\text{Sample on Surface X}}}{\delta^2_{\text{Sample on Surface X}}} \qquad \text{Equation 5.1}$$

$$\frac{\mathrm{SNR}_{\text{Sample on Surface X}}}{\mathrm{SNR}_{\text{Blank PBS on Surface X}}} = \frac{\frac{\mu^2_{\text{Sample on Surface X}}}{\delta^2_{\text{Sample on Surface X}}}}{\frac{\mu^2_{\text{Blank PBS on Surface X}}}{\delta^2_{\text{Blank PBS on Surface X}}}} \qquad \text{Equation 5.2}$$

Outliers can be present in the data at some frequencies due to various reasons including, but not limited to, the measurement error (such as EIS drift), surface modification errors (such as inconsistency between different surfaces), or sampling errors (such as errors in pipetting and serial dilutions). In Method 1.1 (**Figure 5.5**) and Method 2.1 (**Figure 5.6**) we assumed that these outliers do not influence the end results and the data processing was performed without finding the outliers. However, according to literature, the presence of outliers can greatly affect the linear discriminant analysis (LDA) results [237,238]. Therefore, we further investigated the effect of removing outliers on the values for characteristic frequencies (Method 1.2 (**Figure 5.5**) and

method 2.2 (**Figure 5.6**)). The outliers were found by calculating the first quartile (QTL1), the third quartiles (QTL3), the interquartile range (IQR), lower, and upper data limits. Excel functions and equations are shown in **Equation 5.3-5.7**. All the data points that were not within these boundaries were identified as outliers.

QTL1= QUARTILE.INC (EIS data of Sample on Surface X at Frequency Y, 1) Equation 5.3

QTL3= QUARTILE.INC (EIS data of Sample on Surface X at Frequency Y,3) Equation 5.4

IQR= QTL1-QTL3 Equation 5.5

Lower limit= QTL1-1.5 IQR Equation 5.6

Upper limit=QTL3+1.5IQR Equation 5.7

In Method 1.2 (**Figure 5.6**) and Method 2.2 (**Figure 5.7**) the outliers were only removed for the purpose of finding the characteristic frequency values. Therefore, the final datasets for LDA contained all the data at characteristic frequencies including the outliers. Although, in Method 1.3 (**Figure 5.6**) and Method 2.3 (**Figure 5.7**) the outliers were deleted for finding the characteristic frequencies and were replaced with the mean values in the final datasets for LDA. Finally, in Method 1.3 (**Figure 5.6**) and Method 2.3 (**Figure 5.7**), the samples with outliers in 3 or more surfaces were completely removed from the dataset. For example, **Table 5.4** shows the final dataset for LDA using the normalized change in phase angle ($\frac{\Phi-\Phi_0}{\Phi_0} \times 100$) according to Method 1.3. The glucose data point in row 12, cortisol data points in row 22 and 29, and blank PBS data points in row 36 and 37 (highlighted with red) were deleted from the dataset since they had three or more outliers.

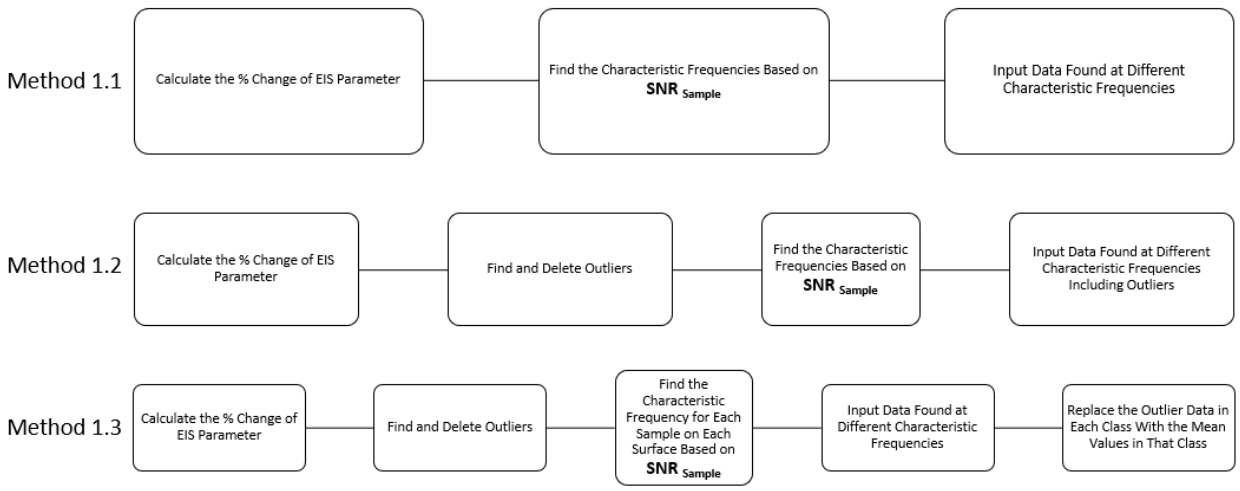

Figure 5.6. 3 different methods for pre-processing the data for LDA. The characteristic frequencies in these methods are calculated based on Equation 5.1 (maximum signal to noise ratio (SNR) of sample on surface X).

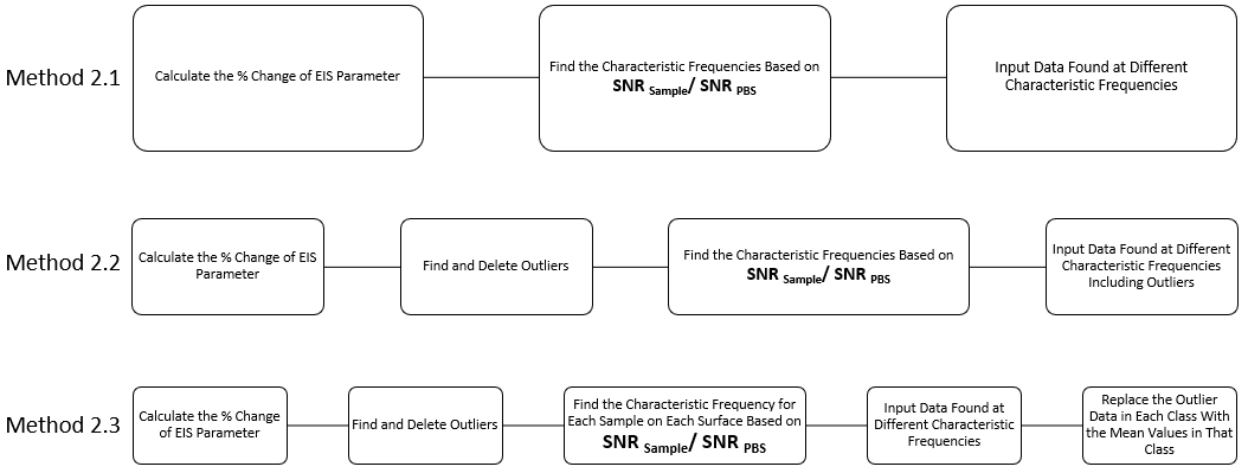

Figure 5.7. 3 different methods for pre-processing the data for LDA. The characteristic frequencies in these methods are calculated based on Equation 5.2 (maximum ratio of the SNR of sample on surface X to SNR of blank PBS (control) on surface X).

Row No.	Analytes	BCD	YCD	HP-BCD	HP-YCD	aCD
1	Creatinine_Oct_CD1	0.24	0.21	-3.80	0.38	-0.74
2	Creatinine_Oct_CD2	0.15	0.26	-4.03	0.26	-1.03
3	Creatinine_Oct_CD3	0.22	0.23	-3.61	0.34	-1.67
4	Creatinine_Oct_CD4	0.13	0.23	-3.76	0.33	-1.06
5	Creatinine_May_CD1	0.16	0.32	-3.65	0.33	-1.42
6	Creatinine_May_CD5	0.11	0.15	-3.71	0.32	-0.10
7	Creatinine_May_CD9	0.14	0.23	-3.42	0.33	-1.19
8	Glucose_Oct_CD1	0.25	-0.65	-3.71	0.23	0.18
9	Glucose_Oct_CD2	0.31	-0.47	0.26	0.19	0.18
10	Glucose_Oct_CD3	0.31	-0.57	0.21	0.20	0.31
11	Glucose_Oct_CD4	0.24	-0.54	0.20	0.21	0.19
12	Glucose_May_CD2	Outlier	Outlier	0.27	Outlier	0.05
13	Glucose_May_CD6	0.23	-0.60	0.18	0.22	0.16
14	Glucose_May_CD10	0.27	-0.61	0.23	0.20	0.17
15	Fumarate_Oct_CD1	-0.67	0.09	0.15	0.28	0.27
16	Fumarate_Oct_CD2	-0.87	0.10	0.17	0.21	0.30
17	Fumarate_Oct_CD3	-0.84	0.08	0.13	0.21	0.26
18	Fumarate_Oct_CD4	-0.92	0.09	0.20	0.17	0.23
19	Fumarate_May_CD3	-0.82	0.08	0.15	0.24	0.27
20	Fumarate_May_CD7	-0.74	0.10	0.14	0.16	0.16
21	Fumarate_May_CD11	-0.88	0.08	0.13	0.21	0.16
22	Cortisol_Oct_CD1	0.37	Outlier	Outlier	Outlier	Outlier
23	Cortisol_Oct_CD2	0.22	0.41	-1.39	-0.08	0.40

24	Cortisol_Oct_CD3	0.31	0.34	-3.32	-0.30	0.47
25	Cortisol_Oct_CD4	0.38	0.45	-2.28	-0.23	0.53
26	Cortisol_Apr_CD1	0.42	0.45	-2.96	-0.19	0.50
27	Cortisol_Apr_CD2	0.27	0.42	-1.87	-0.25	0.53
28	Cortisol_Apr_CD3	0.27	0.42	-2.30	-0.19	0.50
29	Cortisol_May_CD4	Outlier	0.45	Outlier	Outlier	Outlier
30	Cortisol_May_CD8	0.22	0.42	-0.14	-0.20	0.54
31	Cortisol_May_CD12	0.16	0.42	-2.98	-0.07	0.50
32	PBS_June_CD1	0.20	0.14	0.13	0.12	-0.90
33	PBS_June_CD2	0.31	0.13	0.10	0.10	-0.97
34	PBS_June_CD3	0.15	0.17	0.13	0.11	-0.83
35	PBS_June_CD4	0.25	0.13	0.10	0.09	-0.69
36	PBS_July_CD1	Outlier	Outlier	Outlier	Outlier	Outlier
37	PBS_July_CD2	Outlier	Outlier	Outlier	Outlier	Outlier
38	PBS_July_CD3	0.30	0.08	0.11	0.11	-0.93
39	PBS_July_CD4	0.24	0.12	0.11	0.11	-1.10

5.6.2 Classification of Samples Using Linear Discriminant Analysis (LDA)

In Section 1.5, we discussed unsupervised PCA and supervised LDA learning models for variable reduction and data visualization. Unlike PCA which combines variables to achieve maximum variation in the dataset and mostly focuses on dimensionality reduction, LDA uses a labeled (training) dataset to maximize separation between multiple classes. In this chapter, we used LDA for data analysis since our goal was to use the cyclodextrim impedimetric tongue for classification of different bioanalyte samples.

LDA was performed on the datasets that were prepared based on the Methods 1.1-2.3 (**Figures 5.6 and 5.7**) and the 5-fold cross-validation accuracies were calculated (MATLAB Classification Learner) (**Table 5.5**). In a 5-fold cross-validation, the software first divides the dataset into five equal compartments. The software uses one of the five compartments as the

test set (unlabeled) and the other four compartments as the training set (labeled). Then, it evaluates the performance of the test set and computes the model score by training the model using the training set. The software repeats this process for five times and computes the accuracy by averaging the model scores over five trials. **Table 5.5** shows that the Methods 1.1 and 2.1 models have maximum frequency of 70 %. This confirms that some kind of data pre-processing is required to remove the outliers from the datasets. The datasets that were prepared according to Methods 1.2 and 2.2 had the maximum LDA accuracy of 84.6 % and 74.2 %, respectively. The normalized change in phase angle and imaginary capacitance datasets yielded the highest accuracy by using Method 1.2 (84.6 %) and Method 2.2 (74.2 %), respectively. The LDA plot analysis of normalized changes in phase angle using Method 1.2 and the normalized changes in imaginary capacitance using Method 2.2 are demonstrated in **Figure 5.8** and **Figure 5.9**, respectively. Finally, **Table 5.5** reveals that preparing the datasets according to Methods 1.3 and 2.3 improved the accuracy of models significantly. **Figure 5.10-5.14** demonstrate the Method 1.3 characteristic frequencies (**Figure 5.10A-5.14A**), the normalized changes in the EIS parameters at different characteristic frequencies i.e., real impedance (**Figure 5.10B**), imaginary impedance (**Figure 5.11B**), impedance magnitude (**Figure 5.12B**), phase angle (**Figure 5.13B**), and imaginary capacitance (**Figure 5.14B**), and LDA classification results (**Figure 5.10C-5.14C**). Additionally, **Figure 5.15-5.19** demonstrate the Method 2.3 characteristic frequencies (**Figure 5.15A-5.19A**), the normalized changes in the EIS parameters at different characteristic frequencies i.e., real impedance (**Figure 5.15B**), imaginary impedance (**Figure 5.16B**), impedance magnitude (**Figure 5.17B**), phase angle (**Figure 5.18B**), and imaginary capacitance (**Figure 5.19B**), and LDA classification results (**Figure 5.15C-5.19C**).

Comparison between the results from **Figure 5.10-5.19** shows that depending on the method for finding the characteristic frequency (Method 1.3 vs. Method 2.3), the normalized change in phase angle (**Figure 5.13**) and normalized change in imaginary capacitance (**Figure 5.19**) are the best EIS parameters with highest accuracies that can be chosen as the feature of cyclodextrin impedimetric tongue.

We further found out that for the scope of this thesis and classification of 4-5 classes of samples, we do not necessarily need the data from all five cyclodextrin surfaces. **Figure 5.20** shows that the normalized changes in phase angle from three cyclodextrin surfaces including βCD, γCD, and HP-γCD can yield the 100 % 5-fold cross-validation accuracy. In addition, αCD and βCD are the most important surfaces when the imaginary capacitance is chosen as the feature of impedimetric tongue, and we can achieve the 5-fold cross-validation accuracy of 96.4 % by using only αCD and βCD surfaces (**Figure 5.21**).

Finally, in **Figures 5.8-5.21**, we determined a characteristic frequency for each sample on each surface. For example, **Figure 5.13B** shows that for the βCD surface we found the normalized change of phase angle of cortisol at 79 Hz, glucose at 158.36 Hz, creatinine at 19.86 Hz, fumarate at 5015.63 Hz, and PBS at 63.34 Hz. However, this method cannot be applied in classification of real unknown samples, and we need to choose a single frequency for each surface to find the changes in the EIS parameter of all analytes. Therefore, we determined a single frequency for each surface by calculating the median of characteristic frequencies of different analytes on that surface **(Figures 5.22A-5.25A)**. This single frequency feature was used to demonstrate the changes in the EIS parameters of different analytes at a single frequency on each surface **(Figures 5.22B-5.25B),** applied LDA **(Figures 5.22C-5.25C),** 5-fold cross validation accuracies, and

confusion matrices, (**Figures 5.22D-5.25D).** For example, in **Figure 5.22B** the normalized change of phase angle of different samples for the βCD, γCD, and HP-βCD surface are shown at 79 Hz. For HP-γCD and αCD surfaces, the normalized changes of phase angle are demonstrated in 505.5 and 627.8 Hz, respectively. Comparison between and the LDA plots in **Figure 5.13C** and **Figure 5.22C** shows that by using only a single frequency for each surface, the 5-fold cross validation accuracy dropped from 100 % (**Figure 5.13C**) to 50 % (**Figure 5.22C**). However, when we only used two surfaces and applied LDA on γCD at 79 Hz and αCD at 627.8 Hz (**Figure 5.23**), the 5-fold cross validation accuracy became 64 %. **Figure 5.24** shows, when we applied LDA on the normalized changes in imaginary capacitance at a single frequency for each surface, we achieved the 5-fold cross validation accuracy of 62 %. However, when we decreased the number of surfaces from five (**Figure 5.24**) to three (**Figure 5.25**), the 5-fold cross validation accuracy increased from 62 to 69 %. The confusion matrix in **Figure 5.25D** shows that while the impedimetric tongue can predict a glucose samples 100% accurately, the positive predictive percentage for cortisol, fumarate, and creatinine are 80, 67, and 55 %, respectively. We believe in future we can improve the impedimetric tongue performance and increase accuracies by optimizing the cyclodextrin surfaces and data analysis methods.

Table 5.5. LDA 5-fold cross-validation accuracy of datasets prepared by various methods using five different EIS parameters as feature of the cyclodextrin impedimetric tongue biosensor

Variables / Methods	$(\frac{Z'-Z'_0}{Z'_0}\times 100)$	$(\frac{Z''-Z''_0}{Z''_0}\times 100)$	$(\frac{\lvert Z\rvert-\lvert Z_0\rvert}{\lvert Z_0\rvert}\times 100)$	$(\frac{\Phi-\Phi_0}{\Phi_0}\times 100)$	$(\frac{C''-C''_0}{C''_0}\times 100)$
Method 1.1	59	64.1	46.2	76.9	59
Method 1.2	48.7	51.3	33.3	84.6	56.4
Method 1.3	89.20	70.03	58.30	100	80.60
Method 2.1	22.6	41.9	38.7	45.2	64.5
Method 2.2	29	61.3	22.6	48.4	74.2
Method 2.3	53.3	82.8	55.2	93.3	96.4

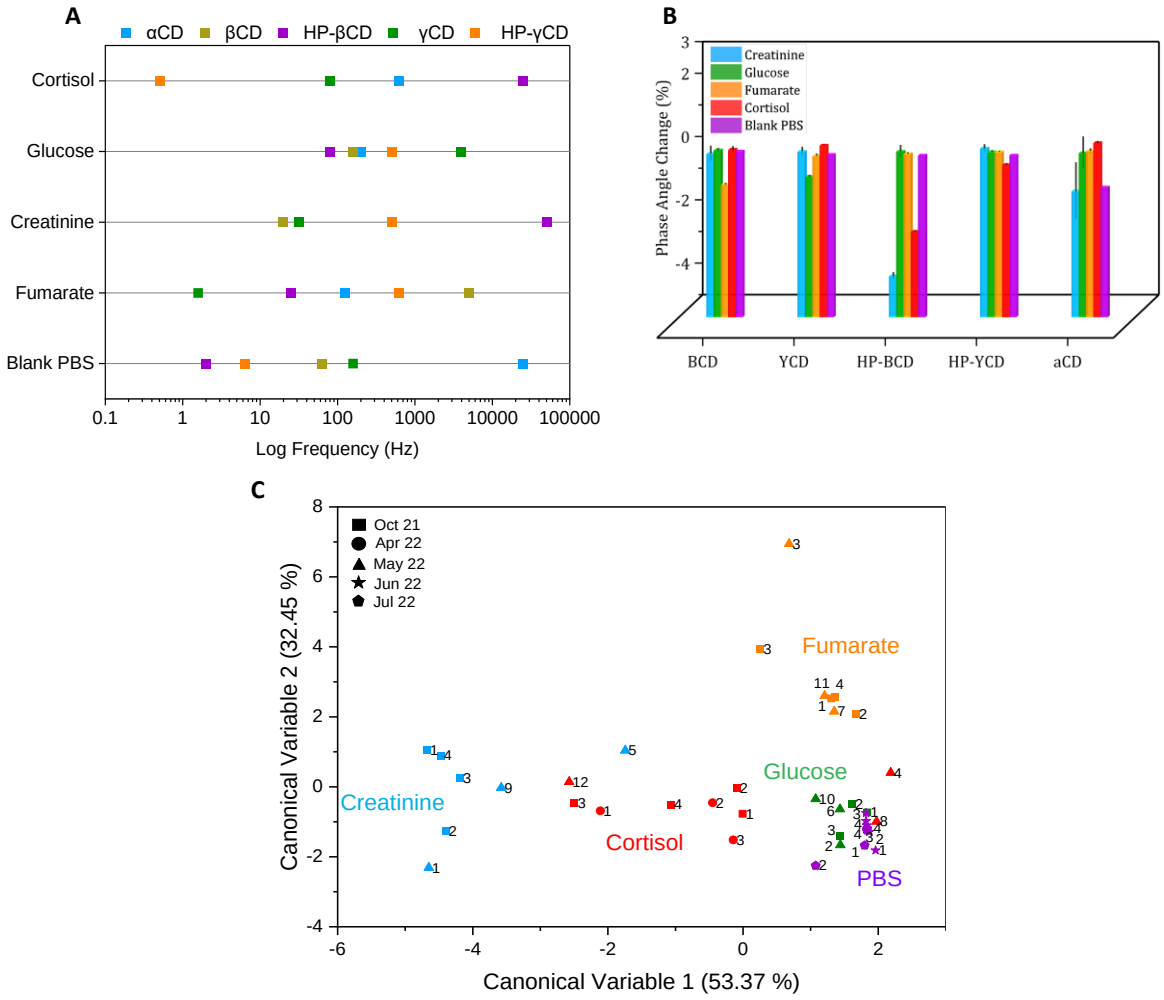

Figure 5.8. Classification of different samples using normalized change in phase angle (Method 1.2) as feature of the cyclodextrin impedimetric tongue biosensor: (A) Characteristic frequencies of different analytes on different surfaces, (B) The normalized changes in phase angle at characteristic frequencies, (C) LDA plot analysis (5-fold cross-validation accuracy: 84.6 %)

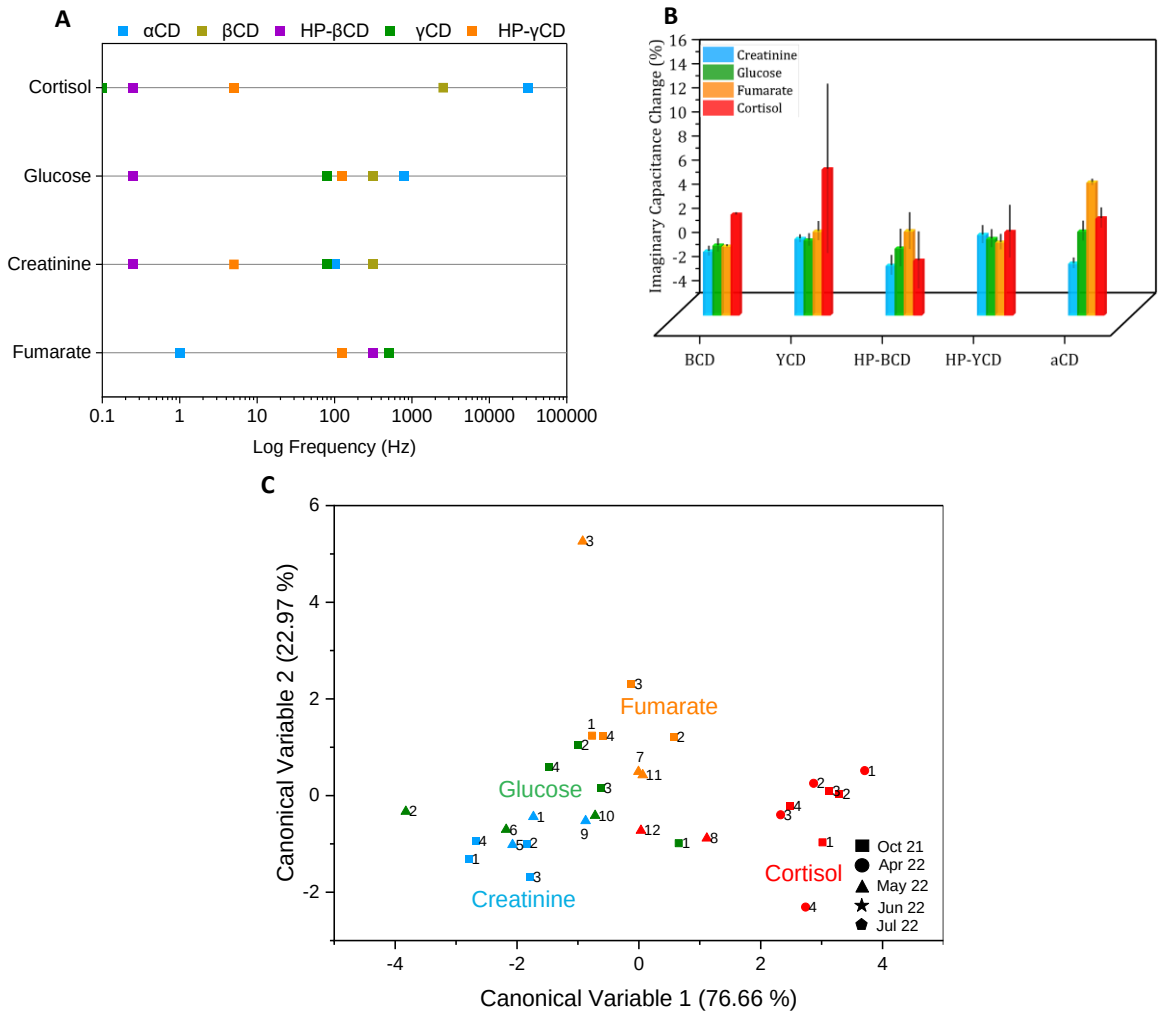

Figure 5.9. Classification of different samples using normalized change in imaginary capacitance (Method 2.2) as feature of the cyclodextrin impedimetric tongue biosensor: (A) Characteristic frequencies of different analytes on different surfaces, (B) The normalized changes in imaginary capacitance at characteristic frequencies, (C) LDA plot analysis (5-fold cross-validation accuracy: 74.2 %)

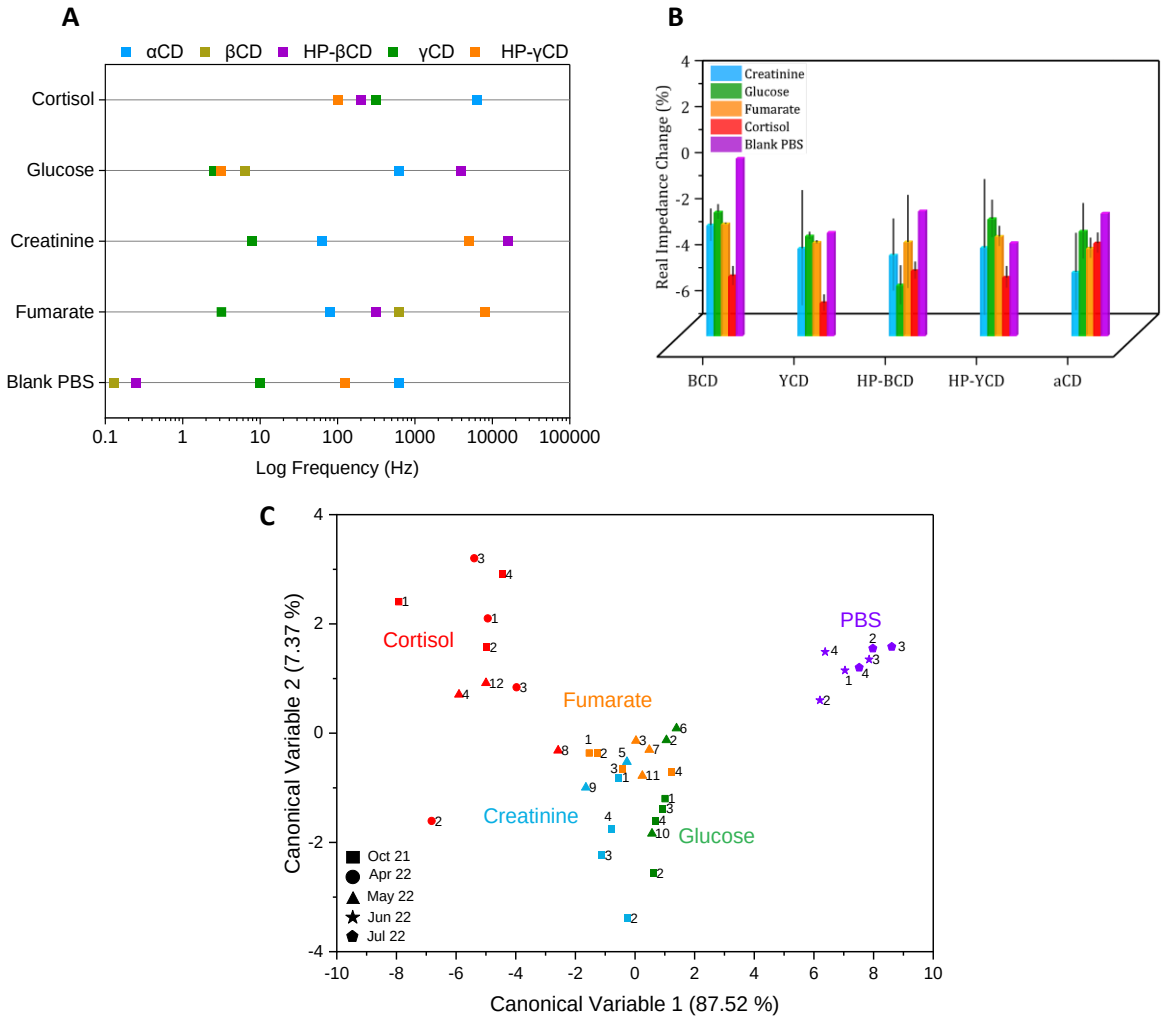

Figure 5.10. Classification of different samples using normalized change in real impedance (Method 1.3) as feature of the cyclodextrin impedimetric tongue biosensor: (A) Characteristic frequencies of different analytes on different surfaces, (B) The normalized changes in real impedance at characteristic frequencies, (C) LDA plot analysis (5-fold cross-validation accuracy: 89.2 %)

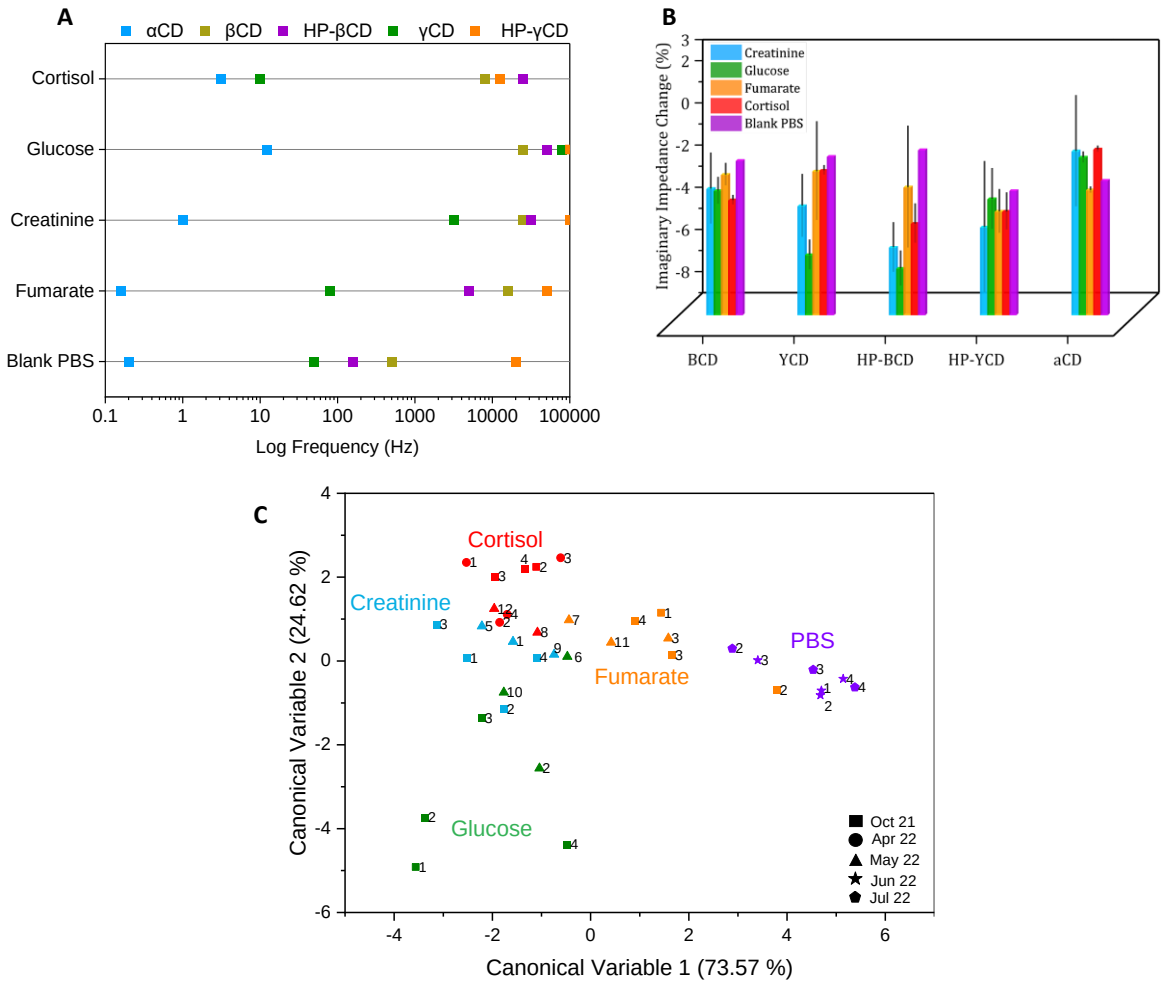

Figure 5.11. Classification of different samples using normalized change in imaginary impedance (Method 1.3) as feature of the cyclodextrin impedimetric tongue biosensor: (A) Characteristic frequencies of different analytes on different surfaces, (B) The normalized changes in imaginary impedance at characteristic frequencies, (C) LDA plot analysis (5-fold cross-validation accuracy: 70.03 %)

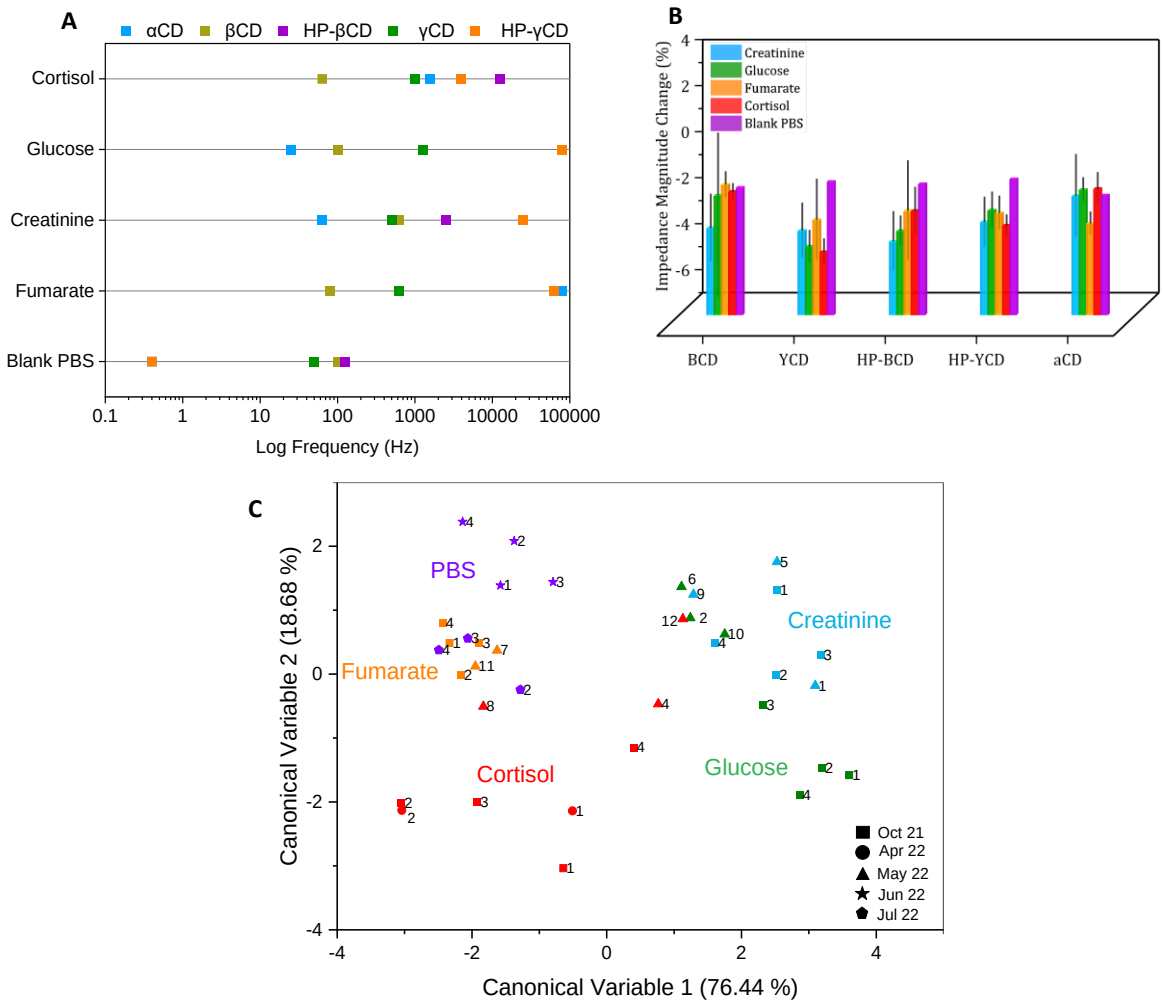

Figure 5.12. Classification of different samples using normalized change in impedance magnitude (Method 1.3) as feature of the cyclodextrin impedimetric tongue biosensor: (A) Characteristic frequencies of different analytes on different surfaces, (B) The normalized changes in impedance magnitude at characteristic frequencies, (C) LDA plot analysis (5-fold cross-validation accuracy: 58.3 %)

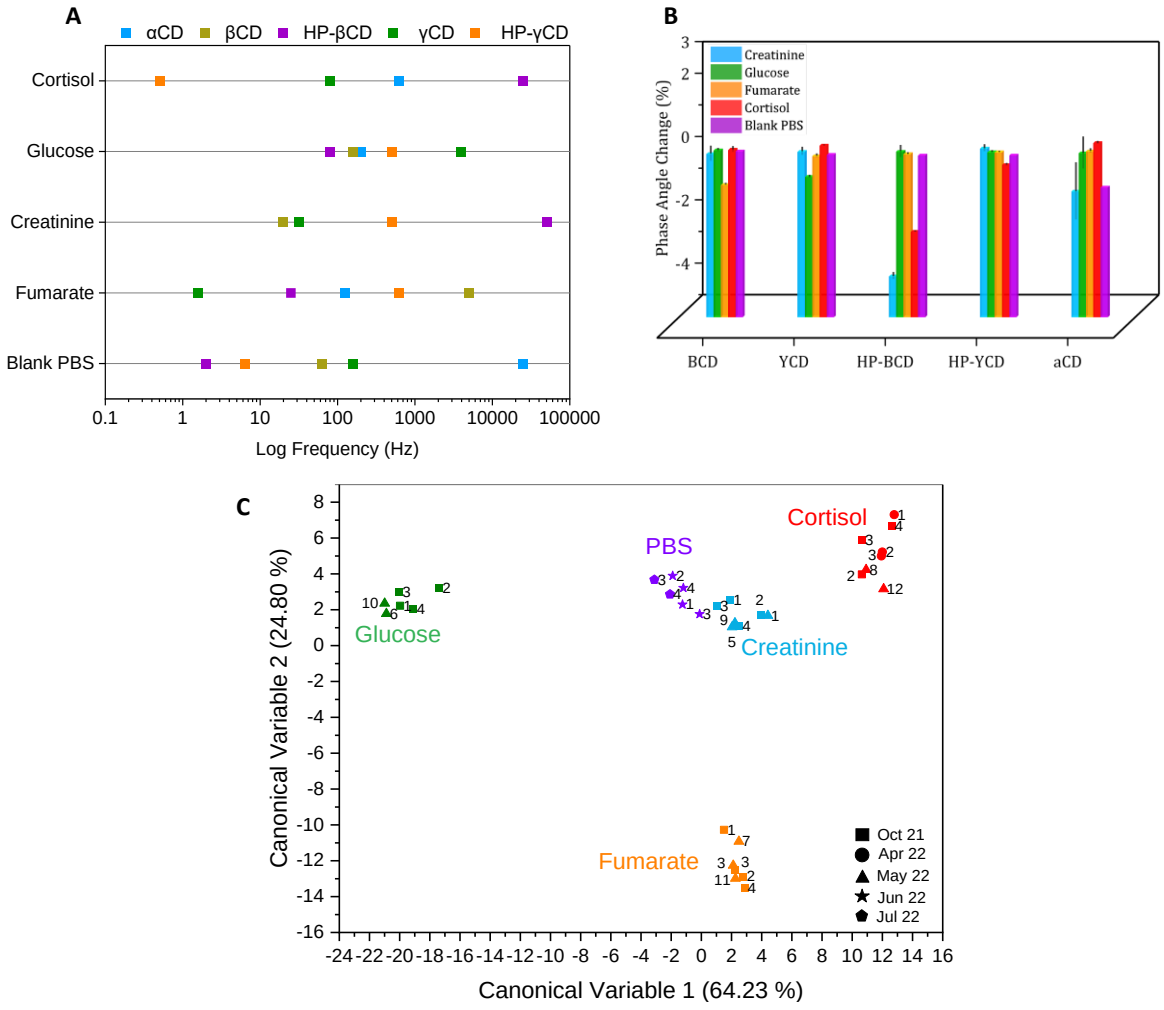

Figure 5.13. Classification of different samples using normalized change in phase angle (Method 1.3) as feature of the cyclodextrin impedimetric tongue biosensor: (A) Characteristic frequencies of different analytes on different surfaces, (B) The normalized changes in phase angle at characteristic frequencies, (C) LDA plot analysis (5-fold cross-validation accuracy: 100 %)

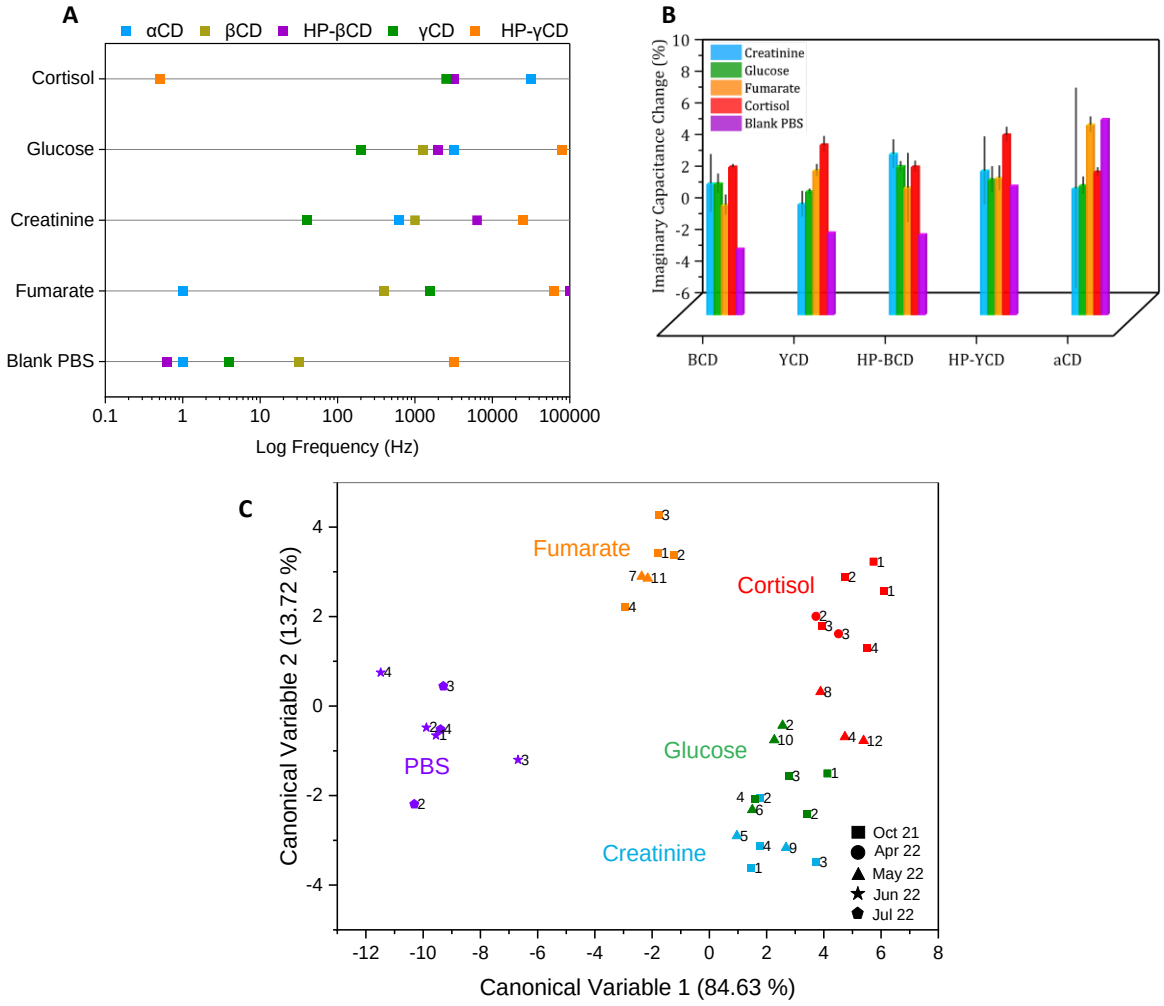

Figure 5.14. Classification of different samples using normalized change in imaginary capacitance (Method 1.3) as feature of the cyclodextrin impedimetric tongue biosensor: (A) Characteristic frequencies of different analytes on different surfaces, (B) The normalized changes in phase angle at characteristic frequencies, (C) LDA plot analysis (5-fold cross-validation accuracy: 80.6 %)

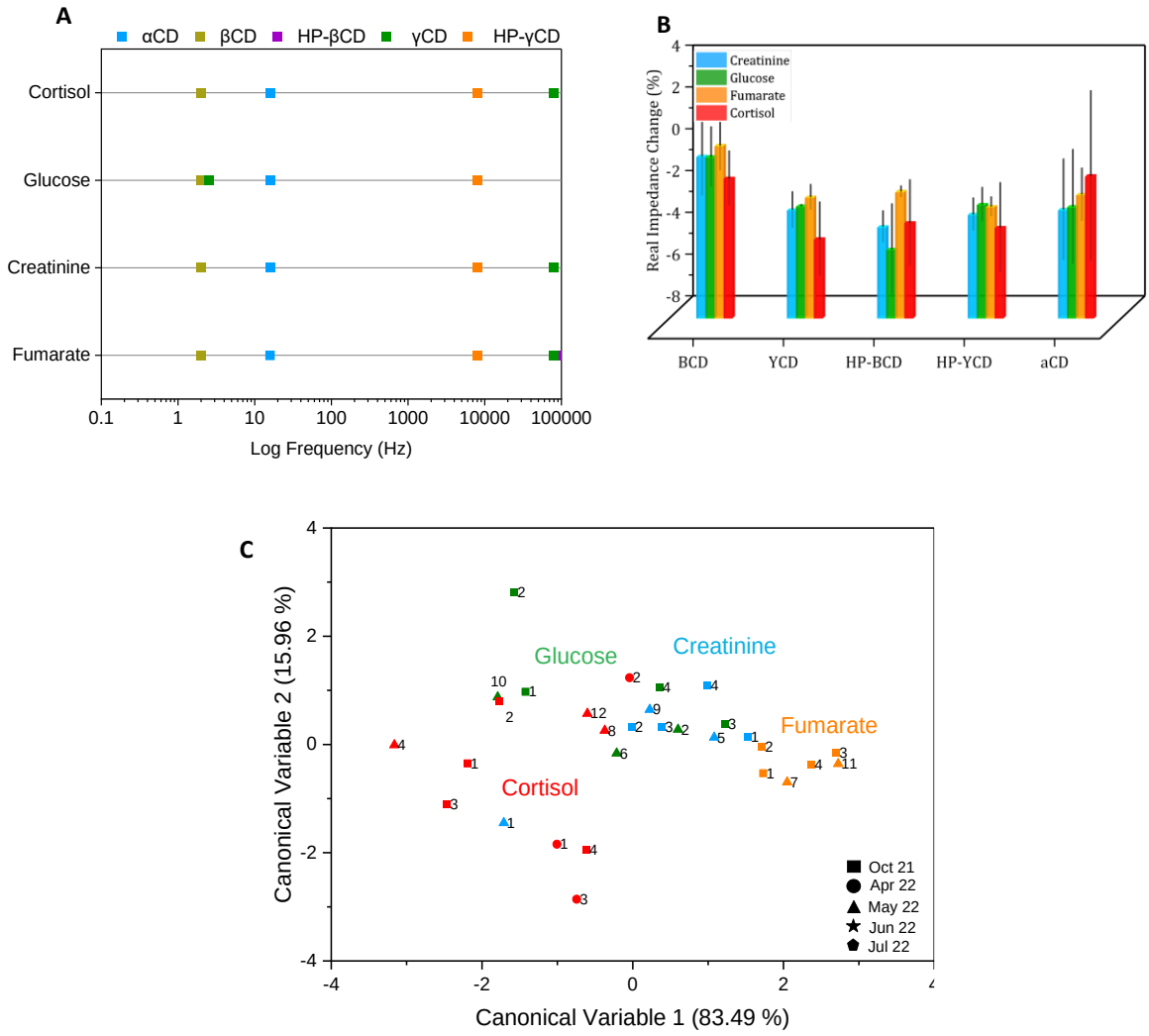

Figure 5.15. Classification of different samples using normalized change in real impedance (Method 2.3) as feature of the cyclodextrin impedimetric tongue biosensor: (A) Characteristic frequencies of different analytes on different surfaces, (B) The normalized changes in real impedance at characteristic frequencies, (C) LDA plot analysis (5-fold cross-validation accuracy: 53.3 %)

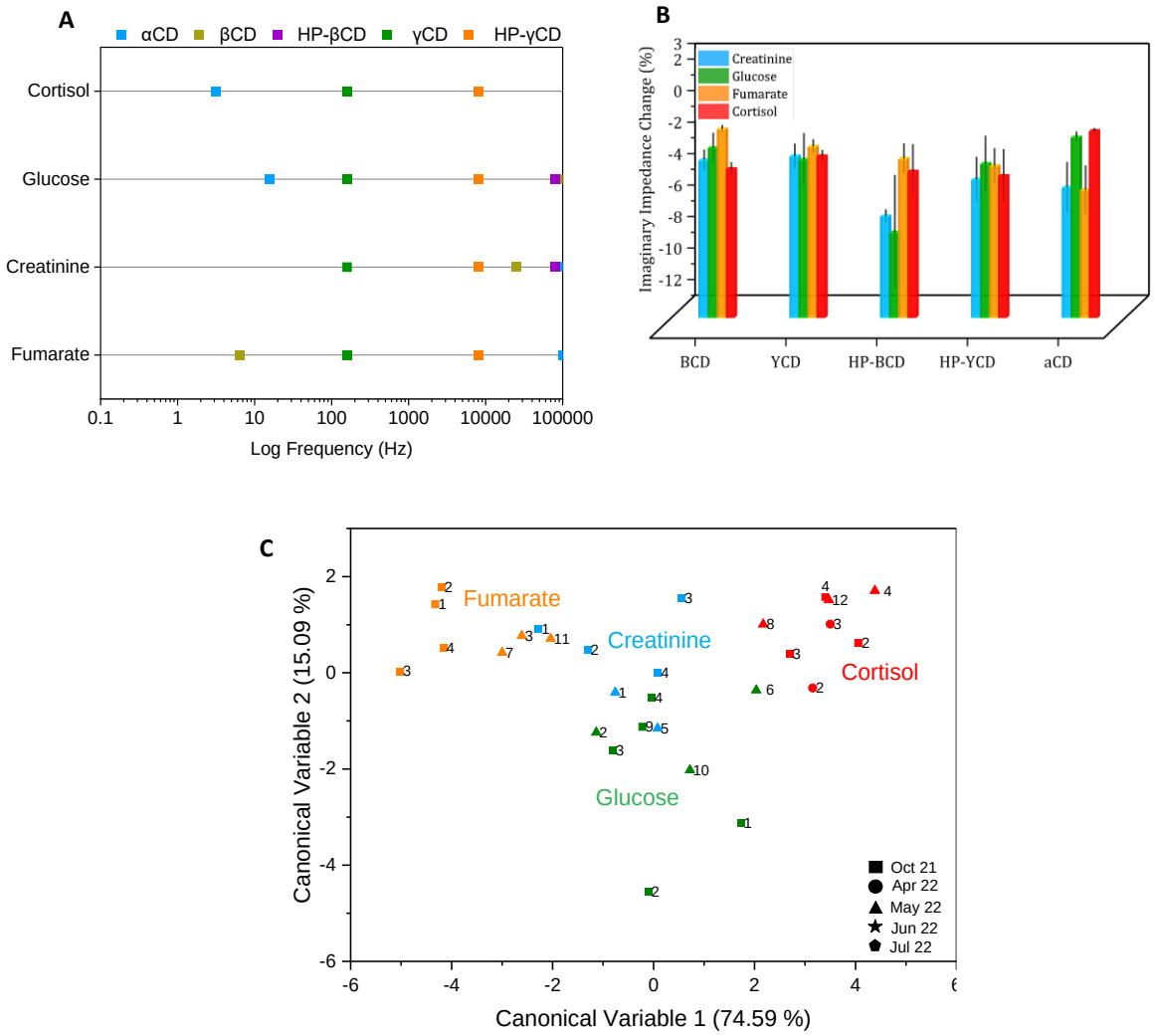

Figure 5.16. Classification of different samples using normalized change in imaginary impedance (Method 2.3) as feature of the cyclodextrin impedimetric tongue biosensor: (A) Characteristic frequencies of different analytes on different surfaces, (B) The normalized changes in imaginary impedance at characteristic frequencies, (C) LDA plot analysis (5-fold cross-validation accuracy: 82.8 %)

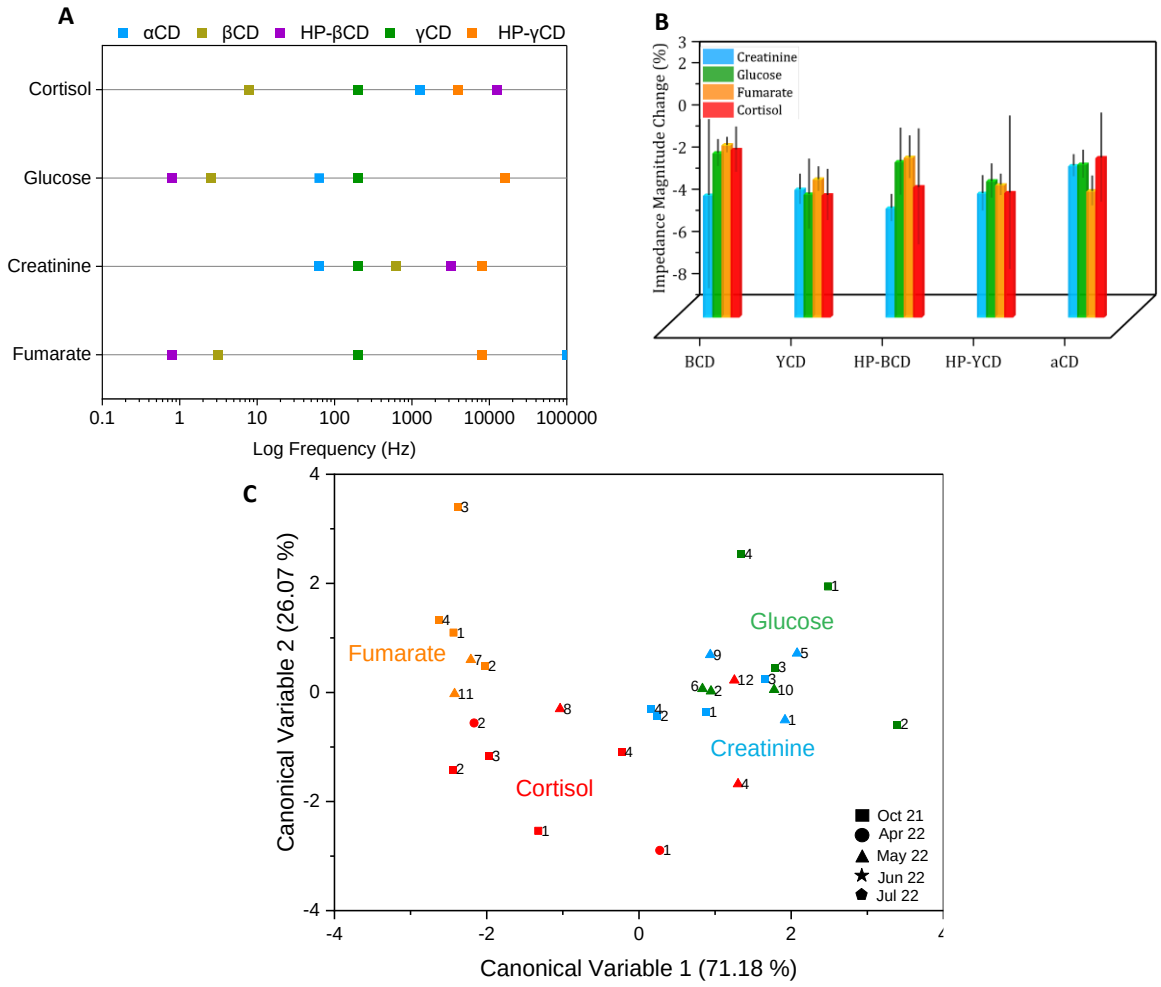

Figure 5.17. Classification of different samples using normalized change in impedance magnitude (Method 2.3) as feature of the cyclodextrin impedimetric tongue biosensor: (A) Characteristic frequencies of different analytes on different surfaces, (B) The normalized changes in impedance magnitude at characteristic frequencies, (C) LDA plot analysis (5-fold cross-validation accuracy: 55.2 %)

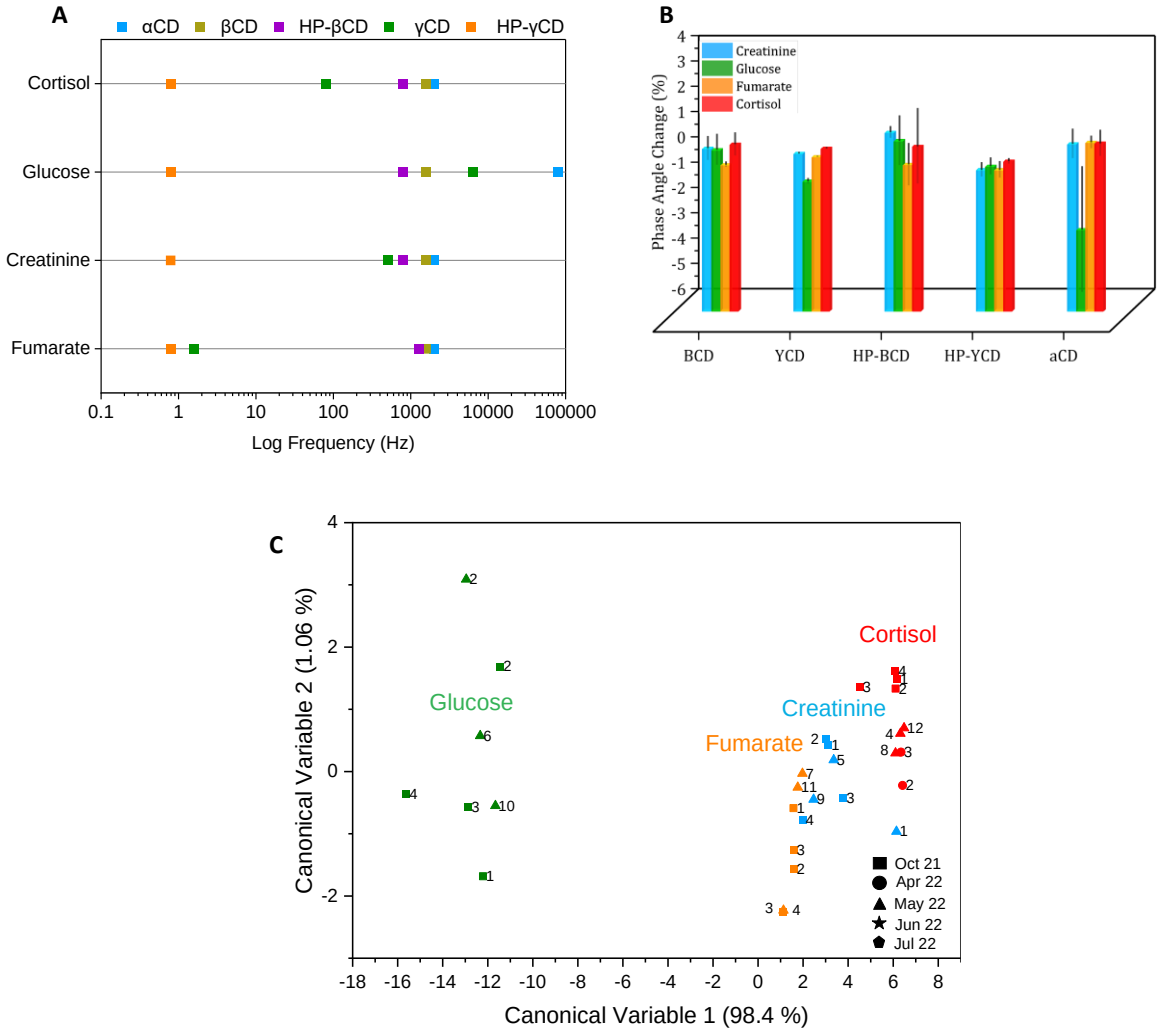

Figure 5.18. Classification of different samples using normalized change in phase angle (Method 2.3) as feature of the cyclodextrin impedimetric tongue biosensor: (A) Characteristic frequencies of different analytes on different surfaces, (B) The normalized changes in phase angle at characteristic frequencies, (C) LDA plot analysis (5-fold cross-validation accuracy: 93.3 %)

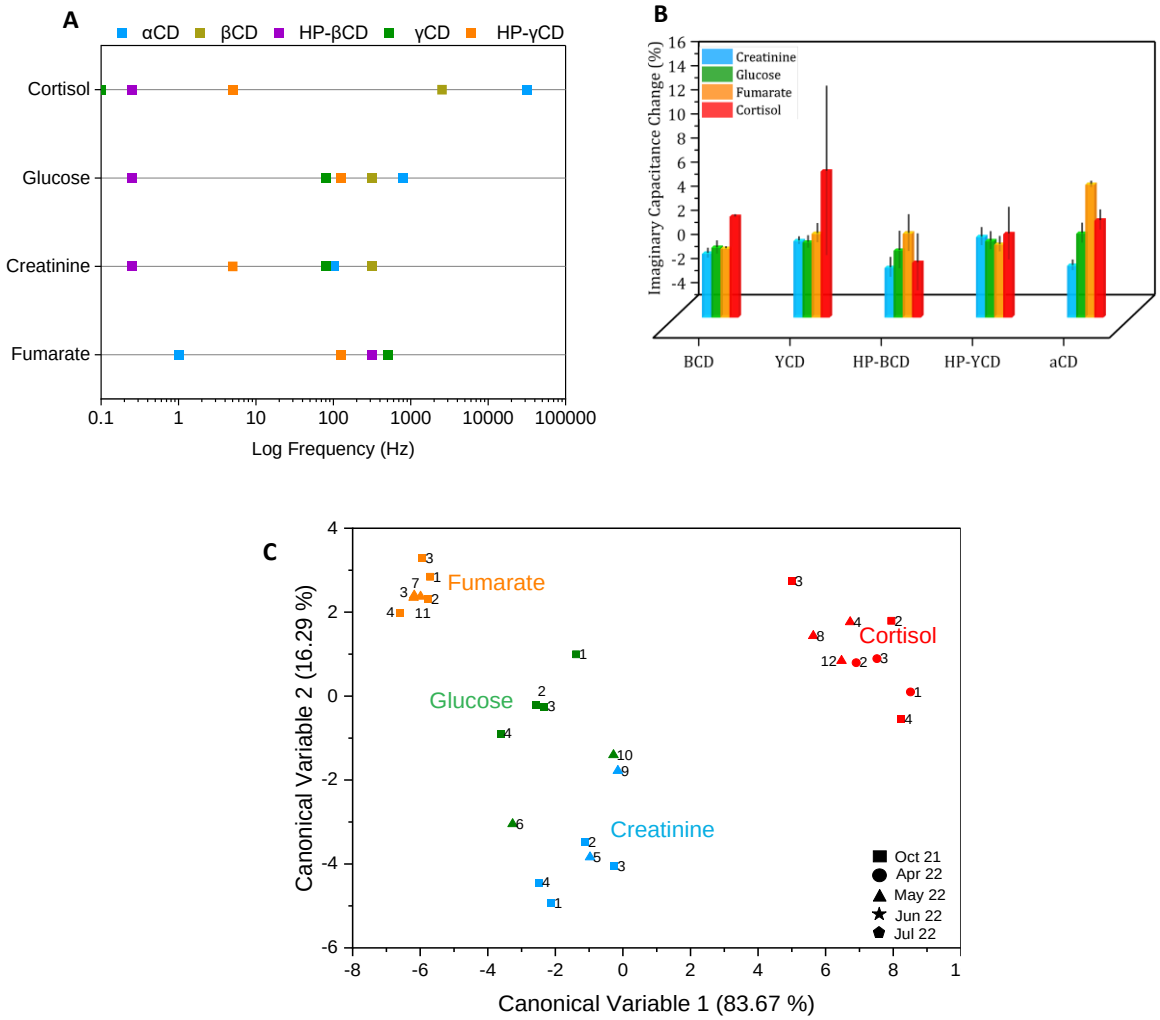

Figure 5.19. Classification of different samples using normalized change in imaginary capacitance (Method 2.3) as feature of the cyclodextrin impedimetric tongue biosensor: (A) Characteristic frequencies of different analytes on different surfaces, (B) The normalized changes in imaginary capacitance at characteristic frequencies, (C) LDA plot analysis (5-fold cross-validation accuracy: 96.4 %)

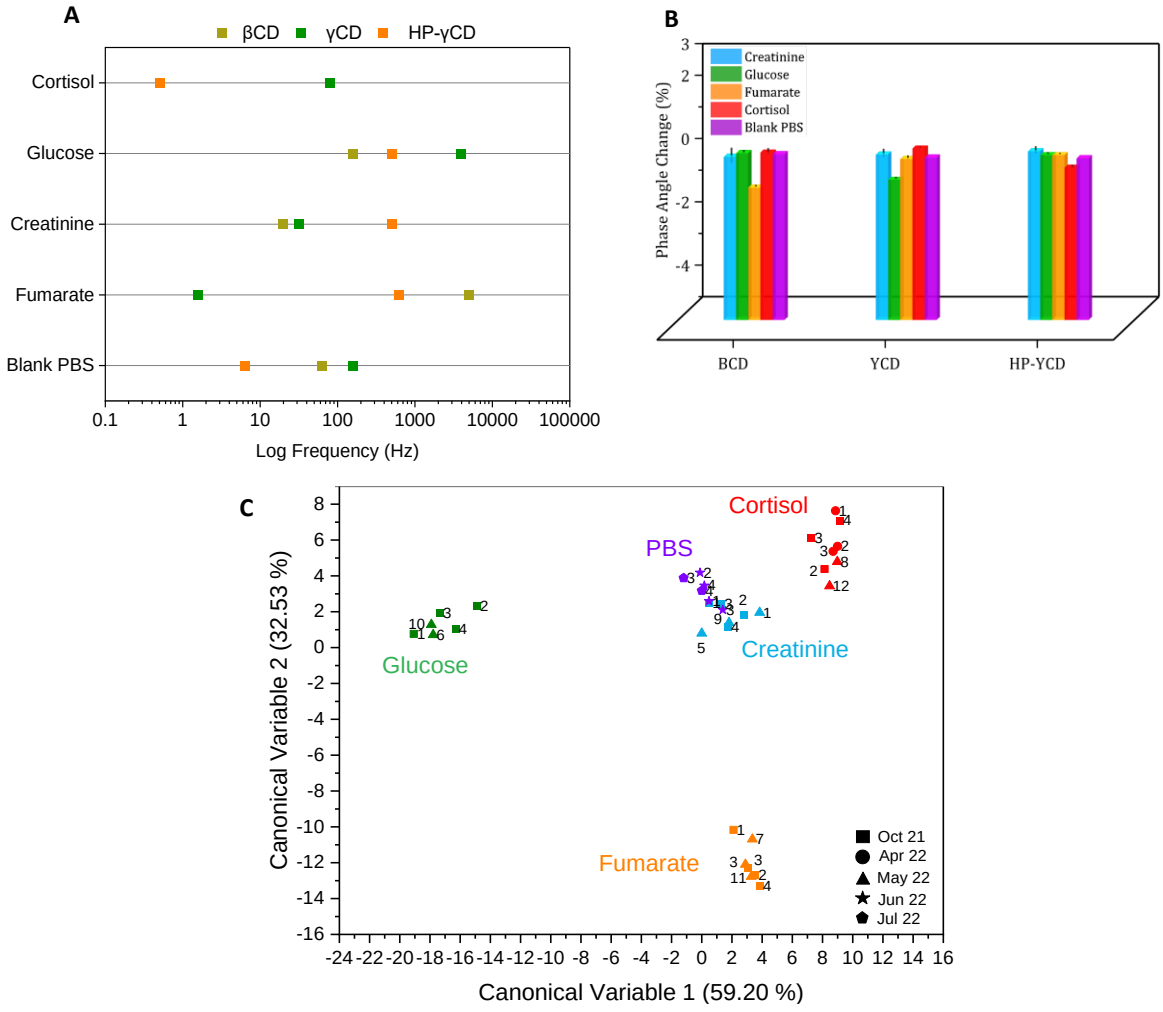

Figure 5.20. Classification of different samples using normalized change in phase angle (Method 1.3) as feature of the cyclodextrin impedimetric tongue biosensor: (A) Characteristic frequencies of different analytes on 3 different surfaces, (B) The normalized changes in phase angle at characteristic frequencies, (C) LDA plot analysis ((5-fold cross-validation accuracy: 100 %))

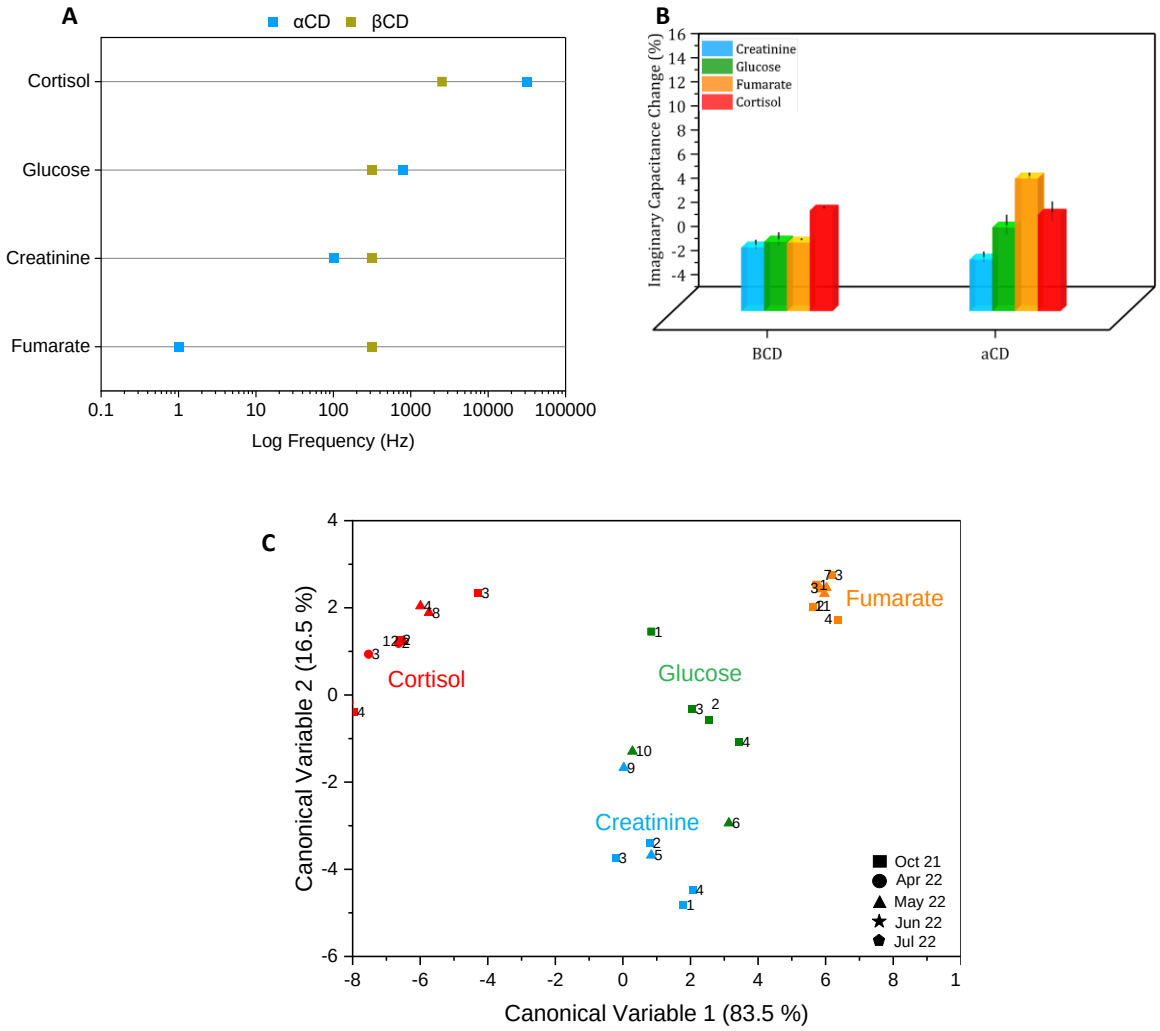

Figure 5.21. Classification of different samples using normalized change in imaginary capacitance (Method 2.3) as feature of the cyclodextrin impedimetric tongue biosensor: (A) Characteristic frequencies of different analytes on 3 different surfaces, (B) The normalized changes in imaginary capacitance at characteristic frequencies, (C) LDA plot analysis (5-fold cross-validation accuracy: 96.4 %)

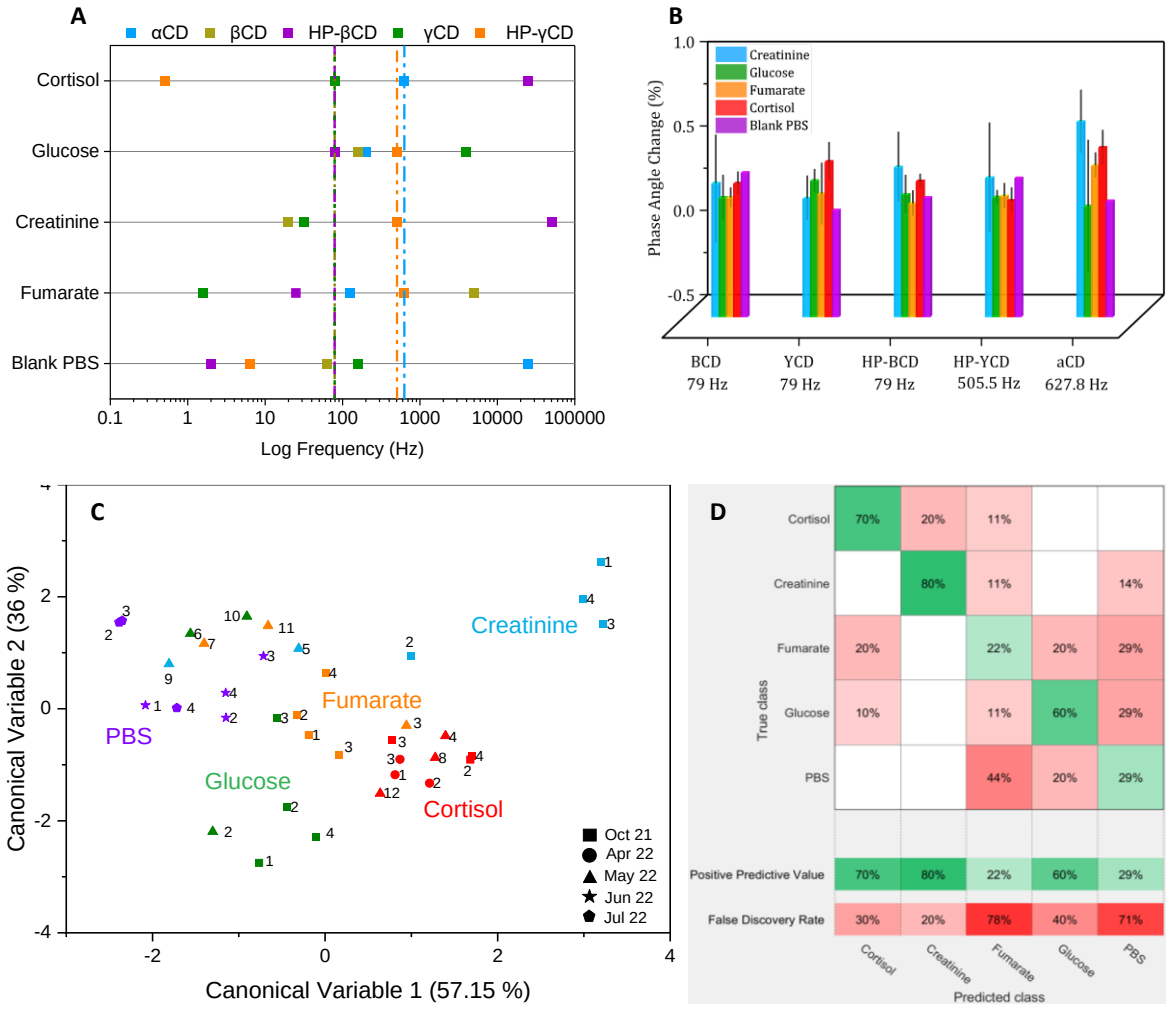

Figure 5.22. Classification of different samples using normalized change in phase angle (Method 1.3) as feature of the cyclodextrin impedimetric tongue biosensor: (A) Characteristic frequencies of different analytes on different surfaces and determination of a single frequency for each surface (i.e., βCD: 79 Hz, γCD: 79 Hz, HP-βCD: 79 Hz, HP-γCD: 505.5 Hz, and αCD: 627.8 Hz), (B) The normalized changes in phase angle of different samples on different surfaces at a single frequency, (C) LDA plot analysis (5-fold cross-validation accuracy: 50 %), (D) Confusion matrix

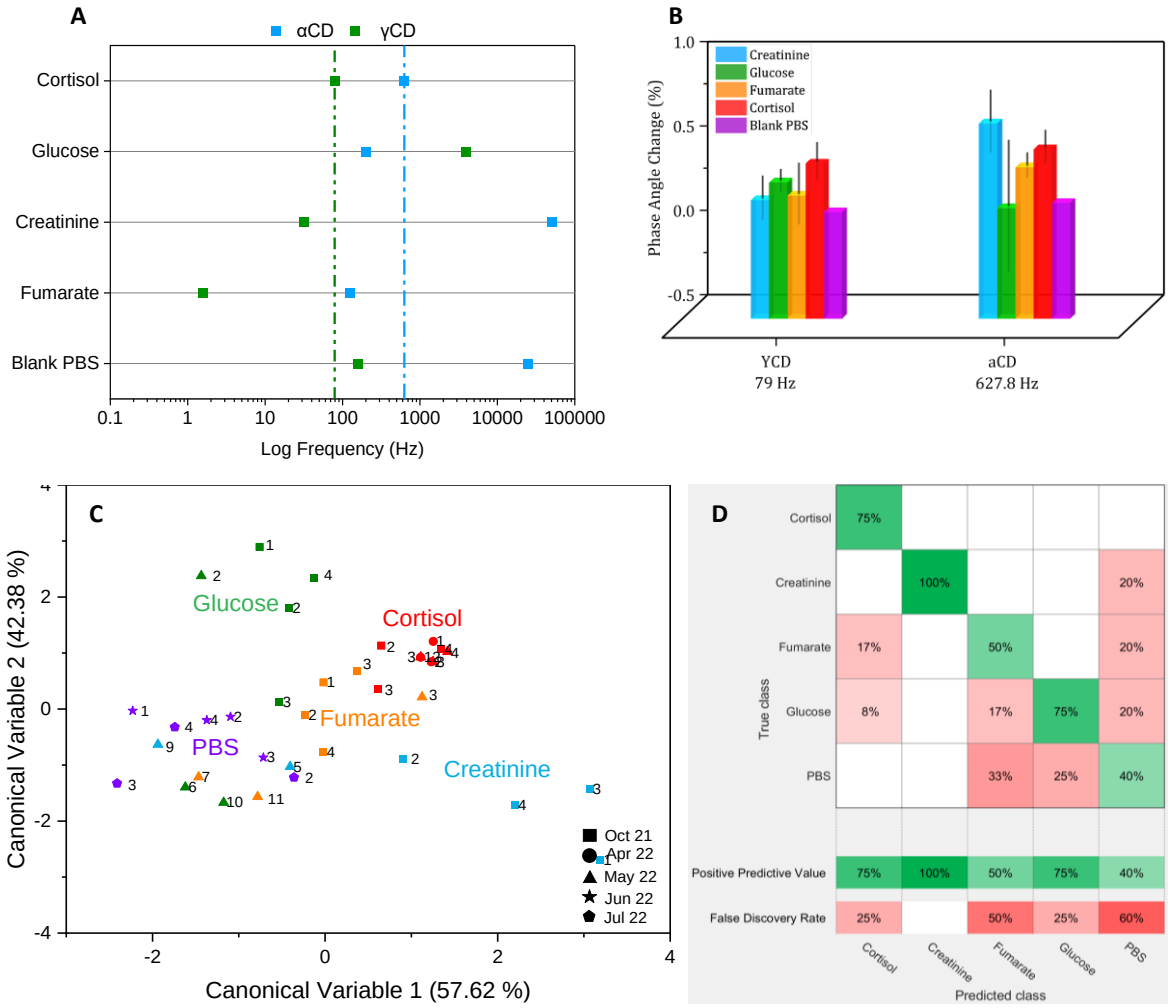

Figure 5.23. Classification of different samples using normalized change in phase angle (Method 1.3) as feature of the cyclodextrin impedimetric tongue biosensor: (A) Characteristic frequencies of different analytes on different surfaces and determination of a single frequency for each surface (i.e., γCD: 79 Hz, and αCD: 627.8 Hz), (B) The normalized changes in phase angle of different samples on different surfaces at a single frequency, (C) LDA plot analysis (5-fold cross-validation accuracy: 64 %), (D) Confusion matrix

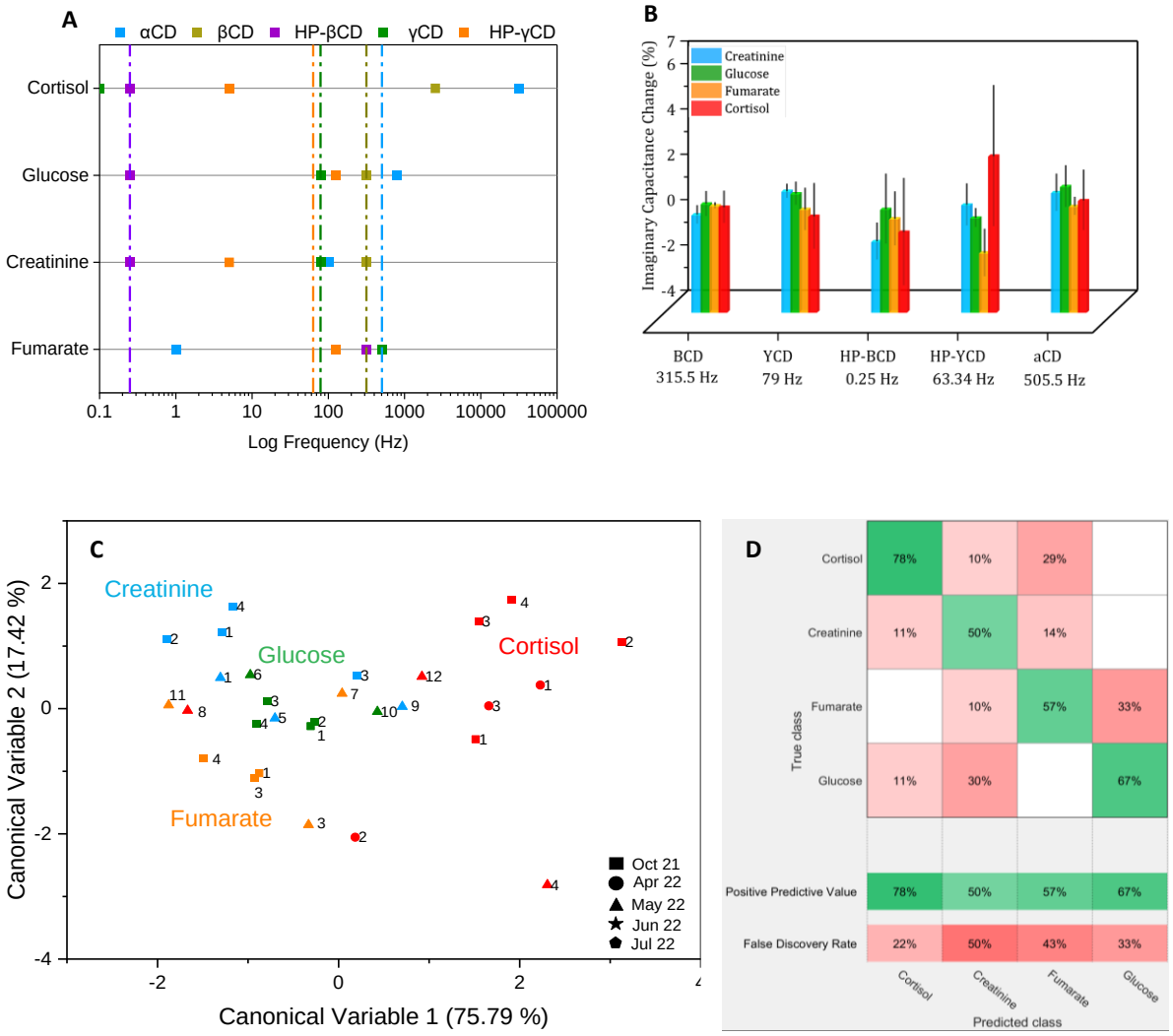

Figure 5.24. Classification of different samples using normalized change in imaginary capacitance (Method 2.3) as feature of the cyclodextrin impedimetric tongue biosensor: (A) Characteristic frequencies of different analytes on different surfaces and determination of a single frequency for each surface (i.e., βCD: 315.5 Hz, γCD: 79 Hz, HP-βCD: 0.25 Hz, HP-γCD: 63.34 Hz, and αCD: 505.5 Hz), (B) The normalized changes in imaginary capacitance of different samples on different surfaces at a single frequency, (C) LDA plot analysis (5-fold cross-validation accuracy: 62 %), (D) Confusion matrix

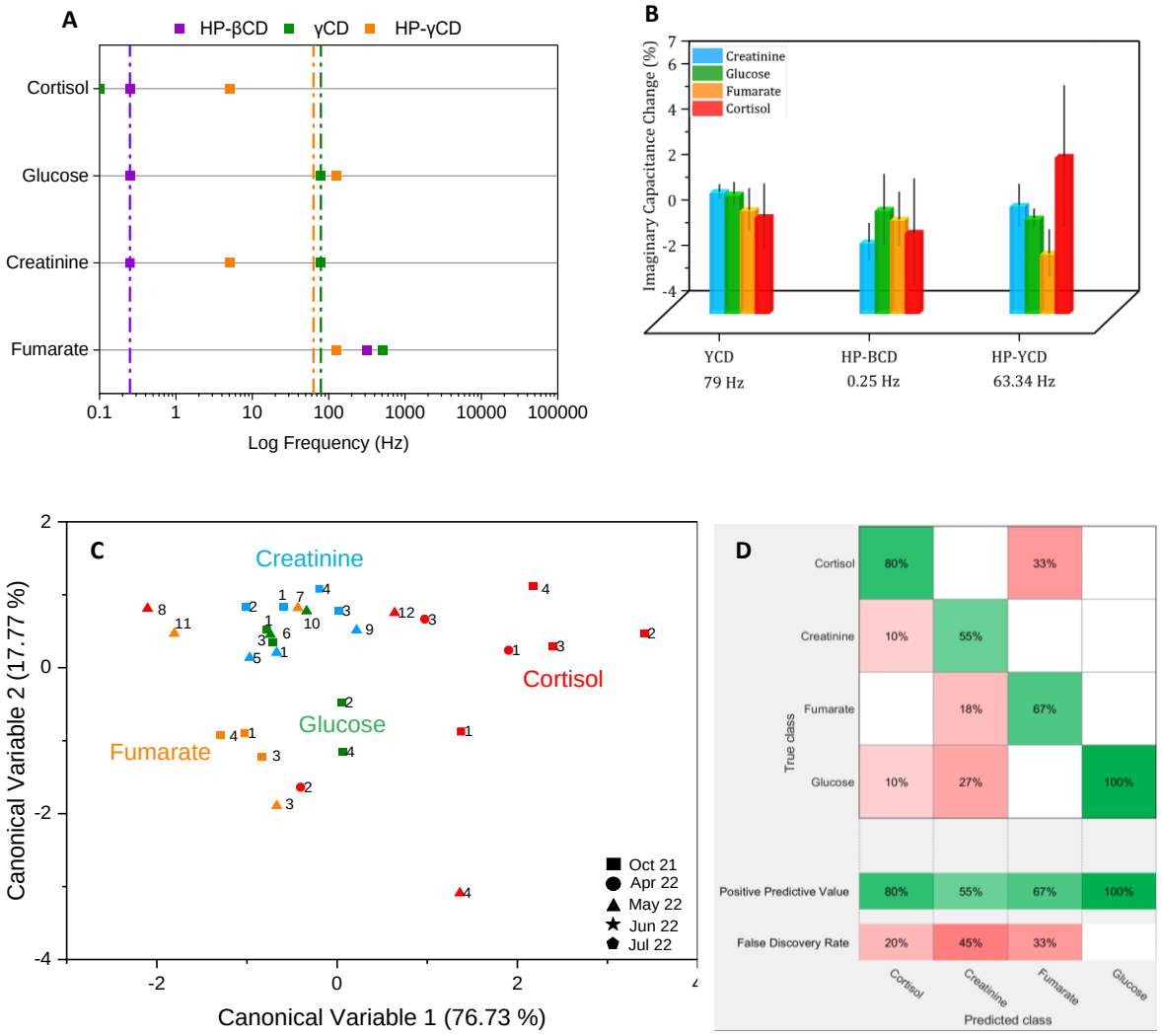

Figure 5.25. Classification of different samples using normalized change in imaginary capacitance (Method 2.3) as feature of the cyclodextrin impedimetric tongue biosensor: (A) Characteristic frequencies of different analytes on different surfaces and determination of a single frequency for each surface (i.e., γCD: 79 Hz, HP-βCD: 0.25 Hz, and HP-γCD: 63.34 Hz), (B) The normalized changes in imaginary capacitance of different samples on different surfaces at a single frequency, (C) LDA plot analysis (5-fold cross-validation accuracy: 69 %), (D) Confusion matrix

5.7 Conclusion

In line with our long-term goal of the project to develop a cyclodextrin impedimetric tongue biosensor that can reliably be used for sepsis diagnosis, in this Chapter, we evaluated the performance of the cyclodextrin impedimetric tongue for classification of 4 sepsis biomarkers including cortisol, creatinine, glucose, and fumarate. The impedimetric tongue consists of five cyclodextrin surfaces: αCD, βCD, γCD, HP-βCD, and HP-γCD. Compared to amperometric and voltametric tongue biosensors, the impedimetric tongues can provide more information of the samples; however, the data preparation and signal processing of impedimetric tongues can be more cumbersome. In this Chapter, we proposed 6 different methods for finding the characteristic frequencies and data preparation, and we studied the normalized changes in five different EIS parameters: real impedance, imaginary impedance, impedance magnitude, phase angle, and imaginary capacitance at characteristic frequencies. We finally used LDA to calculate the accuracy of thirty different datasets to choose the best data preparation method and find the best EIS parameter as the signal for cyclodextrin impedimetric tongue biosensor. Our results showed that both normalized changes in phase angle and imaginary capacitance can be chosen as the features of our cyclodextrin impedimetric tongue. Additionally, further studies on optimization of surfaces and data analysis methods are essential for improving the predictive accuracy and performance of the impedimetric tongue.

6. Conclusions and Recommendations

6.1 The First Reusable Cyclodextrin Biosensor Prototype

The cyclodextrin biosensors that had previously been developed were all single-use devices that could not be utilized for on-line continuous measurement of biomarkers. Thus, the first goal of this project was to create a novel reusable cyclodextrin biosensor platform (**Figure 6.1**). We achieved this goal by modification of a gold surface with polyethylene glycol (PEG) via gold-thiol bonds. αCD molecules were then immobilized on the PEG support. The interactions between PEG and αCD are reversible and the binding affinity of αCD and trans-resveratrol is higher than the binding affinity of αCD and PEG. Therefore, when the surface was exposed to a solution containing trans-resveratrol, the αCD molecules left the PEG support to interact with trans-resveratrol in the solution. After use, the biosensor could be regenerated by reloading αCD. Faradaic EIS, ATR-FTIR, and XPS tests were used to characterize the Gold-PEG:αCD surface.

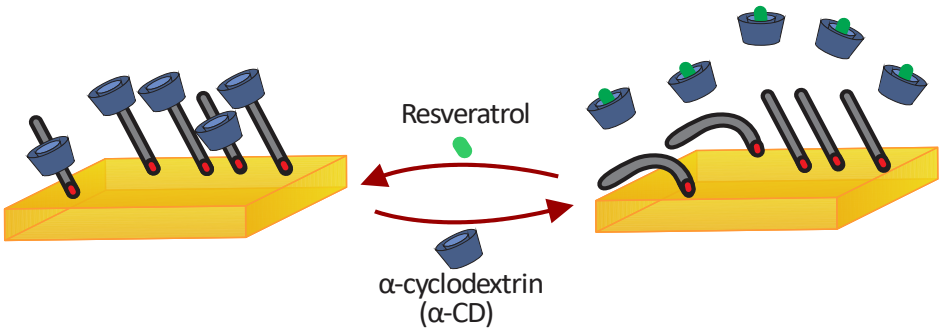

Figure 6.1. The schematic diagram of the first reusable cyclodextrin platform (Gold-PEG:α-CD) for detection of *trans*-resveratrol

Additionally, we demonstrated that:

1. The Gold-PEG:αCD surface can be regenerated and reused for 3 times.
2. When αCD molecules leave the surface to interact with trans-resveratrol (160 nM) or when αCD molecules are removed from the surface by an ethanol soak, PEG polymers change from a porous structure to a mushroom configuration on the gold surface. This causes a change in surface porosity and charge transfer resistance. The changes in charge transfer resistance can be measured by faradaic EIS.
3. The changes in surface porosity affects the coating layer capacitance as well as the leakage resistance of the coating layer. The changes in leakage resistance can be measured by non-faradaic EIS.
4. The Gold-PEG:αCD surface can detect nM concentrations of trans-resveratrol in buffer and human urine.
5. Due to low stability of gold-thiol bond, the Gold-PEG:αCD surface had low stability.

6.2 Enhancing the Stability of Reusable Cyclodextrin Platform

We compared the long-term (storage) and short-term (sensing) stability of gold-thiol 3MPA-PPG and glassy carbon-carboxyphenyl-PPG surfaces. We used faradaic EIS, ATR-FTIR, and XPS to show the changes on gold and glassy carbon after different modification stages. We demonstrated that by using diazonium salt chemistry we can improve the stability of cyclodextrin platform significantly and address the problem of low stability of reusable cyclodextrin surfaces. The schematic diagram of GC-carboxyphenyl-PPG:βCD is shown in **Figure 6.2**.

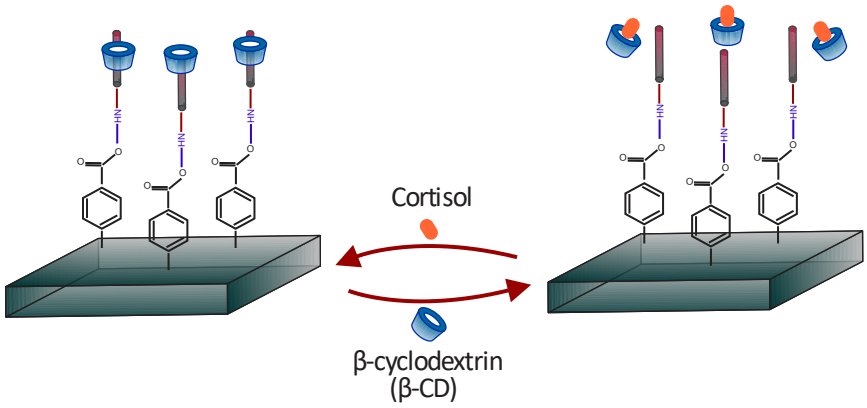

Figure 6.2. Improving the stability of the cyclodextrin platform and development of Glassy Carbon-PPG:βCD for detection of cortisol

We further demonstrated that:

1. The GC-carboxyphenyl-PPG:βCD is stable for at least 1 month.
2. Non-faradaic EIS and XPS confirmed surface regeneration and reusability for up to 10 times.
3. In detecting cortisol, imaginary capacitance at the characteristic frequency (frequency with the highest signal to noise ratio) can be used to analyze non-faradaic EIS data.
4. Using GC-carboxyphenyl-PPG:βCD surface, sensitive detection of cortisol can be achieved in PBS buffer, urine, and saliva with limit of detection of 2.13, 1.29, and 1.33 nM, respectively.

6.3 The First Reusable Cyclodextrin Impedimetric Tongue Prototype

The last part of this dissertation was development of a cyclodextrin impedimetric tongue prototype. Five different cyclodextrin surfaces including GC-carboxyphenyl-PEG:αCD, GC-carboxyphenyl-PPG:βCD, GC-carboxyphenyl-PPG:γCD, GC-carboxyphenyl-PPG:HP-βCD, and GC-carboxyphenyl-PPG:HP-γCD were integrated to create the cross-reactive sensing array for recognition of a class of biomarkers and detection of sepsis (**Figure 6.3**). 390 EIS experiments

were performed to gain 39 data points to assess the performance of the prototype device for separation of four different sepsis biomarkers including cortisol, creatinine, glucose, and fumarate using LDA. Control experiments in blank PBS were also performed for further evaluation of the sensor and/or determination of characteristic frequencies.

Our results showed that:

1. Different EIS parameters such as real impedance, imaginary impedance, impedance magnitude, phase angle, and imaginary capacitance greatly impact the accuracy of the impedimetric tongue.
2. The 5-fold cross validation accuracy of 100% and 96.4% in separation of four classes of analytes could be achieved when the normal changes in phase angle and imaginary capacitance were chosen as the signal, respectively. However, this was an unoptimized, best case, analysis of data to achieve the maximum accuracy. To make the electronic tongue applicable for classification of unknown samples, we found a single frequency for each surface by calculating the median of characteristic frequencies of different analytes on that surface. The highest 5-fold cross validation accuracy of 69% was achieved when we applied LDA on the normalized changes in imaginary capacitance at a single frequency for three cyclodextrin surfaces (YCD at 79 Hz, HP-BCD at 0.25 Hz, and HP-YCD 63.345 Hz).
3. Different methods for data preparation and determining the characteristic frequencies affect the accuracy of the impedimetric tongue.

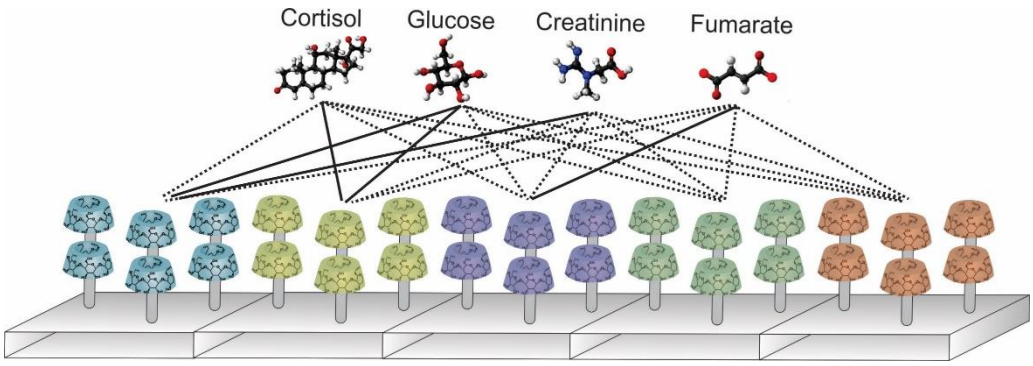

Figure 6.3. The schematic diagram of the first reusable cyclodextrin impedimetric tongue prototype for separation of four groups of sepsis biomarkers

6.4 Recommendations for Future Work

Many achievements have been accomplished in development of the first generation reusable cyclodextrin impedimetric tongues; however, there are some remaining challenges that need to be addressed. The cyclodextrin impedimetric tongue prototype that was described in this thesis consists of five cyclodextrin surfaces. The cyclodextrins used in development of these surfaces are the most common available products in the market. However, other variations of cyclodextrins that were not discussed in this thesis, might be helpful for improving chiral recognition ability of the impedimetric tongue device.

A Gamry multichannel potentiostat (**Figure 6.4**) allows us to combine at least 8 different potentiostats into a single system. Using this system, we can test multiple surfaces simultaneously and increase our throughput significantly. For example, we spent at least 2730 minutes on performing the EIS experiments in **Table 5.3** (39 data points × 5 surfaces × 2 tests × 7 minutes). Testing all five surfaces simultaneously, reduces this time to 546 minutes and provides

more reliable and accurate data. Additionally, automation of this process by a flow cell system can greatly improve the efficiency and accuracy of the device.

Figure 6.4. Gamry's multichannel potentiostat system that can combine multiple electrochemical cells into a single system

Once we gather more data using a multichannel potentiostat and/or the flow cell, we need to revisit our signal processing methods. We need to write a robust program to preprocess and clean the EIS data, find outliers, important EIS variables, the characteristic frequencies of different analytes, and single frequencies of different cyclodextrin surfaces.

To evaluate the cyclodextrin impedimetric tongue prototype, we tested cortisol, glucose, fumarate, creatinine, and blank PBS. We propose further testing of acetone, acetate, glycine, arginine, and ethanol in PBS with at least four replicates. Collecting this information and expanding the dataset will be very helpful in better understanding of the EIS data analysis, implication of classification models, and selecting the most appropriate cyclodextrin surfaces in the final design of the product for sepsis diagnostic applications. We also propose to employ the

prototype for detection of sepsis biomarkers in urine. This is important because there are some molecules in urine that can interact with cyclodextrin biosensors and interfere with biomarkers detection.

However, the cyclodextrin impedimetric tongue does not follow the “lock-and-key” basis and cannot be used for selective determination of any specific biomarkers in a sample. Therefore, the goal here is not to prove that the selectivity of cyclodextrins towards different sepsis biomarkers and we do not want to predict the exitance of the disease from the changes in the concentrations of any single biomarkers. Instead, we want to use the entire metabolic profiles and for the identification of different samples.

The practicality and reliability of the cyclodextrin impedimetric tongue needs to be evaluated by using clinical samples of urine. The goal is to determine the accuracy of the device in differentiating between healthy and septic urine samples. Additionally, the device can be tested to differentiate between sepsis and cytokine storm triggered by COVID-19 in urine samples. To perform these experiments several urine samples from random healthy subjects, patients with sepsis, and patients with cytokine storm need to be obtained. The main disadvantage of testing urine samples is the variation in dilution effects since the concentrations of metabolites in urine samples can vary significantly based on water consumption and other physiological factors [239,240]. Therefore, at least two different normalization technique using creatinine urine tests and specific gravity measurements need to be performed to find the variability and standard deviation of samples. This will help to make sure that the impedimetric tongue will differentiate between different healthy, sepsis and cytokine storm metabolite profiles and the separation results will not be impacted by variations in dilution effects or sample

volumes. However, since urinary creatinine excretion increases with age, the age range of the healthy subjects and patients need to be considered as well [241].

The ideal cyclodextrin impedimetric tongue is a reusable biosensor that can be installed in-line with urinary catheters for early diagnostic of sepsis. This dissertation was an important step toward development of the cyclodextrin impedimetric tongues for detection of sepsis or other diseases in different biological samples.

References

[1] O. Parlak, S.T. Keene, A. Marais, V.F. Curto, A. Salleo, Molecularly selective nanoporous membrane-based wearable organic electrochemical device for noninvasive cortisol sensing, Sci. Adv. 4 (2018) eaar2904. https://doi.org/10.1126/sciadv.aar2904.

[2] S. Pradhan, S. Pramanik, Di.K. Das, R. Bhar, R. Bandyopadhyay, P. Millner, P. Pramanik, Nanosized iron telluride for simultaneous nanomolar voltammetric determination of dopamine, uric acid, guanine and adenine, New J. Chem. 43 (2019) 10590–10600. https://doi.org/10.1039/c9nj02329a.

[3] Z. Cai, Y. Ye, X. Wan, J. Liu, S. Yang, Y. Xia, G. Li, Q. He, Morphology–Dependent Electrochemical Sensing Properties of Iron Oxide–Graphene Oxide Nanohybrids for Dopamine and Uric Acid, Nanomaterials. 9 (2019) 835. https://doi.org/10.3390/nano9060835.

[4] A. Arroquia, I. Acosta, M.P.G. Armada, Self-assembled gold decorated polydopamine nanospheres as electrochemical sensor for simultaneous determination of ascorbic acid, dopamine, uric acid and tryptophan, Mater. Sci. Eng. C. 109 (2020) 110602. https://doi.org/10.1016/j.msec.2019.110602.

[5] A. Gorczyński, M. Kubicki, K. Szymkowiak, T. Łuczak, V. Patroniak, Utilization of a new gold/Schiff-base iron(iii) complex composite as a highly sensitive voltammetric sensor for determination of epinephrine in the presence of ascorbic acid, RSC Adv. 6 (2016) 101888–101899. https://doi.org/10.1039/c6ra22028b.

[6] D.Y. Lee, E. Kim, M.H. Choi, Technical and clinical aspects of cortisol as a biochemical marker of chronic stress, BMB Rep. 48 (2015) 209–216. https://doi.org/10.5483/BMBRep.2015.48.4.275.

[7] V. Narwal, R. Deswal, B. Batra, V. Kalra, R. Hooda, M. Sharma, J.S. Rana, Cholesterol biosensors: A review, Steroids. 143 (2019) 6–17. https://doi.org/10.1016/j.steroids.2018.12.003.

[8] F.J. Van Spronsen, M. Van Rijn, J. Bekhof, R. Koch, P.G.A. Smit, Phenylketonuria: Tyrosine supplementation in phenylalanine-restricted diets, Am. J. Clin. Nutr. 73 (2001) 153–157. https://doi.org/10.1093/ajcn/73.2.153.

[9] V.K. Sharma, F. Jelen, L. Trnkova, Functionalized solid electrodes for electrochemical biosensing of purine nucleobases and their analogues: A review, Sensors (Switzerland). 15 (2015) 1564–1600. https://doi.org/10.3390/s150101564.

[10] Z. Panahi, L. Custer, J.M. Halpern, Recent advances in non-enzymatic electrochemical detection of hydrophobic metabolites in biofluids, Sensors and Actuators Reports. 3 (2021) 100051. https://doi.org/10.1016/J.SNR.2021.100051.

[11] P.L. Clark, K.G. Ugrinov, Measuring cotranslational folding of nascent polypeptide chains

on ribosomes, in: Methods Enzymol., Elsevier, 2009: pp. 567–590.

[12] W.A. Adeosun, A.M. Asiri, H.M. Marwani, M.M. Rahman, Enzymeless Electrocatalytic Detection of Uric Acid Using Polydopamine/Polypyrrole Copolymeric film, ChemistrySelect. 5 (2020) 156–164. https://doi.org/10.1002/slct.201903628.

[13] D. Zhu, H. Ma, Q. Zhen, J. Xin, L. Tan, C. Zhang, X. Wang, B. Xiao, Hierarchical flower-like zinc oxide nanosheets in-situ growth on three-dimensional ferrocene-functionalized graphene framework for sensitive determination of epinephrine and its oxidation derivative, Appl. Surf. Sci. 526 (2020) 146721. https://doi.org/10.1016/j.apsusc.2020.146721.

[14] S. Rison, K.B. Akshaya, V.S. Bhat, G. Shanker, T. Maiyalagan, E.K. Joice, G. Hegde, A. Varghese, MnO_2 Nanoclusters Decorated on GrapheneModified Pencil Graphite Electrode for Non-Enzymatic Determination of Cholesterol, Electroanalysis. (2020) elan.202000049. https://doi.org/10.1002/elan.202000049.

[15] A. Karthika, D.R. Rosaline, S.S.R. Inbanathan, A. Suganthi, M. Rajarajan, Fabrication of Cupric oxide decorated β-cyclodextrin nanocomposite solubilized Nafion as a high performance electrochemical sensor for L-tyrosine detection, J. Phys. Chem. Solids. 136 (2020) 109145. https://doi.org/10.1016/j.jpcs.2019.109145.

[16] J. Zhou, S. Li, M. Noroozifar, K. Kerman, Graphene Oxide Nanoribbons in Chitosan for Simultaneous Electrochemical Detection of Guanine, Adenine, Thymine and Cytosine, Biosensors. 10 (2020) 30. https://doi.org/10.3390/bios10040030.

[17] K. Scott, Electrochemical principles and characterization of bioelectrochemical systems, Microb. Electrochem. Fuel Cells. (2016) 29–66. https://doi.org/10.1016/B978-1-78242-375-1.00002-2.

[18] G. Zhu, L. Wu, X. Zhang, W. Liu, X. Zhang, J. Chen, A New Dual-Signalling Electrochemical Sensing Strategy Based on Competitive Host-Guest Interaction of a β-Cyclodextrin/Poly(N -acetylaniline)/Graphene-Modified Electrode: Sensitive Electrochemical Determination of Organic Pollutants, Chem. - A Eur. J. 19 (2013) 6368–6373. https://doi.org/10.1002/chem.201204635.

[19] S. Alexander, P. Baraneedharan, S. Balasubrahmanyan, S. Ramaprabhu, Modified graphene based molecular imprinted polymer for electrochemical non-enzymatic cholesterol biosensor, Eur. Polym. J. 86 (2017) 106–116. https://doi.org/10.1016/j.eurpolymj.2016.11.024.

[20] M.A.H. Nawaz, M. Majdinasab, U. Latif, M. Nasir, G. Gokce, M.W. Anwar, A. Hayat, Development of a disposable electrochemical sensor for detection of cholesterol using differential pulse voltammetry, J. Pharm. Biomed. Anal. 159 (2018) 398–405. https://doi.org/10.1016/j.jpba.2018.07.005.

[21] L. Yang, H. Zhao, S. Fan, G. Zhao, X. Ran, C.-P. Li, Electrochemical detection of cholesterol based on competitive host–guest recognition using a β-cyclodextrin/poly(N-

acetylaniline)/graphene-modified electrode, RSC Adv. 5 (2015) 64146–64155. https://doi.org/10.1039/C5RA11420A.

[22] S. Kämäräinen, M. Mäki, T. Tolonen, G. Palleschi, V. Virtanen, L. Micheli, A.M. Sesay, Disposable electrochemical immunosensor for cortisol determination in human saliva, Talanta. 188 (2018) 50–57. https://doi.org/10.1016/J.TALANTA.2018.05.039.

[23] A. Salimi, R. Hallaj, G.-R. Khayatian, Amperometric Detection of Morphine at Preheated Glassy Carbon Electrode Modified with Multiwall Carbon Nanotubes, Electroanalysis. 17 (2005) 873–879. https://doi.org/10.1002/elan.200403166.

[24] J.L. Hammond, N. Formisano, P. Estrela, S. Carrara, J. Tkac, J. Tkac, Electrochemical biosensors and nanobiosensors, Essays Biochem. 60 (2016) 69–80. https://doi.org/10.1042/EBC20150008.

[25] J. Salamon, Y. Sathishkumar, K. Ramachandran, Y.S. Lee, D.J. Yoo, A.R. Kim, G. Gnana kumar, One-pot synthesis of magnetite nanorods/graphene composites and its catalytic activity toward electrochemical detection of dopamine, Biosens. Bioelectron. 64 (2015) 269–276. https://doi.org/10.1016/J.BIOS.2014.08.085.

[26] A. Fiorani, J.P. Merino, A. Zanut, A. Criado, G. Valenti, M. Prato, F. Paolucci, Advanced carbon nanomaterials for electrochemiluminescent biosensor applications, Curr. Opin. Electrochem. 16 (2019) 66–74. https://doi.org/10.1016/j.coelec.2019.04.018.

[27] J.C. Ndamanisha, L. ping Guo, Ordered mesoporous carbon for electrochemical sensing: A review, Anal. Chim. Acta. 747 (2012) 19–28. https://doi.org/10.1016/j.aca.2012.08.032.

[28] S. Pilehvar, K. De Wael, Recent advances in electrochemical biosensors based on fullerene-C60 nano-structured platforms, Biosensors. 5 (2015) 712–735. https://doi.org/10.3390/bios5040712.

[29] Z. Lin, G. Wu, L. Zhao, K.W.C. Lai, Carbon Nanomaterial-Based Biosensors: A review of design and applications, IEEE Nanotechnol. Mag. 13 (2019) 4–14. https://doi.org/10.1109/MNANO.2019.2927774.

[30] U. Kamran, Y.J. Heo, J.W. Lee, S.J. Park, Functionalized carbon materials for electronic devices: A review, Micromachines. 10 (2019) 234. https://doi.org/10.3390/mi10040234.

[31] M. Sireesha, V. Jagadeesh Babu, A. Sandeep, K. Kiran, S. Ramakrishna, A review on carbon nanotubes in biosensor devices and their applications in medicine, Nanocomposites. 4 (2018) 36–57. https://doi.org/10.1080/20550324.2018.1478765.

[32] S. Gupta, C.N. Murthy, C.R. Prabha, Recent advances in carbon nanotube based electrochemical biosensors, Int. J. Biol. Macromol. 108 (2018) 687–703. https://doi.org/10.1016/j.ijbiomac.2017.12.038.

[33] F. Foroughi, M. Rahsepar, H. Kim, A highly sensitive and selective biosensor based on nitrogen-doped graphene for non-enzymatic detection of uric acid and dopamine at biological pH value, J. Electroanal. Chem. 827 (2018) 34–41.

https://doi.org/10.1016/j.jelechem.2018.09.008.

[34] K. Movlaee, H. Beitollahi, M.R. Ganjali, P. Norouzi, Electrochemical platform for simultaneous determination of levodopa, acetaminophen and tyrosine using a graphene and ferrocene modified carbon paste electrode, Microchim. Acta. 184 (2017) 3281–3289. https://doi.org/10.1007/s00604-017-2291-3.

[35] S. He, P. He, X. Zhang, X. Zhang, K. Liu, L. Jia, F. Dong, Poly(glycine)/graphene oxide modified glassy carbon electrode: Preparation, characterization and simultaneous electrochemical determination of dopamine, uric acid, guanine and adenine, Anal. Chim. Acta. 1031 (2018) 75–82. https://doi.org/10.1016/j.aca.2018.06.020.

[36] X. Zhang, Y.-C. Zhang, L.-X. Ma, One-pot facile fabrication of graphene-zinc oxide composite and its enhanced sensitivity for simultaneous electrochemical detection of ascorbic acid, dopamine and uric acid, Sensors Actuators B Chem. 227 (2016) 488–496. https://doi.org/10.1016/J.SNB.2015.12.073.

[37] W. Dong, Y. Ren, Z. Bai, J. Jiao, Y. Chen, B. Han, Q. Chen, Synthesis of tetrahexahedral Au-Pd core–shell nanocrystals and reduction of graphene oxide for the electrochemical detection of epinephrine, J. Colloid Interface Sci. 512 (2018) 812–818. https://doi.org/10.1016/J.JCIS.2017.10.071.

[38] B. Sun, Y. Gou, Y. Ma, X. Zheng, R. Bai, A.A. Ahmed Abdelmoaty, F. Hu, Investigate electrochemical immunosensor of cortisol based on gold nanoparticles/magnetic functionalized reduced graphene oxide, Biosens. Bioelectron. 88 (2017) 55–62. https://doi.org/10.1016/j.bios.2016.07.047.

[39] K.S. Kim, S.R. Lim, S.E. Kim, J.Y. Lee, C.H. Chung, W.S. Choe, P.J. Yoo, Highly sensitive and selective electrochemical cortisol sensor using bifunctional protein interlayer-modified graphene electrodes, Sensors Actuators, B Chem. 242 (2017) 1121–1128. https://doi.org/10.1016/j.snb.2016.09.135.

[40] M. Arvand, N. Ghodsi, M.A. Zanjanchi, A new microplatform based on titanium dioxide nanofibers/graphene oxide nanosheets nanocomposite modified screen printed carbon electrode for electrochemical determination of adenine in the presence of guanine, Biosens. Bioelectron. 77 (2016) 837–844. https://doi.org/10.1016/j.bios.2015.10.055.

[41] Z. Zhu, An Overview of Carbon Nanotubes and Graphene for Biosensing Applications, Nano-Micro Lett. 9 (n.d.). https://doi.org/10.1007/s40820-017-0128-6.

[42] J. Chen, P. He, H. Bai, S. He, T. Zhang, X. Zhang, F. Dong, Poly(B-cyclodextrin)/carbon quantum dots modified glassy carbon electrode: Preparation, characterization and simultaneous electrochemical determination of dopamine, uric acid and tryptophan, Sensors Actuators, B Chem. 252 (2017) 9–16. https://doi.org/10.1016/j.snb.2017.05.096.

[43] S. Dong, Q. Bi, C. Qiao, Y. Sun, X. Zhang, X. Lu, L. Zhao, Electrochemical sensor for discrimination tyrosine enantiomers using graphene quantum dots and β-cyclodextrins composites, Talanta. 173 (2017) 94–100. https://doi.org/10.1016/j.talanta.2017.05.045.

[44] T.C. Canevari, M. Nakamura, F.H. Cincotto, F.M. De Melo, H.E. Toma, High performance electrochemical sensors for dopamine and epinephrine using nanocrystalline carbon quantum dots obtained under controlled chronoamperometric conditions, Electrochim. Acta. 209 (2016) 464–470. https://doi.org/10.1016/j.electacta.2016.05.108.

[45] S.E. Elugoke, A.S. Adekunle, O.E. Fayemi, B.B. Mamba, E.S.M. Sherif, E.E. Ebenso, Carbon-Based Quantum Dots for Electrochemical Detection of Monoamine Neurotransmitters-Review, Biosensors. 10 (2020). https://doi.org/10.3390/bios10110162.

[46] A. Sanati, M. Jalali, K. Raeissi, F. Karimzadeh, M. Kharaziha, & Sahar, S. Mahshid, S. Mahshid, A review on recent advancements in electrochemical biosensing using carbonaceous nanomaterials, (2019). https://doi.org/10.1007/s00604-019-3854-2.

[47] M.B. Wayu, M.A. Schwarzmann, S.D. Gillespie, M.C. Leopold, Enzyme-free uric acid electrochemical sensors using β-cyclodextrin-modified carboxylic acid-functionalized carbon nanotubes, J. Mater. Sci. 52 (2017) 6050–6062. https://doi.org/10.1007/s10853-017-0844-9.

[48] L. García-Carmona, M. Moreno-Guzmán, T. Sierra, M.C. González, A. Escarpa, Filtered carbon nanotubes-based electrodes for rapid sensing and monitoring of L-tyrosine in plasma and whole blood samples, Sensors Actuators, B Chem. 259 (2018) 762–767. https://doi.org/10.1016/j.snb.2017.12.090.

[49] O.J. D'souza, R.J. Mascarenhas, A.K. Satpati, L. V Aiman, Z. Mekhalif, Electrocatalytic oxidation of L-tyrosine at carboxylic acid functionalized multi-walled carbon nanotubes modified carbon paste electrode, Ionics (Kiel). 22 (2016) 405–414. https://doi.org/10.1007/s11581-015-1552-6.

[50] Z. Wei, Y. Sun, Q. Yin, L. Wang, … S.C.-I., U. 2018, Electrochemical determination of tyrosine in human serum based on glycine polymer and multi-walled carbon nanotubes modified carbon paste electrode, Int. J. Electrochem. Sci. 13 (2018) 74–78. https://doi.org/10.20964/2018.08.26 (accessed December 8, 2019).

[51] H. Sarıoğulları, A. Şenocak, T. Basova, E. Demirbaş, M. Durmuş, Effect of different SWCNT-BODIPY hybrid materials for selective and sensitive electrochemical detection of guanine and adenine, J. Electroanal. Chem. 840 (2019) 10–20. https://doi.org/10.1016/J.JELECHEM.2019.03.045.

[52] J. Zhang, D. Han, S. Wang, X. Zhang, R. Yang, Y. Ji, X. Yu, Electrochemical detection of adenine and guanine using a three-dimensional WS2 nanosheet/graphite microfiber hybrid electrode, Electrochem. Commun. 99 (2019) 75–80. https://doi.org/10.1016/J.ELECOM.2019.01.007.

[53] K. Wang, C. Wu, F. Wang, M. Liao, G. Jiang, Bimetallic nanoparticles decorated hollow nanoporous carbon framework as nanozyme biosensor for highly sensitive electrochemical sensing of uric acid, Biosens. Bioelectron. 150 (2020) 111869. https://doi.org/10.1016/j.bios.2019.111869.

[54] P. Muthukumaran, C. Sumathi, J. Wilson, G. Ravi, Enzymeless biosensor based on β-NiS@rGO/Au nanocomposites for simultaneous detection of ascorbic acid, epinephrine and uric acid, RSC Adv. 6 (2016) 96467–96478. https://doi.org/10.1039/c6ra19921f.

[55] M. Taleb, R. Ivanov, S. Bereznev, S.H. Kazemi, I. Hussainova, Alumina/graphene/Cu hybrids as highly selective sensor for simultaneous determination of epinephrine, acetaminophen and tryptophan in human urine, J. Electroanal. Chem. 823 (2018) 184–192. https://doi.org/10.1016/j.jelechem.2018.06.013.

[56] Q. Wang, J. Zhang, Q. Li, X. Guo, L. Zhang, Fabrication of WO2/W@C core-shell nanospheres for voltammetric simultaneous determination of thymine and cytosine, Microchim. Acta. 187 (2020) 1–10. https://doi.org/10.1007/s00604-019-3987-3.

[57] M.M. Alam, M.T. Uddin, A.M. Asiri, M.M. Rahman, M.A. Islam, Detection of L-Tyrosine by electrochemical method based on binary mixed CdO/SnO2 nanoparticles, Meas. J. Int. Meas. Confed. 163 (2020) 107990. https://doi.org/10.1016/j.measurement.2020.107990.

[58] N.F.B. Azeredo, J.M. Gonçalves, P.O. Rossini, K. Araki, J. Wang, L. Angnes, Uric acid electrochemical sensing in biofluids based on Ni/Zn hydroxide nanocatalyst, Microchim. Acta. 187 (2020) 1–11. https://doi.org/10.1007/s00604-020-04351-2.

[59] C. Tooley, C. Gasperoni, S. Marnoto, J. Halpern, Evaluation of Metal Oxide Surface Catalysts for the Electrochemical Activation of Amino Acids, Sensors. 18 (2018) 3144. https://doi.org/10.3390/s18093144.

[60] S. Hooshmand, Z. Es'haghi, Microfabricated disposable nanosensor based on CdSe quantum dot/ionic liquid-mediated hollow fiber-pencil graphite electrode for simultaneous electrochemical quantification of uric acid and creatinine in human samples, Anal. Chim. Acta. 972 (2017) 28–37. https://doi.org/10.1016/j.aca.2017.04.035.

[61] S. Bonyadi, K. Ghanbari, M. Ghiasi, All-electrochemical synthesis of a three-dimensional mesoporous polymeric g-C3N4/PANI/CdO nanocomposite and its application as a novel sensor for the simultaneous determination of epinephrine, paracetamol, mefenamic acid, and ciprofloxacin, New J. Chem. 44 (2020) 3412–3424. https://doi.org/10.1039/c9nj05954g.

[62] Ö.A. Yokuş, F. Kardaş, O. Akyildirim, T. Eren, N. Atar, M.L. Yola, Sensitive voltammetric sensor based on polyoxometalate/reduced graphene oxide nanomaterial: Application to the simultaneous determination of l-tyrosine and l-tryptophan, Sensors Actuators, B Chem. 233 (2016) 47–54. https://doi.org/10.1016/j.snb.2016.04.050.

[63] N. Thakur, M. Kumar, S. Das Adhikary, D. Mandal, T.C. Nagaiah, PVIM-Co5POM/MNC composite as a flexible electrode for the ultrasensitive and highly selective non-enzymatic electrochemical detection of cholesterol, Chem. Commun. 55 (2019) 5021–5024. https://doi.org/10.1039/c9cc01534e.

[64] A.E. Martelp, Metal-Catalyzed Reactions of Organic Compounds, 1985.

[65] M. Arvand, Z. Khoshkholgh, S. Hemmati, Trace level detection of guanine and adenine

and evaluation of damage to DNA using electro-synthesised ZnS@CdS core-shell quantum dots decorated graphene oxide nanocomposite, J. Electroanal. Chem. 817 (2018) 149–159. https://doi.org/10.1016/j.jelechem.2018.04.010.

[66] Q. Xie, X. Chen, H. Zhang, M. Liu, Q. Wang, X. Zhang, Y. Shen, F. Yang, Fabrication of a Modified Electrode Based on Fe_3O_4 -Graphene Oxide Hybrid Composite: Applying to Simultaneous Determination of Adenine and Guanine in DNA, Electroanalysis. 27 (2015) 2201–2208. https://doi.org/10.1002/elan.201500186.

[67] P.S. Adarakatti, M. Mahanthappa, E. H, A. Siddaramanna, $Fe_2V_4O_{13}$ Nanoparticles Based Electrochemical Sensor for the Simultaneous Determination of Guanine and Adenine at Nanomolar Concentration, Electroanalysis. 30 (2018) 1971–1982. https://doi.org/10.1002/elan.201800124.

[68] L.E. Kreno, K. Leong, O.K. Farha, M. Allendorf, R.P. Van Duyne, J.T. Hupp, Metal-organic framework materials as chemical sensors, Chem. Rev. 112 (2012) 1105–1125. https://doi.org/10.1021/cr200324t.

[69] M. Ammam, Polyoxometalates: Formation, structures, principal properties, main deposition methods and application in sensing, J. Mater. Chem. A. 1 (2013) 6291–6312. https://doi.org/10.1039/c3ta01663c.

[70] M.A. Rahman, P. Kumar, D.S. Park, Y.B. Shim, Electrochemical sensors based on organic conjugated polymers, Sensors. 8 (2008) 118–141. https://doi.org/10.3390/s8010118.

[71] U. Lange, N. V. Roznyatovskaya, V.M. Mirsky, Conducting polymers in chemical sensors and arrays, Anal. Chim. Acta. 614 (2008) 1–26. https://doi.org/10.1016/j.aca.2008.02.068.

[72] S. Shrestha, R.J. Mascarenhas, O.J. D'Souza, A.K. Satpati, Z. Mekhalif, A. Dhason, P. Martis, Amperometric sensor based on multi-walled carbon nanotube and poly (Bromocresol purple) modified carbon paste electrode for the sensitive determination of L-tyrosine in food and biological samples, J. Electroanal. Chem. 778 (2016) 32–40. https://doi.org/10.1016/j.jelechem.2016.08.010.

[73] N.F. Atta, A. Galal, A.R. El-Gohary, Crown ether modified poly(hydroquinone)/carbon nanotubes based electrochemical sensor for simultaneous determination of levodopa, uric acid, tyrosine and ascorbic acid in biological fluids, J. Electroanal. Chem. 863 (2020) 114032. https://doi.org/10.1016/j.jelechem.2020.114032.

[74] B. Mekassa, M. Tessema, B.S. Chandravanshi, P.G.L. Baker, F.N. Muya, Sensitive electrochemical determination of epinephrine at poly(L-aspartic acid)/electro-chemically reduced graphene oxide modified electrode by square wave voltammetry in pharmaceutics, J. Electroanal. Chem. 807 (2017) 145–153. https://doi.org/10.1016/j.jelechem.2017.11.045.

[75] T. Yang, R. Yang, H. Chen, F. Nan, T. Ge, K. Jiao, Electrocatalytic activity of molybdenum disulfide nanosheets enhanced by self-doped polyaniline for highly sensitive and

synergistic determination of adenine and guanine, ACS Appl. Mater. Interfaces. 7 (2015) 2867–2872. https://doi.org/10.1021/am5081716.

[76] A. Özcan, S. Ilkbaş, Preparation of poly(3,4-ethylenedioxythiophene) nanofibers modified pencil graphite electrode and investigation of over-oxidation conditions for the selective and sensitive determination of uric acid in body fluids, Anal. Chim. Acta. 891 (2015) 312–320. https://doi.org/10.1016/j.aca.2015.08.015.

[77] R. Ramya, P. Muthukumaran, J. Wilson, Electron beam-irradiated polypyrrole decorated with Bovine serum albumin pores: Simultaneous determination of epinephrine and L-tyrosine, Biosens. Bioelectron. 108 (2018) 53–61. https://doi.org/10.1016/j.bios.2018.02.044.

[78] P. Muthukumaran, R. Ramya, P. Thivya, J. Wilson, G. Ravi, Nanocomposite based on restacked crystallites of β-NiS and Ppy for the determination of theophylline and uric acid on screen-printed electrodes, New J. Chem. 43 (2019) 19397–19407. https://doi.org/10.1039/c9nj04246f.

[79] P. Thivya, R. Ramya, J. Wilson, Poly(3,4-ethylenedioxythiophene)/taurine biocomposite on screen printed electrode: Non-enzymatic cholesterol biosensor, Microchem. J. 157 (2020) 105037. https://doi.org/10.1016/j.microc.2020.105037.

[80] N. Dhananjayan, W. Jeyaraj, G. Karuppasamy, Interactive Studies on Synthetic Nanopolymer decorated with Edible Biopolymer and its Selective Electrochemical determination of L-Tyrosine, Sci. Rep. 9 (2019) 1–12. https://doi.org/10.1038/s41598-019-49735-4.

[81] M. Wang, M. Cui, W. Liu, X. Liu, Highly dispersed conductive polypyrrole hydrogels as sensitive sensor for simultaneous determination of ascorbic acid, dopamine and uric acid, J. Electroanal. Chem. 832 (2019) 174–181. https://doi.org/10.1016/j.jelechem.2018.10.057.

[82] K. Ghanbari, M. Moloudi, Flower-like ZnO decorated polyaniline/reduced graphene oxide nanocomposites for simultaneous determination of dopamine and uric acid, Anal. Biochem. 512 (2016) 91–102. https://doi.org/10.1016/j.ab.2016.08.014.

[83] X. Wang, Y. Zheng, L. Xu, An electrochemical adenine sensor employing enhanced three-dimensional conductivity and molecularly imprinted sites of Au NPs bridged poly(3-thiophene acetic acid), Sensors Actuators, B Chem. 255 (2018) 2952–2958. https://doi.org/10.1016/j.snb.2017.09.116.

[84] Q. Qin, X. Bai, Z. Hua, Electropolymerization of a conductive β-cyclodextrin polymer on reduced graphene oxide modified screen-printed electrode for simultaneous determination of ascorbic acid, dopamine and uric acid, J. Electroanal. Chem. 782 (2016) 50–58. https://doi.org/10.1016/j.jelechem.2016.10.004.

[85] K. Ghanbari, A. Hajian, Electrochemical characterization of Au/ZnO/PPy/RGO nanocomposite and its application for simultaneous determination of ascorbic acid,

epinephrine, and uric acid, J. Electroanal. Chem. 801 (2017) 466–479. https://doi.org/10.1016/j.jelechem.2017.07.024.

[86] S. Sen, P. Sarkar, A simple electrochemical approach to fabricate functionalized MWCNT-nanogold decorated PEDOT nanohybrid for simultaneous quantification of uric acid, xanthine and hypoxanthine, Anal. Chim. Acta. 1114 (2020) 15–28. https://doi.org/10.1016/j.aca.2020.03.060.

[87] M. Taei, H. Hadadzadeh, F. Hasanpour, N. Tavakkoli, M.H. Dolatabadi, Simultaneous electrochemical determination of ascorbic acid, epinephrine, and uric acid using a polymer film-modified electrode based on Au nanoparticles/poly(3,3′,5,5′-tetrabromo-m-cresolsulfonphthalein), Ionics (Kiel). 21 (2015) 3267–3278. https://doi.org/10.1007/s11581-015-1515-y.

[88] J.M. Baricaua, J.N. Balitaan, K.S. Santiago, P2EC.25 - Conducting polyaniline/reduced graphene oxide-modified carbon paste electrode for the electrochemical multidetection of ascorbic acid and uric acid, in: Proc. IMCS, Service GmbH, Von-Münchhausen-Str. 49, 2018: pp. 745–746. https://doi.org/10.5162/imcs2018/p2ec.25.

[89] D. Li, M. Liu, Y. Zhan, Q. Su, Y. Zhang, D. Zhang, Electrodeposited poly(3,4-ethylenedioxythiophene) doped with graphene oxide for the simultaneous voltammetric determination of ascorbic acid, dopamine and uric acid, Microchim. Acta. 187 (2020) 1–10. https://doi.org/10.1007/s00604-019-4083-4.

[90] W. Sroysee, S. Chairam, M. Amatatongchai, P. Jarujamrus, S. Tamuang, S. Pimmongkol, L. Chaicharoenwimolkul, E. Somsook, Poly(m-ferrocenylaniline) modified carbon nanotubes-paste electrode encapsulated in nafion film for selective and sensitive determination of dopamine and uric acid in the presence of ascorbic acid, J. Saudi Chem. Soc. 22 (2018) 173–182. https://doi.org/10.1016/j.jscs.2016.02.003.

[91] S. CHAIYO, Non-enzymatic Electrochemical Detection of Cholesterol using β-Cyclodextrin Modified 3D Paper-based Device, Rep. Grant-Supported Res. Asahi Glas. Found. 90 (2021) 2021_090. https://doi.org/10.50867/AFREPORT.2021_090.

[92] S.S. Jambhekar, P. Breen, Cyclodextrins in pharmaceutical formulations I: structure and physicochemical properties, formation of complexes, and types of complex, Drug Discov. Today. 21 (2016) 356–362. https://doi.org/10.1016/J.DRUDIS.2015.11.017.

[93] G. Huang, X. Yang, R. Huang, Z. Yan, F. Sun, L. Xu, Y. Liu, A Simple Ultrasensitive Electrochemical Biosensor for Simultaneous Determination of Dopamine, Uric Acid and Ascorbic Acid Based on β-cyclodextrin/selenium Doped Carbon Quantum Dots Modified Glassy Carbon Electrode, Int. J. Electrochem. Sci. 15 (2020) 9888–9901. https://doi.org/10.20.964/2020.10.47.

[94] Y. Lu, H. Li, X. Qian, W. Zheng, Y. Sun, B. Shi, Y. nan Zhang, Beta-cyclodextrin based reflective fiber-optic SPR sensor for highly-sensitive detection of cholesterol concentration, Opt. Fiber Technol. 56 (2020) 102187. https://doi.org/10.1016/J.YOFTE.2020.102187.

[95] H. Wu, F. Fang, C. Wang, X. Hong, D. Chen, X. Huang, Selective Molecular Recognition of Low Density Lipoprotein Based on β-Cyclodextrin Coated Electrochemical Biosensor, Biosens. 2021, Vol. 11, Page 216. 11 (2021) 216. https://doi.org/10.3390/BIOS11070216.

[96] W. Xiao, Z. Yang, J. Liu, Z.C. Chen, H. Li, Sensitive cholesterol determination by β-cyclodextrin recognition based on fluorescence enhancement of gold nanoclusters, Microchem. J. 175 (2022) 107125. https://doi.org/10.1016/J.MICROC.2021.107125.

[97] N. Agnihotri, A.D. Chowdhury, A. De, Non-enzymatic electrochemical detection of cholesterol using β-cyclodextrin functionalized graphene, Biosens. Bioelectron. 63 (2015) 212–217. https://doi.org/10.1016/J.BIOS.2014.07.037.

[98] S.J. Willyam, E. Saepudin, T.A. Ivandini, β-Cyclodextrin/Fe 3 O 4 nanocomposites for an electrochemical non-enzymatic cholesterol sensor, Anal. Methods. 12 (2020) 3454–3461. https://doi.org/10.1039/D0AY00933D.

[99] H. Ma, Y. He, L. Xu, Y. Wei, Fabrication of polydopamine/hemin-cyclodextrin supramolecular assemblies for mimicking natural peroxidases and their sensitive detection of cholesterol, J. Mol. Liq. 328 (2021) 115490. https://doi.org/10.1016/J.MOLLIQ.2021.115490.

[100] N.M.Y. Zhang, M. Qi, Z. Wang, Z. Wang, M. Chen, K. Li, P. Shum, L. Wei, One-step synthesis of cyclodextrin-capped gold nanoparticles for ultra-sensitive and highly-integrated plasmonic biosensors, Sensors Actuators B Chem. 286 (2019) 429–436. https://doi.org/10.1016/J.SNB.2019.01.166.

[101] J. Zhao, L. Cong, Z. Ding, X. Zhu, Y. Zhang, S. Li, J. Liu, X. Chen, H. Hou, Z. Fan, M. Guo, Enantioselective electrochemical sensor of tyrosine isomers based on macroporous carbon embedded with sulfato-β-Cyclodextrin, Microchem. J. 159 (2020) 105469. https://doi.org/10.1016/J.MICROC.2020.105469.

[102] S. Demirel, Ü. Fen, B.E. Dergisi, E. Zor, Reduced Graphene Oxide/α-Cyclodextrin-Based Electrochemical Sensor: Characterization and Simultaneous Detection of Adenine, Guanine and Thymine, Süleyman Demirel Univ. J. Nat. Appl. Sci. 21 (2017) 146–152. https://doi.org/10.19113/sdufbed.72272.

[103] M.B. Wayu, L.T. DiPasquale, M.A. Schwarzmann, S.D. Gillespie, M.C. Leopold, Electropolymerization of β-cyclodextrin onto multi-walled carbon nanotube composite films for enhanced selective detection of uric acid, J. Electroanal. Chem. 783 (2016) 192–200. https://doi.org/10.1016/j.jelechem.2016.11.021.

[104] R. Wang, X. Zhou, H. Shi, Triple functional DNA-protein conjugates: Signal probes for Pb2+ using evanescent wave-induced emission, Biosens. Bioelectron. 74 (2015) 78–84. https://doi.org/10.1016/j.bios.2015.06.003.

[105] F. Lorestani, A. Khademhosseini, M.R. Dokmeci, Multi Use Microfluidic Biosensors for Continual Monitoring of Biomarkers from Microphysiological Systems, in: 2019 20th Int. Conf. Solid-State Sensors, Actuators Microsystems Eurosensors XXXIII, TRANSDUCERS

2019 EUROSENSORS XXXIII, Institute of Electrical and Electronics Engineers Inc., 2019: pp. 1036–1039. https://doi.org/10.1109/TRANSDUCERS.2019.8808693.

[106] L. Boschis, N. Ciprianetti, D. Spadaro, M.L. Gullino, R. Rinaldi, C. Garino, M. Arlorio, Smart micro-sensing: Antibodies and aptamer-based micro-ELISA as performing offline/on line tool for allergens and mycotoxins detection in foods, in: 2017 IEEE Biomed. Circuits Syst. Conf. BioCAS 2017 - Proc., Institute of Electrical and Electronics Engineers Inc., 2018: pp. 1–4. https://doi.org/10.1109/BIOCAS.2017.8325179.

[107] R. Riahi, S.A.M. Shaegh, M. Ghaderi, Y.S. Zhang, S.R. Shin, J. Aleman, S. Massa, D. Kim, M.R. Dokmeci, A. Khademhosseini, Automated microfluidic platform of bead-based electrochemical immunosensor integrated with bioreactor for continual monitoring of cell secreted biomarkers, Sci. Rep. 6 (2016) 1–14. https://doi.org/10.1038/srep24598.

[108] S.R. Shin, T. Kilic, Y.S. Zhang, H. Avci, N. Hu, D. Kim, C. Branco, J. Aleman, S. Massa, A. Silvestri, J. Kang, A. Desalvo, M.A. Hussaini, S.-K. Chae, A. Polini, N. Bhise, M.A. Hussain, H. Lee, M.R. Dokmeci, A. Khademhosseini, Label-Free and Regenerative Electrochemical Microfluidic Biosensors for Continual Monitoring of Cell Secretomes, Adv. Sci. 4 (2017) 1600522. https://doi.org/10.1002/advs.201600522.

[109] S. Choi, J. Chae, Reusable biosensors via in situ electrochemical surface regeneration in microfluidic applications, Biosens. Bioelectron. 25 (2009) 527–531. https://doi.org/10.1016/j.bios.2009.08.003.

[110] L. Liu, X. Zhou, Y. Lu, D. Shan, B. Xu, M. He, H. Shi, Y. Qian, Facile screening of potential xenoestrogens by an estrogen receptor-based reusable optical biosensor, Biosens. Bioelectron. 97 (2017) 16–20. https://doi.org/10.1016/j.bios.2017.05.026.

[111] C. Camacho, J.C. Matías, B. Chico, R. Cao, L. Gómez, B.K. Simpson, R. Villalonga, Amperometric Biosensor for Hydrogen Peroxide, Using Supramolecularly Immobilized Horseradish Peroxidase on the β-Cyclodextrin-Coated Gold Electrode, Electroanal. An Int. J. Devoted to Fundam. Pract. Asp. Electroanal. 19 (2007) 2538–2542. https://doi.org/10.1002/elan.200703993.

[112] Y. hui Wu, H. Bi, G. Ning, Z. gang Xu, G. qiang Liu, Y. hong Wang, Y. lin Zhao, Cyclodextrin subject-object recognition-based aptamer sensor for sensitive and selective detection of tetracycline, J. Solid State Electrochem. 24 (2020) 2365–2372. https://doi.org/10.1007/s10008-020-04751-7.

[113] G. Thompson, S. Marnoto, J.M. Halpern, Proper Controls to Electrochemically Evaluate Carotenoids Using β-Cyclodextrin Modified Surfaces, ECS Trans. 80 (2017) 1177–1187. https://doi.org/10.1149/08010.1177ecst.

[114] L.S. Hernández-Muñoz, C. Frontana, F.J. González, Covalent modification of carbon surfaces with cyclodextrins by mediated oxidation of β-cyclodextrin monoanions, Electrochim. Acta. 138 (2014) 22–29. https://doi.org/10.1016/j.electacta.2014.06.077.

[115] N. Shadjou, M. Hasanzadeh, F. Talebi, Graphene Quantum Dots Incorporated into β-

cyclodextrin: a Novel Polymeric Nanocomposite for Non-Enzymatic Sensing of L-Tyrosine at Physiological pH, J. Anal. Chem. 73 (2018) 602–612. https://doi.org/10.1134/S1061934818060096.

[116] G. Ning, H. Wang, M. Fu, J. Liu, Y. Sun, H. Lu, X. Fan, Y. Zhang, H. Wang, Dual Signals Electrochemical Biosensor for Point-of-Care Testing of Amino Acids Enantiomers, Electroanalysis. 34 (2022) 316–325. https://doi.org/10.1002/ELAN.202100240.

[117] M.A. Morales, J.M. Halpern, Guide to Selecting a Biorecognition Element for Biosensors, Bioconjug. Chem. 29 (2018) 3231–3239. https://doi.org/10.1021/acs.bioconjchem.8b00592.

[118] D.A. Armbruster, T. Pry, Limit of blank, limit of detection and limit of quantitation., Clin. Biochem. Rev. 29 Suppl 1 (2008) S49-52. http://www.ncbi.nlm.nih.gov/pubmed/18852857 (accessed July 15, 2021).

[119] Q. Wang, J. Zhang, Q. Li, X. Guo, L. Zhang, Fabrication of WO2/W@C core-shell nanospheres for voltammetric simultaneous determination of thymine and cytosine, Microchim. Acta. 187 (2020) 62. https://doi.org/10.1007/s00604-019-3987-3.

[120] R. Pauliukaite, E. Voitechovič, Multisensor Systems and Arrays for Medical Applications Employing Naturally-Occurring Compounds and Materials, Sensors (Basel). 20 (2020) 1–38. https://doi.org/10.3390/S20123551.

[121] K.J. Albert, N.S. Lewis, C.L. Schauer, G.A. Sotzing, S.E. Stitzel, T.P. Vaid, D.R. Walt, Cross-reactive chemical sensor arrays, Chem. Rev. 100 (2000) 2595–2626. https://doi.org/10.1021/CR980102W/ASSET/IMAGES/MEDIUM/CR980102WE00017.GIF.

[122] Y. Vlasov, A. Legin, Non-selective chemical sensors in analytical chemistry: from “electronic nose” to “electronic tongue,” Fresenius’ J. Anal. Chem. 1998 3613. 361 (1998) 255–260. https://doi.org/10.1007/S002160050875.

[123] S. Motia, B. Bouchikhi, N. El Bari, An electrochemical sensor based on molecularly imprinted polymer conjointly with a voltammetric electronic tongue for quantitative diphenyl phosphate detection in urine samples from cosmetic product users, Sensors Actuators B Chem. 332 (2021) 129449. https://doi.org/10.1016/J.SNB.2021.129449.

[124] M. Podrazka, E. Báczyńska, M. Kundys, P.S. Jeleń, E.W. Nery, Electronic Tongue—A Tool for All Tastes?, Biosensors. 8 (2018). https://doi.org/10.3390/BIOS8010003.

[125] A. Diouf, Y. Aghoutane, H. Burhan, F. Sen, B. Bouchikhi, N. El Bari, Tramadol sensing in non-invasive biological fluids using a voltammetric electronic tongue and an electrochemical sensor based on biomimetic recognition, Int. J. Pharm. 593 (2021) 120114. https://doi.org/10.1016/J.IJPHARM.2020.120114.

[126] A. Diouf, M. Moufid, D. Bouyahya, L. Österlund, N. El Bari, B. Bouchikhi, An electrochemical sensor based on chitosan capped with gold nanoparticles combined with a voltammetric electronic tongue for quantitative aspirin detection in human physiological fluids and tablets, Mater. Sci. Eng. C. 110 (2020) 110665.

https://doi.org/10.1016/J.MSEC.2020.110665.

[127] C. Garcia-Hernandez, C. Salvo Comino, F. Martín-Pedrosa, M.L. Rodriguez-Mendez, C. Garcia-Cabezon, Impedimetric electronic tongue based on nanocomposites for the analysis of red wines. Improving the variable selection method, Sensors Actuators B Chem. 277 (2018) 365–372. https://doi.org/10.1016/J.SNB.2018.09.023.

[128] J.L.Z. Zaukuu, G. Bazar, Z. Gillay, Z. Kovacs, Emerging trends of advanced sensor based instruments for meat, poultry and fish quality– a review, Crit. Rev. Food Sci. Nutr. 60 (2020) 3443–3460. https://doi.org/10.1080/10408398.2019.1691972.

[129] R.H. Labrador, R. Masot, M. Alcañiz, D. Baigts, J. Soto, R. Martínez-Mañez, E. García-Breijo, L. Gil, J.M. Barat, Prediction of NaCl, nitrate and nitrite contents in minced meat by using a voltammetric electronic tongue and an impedimetric sensor, Food Chem. 122 (2010) 864–870. https://doi.org/10.1016/J.FOODCHEM.2010.02.049.

[130] O. Barash, W. Zhang, J.M. Halpern, Q.L. Hua, Y.Y. Pan, H. Kayal, K. Khoury, H. Liu, M.P.A. Davies, H. Haick, Differentiation between genetic mutations of breast cancer by breath volatolomics, Oncotarget. 6 (2015) 44864. https://doi.org/10.18632/ONCOTARGET.6269.

[131] D.C. Braz, M.P. Neto, F.M. Shimizu, A.C. Sá, R.S. Lima, A.L. Gobbi, M.E. Melendez, L.M.R.B. Arantes, A.L. Carvalho, F. V. Paulovich, O.N. Oliveira, Using machine learning and an electronic tongue for discriminating saliva samples from oral cavity cancer patients and healthy individuals, Talanta. 243 (2022) 123327. https://doi.org/10.1016/J.TALANTA.2022.123327.

[132] L. Pascual, I. Campos, J.L. Vivancos, G. Quintás, A. Loras, M.C. Martínez-Bisbal, R. Martínez-Máñez, F. Boronat, J.L. Ruiz-Cerdà, Detection of prostate cancer using a voltammetric electronic tongue, Analyst. 141 (2016) 4562–4567. https://doi.org/10.1039/C6AN01044J.

[133] I.T. Jollife, J. Cadima, Principal component analysis: a review and recent developments, Philos. Trans. R. Soc. A Math. Phys. Eng. Sci. 374 (2016). https://doi.org/10.1098/RSTA.2015.0202.

[134] C. Ricciardi, A.S. Valente, K. Edmund, V. Cantoni, R. Green, A. Fiorillo, I. Picone, S. Santini, M. Cesarelli, Linear discriminant analysis and principal component analysis to predict coronary artery disease, Health Informatics J. 26 (2020) 2181–2192. https://doi.org/10.1177/1460458219899210.

[135] K. Fukunaga, Introduction to statistical pattern recognition, Elsevier, 2013.

[136] A.M. Martõ Ânez, A.C. Kak, PCA versus LDA, IEEE Trans. Pattern Anal. Mach. Intell. 23 (2001) 228–233. https://doi.org/10.1109/34.908974.

[137] Y. Al-Issa, J. Njagi, S.C. Schuckers, I.I. Suni, Amperometric Bioelectronic Tongue for glucose determination, Sens. Bio-Sensing Res. 3 (2015) 31–37. https://doi.org/10.1016/J.SBSR.2014.10.015.

[138] T.A. da Silva, M.L. Braunger, M.A.N. Coutinho, L.R. do Amaral, V. Rodrigues, A. Riul, 3D-printed graphene electrodes applied in an impedimetric electronic tongue for soil analysis, Chemosensors. 7 (2019). https://doi.org/10.3390/CHEMOSENSORS7040050.

[139] W.A. Christinelli, F.M. Shimizu, M.H.M. Facure, R. Cerri, O.N. Oliveira, D.S. Correa, L.H.C. Mattoso, Two-dimensional MoS2-based impedimetric electronic tongue for the discrimination of endocrine disrupting chemicals using machine learning, Sensors Actuators B Chem. 336 (2021) 129696. https://doi.org/10.1016/J.SNB.2021.129696.

[140] A. Pal, S. Biswas, S.P. O Kare, P. Biswas, S.K. Jana, S. Das, K. Chaudhury, Development of an impedimetric immunosensor for machine learning-based detection of endometriosis: A proof of concept, Sensors Actuators B Chem. 346 (2021) 130460. https://doi.org/10.1016/J.SNB.2021.130460.

[141] H.A. Hassan-Nixon, N. Singh, A.E.G. Cass, A sensitive impedimetric immunosensor for the detection of Interleukin-8 in nasal epithelial lining fluid of asthma patients, Biosens. Bioelectron. X. 10 (2022) 100118. https://doi.org/10.1016/J.BIOSX.2022.100118.

[142] D. Loveday, P. Peterson, B. Rodgers, Evaluation of organic coatings with electrochemical impedance spectroscopy, JCT Coatings Tech. 8 (2004) 46–52.

[143] D. Loveday, P. Peterson, B. Rodgers, Evaluation of organic oatings with electrochemical impedance spectroscopy. Part 2: Application of EIS to coatings, JCT Coatingstech. 1 (2004) 88–93.

[144] M.E. Orazem, B. Tribollet, Electrochemical impedance spectroscopy, John Wiley & Sons, Hoboken, New Jersey, 2017.

[145] D. Kang, X. Zuo, R. Yang, F. Xia, K.W. Plaxco, R.J. White, Comparing the properties of electrochemical-based DNA sensors employing different redox tags, Anal. Chem. 81 (2009) 9109–9113. https://doi.org/10.1021/AC901811N.

[146] R.A. Dorledo de Faria, L.G. Dias Heneine, T. Matencio, Y. Messaddeq, Faradaic and non-faradaic electrochemical impedance spectroscopy as transduction techniques for sensing applications, Int. J. Biosens. Bioelectron. Volume 5 (2019). https://doi.org/10.15406/IJBSBE.2019.05.00148.

[147] R. Pruna, M. López, F. Teixidor, Tuning the deposition parameters for optimizing the faradaic and non-faradaic electrochemical performance of nanowire array-shaped ITO electrodes prepared by electron beam evaporation, Nanoscale. 11 (2019) 276–284. https://doi.org/10.1039/c8nr07908k.

[148] A. Qureshi, J.H. Niazi, S. Kallempudi, Y. Gurbuz, Label-free capacitive biosensor for sensitive detection of multiple biomarkers using gold interdigitated capacitor arrays, Biosens. Bioelectron. 25 (2010) 2318–2323. https://doi.org/10.1016/j.bios.2010.03.018.

[149] S.H. Kazemi, M. Shanehsaz, M. Ghaemmaghami, Non-Faradaic electrochemical impedance spectroscopy as a reliable and facile method: Determination of the potassium ion concentration using a guanine rich aptasensor, Mater. Sci. Eng. C. 52 (2015) 151–154.

https://doi.org/10.1016/j.msec.2015.03.058.

[150] J. Liu, M.M. Chisti, X. Zeng, General Signal Amplification Strategy for Nonfaradic Impedimetric Sensing: Trastuzumab Detection Employing a Peptide Immunosensor, Anal. Chem. 89 (2017) 4013–4020. https://doi.org/10.1021/acs.analchem.6b04570.s001.

[151] J. Halliwell, A.C. Savage, N. Buckley, C. Gwenin, Electrochemical impedance spectroscopy biosensor for detection of active botulinum neurotoxin, Sens. Bio-Sensing Res. 2 (2014) 12–15. https://doi.org/10.1016/j.sbsr.2014.08.002.

[152] X. Luo, M. Xu, C. Freeman, T. James, J.J. Davis, Ultrasensitive label free electrical detection of insulin in neat blood serum, Anal. Chem. 85 (2013) 4129–4134. https://doi.org/10.1021/ac4002657.

[153] J.S. Daniels, N. Pourmand, Label-free impedance biosensors: Opportunities and challenges, Electroanal. An Int. J. Devoted to Fundam. Pract. Asp. Electroanal. 19 (2007) 1239–1257. https://doi.org/10.1002/elan.200603855.

[154] K.-C. Lin, V. Kunduru, M. Bothara, K. Rege, S. Prasad, B.L. Ramakrishna, Biogenic nanoporous silica-based sensor for enhanced electrochemical detection of cardiovascular biomarkers proteins, Biosens. Bioelectron. 25 (2010) 2336–2342. https://doi.org/10.1016/j.bios.2010.03.032.

[155] M. ITAGAKI, S. SUZUKI, I. SHITANDA, K. WATANABE, Electrochemical Impedance and Complex Capacitance to Interpret Electrochemical Capacitor, Electrochemistry. 75 (2007) 649–655. https://doi.org/10.5796/ELECTROCHEMISTRY.75.649.

[156] L. Wang, M. Veselinovic, L. Yang, B.J. Geiss, D.S. Dandy, T. Chen, A sensitive DNA capacitive biosensor using interdigitated electrodes, Biosens. Bioelectron. 87 (2017) 646–653. https://doi.org/10.1016/J.BIOS.2016.09.006.

[157] M. DuToit, E. Ngaboyamahina, M. Wiesner, Pairing electrochemical impedance spectroscopy with conducting membranes for the in situ characterization of membrane fouling, J. Memb. Sci. 618 (2021) 118680. https://doi.org/10.1016/J.MEMSCI.2020.118680.

[158] I.C.P. Margarit-Mattos, EIS and organic coatings performance: Revisiting some key points, Electrochim. Acta. 354 (2020) 136725. https://doi.org/10.1016/J.ELECTACTA.2020.136725.

[159] T.J. Smith, K.J. Stevenson, Reference Electrodes, Handb. Electrochem. (2007) 73–110. https://doi.org/10.1016/B978-044451958-0.50005-7.

[160] J. Eveness, L. Cao, J. Kiely, R. Luxton, Equivalent circuit model of a non-faradaic impedimetric ZnO nano-crystal biosensor, J. Electroanal. Chem. 906 (2022) 116003. https://doi.org/10.1016/J.JELECHEM.2021.116003.

[161] B. Chen, J. Kiely, R. Luxton, I. Williams, Article a Non-Faradaic Impedimetric Biosensor for Monitoring of Caspase 9 in Mammalian Cell Culture, SSRN Electron. J. (2022).

https://doi.org/10.2139/SSRN.4070649.

[162] G.N. Abdelrasoul, A. Anwar, S. MacKay, M. Tamura, M.A. Shah, D.P. Khasa, R.R. Montgomery, A.I. Ko, J. Chen, DNA aptamer-based non-faradaic impedance biosensor for detecting E. coli, Anal. Chim. Acta. 1107 (2020) 135–144. https://doi.org/10.1016/J.ACA.2020.02.004.

[163] R.D. Munje, S. Muthukumar, A. Panneer Selvam, S. Prasad, Flexible nanoporous tunable electrical double layer biosensors for sweat diagnostics, Sci. Reports 2015 51. 5 (2015) 1–11. https://doi.org/10.1038/srep14586.

[164] I.G. Subramani, R.M. Ayub, S.C.B. Gopinath, V. Perumal, M.F.M. Fathil, M.K. Md Arshad, Lectin bioreceptor approach in capacitive biosensor for prostate-specific membrane antigen detection in diagnosing prostate cancer, J. Taiwan Inst. Chem. Eng. 120 (2021) 9–16. https://doi.org/10.1016/J.JTICE.2021.03.004.

[165] A.K. Assaifan, F.A. Alqahtani, S. Alnamlah, R. Almutairi, H.I. Alkhammash, Detection and Real-Time Monitoring of LDL-Cholesterol by Redox-Free Impedimetric Biosensors, Biochip J. 16 (2022) 197–206. https://doi.org/10.1007/S13206-022-00058-Z/FIGURES/8.

[166] H.T.N. Le, J. Park, S. Cho, A probeless capacitive biosensor for direct detection of amyloid beta 1-42 in human serum based on an interdigitated chain-shaped electrode, Micromachines. 11 (2020) 791. https://doi.org/10.3390/MI11090791.

[167] L. Wang, W. Zhang, S. Samavat, D. Deganello, K.S. Teng, Vertically aligned graphene prepared by photonic annealing for ultrasensitive biosensors, ACS Appl. Mater. Interfaces. 12 (2020) 35328–35336. https://doi.org/10.1021/acsami.0c08036.

[168] L.C.T. Shoute, A. Anwar, S. MacKay, G.N. Abdelrasoul, D. Lin, Z. Yan, A.H. Nguyen, M.T. McDermott, M.A. Shah, J. Yang, J. Chen, X.S. Li, Immuno-impedimetric Biosensor for Onsite Monitoring of Ascospores and Forecasting of Sclerotinia Stem Rot of Canola, Sci. Reports 2018 81. 8 (2018) 1–9. https://doi.org/10.1038/s41598-018-30167-5.

[169] A.K. Assaifan, M. Hezam, M.A. Al-Gawati, K.E. Alzahrani, A. Alswieleh, P. Arunachalam, A. Al-Mayouf, A. Alodhayb, H. Albrithen, Label-free and simple detection of trace Pb(II) in tap water using non-faradaic impedimetric sensors, Sensors Actuators A Phys. 329 (2021) 112833. https://doi.org/10.1016/J.SNA.2021.112833.

[170] E. Ziino, S. Marnoto, J.M. Halpern, Investigation to Minimize Electrochemical Impedance Spectroscopy Drift, ECS Trans. 97 (2020) 737–745. https://doi.org/10.1149/09707.0737ECST/XML.

[171] P.C. Gao, W.Y. Tsai, B. Daffos, P.L. Taberna, C.R. Pérez, Y. Gogotsi, P. Simon, F. Favier, Graphene-like carbide derived carbon for high-power supercapacitors, Nano Energy. 12 (2015) 197–206. https://doi.org/10.1016/J.NANOEN.2014.12.017.

[172] R. Wang, Y. Xiang, X. Zhou, L. hua Liu, H. Shi, A reusable aptamer-based evanescent wave all-fiber biosensor for highly sensitive detection of Ochratoxin A, Biosens. Bioelectron. 66 (2015) 11–18. https://doi.org/10.1016/j.bios.2014.10.079.

[173] H. Berney, J. Alderman, W. Lane, J.K. Collins, A differential capacitive biosensor using polyethylene glycol to overlay the biolayer, Sensors Actuators B Chem. 44 (1997) 578–584. https://doi.org/https://doi.org/10.1016/s0925-4005(97)00239-6.

[174] A. Harada, M. Kamachi, Complex formation between poly (ethylene glycol) and α-cyclodextrin, Macromolecules. 23 (1990) 2821–2823.

[175] B. Pekec, A. Oberreiter, S. Hauser, K. Kalcher, A. Ortner, Electrochemical sensor based on a cyclodextrin modified carbon paste electrode for Trans-resveratrol analysis, Int. J. Electrochem. Sci. 7 (2012) 4089–4098.

[176] J.A. Baur, K.J. Pearson, N.L. Price, H.A. Jamieson, C. Lerin, A. Kalra, V. V. Prabhu, J.S. Allard, G. Lopez-Lluch, K. Lewis, P.J. Pistell, S. Poosala, K.G. Becker, O. Boss, D. Gwinn, M. Wang, S. Ramaswamy, K.W. Fishbein, R.G. Spencer, E.G. Lakatta, D. Le Couteur, R.J. Shaw, P. Navas, P. Puigserver, D.K. Ingram, R. De Cabo, D.A. Sinclair, Resveratrol improves health and survival of mice on a high-calorie diet, Nature. 444 (2006) 337–342. https://doi.org/10.1038/nature05354.

[177] J. Tomé-Carneiro, M. Larrosa, A. González-Sarrías, F.A. Tomás-Barberán, M.T. García-Conesa, J.C. Espín, Resveratrol and clinical trials: the crossroad from in vitro studies to human evidence., Curr. Pharm. Des. 19 (2013) 6064–6093. https://doi.org/10.2174/13816128113199990407.

[178] A.P. Singh, R. Singh, S.S. Verma, V. Rai, C.H. Kaschula, P. Maiti, S.C. Gupta, Health benefits of resveratrol: Evidence from clinical studies, Med. Res. Rev. 39 (2019) 1851–1891. https://doi.org/10.1002/med.21565.

[179] L.G. Carter, J.A. D'Orazio, K.J. Pearson, Resveratrol and cancer: focus on in vivo evidence, Endocr. Relat. Cancer. 21 (2014) 209–225. https://doi.org/10.1530/ERC-13-0171.

[180] J. Tomé-Carneiro, M. Larrosa, A. González-Sarrías, F. A Tomas-Barberan, M. Teresa Garcia-Conesa, J. Carlos Espin, Resveratrol and clinical trials: the crossroad from in vitro studies to human evidence, Curr. Pharm. Des. 19 (2013) 6064–6093. https://doi.org/10.2174/13816128113199990407.

[181] Z. Panahi, M.A. Merrill, J.M. Halpern, Reusable Cyclodextrin-Based Electrochemical Platform for Detection of trans -Resveratrol , ACS Appl. Polym. Mater. 2 (2020) 5086–5093. https://doi.org/10.1021/acsapm.0c00866.

[182] Y. Xue, X. Li, H. Li, W. Zhang, Quantifying thiol–gold interactions towards the efficient strength control, Nat. Commun. 5 (2014) 4348. https://doi.org/https://doi.org/10.1038/ncomms5348.

[183] E. Kaya, L.J. Mathias, Synthesis and characterization of physical crosslinking systems based on cyclodextrin inclusion/host-guest complexation, J. Polym. Sci. Part A Polym. Chem. 48 (2010) 581–592. https://doi.org/10.1002/pola.23771.

[184] I. Bontidean, C. Berggren, G. Johansson, E. Csöregi, B. Mattiasson, J.R. Lloyd, K.J. Jakeman, N.L. Brown, Detection of Heavy Metal Ions at Femtomolar Levels Using Protein-

Based Biosensors, Anal. Chem. 70 (1998) 4162–4169. https://doi.org/10.1021/ac9803636.

[185] C. Cao, Y. Zhang, C. Jiang, M. Qi, G. Liu, Advances on Aryldiazonium Salt Chemistry Based Interfacial Fabrication for Sensing Applications, ACS Appl. Mater. Interfaces. 9 (2017) 5031–5049. https://doi.org/10.1021/ACSAMI.6B16108.

[186] P. Bollella, Y. Hibino, K. Kano, L. Gorton, R. Antiochia, Enhanced Direct Electron Transfer of Fructose Dehydrogenase Rationally Immobilized on a 2-Aminoanthracene Diazonium Cation Grafted Single-Walled Carbon Nanotube Based Electrode, ACS Catal. 8 (2018) 10279–10289. https://doi.org/10.1021/ACSCATAL.8B02729.

[187] S. Eissa, L. L'Hocine, M. Siaj, M. Zourob, A graphene-based label-free voltammetric immunosensor for sensitive detection of the egg allergen ovalbumin, Analyst. 138 (2013) 4378–4384. https://doi.org/https://doi.org/10.1039/c3an36883a.

[188] Z. Panahi, T. Ren, J.M. Halpern, Nanostructured Cyclodextrin-Mediated Surface for Capacitive Determination of Cortisol in Multiple Biofluids, ACS Appl. Mater. Interfaces. 14 (2022) 42374–42387. https://doi.org/10.1021/acsami.2c07701.

[189] A. Harada, M. Kamachi, Complex formation between cyclodextrin and poly(propylene glycol), J. Chem. Soc. Chem. Commun. 19 (1990) 1322–1323. https://doi.org/10.1039/C39900001322.

[190] Y. Liu, Y.W. Yang, Y. Chen, H.X. Zou, Polyrotaxane with cyclodextrins as stoppers and its assembly behavior, Macromolecules. 38 (2005) 5838–5840. https://doi.org/10.1021/ma047327v.

[191] J. Filipović-Grčić, D. Voinovich, M. Moneghini, M. Bećirević-Laćan, L. Magarotto, I. Jalšenjak, Chitosan microspheres with hydrocortisone and hydrocortisone-hydroxypropyl-β-cyclodextrin inclusion complex, Eur. J. Pharm. Sci. 9 (2000) 373–379. https://doi.org/10.1016/S0928-0987(99)00078-0.

[192] S.L. Chang, A.K. Banga, Transdermal iontophoretic delivery of hydrocortisone from cyclodextrin solutions, J. Pharm. Pharmacol. 50 (1998) 635–640. https://doi.org/10.1111/j.2042-7158.1998.tb06897.x.

[193] G. Tiao, S. Hobler, J.J. Wang, T.A. Meyer, F.A. Luchette, J.E. Fischer, P.O. Hasselgren, Sepsis is associated with increased mRNAs of the ubiquitin-proteasome proteolytic pathway in human skeletal muscle, J. Clin. Invest. 99 (1997) 163–168. https://doi.org/10.1172/JCI119143.

[194] R.C. vaz de Mello, E.F. Sad, B.C. Andrade, S.P.F. Neves, S.M.E. Santos, M.M.S. Sarquis, P.E. Marik, E.P. Dias, Serum and salivary cortisol in the diagnosis of adrenal insufficiency and as a predictor of the outcome in patients with severe sepsis, Arq. Bras. Endocrinol. Metabol. 55 (2011) 455–459. https://doi.org/10.1590/S0004-27302011000700004.

[195] D.N. Nguyen, L. Huyghens, H. Zhang, J. Schiettecatte, J. Smitz, J.L. Vincent, Cortisol is an associated-risk factor of brain dysfunction in patients with severe sepsis and septic

shock, Biomed Res. Int. 2014 (2014). https://doi.org/10.1155/2014/712742.

[196] M. Holub, O. Džupová, M. Růžková, A. Stráníková, E. Bartáková, J. Máca, J. Beneš, H. Herwald, O. Beran, Selected Biomarkers Correlate with the Origin and Severity of Sepsis, Mediators Inflamm. 2018 (2018) 1–11. https://doi.org/10.1155/2018/7028267.

[197] S. Dalirirad, D. Han, A.J. Steckl, Aptamer-Based Lateral Flow Biosensor for Rapid Detection of Salivary Cortisol, ACS Omega. 5 (2020) 32890–32898. https://doi.org/10.1021/acsomega.0c03223.

[198] A. Singh, A. Kaushik, R. Kumar, M. Nair, S. Bhansali, Electrochemical Sensing of Cortisol: A Recent Update, Appl. Biochem. Biotechnol. 174 (2014) 1115–1126. https://doi.org/10.1007/s12010-014-0894-2.

[199] X. Liu, S.P.C. Hsu, W.C. Liu, Y.M. Wang, X. Liu, C.S. Lo, Y.C. Lin, S.C. Nabilla, Z. Li, Y. Hong, C. Lin, Y. Li, G. Zhao, R.J. Chung, Salivary Electrochemical Cortisol Biosensor Based on Tin Disulfide Nanoflakes, Nanoscale Res. Lett. 14 (2019) 189. https://doi.org/10.1186/s11671-019-3012-0.

[200] M.S. Khan, S.K. Misra, Z. Wang, E. Daza, A.S. Schwartz-Duval, J.M. Kus, D. Pan, D. Pan, Paper-Based Analytical Biosensor Chip Designed from Graphene-Nanoplatelet-Amphiphilic-diblock-co-Polymer Composite for Cortisol Detection in Human Saliva, Anal. Chem. 89 (2017) 13. https://doi.org/10.1021/acs.analchem.6b04769.

[201] N. Dhull, G. Kaur, V. Gupta, M. Tomar, Highly sensitive and non-invasive electrochemical immunosensor for salivary cortisol detection, Sensors Actuators, B Chem. 293 (2019) 281–288. https://doi.org/10.1016/j.snb.2019.05.020.

[202] S.K. Tuteja, C. Ormsby, S. Neethirajan, Noninvasive Label-Free Detection of Cortisol and Lactate Using Graphene Embedded Screen-Printed Electrode, Nano-Micro Lett. 10 (2018) 41. https://doi.org/10.1007/s40820-018-0193-5.

[203] M. Sekar, M. Pandiaraj, S. Bhansali, N. Ponpandian, C. Viswanathan, Carbon fiber based electrochemical sensor for sweat cortisol measurement, Sci. Rep. 9 (2019) 1–14. https://doi.org/10.1038/s41598-018-37243-w.

[204] Q. Zhou, P. Kannan, B. Natarajan, T. Maiyalagan, P. Subramanian, Z. Jiang, S. Mao, MnO2 cacti-like nanostructured platform powers the enhanced electrochemical immunobiosensing of cortisol, Sensors Actuators, B Chem. 317 (2020) 128134. https://doi.org/10.1016/j.snb.2020.128134.

[205] Y. Kim, J. Yang, H. Hur, S. Oh, H.H. Lee, Highly Sensitive Colorimetric Assay of Cortisol Using Cortisol Antibody and Aptamer Sandwich Assay, Biosensors. 11 (2021) 163. https://doi.org/10.3390/bios11050163.

[206] C. Leitão, A. Leal-Junior, A.R. Almeida, S.O. Pereira, F.M. Costa, J.L. Pinto, C. Marques, Cortisol AuPd plasmonic unclad POF biosensor, Biotechnol. Reports. 29 (2021) e00587. https://doi.org/10.1016/j.btre.2021.e00587.

[207] J. Briegel, C.L. Sprung, D. Annane, M. Singer, D. Keh, R. Moreno, P. Möhnle, Y. Weiss, A. Avidan, F.M. Brunkhorst, F. Fiedler, M. Vogeser, Multicenter comparison of cortisol as measured by different methods in samples of patients with septic shock, Intensive Care Med. 35 (2009) 2151–2156. https://doi.org/10.1007/s00134-009-1627-9.

[208] V. Anandan, R. Gangadharan, G. Zhang, Role of SAM chain length in enhancing the sensitivity of nanopillar modified electrodes for glucose detection, Sensors. 9 (2009) 1295–1305. https://doi.org/10.3390/s90301295.

[209] M. Sheng, D. Frurip, D. Gorman, Reactive chemical hazards of diazonium salts, J. Loss Prev. Process Ind. 38 (2015) 114–118. https://doi.org/10.1016/J.JLP.2015.09.004.

[210] J.A. Ribeiro, M.G.F. Sales, C.M. Pereira, Electrochemistry-Assisted Surface Plasmon Resonance Biosensor for Detection of CA 15-3, Anal. Chem. 93 (2021) 7815–7824. https://doi.org/10.1021/acs.analchem.0c05367.

[211] H. Shinzawa, T. Uchimaru, J. Mizukado, S.G. Kazarian, Non-equilibrium behavior of polyethylene glycol (PEG)/polypropylene glycol (PPG) mixture studied by Fourier transform infrared (FTIR) spectroscopy, Vib. Spectrosc. 88 (2017) 49–55. https://doi.org/10.1016/j.vibspec.2016.11.001.

[212] V. Haziri, S. Phal, J.F. Boily, A. Berisha, S. Tesfalidet, Oxygen Interactions with Covalently Grafted 2D Nanometric Carboxyphenyl Thin Films—An Experimental and DFT Study, Coatings. 12 (2022) 49. https://doi.org/10.3390/coatings12010049.

[213] P. Persoff, J.F. Thomas, Estimating Michaelis-Menten or Langmuir Isotherm Constants by Weighted Nonlinear Least Squares, Soil Sci. Soc. Am. J. 52 (1988) 886–889. https://doi.org/10.2136/sssaj1988.03615995005200030052x.

[214] T.A. Osmari, R. Gallon, M. Schwaab, E. Barbosa-Coutinho, J.B. Severo, J.C. Pinto, Statistical Analysis of Linear and Non-Linear Regression for the Estimation of Adsorption Isotherm Parameters, Adsorpt. Sci. Technol. 31 (2013) 433–458. https://doi.org/10.1260/0263-6174.31.5.433.

[215] Y. Huang, M.C. Bell, I.I. Suni, Impedance biosensor for peanut protein Ara h 1, Anal. Chem. 80 (2008) 9157–9161. https://doi.org/10.1021/ac801048g.

[216] D.A. Armbruster, T. Pry, Limit of blank, limit of detection and limit of quantitation., Clin. Biochem. Rev. 29 Suppl 1 (2008) S49-52.

[217] C.-L. Lin, T.-J. Wu, D.A. Machacek, N.-S. Jiang, P.C. Kao, Urinary Free Cortisol and Cortisone Determined by High Performance Liquid Chromatography in the Diagnosis of Cushing's Syndrome [1], J. Clin. Endocrinol. Metab. 82 (1997) 151–155. https://doi.org/10.1210/jcem.82.1.3687.

[218] E. Aardal, A.C. Holm, Cortisol in Saliva — Reference Ranges and Relation to Cortisol in Serum, Clin. Chem. Lab. Med. 33 (1995) 927–932. https://doi.org/10.1515/cclm.1995.33.12.927.

[219] T.J. Moore, B. Sharma, Direct Surface Enhanced Raman Spectroscopic Detection of Cortisol at Physiological Concentrations, Anal. Chem. 92 (2019) 2052–2057. https://doi.org/10.1021/ACS.ANALCHEM.9B04532.

[220] J.E.L. Villa, I. Garcia, D. Jimenez de Aberasturi, V. Pavlov, M.D.P.T. Sotomayor, L.M. Liz-Marzán, SERS-based immunoassay for monitoring cortisol-related disorders, Biosens. Bioelectron. 165 (2020) 112418. https://doi.org/10.1016/J.BIOS.2020.112418.

[221] B.E.F. de Ávila, M. Zhao, S. Campuzano, F. Ricci, J.M. Pingarrón, M. Mascini, J. Wang, Rapid micromotor-based naked-eye immunoassay, Talanta. 167 (2017) 651–657. https://doi.org/10.1016/J.TALANTA.2017.02.068.

[222] G. Finco, P. Scano, E. D'Aloja, E. Locci, M. Musu, P. Mura, V. Fanos, A. Noto, Metabolomics: which role in asphyxia and Sepsis?, Anesth. Clin. Res. 5 (2014) 420. https://doi.org/http://dx.doi.org/10.4172/2155-6148.1000420.

[223] M. Garcia-Simon, J.M. Morales, V. Modesto-Alapont, V. Gonzalez-Marrachelli, R. Vento-Rehues, A. Jorda-Miñana, J. Blanquer-Olivas, D. Monleon, Prognosis biomarkers of severe sepsis and septic shock by 1h NMR urine metabolomics in the intensive care unit, PLoS One. 10 (2015). https://doi.org/10.1371/JOURNAL.PONE.0140993.

[224] Qun Liang, Han Liu, Tianyu Zhang, Yan Jiang, Haitao Xing, Ai-hua Zhang, Potential urine biomarkers from a high throughput metabolomics study of severe sepsis in a large Asian cohort, RSC Adv. 5 (2015) 102204–102209. https://doi.org/10.1039/C5RA19875E.

[225] L. Ambroggio, T.A. Florin, S.S. Shah, R. Ruddy, L. Yeomans, J. Trexel, K.A. Stringer, Emerging Biomarkers of Illness Severity: Urinary Metabolites Associated with Sepsis and Necrotizing Methicillin-Resistant Staphylococcus aureus Pneumonia, Pharmacotherapy. 37 (2017) 1033–1042. https://doi.org/10.1002/phar.1973.

[226] B. Mickiewicz, H.J. Vogel, H.R. Wong, B.W. Winston, Metabolomics as a novel approach for early diagnosis of pediatric septic shock and its mortality, Am. J. Respir. Crit. Care Med. 187 (2013) 967–976. https://doi.org/10.1164/RCCM.201209-1726OC.

[227] F. V, B. L, A. R, A. L, Pharma-metabolomics in neonatology: is it a dream or a fact?, Curr. Pharm. Des. 18 (2012) 2996–3006. https://doi.org/10.2174/1381612811209022996.

[228] H.A. Tsai, M.J. Syu, Synthesis of creatinine-imprinted poly(β-cyclodextrin) for the specific binding of creatinine, Biomaterials. 26 (2005) 2759–2766. https://doi.org/10.1016/J.BIOMATERIALS.2004.07.037.

[229] I. Nicolis, F. Villain, A.W. Coleman, C. DeRango, X-ray crystallographic structure of the two-to-one a-cyclodextrin-acetone. 9H20 compound, Supramol. Chem. 3 (1994) 251–259. https://doi.org/10.1080/10610279408034923.

[230] Shin-Jung Choi, and Bo-Geum Choi, S.-M. Park*, Electrochemical Sensor for Electrochemically Inactive β-d(+)-Glucose Using α-Cyclodextrin Template Molecules, Anal. Chem. 74 (2002) 1998–2002. https://doi.org/10.1021/AC0107913.

[231] W. Hirsch, T. Muller, R. Pizer, P.J. Ricatto, Complexation of glucose by α- and β-cyclodextrins, Can. J. Chem. 73 (1995) 12–15. https://doi.org/10.1139/v95-003.

[232] D.L. Wernick, Z. Savion, J. Levy, Selective esterolysis of nitrophenyl acetates in crystalline α-cyclodextrin complexes, J. Incl. Phenom. 6 (1988) 483–490. https://doi.org/10.1007/BF00660746.

[233] A.J. Kapor, L.B. Nikolić, V.D. Nikolić, M.Z. Stanković, M.D. Cakić, D.P. Ilić, I.I. Mladenović-Ranisavljević, I.S. Ristić, The synthesis and characterization of iron(II) fumarate and its inclusion complexes with cyclodextrins, Adv. Technol. 1 (2012) 7–15.

[234] J. Szejtli, Cyclodextrins in Foods, Cosmetics and Toiletry, (1988) 307–334. https://doi.org/10.1007/978-94-015-7797-7_4.

[235] V. Suvarna, A. Kajwe, M. Murahari, G. V Pujar, B.K. Inturi, A.P. Sherje, Inclusion Complexes of Nateglinide with HP–β–CD and L-Arginine for Solubility and Dissolution Enhancement: Preparation, Characterization, and Molecular Docking Study, J. Pharm. Innov. 12 (2017) 168–181. https://doi.org/10.1007/s12247-017-9275-z.

[236] A. Patil, Y. Pore, B. Kuchekar, Effect of L-arginine on bicalutamide complexation with hydroxypropyl-beta-cyclodextrin, Dig. J. Nanomater. Biostructures. 3 (2008) 89–98.

[237] M.J. Alrawashdeh, T.R. Radwan, K.A. Abunawas, Performance of Linear Discriminant Analysis Using Different Robust Methods, Eur. J. Pure Appl. Math. 11 (2018) 284–298. https://doi.org/10.29020/NYBG.EJPAM.V11I1.3176.

[238] M.J. Gomez, Z. De Benzo, C. Gomez, E. Marcano, H. Torres, M. Ramirez, Comparison of methods for outlier detection and their effects on the classification results for a particular data base, Anal. Chim. Acta. 239 (1990) 229–243. https://doi.org/10.1016/S0003-2670(00)83857-X.

[239] B.D. Wagner, F.J. Accurso, T.A. Laguna, THE APPLICABILITY OF URINARY CREATININE AS A METHOD OF SPECIMEN NORMALIZATION IN THE CYSTIC FIBROSIS POPULATION, J. Cyst. Fibros. 9 (2010) 212. https://doi.org/10.1016/J.JCF.2010.02.004.

[240] B.M. Warrack, S. Hnatyshyn, K.H. Ott, M.D. Reily, M. Sanders, H. Zhang, D.M. Drexler, Normalization strategies for metabonomic analysis of urine samples, J. Chromatogr. B. Analyt. Technol. Biomed. Life Sci. 877 (2009) 547–552. https://doi.org/10.1016/J.JCHROMB.2009.01.007.

[241] M.D. Martin, J.S. Woods, B.G. Leroux, T. Rue, T.A. Derouen, J. Leitão, M.F. Bernardo, H.S. Luis, T.S. Benton, J. Kushleika, Longitudinal urinary creatinine excretion values among preadolescents and adolescents, Transl. Res. 151 (2008) 51–56. https://doi.org/10.1016/j.trsl.2007.10.001.

Appendix

Appendix A-Abbreviations

SERS: Surface enhanced raman spectroscopy
HPLC: High performance liquid chromatography
SPE: Solid phase extraction
SPME: Solid phase microextraction
UA: Uric acid
EP: Epinephrine
Tyr: Tyrosine
CA: Chronoamperometry
EIS: Electrochemical impedance spectroscopy
DPV: Differential pulse voltammetry
AdDPSV: Adsorptive differential pulse stripping voltammetry
SWV: Square wave voltammetry
LSV: Linear sweep voltammetry
CV: Cyclic voltammetry
GO: Graphene oxide
GON: Graphene oxide nanosheet
RGO: Reduced graphene oxide
CQD: Carbon quantum dot
GQD: Graphene quantum dot
CNT: Carbon nanotube
SWCNT: Single-walled carbon nanotube
MWCNT: Multi-walled carbon nanotube
LOD: Limit of detection
TMD: Transition metal dichalcogenides
MOFs: Metal organic frameworks
CP: Conjugated polymer
POMs: Polyoxometalates
PEDOT: Poly(3,4-ethylenedioxythiophene)
PANI: Poly(aniline)
PPY: Poly(pyrrole)
CD: Cyclodextrin
αCD: α cyclodextrin
βCD: β cyclodextrin
γCD: γ cyclodextrin
HP-βCD: Hydroxypropyl-β cyclodextrin
HP-γCD: Hydroxypropyl-γ cyclodextrin

GCE: Glassy carbon electrode
P-GLY: Poly(glycine)
MIP: Molecular imprinted polymer
EFTA: Ethyl 2-(4-ferrocenyl-[1,2,3]triazol-1-yl) acetate
CPE: Carbon paste electrode
MCPE: Modified carbon paste electrode
MW-Fes: Filtered multi-walled carbon nanotubes
GONRs-CH: Graphene oxide nanoribbons in chitosan
BODIPY: Borondipyrromethene
SPCE: Screen printed carbon electrode
TNFs: Titanium dioxide nanofibers
PGE: Pencil graphite electrode
GPE: Graphite paste electrode
PVIM: Poly(ionic liquid)
Poly(DA): Poly(dopamine)
Poly(HQ): Poly(hydroquinone)
β-NiS: Restacked nanosheets of nickel sulfide
Poly(BCG): Poly(3,3’,5,5’-tetrabromo-mcresolsulfonphthalein)
EB-PPY: Electron beam irradiated Poly(pyrrole)
BSA: Bovine serum albumin
Poly(BCP): Poly(bromocresol purple)
ePAD: Electrochemical paper-based analytical device
MPC: Macroporous carbon embedded
PPy: Polypyrrole
PEG: Polyethylene glycol
PPG: polypropylene glycol
3MPA: 3-Mercaptopropionic Acid
EDC: 1-Ethyl-3-(3-dimethylaminopropyl)carbodiimide
NHS: N-hydroxysuccinimide
LDA: Linear discriminant analysis
PCA: Principal Component Analysis

Appendix B-Copyright

Figure 1.4

ELSEVIER LICENSE
TERMS AND CONDITIONS

Aug 15, 2022

This Agreement between University of New Hampshire -- Zahra Panahi ("You") and Elsevier ("Elsevier") consists of your license details and the terms and conditions provided by Elsevier and Copyright Clearance Center.

License Number	5370330754555
License date	Aug 15, 2022
Licensed Content Publisher	Elsevier
Licensed Content Publication	Microchemical Journal
Licensed Content Title	Sensitive cholesterol determination by β-cyclodextrin recognition based on fluorescence enhancement of gold nanoclusters
Licensed Content Author	Wenxiang Xiao,Zhenzhen Yang,Jing Liu,ZhenCheng Chen,Hua Li
Licensed Content Date	Apr 1, 2022
Licensed Content Volume	175
Licensed Content Issue	n/a
Licensed Content Pages	1
Start Page	107125

End Page	0
Type of Use	reuse in a thesis/dissertation
Portion	figures/tables/illustrations
Number of figures/tables /illustrations	1
Format	both print and electronic
Are you the author of this Elsevier article?	No
Will you be translating?	No
Title	Electrochemical Impedance Spectroscopy Biosensors Based on Nanostructured Cyclodextrin Surfaces for Detection of Hydrophobic Metabolites
Institution name	University of New Hampshire
Expected presentation date	Jan 2023
Portions	Scheme 1 on page 3
Requestor Location	University of New Hampshire 1150 Woodbury Avenue, Apt 1 PORTSMOUTH, NH 03801 United States Attn: University of New Hampshire
Publisher Tax ID	98-0397604
Total	0.00 USD

Figure 1.5

ELSEVIER LICENSE
TERMS AND CONDITIONS

Dec 02, 2022

This Agreement between University of New Hampshire -- Zahra Panahi ("You") and Elsevier ("Elsevier") consists of your license details and the terms and conditions provided by Elsevier and Copyright Clearance Center.

License Number	5440821362972
License date	Dec 02, 2022
Licensed Content Publisher	Elsevier
Licensed Content Publication	Journal of Electroanalytical Chemistry
Licensed Content Title	Electropolymerization of β-cyclodextrin onto multi-walled carbon nanotube composite films for enhanced selective detection of uric acid
Licensed Content Author	Mulugeta B. Wayu,Luke T. DiPasquale,Margaret A. Schwarzmann,Samuel D. Gillespie,Michael C. Leopold
Licensed Content Date	Dec 15, 2016
Licensed Content Volume	783
Licensed Content Issue	n/a
Licensed Content Pages	9
Start Page	192

End Page	200
Type of Use	reuse in a thesis/dissertation
Portion	figures/tables/illustrations
Number of figures/tables /illustrations	1
Format	both print and electronic
Are you the author of this Elsevier article?	No
Will you be translating?	No
Title	Electrochemical Impedance Spectroscopy Biosensors Based on Nanostructured Cyclodextrin Surfaces for Detection of Hydrophobic Metabolites
Institution name	University of New Hampshire
Expected presentation date	Jan 2023
Portions	Scheme 1
Requestor Location	University of New Hampshire 1150 Woodbury Avenue, Apt 1 PORTSMOUTH, NH 03801 United States Attn: University of New Hampshire
Publisher Tax ID	98-0397604

Figure 1.6

ELSEVIER LICENSE
TERMS AND CONDITIONS

Dec 02, 2022

This Agreement between University of New Hampshire -- Zahra Panahi ("You") and Elsevier ("Elsevier") consists of your license details and the terms and conditions provided by Elsevier and Copyright Clearance Center.

License Number	5440830430159
License date	Dec 02, 2022
Licensed Content Publisher	Elsevier
Licensed Content Publication	Biosensors and Bioelectronics
Licensed Content Title	Non-enzymatic electrochemical detection of cholesterol using β-cyclodextrin functionalized graphene
Licensed Content Author	Nidhi Agnihotri,Ankan Dutta Chowdhury,Amitabha De
Licensed Content Date	Jan 15, 2015
Licensed Content Volume	63
Licensed Content Issue	n/a
Licensed Content Pages	6
Start Page	212

End Page	217
Type of Use	reuse in a thesis/dissertation
Portion	figures/tables/illustrations
Number of figures/tables /illustrations	1
Format	both print and electronic
Are you the author of this Elsevier article?	No
Will you be translating?	No
Title	Electrochemical Impedance Spectroscopy Biosensors Based on Nanostructured Cyclodextrin Surfaces for Detection of Hydrophobic Metabolites
Institution name	University of New Hampshire
Expected presentation date	Jan 2023
Portions	Scheme 1
Requestor Location	University of New Hampshire 1150 Woodbury Avenue, Apt 1 PORTSMOUTH, NH 03801 United States Attn: University of New Hampshire
Publisher Tax ID	98-0397604

Chapter 3

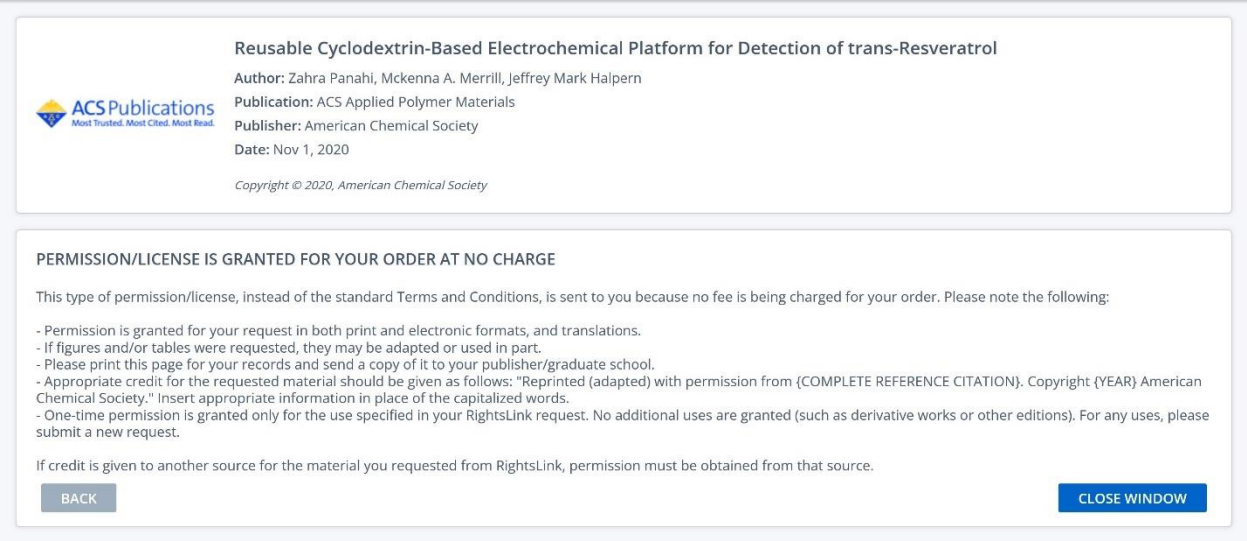

Reusable Cyclodextrin-Based Electrochemical Platform for Detection of trans-Resveratrol

Author: Zahra Panahi, Mckenna A. Merrill, Jeffrey Mark Halpern
Publication: ACS Applied Polymer Materials
Publisher: American Chemical Society
Date: Nov 1, 2020

Copyright © 2020, American Chemical Society

PERMISSION/LICENSE IS GRANTED FOR YOUR ORDER AT NO CHARGE

This type of permission/license, instead of the standard Terms and Conditions, is sent to you because no fee is being charged for your order. Please note the following:

- Permission is granted for your request in both print and electronic formats, and translations.
- If figures and/or tables were requested, they may be adapted or used in part.
- Please print this page for your records and send a copy of it to your publisher/graduate school.
- Appropriate credit for the requested material should be given as follows: "Reprinted (adapted) with permission from {COMPLETE REFERENCE CITATION}. Copyright {YEAR} American Chemical Society." Insert appropriate information in place of the capitalized words.
- One-time permission is granted only for the use specified in your RightsLink request. No additional uses are granted (such as derivative works or other editions). For any uses, please submit a new request.

If credit is given to another source for the material you requested from RightsLink, permission must be obtained from that source.

BACK CLOSE WINDOW

Chapter 4

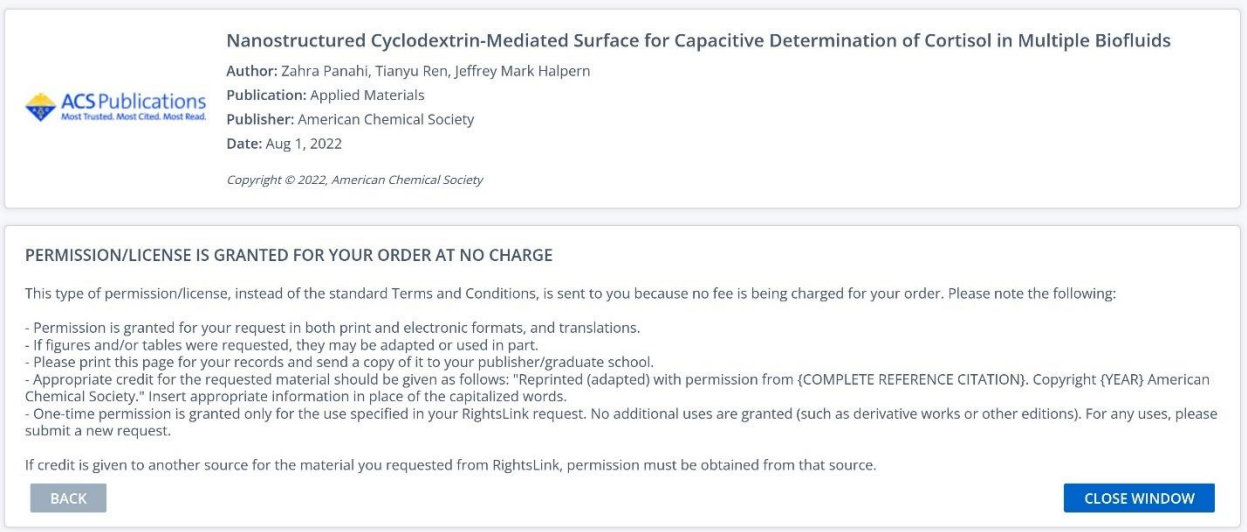

Nanostructured Cyclodextrin-Mediated Surface for Capacitive Determination of Cortisol in Multiple Biofluids

Author: Zahra Panahi, Tianyu Ren, Jeffrey Mark Halpern
Publication: Applied Materials
Publisher: American Chemical Society
Date: Aug 1, 2022

Copyright © 2022, American Chemical Society

PERMISSION/LICENSE IS GRANTED FOR YOUR ORDER AT NO CHARGE

This type of permission/license, instead of the standard Terms and Conditions, is sent to you because no fee is being charged for your order. Please note the following:

- Permission is granted for your request in both print and electronic formats, and translations.
- If figures and/or tables were requested, they may be adapted or used in part.
- Please print this page for your records and send a copy of it to your publisher/graduate school.
- Appropriate credit for the requested material should be given as follows: "Reprinted (adapted) with permission from {COMPLETE REFERENCE CITATION}. Copyright {YEAR} American Chemical Society." Insert appropriate information in place of the capitalized words.
- One-time permission is granted only for the use specified in your RightsLink request. No additional uses are granted (such as derivative works or other editions). For any uses, please submit a new request.

If credit is given to another source for the material you requested from RightsLink, permission must be obtained from that source.

BACK CLOSE WINDOW